The Hashemite Kingdom of Jordan
Scientific Research Support Fund
The Hashemite University

JJEES

Jordan Journal of Earth and Environmental Sciences

Indexed by Scopus
ELSEVIER

Volume (15) Number (4)

Cover photo © Dr. Safeia Hamasha

JJEES is an International Peer-Reviewed Research Journal

ISSN 1995-6681 jjees.hu.edu.jo December 2024

Jordan Journal of Earth and Environmental Sciences (JJEES)

JJEES is an International Peer-Reviewed Research Journal, Issued by Deanship of Scientific Research, The Hashemite University, in corporation with, the Jordanian Scientific Research Support Fund, the Ministry of Higher Education and Scientific Research.

Editorial Board:

Associate Editorial Board: (Arranged Alphabetically)

International Advisory Board: (Arranged Alphabetically)

Editorial Board Support Team:

Submission address:

Manuscripts should be submitted electronically to the following e-mail:

jjees@hu.edu.jo

For more information and previous issues:

www.jjees.hu.edu.jo

Hashemite Kingdom of Jordan

Scientific Research Support Fund

Hashemite University

Jordan Journal of Earth and Environmental Sciences

JJEES

An International Peer-Reviewed Scientific Journal

Financed by the Scientific Research Support Fund

Volume 15 Number (4)

http:// jjees.hu.edu.jo/

ISSN 1995-6681

Nature's artistry: Weathering rocks of Wadi Rum
Photograph by Dr. Safeia Hamasha

JJEES
Jordan Journal of Earth and Environmental Sciences

JJEES

JJEES (2024) 15 (4): 225-233
ISSN 1995-6681

Jordan Journal of Earth and Environmental Sciences

Biochar for Lead Removal from Aqueous Solution

Maamoun Al Jedaih, Zaydoun Abu Salem*, Kamel Alzboon

Al-Balqa Applied University, Department of Environmental Engineering, Al-Huson University College, Al-Huson, Irbid, Jordan

Received on May 30, 2024; Accepted on August 25, 2024

Abstract

Biochar as an eco-friendly and low-cost material generally produced from organic wastes such as agricultural wastes, forestry residues, and municipal wastes has attracted increasing attention shown by its increasing use in different environmental applications. This work has been conducted to determine the effectiveness of biochar in immobilizing and removing Pb^{+2} from aqueous solution. This work includes the production of biochar from the branches of lemon and olive trees and utilizing it for Pb^{+2} removal from an aqueous solution. The effects of pH, biochar doses, and contact time were investigated. The results showed that Pb^{+2} can be removed successfully using a low dose of biochar within a short time. A removal efficiency of 99.4% of 50ppm of Pb^{+2} can be achieved by a dose of 0.5g of biochar. A high concentration of Pb^{+2} needs higher doses up to 3g and a lengthy time up to 180 minutes. The pseudo-second order model provided the best fitting for isotherm data and is the best in describing kinetic behavior.

Keywords: *Biochar, Lead, Heavy Metal Ions, Pollutants, Removal Efficiency.*

1. Introduction

The world's water resources are deteriorating due to the continuous discharge of many organic and inorganic contaminants such as dyes, heavy metals, surfactants, pharmaceuticals, pesticides, and personal care products from industries and municipalities into water bodies. Most of these pollutants are highly persistent in nature and are otherwise converted into recalcitrant form. The uncontrolled discharge of these pollutants is a concern because of their suspected negative effects on ecosystems (Zulfiqar et al., 2019).

Several conventional technologies are applied worldwide for the removal of wastewater pollutants including coagulation-flocculation, adsorption, membrane filtration, reverse osmosis, chemical precipitation, ion exchange, electrochemical treatment, solvent extraction, and flotation for the removal of inorganic pollutants (Razzak et al., 2022). However, these technologies suffer from a range of disadvantages stretching from inefficiency in removing pollutants at low concentrations to completely converting pollutants into biodegradable materials, less toxic byproducts, high energy and chemicals consumption, process complexity, high maintenance, and operation costs, etc. An efficient and workable treatment process should meet both economic and environmental requirements to be marketed and applied on a large scale. The incorporation of low-cost and available materials in different treatment processes could decrease the global treatment cost and increase the process efficiency (Al-Zboon et al., 2011; Hamad, 2013).

Biochar is a carbon-rich material produced by pyrolysis of organic matter, such as wood, crop residues, and animal manure. When used as a soil amendment, biochar has proven various mechanisms for removing pollutants (Tomczyk et al., 2020; Ahmad et al., 2014; Tang et al., 2013).

Biochar, as an eco-friendly and low-cost material generally produced from organic wastes such as agricultural wastes, forestry residues, and municipal wastes, has attracted increasing attention due to its increasing use in different environmental applications. As a stable carbon-rich material, it shows incredible potential to handle water/wastewater contaminants. Its application is gaining increasing interest due to the availability of feedstock, the simplicity of the preparation methods, and their enhanced physic-chemical properties. In addition to biochar, compost is also produced by converting organic wastes through biological fermentation. (Al-Zawahreh et al., 2022)

Biochar application improves soil fertility via two mechanisms: supplying nutrients to the soil, such as potassium and, to a lesser degree, micronutrients, or keeping nutrients from other sources, including the soil itself. Adding biochar into the soil increased the pH of acidic soils by 0.5-1, such as yellow-brown soil and fluvial-aquic soil. However, the charcoal and fertilizer treatments had a different effect. Biochar, rather than being a key source of nutrients for microorganisms, is thought to enhance the physical and chemical soil environment, making bacteria more comfortable (Lehmann et al., 2006; Qadan, 2022). Biochar, applied to soil, improves plant growth and crop yields, enhancing food production and sustainability in areas of depleted soils, low organic resources, insufficient water, and/or limited access to agrochemical fertilizers (Chen et al., 2011). It is a carbonaceous residue created by the pyrolysis of biomass that has been shown to improve moisture retention, air permeability, and soil structure. Biochar contains both organic C and inorganic C (ash). It also increases the overall porosity of clayey soil. Similarly, a rise in porosity has been

* Corresponding author e-mail: zaydoun@bau.edu.jo

recorded in coarser soils(Cimo et al., 2014; De Ridder et al., 2012).

During biochar production, bio-oil and gases, such as hydrogen, are produced and can be used as energy sources supplying power to homes or automobiles. Biochar has the capacity for remediation of contaminated soil and provides additional benefits to the environment.

Biochar is formed by the pyrolysis (thermal decomposition) of organic biomass or agricultural residues (Xiao et al., 2014). It is mainly used to improve soil nutrient content and to sequester carbon from the environment (Lehmann, 2006). Its highly porous structure makes it an attractive choice for soil amendment as it improves the water-holding capacity of the soil by increasing its total surface area. After adding biochar, improvements in the physicochemical characteristics of the soil and crop productivity are anticipated since it may retain moisture and nutrients. Biochar raises soil pH and organic carbon content, increases soil water-holding capacity, lowers pollutant levels, and increases crop yields. Meta-analyses show average crop yield increases 10%–42% after adding biochar, with the greatest increases in low-nutrient P-sorbing acidic soils (common in the tropics) and in sandy soils in drylands due to an increase in nutrient retention and water-holding capacity (Srinivasarao et al., 2013).

Biochar is considered a cost-effective alternative to the activated carbon in water and soil treatment due to its practical production and low cost. It has been used to remove various pollutants, including volatile organic compounds, heavy metal ions, pesticides, drugs, dyes, and polycyclic aromatic hydrocarbons (El-Naggar et al., 2021; Zhao et al., 2021). Biochar's efficiency in removing pollution is due to its high surface area, porous structure, and chemical properties (Liang et al., 2021).

A clean biochar has limited potential for absorbing and removing pollutants, as its surface area is relatively modest. The characteristics of pollutants can be influenced by abiotic and/or biotic processes. Various modification approaches, such as coating, enhancing additives, base treatment, acid treatment, magnetic modification, and composites with other materials, have been increasingly highlighted to improve biochar's surface and mechanical characteristics (Arif et al., 2021).

Biochar properties are influenced by various parameters, such as heating speed, pyrolysis temperature, biomass type, and residence time. The interaction between heavy metals and biomass involves reduction, electrostatic attraction, complexation, precipitation, and cation exchanges. which are influenced by factors such as pH levels, dissolved organic carbon, and biomass content. Organic pollutants interact with biochar through hydrophobic interactions, Pi-interactions, and hydrogen bond interactions (Khalid et al., 2020).

These properties enable biochar to efficiently immobilize inorganic pollutants in soil, thereby reducing their bioavailability and potential environmental and human health risks. However, the effectiveness of biochar for pollution removal can vary depending on factors such as the type and concentration of pollutants, soil characteristics, and biochar properties (Mohanty et al., 2018; Qambrani et al., 2017; Xiang et al., 2022).

According to the most recent study, biochar can be used in various wastewater treatment applications, including catalysis, adsorption, redox, and biocidal processes. all of these applications involve different reaction mechanisms (Zhao et al., 2021; Zhou et al., 2014). Biochar-based materials offer several advantages, such as high porosity, large surface area, improved ion exchange capacity, and abundant functional groups. Numerous publications have supplied detailed discussions on the physicochemical properties of biochar and its potential environmental applications (Yuan et al., 2019).

Liang et al., (2021) investigated preparation techniques and physicochemical features of biochar composites and their performance in removing sewage contaminants. They discussed the use of biochar and biochar-based materials for breaking down and changing organic pollutants, as well as sorbing heavy metals and radionuclides. Biochar is typically produced from low-cost biomass, such as forest wastes, agricultural residues, food waste, fertilizers, and sludge, which are widely available and abundant worldwide. However, these different types of byproducts pose disposal challenges, making the conversion of waste to biochar a workable and sustainable solution.

In a batch study, Karishma et al., (2021) investigated the efficiency of Ulva lactuca carbon for removing lead from aqueous solutions. The study considered the effects of various parameters, including pH, adsorbent dosage, effective contact time, and initial concentration. The optimal conditions were found to be a pH of 3, an adsorbent dose of 0.8 g, and a contact time of 30 minutes. The results indicated that Ulva lactuca carbon is a cost-effective and efficient material for removing lead from aqueous solutions. The carbon can be reused by removing lead after being treated with 0.1M HNO_3, and the study concluded that seaweed carbon is more efficient when activated than when untreated.

Lei et al., (2019) prepared biochar from bio-physical dry sludge and found that increasing the pyrolysis temperature has improved the adsorption effect of biochar on Pb^{+2}, and the adsorption capacity of lead has also increased with increasing of the pH solutionvalue. Mireles et al., (2018) conducted a study on lead removal from aqueous solutions using biochars derived from corn stover, orange peels, and pistachio shells in the Lower Rio Grande Valley in South Texas, USA. The study found that the efficiency of lead ion (Pb^{+2}) removal through batch adsorption experiments has increased with increasing pH from 2 to 6, reaching a maximum adsorption of Pb^{+2} at a pH of 6. The results also indicated that biochar is a cost-effective adsorbent material for heavy metals in water.

Mahdi et al., (2018) conducted a study on the removal of lead (II) from aqueous solutions using biochars produced from date seed biomass in Riyadh, Saudi Arabia. The study found that the amount of Pb^{+2} adsorbed varied significantly with initial Pb^{+2} concentration, solution pH, and contact

time. The study found that the maximum adsorption capacity of DSB550-3 was obtained at a pH of 6. Yonggang et al., (2020) investigated the influence of pyrolysis temperature on the characteristics and lead(II) adsorption capacity of phosphorus-engineered poplar sawdust biochar.

Inorganic pollution has several adverse effects on the environment, including soil degradation, decreased soil fertility, and contamination of groundwater and surface water. Moreover, inorganic pollutants can accumulate in plants and animals, leading to bioaccumulation and biomagnification in food chains, which can ultimately impact human health (Kristanti et al., 2021; Khan et al., 2018; Khudhur et al., 2018; Rashmi et al., 2020).

Researchers have extensively studied the negative impacts of inorganic pollution in soil on the environment and human health. Overall, inorganic pollution in soil poses a significant threat to the environment and human health, highlighting the need for effective pollution remediation strategies such as the use of biochar as a soil amendment. Inorganic pollutants have the potential to change the physical and chemical properties of soil, resulting in soil degradation and reduced fertility, which can have significant impacts on agricultural productivity and food security (Gautam et al., 2023; Qin et al., 2021; Cui et al., 2023). Exposure to heavy metals, such as lead, cadmium, and mercury, can result in neurological and developmental disorders, kidney damage, and cancer. (Sevim et al., 2020; Jyothi et al., 2020; Fu et al., 2020; Engwa et al., 2019).

Bolan et al. (2022) emphasized the necessity of implementing effective management and remediation strategies to decrease the negative impacts of inorganic pollution in soil on the environment and human health. The use of biochar as a soil amendment is one potential strategy that has shown promise in reducing the bioavailability of inorganic pollutants in soil.

Biochar has mechanisms for pollution removal through various methods, such as adsorption, precipitation, and ion exchange. Adsorption occurs when pollutants bind to the surface of biochar through physical and chemical interactions, helped by the high surface area and porous structure of biochar. Biochar can also ease the precipitation of inorganic pollutants by changing soil pH or providing a surface for the formation of mineral phases. Precipitation occurs when pollutants react with biochar or other soil components to form insoluble compounds that can be immobilized in the soil. Additionally, biochar can remove inorganic pollutants through ion exchange, where the positively charged biochar surface attracts and binds with negatively charged ions of pollutants, such as heavy metals (Barquilha and Braga, 2021; Zeghioud et al., 2022).

Pyrolysis is a thermochemical conversion process of biomass that occurs under a low or no-oxygen environment. It can be categorized into three broad types: fast pyrolysis, intermediate pyrolysis, and slow pyrolysis. The first type occurs within a few seconds and is influenced by phase transition phenomena, heat and mass transfer processes, and chemical reaction kinetics. Depending on the process parameters such as temperature, residence time, heating rate, and flow rate of sweeping gas, slow pyrolysis can retain up to 50% of the feedstock carbon,yielding more biochar than any other type of pyrolysis. Temperature increases also result in a decrease in the amount of final solid product, with a concurrent rise in ash content due to naturally existing inorganic components in all biomasses (Shaaban et al., 2014).

The biochar structure is made up of aligned honeycomb-like groups of pores, generated by the carbonaceous skeleton, and is formed during the thermal decomposition of the raw material. This structure is the outcome of the raw material's biological capillary structure. Volume is reduced due to the loss of volatile organic molecules during thermal decomposition (Lehmann et al., 2006).

Lead is a bluish-white metal with a glossy finish that is extremely soft, pliable, ductile, and a poor electrical conductor. Although it is highly corrosion-resistant, it tarnishes when exposed to air. Most lead found in the environment originates from human activity. Lead is among the metals that have the most significant negative effects on human health, including increased blood pressure, kidney damage, and fever. Due to the presence of oxygen-containing functional groups such as phenolic, lactones, and carboxyl in their structure, lead can bond with heavy metals. (Mohan and Pittman, 2007; Liu and Zhang, 2009).

The pH of an aqueous solution has been proven in studies to impact the sorption of pollutants onto biochar. This impact is due to the fact that the oxygen-containing functional groups in biochar are pH-dependent, resulting in variations in surface charge and ionization at the biochar surface. As a result, biochar's adsorption ability for eliminating pollutants varies with pH (Barquilha and Braga, 2021).

Lead has been removed from water using a variety of techniques, including filtration, sedimentation, coagulation/flocculation, precipitation, ion exchange, chemical reduction, phytoremediation, bioremediation, immobilization, electrocoagulation, and electrokinetic remediation (Lei et al., 2019; Liang et al., 2021; Liu and Zhang 2009). Adsorption is preferred over other removal methods because it is less expensive, natural adsorbents are available, the process is safe, and it is simple to separate the adsorbate from the solution (Hosseini et al., 2022). Hosseini et al. found that a novel ligand-based conjugate material (CMA) corresponded well with the Langmuir isotherm model, had a maximum adsorption capacity of 196.35 mg/g, and could remove 99 percent of Pb^{+2} from water under ideal conditions. Researchers discovered that lead could be effectively removed from water-based solutions, using biochar generated from solid and liquid waste from olive mills. The maximum lead removal percentages were obtained when a high dose of biochar was combined with slightly acidic pH values (Kypritidou et al., 2022). With an estimated maximum adsorption capacity of 40.8 mg/g, this biochar fared better than others derived from other biomass sources.

As mentioned earlier, biochar is anticipated to be an effective product in reducing lead contamination because of its intense porous structure and high adsorption affinity for pollutants. Biochar was selected due to its ease of use, low cost, and flexible preparation methods that can be employed in various ways. Additionally, agricultural waste, such as fruit and vegetable scraps, dried branches, and fallen leaves, can be used to produce biochar, which can enhance soil health and provide agricultural benefits. In the current research, biochar was derived from accumulated lemon and olive tree branches under controlled heating conditions. The produced biochar is tested by removing Pb ions under different operational conditions including pH, adsorbent dosage, and contact time. Under optimized conditions, kinetic tests, and equilibrium isotherms are measured. Both kinetic profiles and isotherms are presented by different models to elucidate the Pb interaction mechanism with biochar.

2. Methodology

2.1 Production of Biochar

The experiments were prepared at Al-Huson College, Al-Balqa University campus, Jordan. A thorough cone-shaped hole has been dug into the ground, and a fire has been ignited from the base of the hole to keep the lemon and olive tree branches from drying out by exposing them to light. The fire spread, and more branches and twigs were placed on top of the layer that had previously prevented the stick surfaces from being coated in ash. The expert continued to add boards to the fire until the material was completely burned, and he reached the top of the cone. The next step is to submerge the object in water and maintain a suitable temperature. Regular application of biochar to the floor of the shed increased its surface area, which accelerated the drying process and reduced biochar particle size (passing sieve #50). The final product is shown in Figure 1 which illustrates the steps used for the preparation process.

Figure 1. Biochar preparation

2.2 Adsorption Experiments

The Pb^{+2} stock solution (1000 mg/L) was prepared by mixing 1.599 g of lead nitrate ($Pb(NO_3)_2$) with 1000 mL of deionized water. The base solution included $NaNO_3$ (0.01 mol/L). Before the adsorption trials, the stock solution was diluted to 200 and 20 mg/L. All adsorption studies were carried out in 100-ml glass bottles containing 50 ml of Pb^{+2} stock solution. Three different tests with parallel results and a blank experiment were carried out for each measurement.

After making the lead solution, 50 ml of 200 mg/l Pb^{+2} stock solution was added to four flasks for the initial studies on the influence of pH on lead adsorption. Each flask received 0.5g of biochar smaller in size than 2 mm, which was stirred for one minute. Using NaOH and H_2SO_4, the pH was changed to different levels (5, 6, 7, and 8). The samples were then filtered in a Büchner funnel using filtering paper, and the pH values of each sample were recorded.

In the second experiment, 50ml of 20 mg/l Pb^{+2} stock solution was introduced to three flasks to investigate the effect of biochar dosage on lead adsorption. The pH of all flasks was adjusted to the optimal level when mixing with NaOH and H_2SO_4. Biochar dosages of less than 2 mm were applied to each flask of 1, 2, and 3 grams before mixing for one minute. Filtration paper was used to filter the samples in a Büchner funnel.

In the third experiment, the impact of contact time on lead adsorption was investigated by adding 50ml of 1000 mg/l Pb^{+2} stock solution to five flasks. The pH of all flasks was adjusted to the optimal level when mixing with NaOH and H_2SO_4. At varying rater durations of 5, 30, 60, 90, and 180 minutes, fast mixing at 200 RPM was applied to the samples. Filtration paper was used to filter the samples in a Büchner funnel.

The lead concentrations in the treated samples were determined by atomic absorption spectrometry (SHIMADZU AA-7000). To adjust the pH of the solution, a digital pH meter (pH Meter, Zonedeal) was used for this purpose.

2.3 Adsorption Parameters:

Adsorption tests Removal efficiency and Equilibrium capacity were used to determine the efficiency of the biochar adsorption. The percentage removal efficiency (E) was calculated using the following equation (Al-Zboon, 2016):

$$E=(Co-Ce)/C0\times 100\% \quad (1)$$

where: Co is the initial concentration of Pb^{+2} (ppm), and Ce is the residual concentration of Pb^{+2} ion in solution after equilibrium (ppm). The amount of Pb^{+2} uptake by biochar was calculated as the following [AlHarahshah et al., 2015]:

$$q=(Co-Ce)\times V/m \quad (2)$$

where q is the amount of Pb^{+2} uptake by biochar (mg (metal)/g (Biochar), V is the volume of sample (l), and m is the mass of Biochar (g).

2.4 Isotherm Study

Three isotherm models were used in this research: Langmuir, Freundlich, and Temkin models, as shown in Equations (3-5), respectively (Alzboon, 2023):

$$1/qe=(1/kaqm)*(1/Ce)+(1/qm) \quad (3)$$

$$\log(qe)=\log(kf)+(1/n)\log(ce) \quad (4)$$

$$qe=B\ln(At)-B\ln Ce \quad (5)$$

where qe is the equilibrium adsorption capacity at a certain concentration, Co, qm refer to the optimum equilibrium uptake capacity, Ka is a constant related to the heat of adsorption, and Ce is the remaining concentration. The linear trend of plotting of 1/qe vs. 1/Ce results in 1/qm (the constant), and the slope is 1/(ka*qm) where Kf, n, and k are the Freundlich model's coefficients.

The term A in Equation (5) is the constant of equilibrium binding (l/g), and B is a constant of heat adsorption (J/mol) which can be calculated by Equation (6):

$$B=RT/bt \quad (6)$$

where R is the universal gas constant (8.314 J/ mol.K), T is the temperature (K), bt is the isotherm constant.

2.5 Kinetic Study

Three kinetic models were used: second-order pseudo-kinetic, first-order pseudo-kinetic, and intraparticle models. While second-order and first-order pseudo-kinetic models are functions of time, the intraparticle model is a function of t^0.5. The linear forms of the mentioned models are shown in Equations (7–9), respectively (Al-Zboon et al., 2011):

$$t/qt=1/k_1q_e^{\,2}+t/qe \quad (7)$$

$$\ln(qe-qt)=\ln(qe)-k_2t \quad (8)$$

$$qt=k_3t^{1/2}+k_4 \quad (9)$$

where qe is the equilibrium adsorption capacity, qt is the adsorption capacity at time t, k_1, k_2, k_3, and k_4 are constants of the models, respectively, while t is the time in minutes. K_1, k_2, and k_3 values can be obtained by plotting a graph of t/q against t, ln (q e − q t) against t and qt against t 0.5, respectively.

3. Results and Discussion

3.1 Effect of pH on Adsorption

Figure (2) shows how different pH values (5, 6, 7, and 8) affect adsorption efficiency. Equation (1) was used to determine the lead removal efficiency (E%), while Equation (2) was used to estimate the equilibrium capacity (qe). The results indicate that when pH rises, lead removal effectiveness (E%) increases until it reaches about 99.4% at a pH of 8. Similarly, qe increased in tandem with increasing pH. The phenomenon could be caused by the minerals in biochar having a higher concentration of positively charged sites. Static energy effectively attracts and attaches lead ions to these sites in this environment (Al-Zboon et al., 2016). Low pH causes a significant rivalry between H^+ and Pb^{+2}, which explains why there is less H^+ in the solution. This low pH decreases the competition between H^+ and Pb^{+2} and increases the likelihood that Pb^{+2} will be adsorbed on the accessible pores (Al-Zboon, 2023). pH impacts biochar's sorption of pollutants due to surface charge variations. The surface charge of biochar is dependent on the pH of the surrounding environment. On the other hand, the biochar surface may produce a greater negative charge at higher pH values, which would enable it to draw positively charged contaminants. The pore structure of biochar is also important because it provides a surface area on which pollutants may be adsorbed. Compared to materials with a less developed porous structure, biochar with a high porosity and well-formed pore network may be more able to extract contaminants from water or soil.

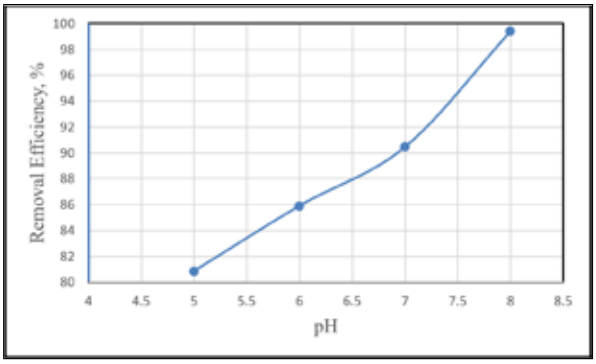

Figure 2. Effect of pH on the removal of Pb^{+2} from aqueous solution.

3.2 Effect of Biochar Dose on Adsorption

The effect of biochar dose on the removal efficiency is shown in Figure 3. As the dose increases from 1-3 g/L, the removal of Pb^{+2} increases from 83.25% to almost 99.8%. It becomes anticipated that the removal process depends on the availability of unoccupied pores surfaces. Because of that, the high biochar dose offers additional active sites for Pb^{+2} adsorption, hence increasing Pb uptake from the solution. No significant increase in Pb uptake was observed at dose ≥ 2.0 g/L. The usefulness of using low dosages of low-cost biochar for the removal of heavy metals is demonstrated by 80% Pb removal at only 1.0 g/L does, hence the earlier dose was used in the coming tests. Consequently, biochar offers an effective material for Pb^{+2} removal through a simple safe procedure. The high removal efficiency that was attained within the first 5.0 min as shown in Fig 4 suggests that biochar has a high porosity and is effective at removing low concentrations of Pb^{+2} quickly.

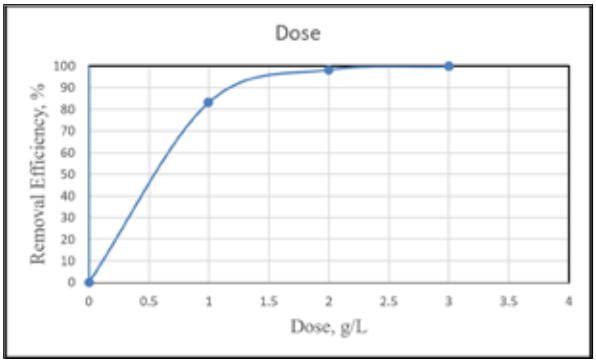

Figure 3. Effects of biochar dose on the removal of Pb^{+2}

3.3 Effects of Contact Time on Adsorption

Figure (4) shows the effects of contact time between a 1.0 g/L dose of (biochar) and a 1000 mg/l lead solution. Equation (1) was used to determine the lead removal efficiency (E%), while Equation (2) was used to estimate the equilibrium capacity (qe). The removal efficiency rises with longer contact times and reaches about 100% after 180 minutes. In a similar trend, qe increased with increasing contact duration, rising from 35.3 mg/g after 30 minutes to 50 mg/g after 180 minutes. The fast Pb adsorption at the beginning of the process was attributed to the availability of excess active sites on biochar. Over time, the active sites filled with Pb until the equilibrium of the process which was achieved around 100 min. (Al-Hamaiedah et al., 2023). The experiment's findings suggest that, with a lengthy contact time, biochar can be utilized to remove high concentrations of lead (1000 ppm) from aqueous solutions. After 90 minutes, an adequate removal efficiency of 94.4% can be attained, suggesting that more time is not practical.

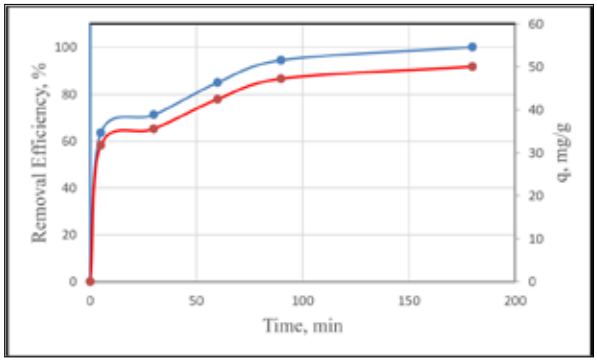

Figure 4. Effect of the contact time on the removal of Pb^{+2}

3.4 Adsorption Kinetics

Adsorption kinetics models are used to determine the required time for the adsorption process to reach the equilibrium status.

Based on the correlation coefficient, the model's validity can be ranked as pseudo-second order (R^2=0.99)> pseudo-first order (R^2= 0.86)> intraparticle model (R^2=0.76) as shown in figure 5. The obtained values of variables in Equations 7,8, and 9 are 0.02 for k1 in Equation 7, 0.043 for k2 in Equation 8, 3.25 for k3 in Equation, and 13.67 for k4 in Equation 9.

The second order pseudo-kinetic model assumes that the adsorption rates are a function of the absorption capacity and independent of the absorbate concentration. The second order models also anticipate behavior across the whole adsorption range and indicate that chemical sorption, or chemisorption, is the rate-limiting step.

This model assumed the following assumptions:

A non-reversible adsorption reaction between Pb and active sites of biochar:

$$2Pb^{2+} + -S \rightarrow -S(Pb)_2$$

where –S is the active site of biochar.

b) There is no interaction between adsorbed Pb^{2+} and the adsorption process at discrete active sites.

c) Adsorption energy is independent of surface coverage.

d) A saturated monolayer of adsorbates on the adsorbent surface equates to maximum adsorption.

e) Chemisorption, which is the rate-limiting phase, works by exchanging or sharing electrons between Pb2+ and the biochar.

The first-order model assumes that the adsorption is directly proportional to the difference in the concentration of ions with time and the amount of solid absorbed. According to the first-order concentration model, there are three stages in the adsorption process: the external diffusion stage, which lasts from 0 to 5 minutes and has a sharp increase in Pb^{+2}'s removal and adsorption capacity. The intra-diffusion stage, which lasts from 5 to 90 minutes, is represented by a linear

line with a medium slope. The third stage, which lasts from 90 to 180 minutes, represents the near-equilibrium low-diffusion process because of limited metal concentrations, which is explained by Al Jarrah et al., (2018).

Intraparticle models assume that the diffusion process depends mainly on the particle porosity and tortuosity. Since the second-order model provides the best fitting, it means that adsorption process might be the rate-limiting step, and the adsorption capacity is the key parameter that determines the adsorption rate while the concentration of Pb^{+2} is not an important factor (Sahoo and Prelot, 2020). Many researchers reported the effectiveness of 2nd order model in describing the kinetic adsorption process (Al-Zboon, 2023; Al-Zboon et al., 2016; Al-Hamaiedh et al., 2024). In general, the limited application of intraparticle diffusion model ($R^2 = 0.76$) would indicate that intraparticle diffusion of Pb ions inside biochar was not dominating the entire process.

3.5 Adsorption Isotherms

Langmuir, Freundlich, and Temkin were used in this paper to determine the isotherm behavior of Pb^{+2} adsorption on biochar. While Temkin model provided the highest correlation (R^2=1), Langmuir model provided the lowest one (R^2= 0.93). Temkin model suggests that there is an indirect interaction between the adsorbent and the adsorbate, and the adsorption heat (enthalpy) decreases linearly (not logarithmically) with the increase in the surface coverage (Ayawei et al., 2017). It was reported that the Temkin model is valid for intermediate concentration of ions which explains the high R^{+2} of the model in comparison with other models. Langmuir model assumes that the adsorption occurs on a single layer and stops when all the sites on the adsorbent's surface are equal, however, the Freundlich model states that adsorption occurs on many levels (multilayers) and that the adsorbent's surface is heterogeneous (Ayawei et al., 2017). This demonstrates that the adsorption process takes place in a heterogeneous manner over multilayers of the used biochar and Pb^{+2} with a reduction in the adsorption heat with surface coverage. The Freundlich model showed n values of 6.1 as shown in Table 1, indicating a favorable sorption process (Dada et al., 2012).

The Temkin model was used successfully to describe the adsorption of methylene blue by miswak leaves and the adsorption of cadmium by Fe nanoparticles (Ayawei et al., 2017). Others reported that the adsorption of Pb^{+2} on fly ash-based geopolymer followed the Langmuir model (Al-Zboon et al., 2011), or Dubinin-Radeshkovich model in the case of using the Dead Sea mud as an adsorbent (Al-Hamaiedh et al., 2024).

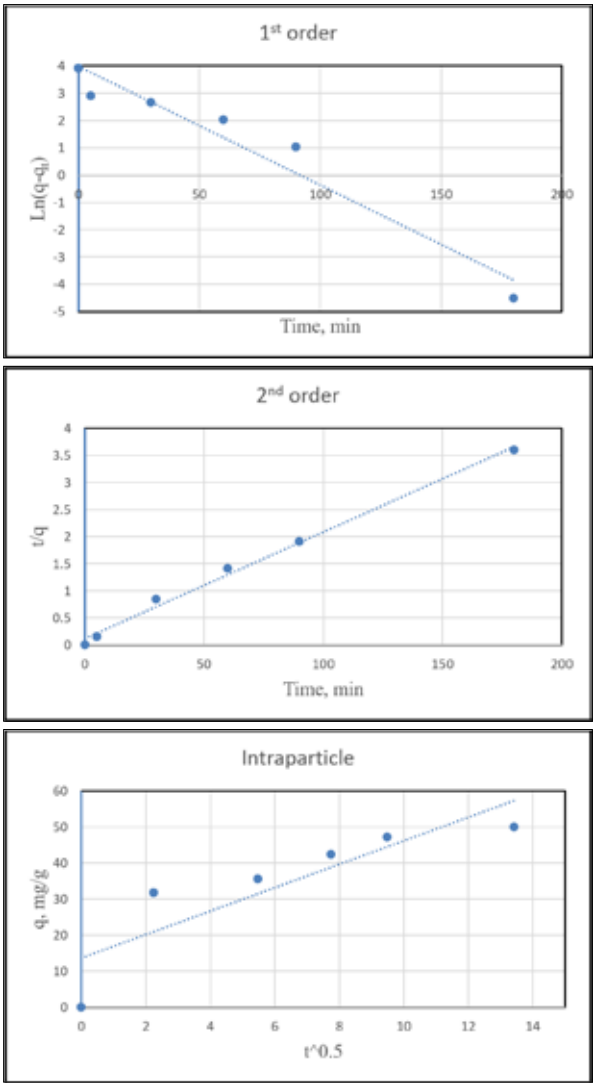

Figure 5. Modeling of adsorption rate of Pb^{+2} by biochar using different equations.

Table 1. Results of Langmuir, Freundlich, and Temkin Models Parameters

Model	Langmuir model	Frendluich Model	Temkin Model
Equation	1/qe = (1/kaqm)*(1/Ce)+(1/qm) (g mol^{-1})	log(qe)=log(kf)+ (1/n) log(ce)	qe = B ln(At) - B lnCe (mol g^{-1})
R^2	0.93	0.99	1
Variable 1	qm = 12.02 mol g^{-1}	n= 6.1	B = -1.59 J g mol^{-2}
Variable 2	ka = 12.24 L mol^{-1}	Kf = 9.89 L mol^{-1}	At = 0.20 L mol^{-1}

4. Conclusion

Biosorption of lead, using biochar produced from the branches of olive and lemon trees, has been studied in this research. The results of these experiments strongly suggested that this biochar is cost-effective and capable of removing lead from aqueous solutions. The findings show that biochar is an effective natural adsorbent for eliminating lead ions (Pb^{+2}) from water.

Because of its low cost, abundance of raw materials, and ease of preparation, the use of biochar to remove lead from polluted water is a viable option. Biochar has a high adsorption capacity for lead ions in water and may be made more efficient by adjusting variables such as pH, temperature, and contact duration time.

The results show that the increasing in pH of the solutions helps to improve the adsorption process by which at value of

pH=8 reaching 99.4% efficiency. At a dose of 1g of (Biochar) per batch (200 ml), a starting concentration of 1000 mg/l of lead ion in the solution, a temperature of 25 ◦C, a mixing speed of 15 rpm, and a contact period of 3 hours, 100% lead ion removal efficiency was attained, and a more contact time leads to more increase of the adsorption of Pb^{+2}. The study includes both kinetic and isothermal models to determine the optimal parameters for achieving the highest adsorption capacity.

Second-order pseudo-kinetic model was found to be more suitable since it had a higher R^{+2} than the first-order model. The most effective model for illustrating the adsorption process was Temkin isothermal model. Physically, the exothermic, spontaneous adsorption process took place. To further understand how well (Biochar) absorbs other heavy metals, further research is necessary. Despite this, the data demonstrate that the zero-order- model well describes the concentration-pH relationship. Finally, more studies are needed to examine biochar's long-term stability and environmental impact on soil microbial communities and ecosystems.

Funding

The author(s) received no specific funding for this work. Special thanks to Al-Balqa Applied University, Al-Huson College for making this work possible.

Declaration of competing interest

The authors declare that they have no known competing financial interests or personal relationships that could have appeared to influence the work reported in this paper.

Data availability

Data will be made available on request.

References

Al-Hamaiedh, H., Al-Zawahra, N. K., & Al-Zboon, K. (2024). Removal of lead from aqueous solution using Dead Sea mud. Results in Engineering, 21, 101714.

Al-Zawahreh, K., Barral, M. T., Al-Degs, Y., & Paradelo, R. (2022). Competitive removal of textile dyes from solution by pine bark-compost in batch and fixed bed column experiments. Environmental Technology & Innovation, 27, 102421.

Al-Zboon, K. K. (2023). Single and Ternary Removal of Heavy Metals from Aqueous Solution Using Fe 3 O 4 Magnetic Nano-particles. Jordan Journal of Civil Engineering, 17(2).

Al-Zboon, K. K., Al-Smadi, B. M., & Al-Khawaldh, S. (2016). Natural volcanic tuff-based geopolymer for Zn removal: adsorption isotherm, kinetic, and thermodynamic study. Water, Air, & Soil Pollution, 227, 1-22.

Al-Zboon, K., Al-Harahsheh, M. S., & Hani, F. B. (2011). Fly ash-based geopolymer for Pb removal from aqueous solution. Journal of hazardous materials, 188(1-3), 414-421.

Ahmad, M., Rajapaksha, A. U., Lim, J. E., Zhang, M., Bolan, N., Mohan, D., ... & Ok, Y. S. (2014). Biochar as a sorbent for contaminant management in soil and water: a review. Chemosphere, 99, 19-33.

Arif, M., Liu, G., Yousaf, B., Ahmed, R., Irshad, S., Ashraf, A., ... & Rashid, M. S. (2021). Synthesis, characteristics and mechanistic insight into the clays and clay minerals-biochar surface interactions for contaminants removal-A review. Journal of Cleaner Production, 310, 127548.

Ayawei, N., Ebelegi, A. N., & Wankasi, D. (2017). Modelling and interpretation of adsorption isotherms. Journal of chemistry, 2017(1), 3039817.

Barquilha, C. E., & Braga, M. C. (2021). Adsorption of organic and inorganic pollutants onto biochars: Challenges, operating conditions, and mechanisms. Bioresource Technology Reports, 15, 100728.

Bolan, N., Hoang, S. A., Beiyuan, J., Gupta, S., Hou, D., Karakoti, A., ... & Van Zwieten, L. (2022). Multifunctional applications of biochar beyond carbon storage. International Materials Reviews, 67(2), 150-200.

Chen, B., Chen, Z., & Lv, S. (2011). A novel magnetic biochar efficiently sorbs organic pollutants and phosphate. Bioresource technology, 102(2), 716-723.

Cimò, G., Kucerik, J., Berns, A. E., Schaumann, G. E., Alonzo, G., & Conte, P. (2014). Effect of heating time and temperature on the chemical characteristics of biochar from poultry manure. Journal of agricultural and food chemistry, 62(8), 1912-1918.

Cui, X., Cao, X., Xue, W., Xu, L., Cui, Z., Zhao, R., & Ni, S. Q. (2023). Integrative effects of microbial inoculation and amendments on improved crop safety in industrial soils co-contaminated with organic and inorganic pollutants. Science of The Total Environment, 873, 162202.

De Ridder, M., De Jong, S., Polchar, J., & Lingemann, S. (2012). Risks and opportunities in the global phosphate rock market: robust strategies in times of uncertainty.

El-Naggar, A., Ahmed, N., Mosa, A., Niazi, N. K., Yousaf, B., Sharma, A., ... & Chang, S. X. (2021). Nickel in soil and water: Sources, biogeochemistry, and remediation using biochar. Journal of hazardous materials, 419, 126421.

Engwa, G. A., Ferdinand, P. U., Nwalo, F. N., & Unachukwu, M. N. (2019). Mechanism and health effects of heavy metal toxicity in humans. Poisoning in the modern world-new tricks for an old dog, 10, 70-90.

Fu, Z., & Xi, S. (2020). The effects of heavy metals on human metabolism. Toxicology mechanisms and methods, 30(3), 167-176.

Gautam, K., Sharma, P., Dwivedi, S., Singh, A., Gaur, V. K., Varjani, S., ... & Ngo, H. H. (2023). A review on control and abatement of soil pollution by heavy metals: Emphasis on artificial intelligence in recovery of contaminated soil. Environmental Research, 225, 115592.

Hamad, A. A., Jasper, A., & Uhl, D. (2013). Charcoal remains from the Mukheiris Formation of Jordan—the first evidence of palaeowildfire from the Anisian (Middle Triassic) of Gondwana. Jordan Journal of Earth and Environmental Sciences, 5, 17-22.

Hosseini, S. S., Hamadi, A., Foroutan, R., Peighambardoust, S. J., & Ramavandi, B. (2022). Decontamination of Cd2+ and Pb2+ from aqueous solution using a magnetic nanocomposite of eggshell/starch/Fe3O4. Journal of Water Process Engineering, 48, 102911.

Jyothi, N. R. (2020). Heavy metal sources and their effects on human health. Heavy metals-their environmental impacts and mitigation, 1-12.

Shah, K. D., Brahmbhatt, N. H., & Thaker, P. N. (2021). Study of Green Seaweed Biochar for Lead Adsorption from Aqueous Solution. Oriental Journal of Chemistry, 37(5).

Khalid, S., Shahid, M., Murtaza, B., Bibi, I., Naeem, M. A., & Niazi, N. K. (2020). A critical review of different factors governing the fate of pesticides in soil under biochar application. Science of the Total Environment, 711, 134645.

Khan, M. N., Mobin, M., Abbas, Z. K., & Alamri, S. A. (2018). Fertilizers and their contaminants in soils, surface and groundwater. Encyclopedia of the Anthropocene, 5, 225-240.

Khudhur, N. S., Khudhur, S. M., & Ahmad, I. N. (2018). An Assessment of heavy metal soil contamination in a Steel Factory and the surrounding area in Erbil City. Jordan Journal of Earth and Environmental Sciences, 9(1), 1-11.

Kristanti, R. A., Ngu, W. J., Yuniarto, A., & Hadibarata, T. (2021). Rhizofiltration for removal of inorganic and organic pollutants in groundwater: a review. Biointerface Res. Appl. Chem, 11, 12326-12347.

Kypritidou, Z., El-Bassi, L., Jellali, S., Kinigopoulou, V., Tziritis, E., Akrout, H., ... & Doulgeris, C. (2022). Lead removal from aqueous solutions by olive mill wastes derived biochar: Batch experiments and geochemical modelling. Journal of Environmental Management, 318, 115562.

Lehmann, J., Gaunt, J., & Rondon, M. (2006). Bio-char sequestration in terrestrial ecosystems–a review. Mitigation and adaptation strategies for global change, 11, 403-427.

Lei, W., Li, T. T., Lv, N. Q., Liu, H., Zhang, Y., & Xi, B. D. (2019, February). Study on adsorption of lead by biochar prepared from sludge of municipal wastewater treatment plant. In IOP Conference Series: Materials Science and Engineering (Vol. 479, No. 1, p. 012007). IOP Publishing.

Liang, L., Xi, F., Tan, W., Meng, X., Hu, B., & Wang, X. (2021). Review of organic and inorganic pollutants removal by biochar and biochar-based composites. Biochar, 3, 255-281.

Liu, Z., & Zhang, F. S. (2009). Removal of lead from water using biochars prepared from hydrothermal liquefaction of biomass. Journal of hazardous materials, 167(1-3), 933-939.

Mahdi, Z., Yu, Q. J., & El Hanandeh, A. (2018). Removal of lead (II) from aqueous solution using date seed-derived biochar: batch and column studies. Applied Water Science, 8, 1-13.

Mireles, S., Parsons, J., Trad, T., Cheng, C. L., & Kang, J. (2019). Lead removal from aqueous solutions using biochars derived from corn stover, orange peel, and pistachio shell. International Journal of Environmental Science and Technology, 16, 5817-5826.

Mohan, D., & Pittman Jr, C. U. (2007). Arsenic removal from water/wastewater using adsorbents—a critical review. Journal of hazardous materials, 142(1-2), 1-53.

Mohanty, S. K., Valenca, R., Berger, A. W., Iris, K. M., Xiong, X., Saunders, T. M., & Tsang, D. C. (2018). Plenty of room for carbon on the ground: Potential applications of biochar for stormwater treatment. Science of the total environment, 625, 1644-1658.

Qambrani, N. A., Rahman, M. M., Won, S., Shim, S., & Ra, C. (2017). Biochar properties and eco-friendly applications for climate change mitigation, waste management, and wastewater treatment: A review. Renewable and Sustainable Energy Reviews, 79, 255-273.

Rashmi, I., Roy, T., Kartika, K. S., Pal, R., Coumar, V., Kala, S., & Shinoji, K. C. (2020). Organic and inorganic fertilizer contaminants in agriculture: Impact on soil and water resources. Contaminants in Agriculture: Sources, Impacts and Management, 3-41.

Qadan, H. A. K., Al Tarazi, E., & Jaradat, R. (2022). Updated Seismic Hazard Assessment Evaluation for the City of Aqaba, Jordan.

Qin, G., Niu, Z., Yu, J., Li, Z., Ma, J., & Xiang, P. (2021). Soil heavy metal pollution and food safety in China: Effects, sources and removing technology. Chemosphere, 267, 129205.

Razzak, S. A., Faruque, M. O., Alsheikh, Z., Alsheikhmohamad, L., Alkuroud, D., Alfayez, A., ... & Hossain, M. M. (2022). A comprehensive review on conventional and biological-driven heavy metals removal from industrial wastewater. Environmental Advances, 7, 100168.

Sahoo, T. R., & Prelot, B. (2020). Adsorption processes for the removal of contaminants from wastewater: the perspective role of nanomaterials and nanotechnology. In Nanomaterials for the detection and removal of wastewater pollutants (pp. 161-222). Elsevier.

Sevim, Ç., Doğan, E., & Comakli, S. (2020). Cardiovascular disease and toxic metals. Current Opinion in Toxicology, 19, 88-92.

Shaaban, A., Se, S. M., Dimin, M. F., Juoi, J. M., Husin, M. H. M., & Mitan, N. M. M. (2014). Influence of heating temperature and holding time on biochars derived from rubber wood sawdust via slow pyrolysis. Journal of Analytical and Applied Pyrolysis, 107, 31-39.

Srinivasarao, C., Kundu, S., Ramachandrappa, B. K., Reddy, S., Lal, R., Venkateswarlu, B., ... & Naik, R. P. (2014). Potassium release characteristics, potassium balance, and fingermillet (Eleusine coracana G.) yield sustainability in a 27-year long experiment on an Alfisol in the semi-arid tropical India. Plant and soil, 374, 315-330.

Tang, J., Zhu, W., Kookana, R., & Katayama, A. (2013). Characteristics of biochar and its application in remediation of contaminated soil. Journal of bioscience and bioengineering, 116(6), 653-659.

Tomczyk, A., Sokołowska, Z., & Boguta, P. (2020). Biochar physicochemical properties: pyrolysis temperature and feedstock kind effects. Reviews in Environmental Science and Bio/Technology, 19(1), 191-215.

Xiao, X., Chen, B., & Zhu, L. (2014). Transformation, morphology, and dissolution of silicon and carbon in rice straw-derived biochars under different pyrolytic temperatures. Environmental science & technology, 48(6), 3411-3419.

Xiang, L., Harindintwali, J. D., Wang, F., Redmile-Gordon, M., Chang, S. X., Fu, Y., ... & Xing, B. (2022). Integrating biochar, bacteria, and plants for sustainable remediation of soils contaminated with organic pollutants. Environmental Science & Technology, 56(23), 16546-16566.

Xu, Y., Bai, T., Li, Q., Yang, H., Yan, Y., Sarkar, B., ... & Bolan, N. (2021). Influence of pyrolysis temperature on the characteristics and lead (II) adsorption capacity of phosphorus-engineered poplar sawdust biochar. Journal of Analytical and Applied Pyrolysis, 154, 105010.

Yuan, P., Wang, J., Pan, Y., Shen, B., & Wu, C. (2019). Review of biochar for the management of contaminated soil: Preparation, application and prospect. Science of the total environment, 659, 473-490.

Zeghioud, H., Fryda, L., Djelal, H., Assadi, A., & Kane, A. (2022). A comprehensive review of biochar in removal of organic pollutants from wastewater: Characterization, toxicity, activation/functionalization and influencing treatment factors. Journal of Water Process Engineering, 47, 102801.

Zhao, C., Hu, L., Zhang, C., Wang, S., Wang, X., & Huo, Z. (2021). Preparation of biochar-interpenetrated iron-alginate hydrogel as a pH-independent sorbent for removal of Cr (VI) and Pb (II). Environmental Pollution, 287, 117303.

Zhou, Y., Gao, B., Zimmerman, A. R., Chen, H., Zhang, M., & Cao, X. (2014). Biochar-supported zerovalent iron for removal of various contaminants from aqueous solutions. Bioresource technology, 152, 538-542.

Zulfiqar, M., Samsudin, M. F. R., & Sufian, S. (2019). Modelling and optimization of photocatalytic degradation of phenol via TiO2 nanoparticles: An insight into response surface methodology and artificial neural network. Journal of Photochemistry and Photobiology A: Chemistry, 384, 112039.

JJEES

JJEES (2024) 15 (4): 234-243
ISSN 1995-6681

Jordan Journal of Earth and Environmental Sciences

Dolomite Geochemistry and Distribution in the Jurassic Samana Suk Formation, Salhad Section, Lesser Himalayas, North Pakistan

Syed Muhammad Wasim Sajjad*, Junaid Mehmood, Usman Said, Imran Ahmad, Ibrar Ul Haq, Salman Khurshid, Asad Muhammad

Department of Geology, University of Malakand, Chakdara, Dir Lower, Khyber Pakhtunkhwa, Pakistan

Received on February 3, 2024; Accepted on October 2, 2024

Abstract

The current study documents dolomites' occurrence, geometry, and distribution within the Middle Jurassic Samana Suk Formation, Salhad Section, Southern Hazara Basin of Lesser Himalayas, Northern Pakistan. Field observations in conjunction with petrographic and geochemical investigations revealed that the host limestone is diagenetically modified by various dolomitization phases. During field studies, it has been noticed that 75% of the lithology of the studied formation is unaltered limestone, while 25% has been dolomitized. The limestone is mostly light grey and oolitic while dolomite exhibits dark grey color. The diagenetic features observed in the field include stylolite, fractures, and calcite veins. Petrographic examination illustrates that the mud-dominated facies are more susceptible to dolomitization while the grainstone facies show resistance due to the earlier pore-filling marine cementation. The dolomites were classified into coarsely crystalline euhedral dolomites (DI), medium to coarse crystalline euhedral zoned dolomites (DII), and coarsely crystalline anhedral dolomites (DIII). These dolomites' carbon and oxygen isotope values range from +0.88‰ to +1.71‰ V-PDB and −2.98% to −6.84% V-PDB respectively. The highly depleted stable C & O isotopic signatures of different dolomites show significant deviation from original marine Middle Jurassic signatures (-8.87 to -4.47% V-PDB) and suggest multiphase dolomitization events.

Keywords: Petrography, Diagenesis, Samana Suk Formation, C & O –Isotopes, Dolomitization, North Pakistan

1. Introduction

Carbonate rocks are a class of sedimentary rocks that primarily comprise (>50%) of carbonate minerals and are broadly categorized into two types: limestone and dolostone. Limestones are considered the principal carbonate rocks that consist of the mineral calcite and/or aragonite. They have similar $CaCO_3$ composition with different crystal structures, i.e., calcite is trigonal while aragonite is orthorhombic (Bell, 2016). Aragonite is metastable and readily converted into low magnesium calcite with time by losing magnesium (Flugel and Flugel, 2004). Therefore, calcite and, to a lesser extent, dolomite are regarded as the major constituent of carbonate rocks (Flugel and Flugel, 2004). Dolostone is a carbonate rock that is predominantly comprised of mineral dolomite, induced by the secondary alteration or replacement of limestone during diagenesis. Diagenesis includes all the physical, chemical, and biological changes that the sediments undergo from the moment of deposition till before the domain of metamorphism (Tucker and Bathurst, 2009). The major processes, involved in carbonate diagenesis, are dissolution, cementation, lithification, alteration, bacterial action, and soft sediment deformations (Tucker and Bathurst, 2009). These diagenetic alterations are mainly controlled by the depositional environments which include marine, meteoric, and burial diagenesis (Purdy, 1968; Tucker and Bathurst, 2009; Abed et al., 2023). In recent decades, many researchers have focused on the dolomitization since the dolomite reservoirs have great hydrocarbon potential (Azmy et al., 2001; Swart et al., 2005; Azmy et al., 2008; Jiang et al., 2014; Jiang et al., 2016; Jiang et al., 2019; Liu et al., 2020; Zhemchugova et al., 2020; Xu et al., 2021). During the dolomitization event, the net calcite dissolution contributes to the porosity enhancement (Tucker and Wright, 1990; Tucker, 1993). The current study aims to investigate the distribution of dolomites and dolomitization process that occur in the Jurassic Samana Suk Limestone from Lower Salhad area, Abbottabad, Pakistan. It is the first study of their own kind, and previously no such detailed work has been carried out in the area.

2. Previous Studies

The carbonates of the Jurassic Samana Suk Formation exposed in Salhad area, Abbottabad Pakistan, have also been dolomitized which was not yet studied. Previously, different authors worked on and highlighted the important aspects of the Jurassic Samana Suk Formation from the Indus Basin, Trans-Indus Ranges, Kohat Ranges, Samana Ranges, and Kala Chitta Ranges. Shah et al., (2016 and 2020) studied the dolomitization and the effect of dolomitization on the reservoir quality of Samana Suk formation from Margalla Hill Ranges and Southern Hazara Basin. Rahim et al., (2020 and 2022) analyzed the various diagenetic and dolomitization events of Samana Suk Formation from the Himalayan Foreland Basin. Khan et al., (2021 and 2022) focused on the

* Corresponding author e-mail: geowaseem777@yahoo.com

diagenetic alteration of Jurassic carbonates from the Kohat Ranges. The sedimentological, sequence stratigraphic, and diagenetic alteration and their effect on reservoir properties of the Samana Suk Formation have been focused on by many researchers in several previous studies (Khan et al., 2020; Nizami and Sheikh, 2020; Rahim et al., 2020; Sajjad et al., 2020; Saboor et al., 2020; Wadood et al., 2021; Qamar et al., 2023; Ali et al., 2023; Khan et al., 2024). Miraj et al., (2021) and Shah et al., (2021) studied the marine deposits of the Samana Suk Formation in terms of source rock evaluation from the Middle Indus Basin and Punjab Platform, Pakistan.

3. Geological Setting

The youngest single supercontinent Pangea was initially comprised of all the earth landmasses. About 220Ma, the Pangea broke up into the Northern Laurasia and Southern Gondwana landmasses (Le Pichon et al., 2022). The present-day North America and Eurasia occupied Laurasia, while India, along with the current southern hemisphere continents, was originally part of the Southern Gondwana land (Plummer et al., 2016). Almost 167 million years ago, the Indian plate started to break up and subsequently fragmented from Gondwana, East Gondwana, Madagascar, Seychelles and moved toward northern hemisphere (Chatterjee and Scotese, 1999; Bandyopadhyay et al., 2010). The Indian continental breakup from Gondwana (~167 Ma) till its collisional orogeny with Asia during Eocene (~50 Ma) represents the longest journey 9000 km in 160 million years (Dietz and Holden 1970; Chatterjee 1992; Chatterjee and Scotese 2010; Chatterjee et al., 2013). This journey started from continental breakup followed by northward continental drifting, sea floor spreading, new ocean formations, volcanisms, fault systems, continental and oceanic subduction, continental collision, accretion, and mountain building process (Chatterjee et al., 2013). The collisional orogeny of Indian and Eurasian plate gives rise to the formation of Himalayas and Himalayan fold and thrust belt system (Klootwijk et al., 1992; Searle et al., 1997; Hussain et al., 2020). The study identified the northwestern part of Hazara Kashmir Syntaxis (Figure 1), situated in the lesser Himalayas of Pakistan (Yeats and Hussain, 1987). The study area is bound by the Panjal Thrust toward NNW while Nathia Gali Thrust marks the SSE boundary (Figure 1).

The stratigraphy of the area comprises Precambrian, Precambrian to early Cambrian, and Jurassic to Cretaceous rock sequences (Figure 2). The distribution, nomenclatures, thickness, and revised stratigraphy of the area are still under consideration, but here in this study, we follow the stratigraphy of Pakistan approved by the Stratigraphic Committee of Pakistan (Shah, 1977). The Hazara and Tawanal Formation represents the Precambrian sequence. Lithologically, the Hazara Formation dominantly comprises slate, while the Tanawal Formation is composed of quartzose schist (Calkins et al., 1975).

Abbottabad Formation and Hazira Formation represent the early Cambrian rock units of the area. The Abbottabad formation comprises the dolomites and sandstone lithology (Shah, 1977). The Hazira Formation is composed of the mudstone, siltstone, and sandstone (Shah, 1977). The Jurassic and Cretaceous rock sequence, exposed in the study area, includes the Samana Suk, Chichali, Lumshiwal, and Kawagarh Formations (Shah, 1977). The name Samana Suk Formation is derived from the type section Samana Ranges where a 365m thick outcrop is well exposed (Iqbal and Shah, 1980). The formation is comprised of bedded limestone, fossiliferous limestone, oolitic limestone, ferruginous sandy limestone, dolomites, and calcareous sandstone. In the study area, the lower contact of the formation is unconformable with the Hazira Formation (Figure 2), while the upper layer has a conformable contact with the Chichali Formation (Shah, 1977; Naka et al., 1996). From the well-preserved macro and microfossils, the formation has been assigned to the Middle Jurassic age (Fatmi, 1977). The Chichali and Lumshiwal Formations generally comprise glauconitic sandstone shale and minor phosphorite and glauconitic sandy mudstone. The Late Cretacous Kawagarh Formation is composed of thick to thin-bedded limestone, sandstone, and dolomites. In the field, it is very difficult to differentiate the Samana Suk Formation from Kawgarh Formation. However, it can be easily differentiated through the diagnostic oolitic limestone bed of Samana Suk Formation which is completely absent in the Kawagarh Formation (Naka et al., 1996).

4. Methodology

4.1 Field Work

The 35-meter-thick Salhad section is located on the Hazara Motorway along the Silk Route Salhad, Abbottabad. The section was traced and measured. The limestone and dolomite were differentiated through 10% dilute HCl and other field features like clear color contrast and Butcher Chop Weathering. In the study area, the Samana Suk Formation was identified by the presence of diagnostic oolitic limestone. Twenty samples were collected from limestone and dolomite for thin section and stable isotope analysis.

4.2 Laboratory Work

The collected samples were cut through a rock cutting machine in the thin-section laboratory of the National Centre of Excellence in Geology (NCEG), Peshawar University, Pakistan. The slabs were polished and marked for thin section preparation. Fifteen representative thin sections were prepared which were then studied by using a conventional microscope (NIKON LV100ND with 5 megapixels digital camera) in the petrographic lab of NCEG, University of Peshawar. The detailed petrography includes crystal morphology, size and textures, dolomite sizes, textures and their relationships with matrix, and various cement types.

4.3 Stable Isotope Analysis

Based on field investigation and petrographic observations, the different dolomite phases were analyzed for stable oxygen ($\delta^{18}O$) and carbon isotopes ($\delta^{13}C$). For δ18O & δ13C isotopes analysis, rocks powdering of different phases were carried out. During the powdering process, caution was followed to avoid contamination. A total of nine samples from different dolomite phases were first micro drilled (up to 2 grams) by using a hand-held dental driller and were packed in a sample holder tube. The dolomite samples were further analyzed for stable oxygen ($\delta^{18}O$) and carbon isotopic (δ13C) isotopes in the Isotope Application Division of PINSTECH,

Islamabad, Pakistan. The obtained results were presented as per mill (‰) relative to Vienna Pee Dee Belemnite (V-PDB). The stable isotope analyses were performed by using the proposed digestion method, via reacting the carbonate powder with 100 percent phosphoric acid having density lesser than 1.9 under a temperature of 75 °C in Carbo Kiel single sample acid bath coupled to a Finnigan-M.A.T 252 mass-spectrometer apparatus. As a result of carbonate powder digestion CO2 gas is produced from which the ratio 18O & 16O and 13C & 12C were restrained. The stable isotopic results are designated in per mill (‰) relative to (V-PDB) via allocating a δ13C range of +1.95‰ & δ18O ranging from −2.20‰ to NBS 19. In dolomite, the composition of oxygen isotopic results are revised through a fractional process provided by (Rosenbaum &Sheppard, 1986).

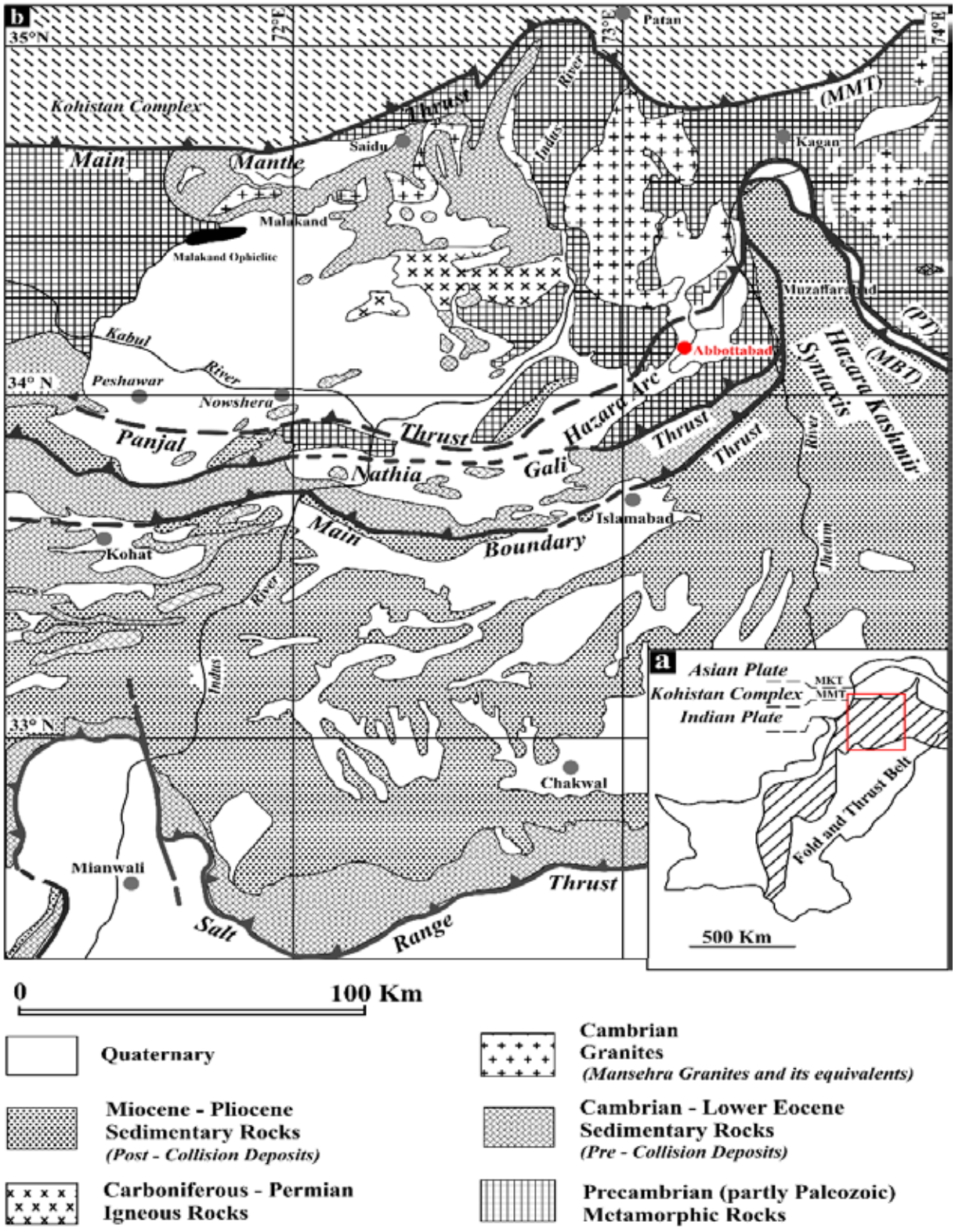

Figure 1. (a) A generalized tectonic map of Pakistan showing the Himalayan fold and thrust belt. The red box shows the study area in the Figure. **(b)** Geological map of Northern Pakistan illustrates major thrusts. The red solid circle shows the location of the study area (Hylland et al., 1988: Qureshi et al., 1993: Naka et al., 1996).

5. Results

5.1 Field Observations

The Salhad section of Samana Suk Formation comprises limestone and dolomite beds (Figure 3). The limestone is differentiated from dolomite through clear color contrast and a 10‰ dilute HCL test. In the area, the lower contact of the Samana Suk Formation is the Cambrian Hazira Formation (Figure 3b). The Samana Suk Formation comprises the diagnostic oolitic limestone bed showing a sharp contact with dark grey dolomite (Figure 3c). The formation also comprises the golden dolomites that usually fill veins and fractures (Figure 3d). Bedding parallel stylolite (BPS) is also observed (Figure 3e).

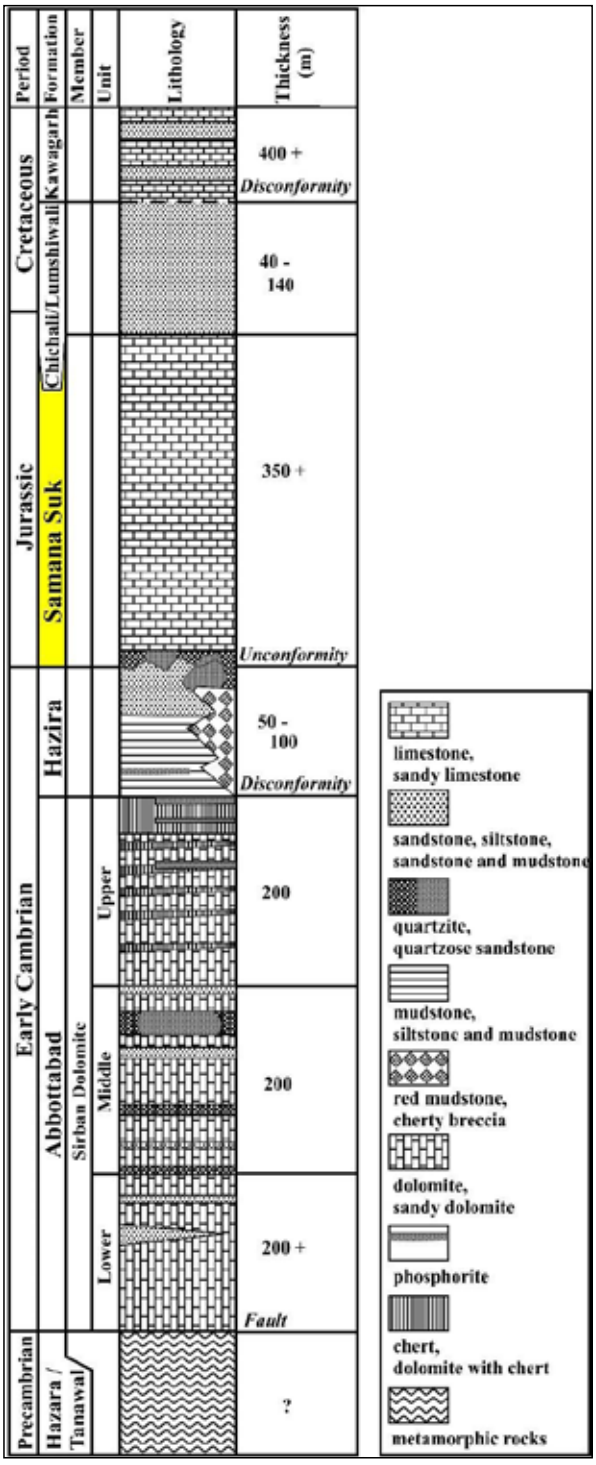

Figure 2. Generalized stratigraphic column of the study area Abbottabad. The current study is carried out on the Jurassic Samana Suk Formation which is highlighted by yellow color.

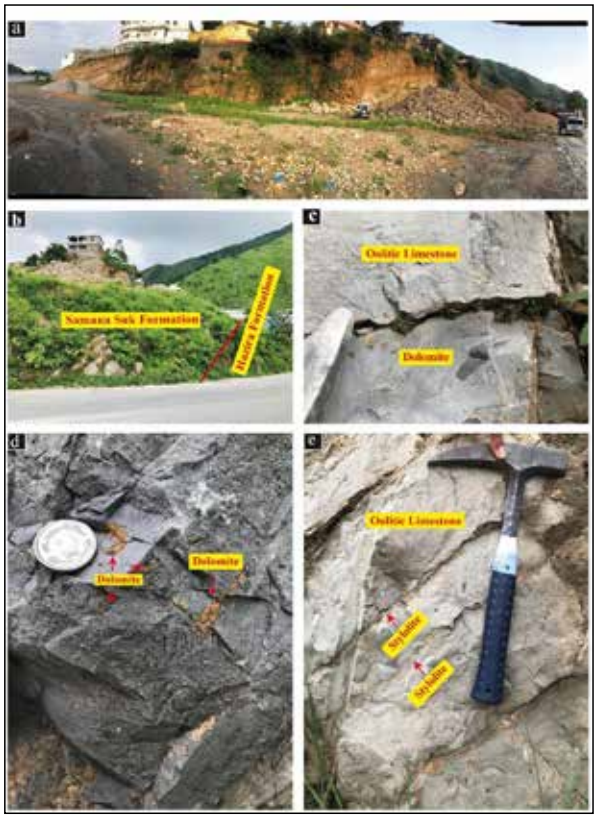

Figure 3. Field photographs **(a)** Panoramic view of the Jurassic Samana Suk Formation, Salhad Section, Abbottabad **(b)** Lower contact of Jurassic Samana Suk Formation with Cambrian Hazira Formation. **(c)** Sharp contact between the light grey oolitic limestone and dark grey dolomite. **(d)** Arrow indicating the occurrence of golden colour dolomites along vugs and fractures. **(e)** Arrow showing low to high amplitude bedding parallel stylolites.

5.2 Petrography

Based on field observations and microscopic examination, host limestone and different dolomite types were recognized within the Salhad section. The current study is not considered to show the entire petrographic details but only presents the diagenetic alterations that are important to the objectives of this paper. The detailed work on the limestone petrography was previously carried out by Ullah et al., (2016) and recognized five microfacies including Bioclastic Grainstone, Bioclastic Ooidal Peloidal Packstone, Siliciclastic Bioclastic Wackestone, and Peloidal Mudstone. The petrographic study shows that the limestone underwent through a complex diagenetic alteration i.e., dolomitization which was studied here in detail. During petrography, different dolomite types were recognized by using Sibley and Gregg's dolomite classification scheme (1987). Three replacive matrix dolomite types: coarse grain euhedral dolomite (DI), medium to coarse grain euhedral zooned dolomite (DII), and coarse grain anhedral dolomite (DIII), were recognized (Figure 4 and 5). The replacive matrix dolomite DI is characterized by their equigranular crystals and shows a crystal size up to 250 µm (Figure 4c and d). This type of dolomites mostly possesses euhedral shape having cloudy appearance and clear oval crystal rims (Figure 4c and d). DI mostly occurs in association with micrite and sparite of host limestone (Figure 4c and d). It doesn't show any significant occurrence and is present all about 5% of the total host rock volume (Figure 4c and d).

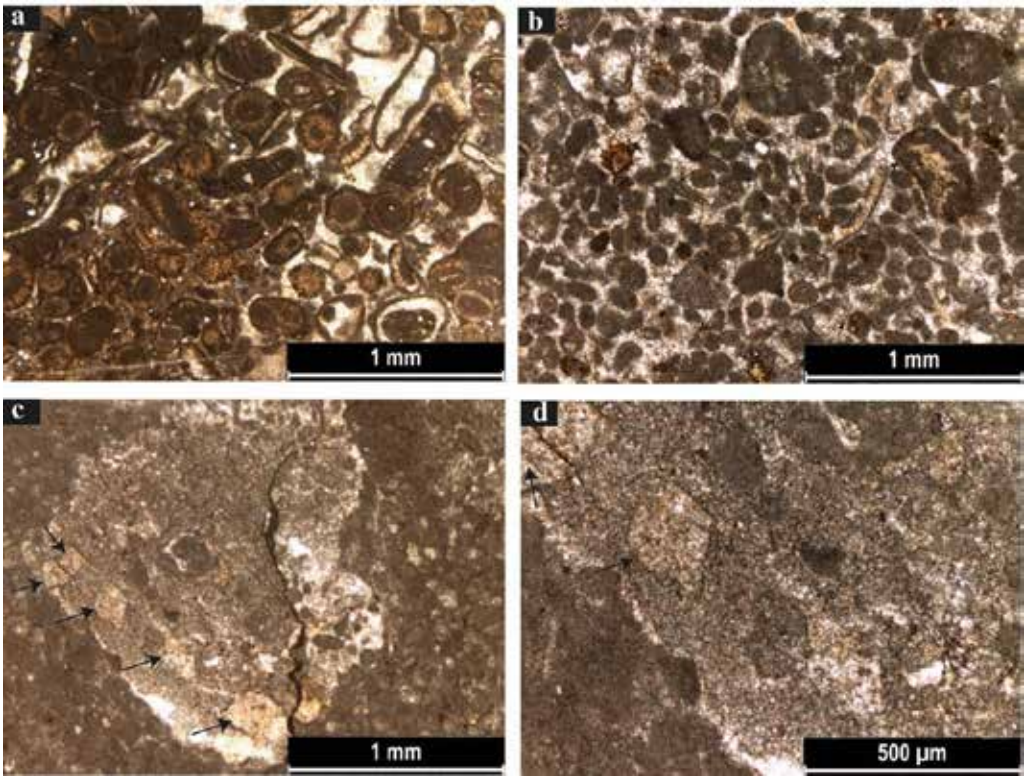

Figure 4. Photomicrographs showing (**a** and **b**) peloidal grain-stone microfacies which shows resistance to dolomitization event. (**c** and **d**) arrows indicate coarse crystalline euhedral dolomites (DI), representing the first stage of multiphase dolomitization events.

DII is the second type of replacive matrix dolomite which is characterized by its euhedral shape, having perfectly rhombohedral successive zones (Figure 5a and b). This type of dolomite shows minor to densely packing and preserved the original limestone texture (Figure 5a and b). The dolomite DII shows inequigranular crystals of euhedral shape with alternate cloudy and clear crystal bands (Figure 5a and b). These dolomites commonly infill the veins and fractures (Figure 3d and 5b). The dolomite DIII is characterize by its non-planar anhedral crystal shapes (Figure 5c and d). This type of dolomite shows densely packing, inequigranular size and is completely diminishing the original texture of host limestone (Figure 5c and d).

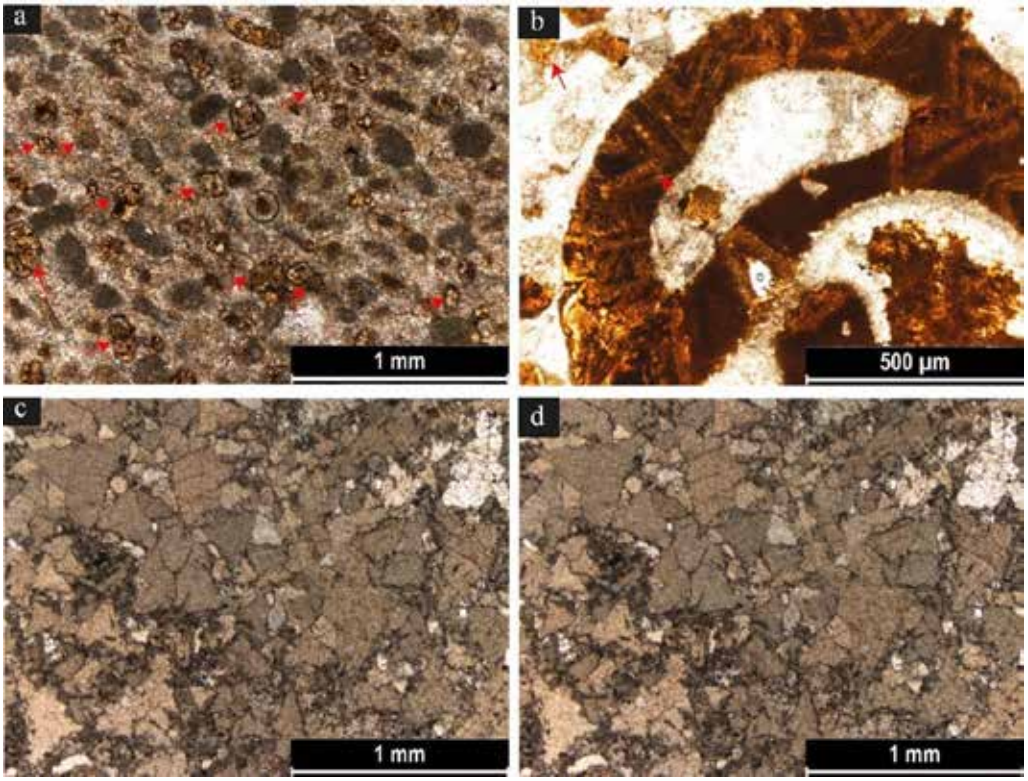

Figure 5. Photomicrographs of dolomite phases. **(a)** Medium to coarse crystalline euhedral zooned dolomites DII. **(b)** The dolomite DII filling the weak zones and void spaces of host limestone which occurs as a void filling. (**c** and **d**) later stage coarse crystalline anhedral dolomites DIII.

5.3 Stable Carbon and Oxygen Isotope analysis

Nine representative samples from dolomites were analyzed for stable carbon and oxygen isotopes ($\delta^{13}C$ and $\delta^{18}O$). The $\delta^{13}C$ and $\delta^{18}O$ values of these dolomites are listed in Table 1. The obtained results were then compared with the original Jurassic Marine (sea) carbonate signatures of Fursich et al., (2004). The dolomite DI hold $\delta^{18}O$ values in the range of -2.98‰ and -3.94‰ V-PDB while the $\delta^{13}C$ values varies from +1.32‰ to +1.53‰ V-PDB. The $\delta^{18}O$ and $\delta^{13}C$ results of DII varies from -4.89‰ to -5.37‰ V-PDB and +0.88‰ to +1.32‰ V-PDB respectively. The dolomite DIII exhibit $\delta^{18}O$ signatures in the range of -6.11‰ and -6.84‰ V-PDB while the δ13C values varies from +1.19‰ to +1.46‰ V-PDB. All the obtained results were then compared with the known Middle Jurassic original sea water values which range from −2.8% to −1.8% δ18O V-PDB and +0.0% to +1.8% $\delta^{13}C$ V-PDB (Fursich et al., 2004, Khan et al., 2021).

Table 1. The stable carbon and oxygen isotope values of the dolomite phases from the Jurassic Samana Suk Formation

Sr. No	Sample Code	Dolomite Types	$\delta^{13}C$ V-PDB	$\delta^{18}O$ V-PDB
01	JSS 3	DI	+1.35	-3.94
02	JSS 4A	DI	+1.53	-3.63
03	JSS 6	DI	+1.32	-2.98
04	JSS 10	DII	+0.88	-4.89
05	JSS 13	DII	+1.11	-5.37
06	JSS 14A1	DII	+1.71	-5.16
07	JSS 16	DIII	+1.46	-6.11
08	JSS 17A1	DIII	+1.41	-6.47
09	JSS 18	DIII	+1.19	-6.84

6. Discussions

The Jurassic Samana Suk Formation is composed of carbonates assemblage which represents a typical Mesozoic succession that attracts the interest of many researchers. The formation comprises oolitic, pelitic and fossiliferous limestone that are deposited in the inner to middle shelf environment during Jurassic (Qureshi et al., 2008; Nizami and Sheikh, 2009; Hussain et al., 2013; Rahim et al., 2020). In the study area, after their deposition, the formation passes through various diagenetic phases like micritization, neomorphism, compaction, recrystallization, cementations, and dolomitization (Ullah et al., 2016). In the current study, the process of dolomitization is investigated in detail in terms of field observations, petrography, and stable isotope analysis. According to Ullah et al., (2016), the micritization occurs most commonly as a micritic rim around skeletal and non-skeletal grains and represents the early marine diagenetic phase (Tucker and Wright, 1990). It is also reported by Rahim et al., (2020) and Khan et al., (2022) in the Jurassic Samana Suk Formation from Himalayan Hill Ranges and Kohat Basin respectively. In the field observations, the early diagenesis is observed in the form of mechanical and chemical compaction (Figure 3d and e). During shallow to deep burial conditions, the overburdened depositional pressure which combines with the tectonic stresses creates various fractures (Ahmad et al., 2017; Rahim et al., 2020). The mechanical compaction starts soon after the initial few meters of burial conditions (Shinn and Robbin, 1983). Based on its peaks (tooths), the stylolites are either bedding parallel (horizontal peaks) or bedding perpendicular (vertical peaks). Vertical peak stylolites are when the peak direction is vertical and perpendicular to bedding planes. Horizontal peak stylolites are defined where the peak (teeth) direction is horizontal and parallel to bedding planes (Al-Hejoj et al., 2013). The bedding parallel stylolites (Figure 3e) are induced through the pressure dissolution process of chemical compaction (Lloyd, 1977; Alhejoj et al., 2018; Khan et al., 2022). The mechanical and physical compaction most occurred in Samana Suk Formation which is observed and reported by many authors (Shah et al., 2016; Khan et al., 2020; Rahim et al., 2020; Shah et al., 2020; Wadood et al., 2021; Khan et al., 2021 and 2022; Rahim et al., 2022). This early diagenetic episode is followed by the formation of various dolomites representing later diagenetic phases. The fractures and voids are filled by the later diagenetic golden color dolomite (Figure 3d). The dark grey color of dolomite shows a sharp contact with the oolitic limestone (Figure 3c) suggesting a later dolomitization event (Rahim et al., 2022).

Petrographically, the dolomites were classified into three types following Sibley and Gregg's (1987) classification. These various dolomite texture shows the occurrences of multiphase dolomitization events (Khan et al., 2020). The dolomite (DI) exhibits a planar euhedral crystal shape which perceives their formation at near-surface conditions (Sibley 1982; Rahim et al., 2020). The coarser rhomb of dolomite DI shows clear crystal boundaries (Figure 4c and d) and represents the earlier dolomitization stage, replacing the matrix and grains of precursor limestone. The formation of coarser grain euhedral dolomite DI originates from shallow burial conditions of later diagenetic event (Amthor et al., 1991; Khan et al., 2020). Contrary to dolomite DI, the dolomite DII shows planar euhedral crystals and coarser grains that fill the vugs and fractures of host limestone (Figure 5a and b) which endorsed their precipitation from hot saline brines with temperature more than 60°C of deep burial regime (Al-Aasm et al., 2002; Shembilu et al., 2021; Liang et al., 2022). The occurrence of dolomites along stylolites and fractures indicates that the fractures provide a possible pathway for these dolomitizing fluids (Martín-Martín et al., 2017; Rahim et al., 2020). DII is zoned dolomite which attributes their origin from hydrothermal fluids (Gregg and Shelton, 1990; Warren, 2000; Rahim et al., 2022). According to Gao et al., (2016), the concentric zones of dolomites are for the reason of their burial origin. Such kind of zoned dolomite of the same kind and nature has been reported regionally and locally (Drivet and Mountjoy, 1997; Al-Aasm and Packard, 2000; Chen et al., 2004; Azmy et al., 2009; Conliffe et al., 2012; Rott and Qing, 2013; Khan et al., 2020; Shah et al., 2020; Khan et al., 2022). The DIII is coarse-grained anhedral dolomite showing tight packing and more curved faces (Figure 5c and d) which shows a rapid growth rate at higher temperatures (Montañez and Read, 1992; Al-Aasm and Packard, 2000; Warren, 2000; Huang et al., 2003; Machel, 2004; Khan et al., 2022; Saleem et al., 2022; Saleema et al., 2022).

The results δ13C and δ18O were cross-plotted and compared with the known original Jurassic marine signatures of δ13C and δ18O varies from +0.0% to +1.8% (V-PDB) and from −2.8% to −1.8% (V-PDB) respectively (Figure 6; Fürsich et al., 2004; Khan et al., 2021). The δ18O values of three dolomite types lie between -6.88 and -2.98 which are very lighter and depleted from original Jurassic marine signature and are consistent with multiphase dolomitization events (Dickson and Coleman, 1980; Swart, 2015; Rahim et al., 2020; Khan et al., 2021; Saleem et al., 2022;). The lighter $\delta^{18}O$ values indicate to rock fluids interaction where the fluid temperature is higher than the ambient temperature of precursor limestone (Shah et al., 2016; Khan et al., 2021). The $\delta^{18}O$ values of dolomite DI range between -2.98 and -3-94 ‰ V-PDB (Table 1 and Figure 6) which show relatively less depletion and mark the earlier phase of dolomitization event of low temperature (Sibley and Gregg, 1987; Gregg and Shelton, 1990; Shah et al., 2019). In contrast, the dolomite DII represents more depleted $\delta^{18}O$ values (Table 1 and Figure 6) and represents relative burial and high temperature for their formation. The occurrence of dolomite DII along fractures, its zoned crystals, and depleted $\delta^{18}O$ values represents its formation during burial conditions from hydrothermal fluid interactions (Gregg and Shelton, 1990; Warren, 2000; Al-Aasm et al., 2002; Gao et al., 2016; Martín-Martín et al., 2017; Rahim et al., 2020; Shembilu et al., 2021; Liang et al., 2022). Among all the observed dolomite phases, the dolomite DIII shows more depleted $\delta^{18}O$ signatures from standard marine values (Table 1 and Figure 6) and endorsed a later diagenetic hydrothermal origin (Sibley and Gregg, 1987; Allan and Wiggins, 1993; Moore, 2001; Shah et al., 2019).

The currents isotope results were also compared with previous published isotope values of various dolomite types of the Samana Suk Formation (Figure 6b). The isotope values of the current section show consistency with the isotope values from different reported sections of the Samana Suk Formation (Figure 6b). More information is available in Figure 6. Moreover, in the current study, the packstone and grainstone facies are not affected by dolomitization events since the pore spaces and conduit for hydrothermal fluids have already been occupied by the calcite cements (Figure 4a and b). These grain-supported facies have negligible porosity and don't allow dolomitization fluids to pass and cause dolomitizations,while the wackestone and mudstone units shows minute primary porosity and permeability and show resistance to significant calcite cementation during earlier diagenetic processes. These facies possess intergranular pore-network which were the target zones for Mg-rich fluids during dolomitization process. Same grainstone, and packstone facies show resistance to dolomitization and mudstone, and wackstone facies underwent through dolomitization process in the Samana Suk Formation were reported by many authors (Rahim et al., 2020; Shah et al., 2020, Khan et al., 2020; Saboor et al., 2020; Khan et al., 2022).

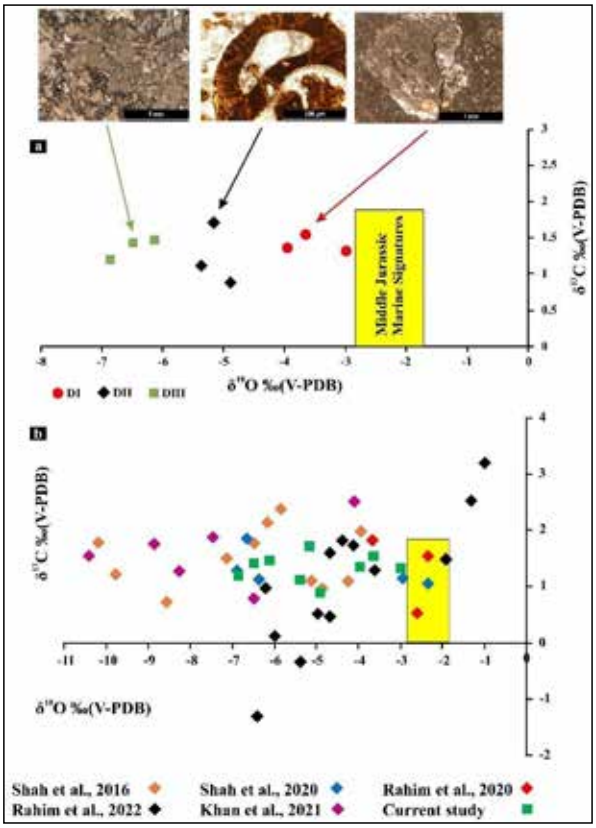

Figure 6. Cross plots between $\delta_{13}C$ and $\delta_{18}O$ (V-PDB) values representing various dolomite phases of Jurassic Samana Suk Formation which are compareed with the known Middle Jurassic marine seawater signatures after Fürsich et al., (2004). (a) Various dolomites phases showing depletion from original marine condition. (b) The result of the current study is compared with previously reported data. The data distribution documents the progressive depletion of isotopic composition from the known Jurassic marine sea water signatures. Note that the value of the current study shows consistency with the published data.

7. Conclusions

The Jurassic Smana Suk Formation is characterized by a thick carbonate sequence which passes through various diagenetic alteration. The diagenetic modification is traced by means of field observation, petrography, and stable isotopes analysis. From this study, it is concluded that a multiphase dolomitization processes occur in the Samana Suk Formation. Soon after the deposition, the first phase of dolomitization initiated which is supported by the occurrence of stylolite and less depleted $\delta^{18}O$ values. It is followed by the second phase of dolomitization along vugs and fractures which is supported through more depleted $\delta^{18}O$ values and dolomite zonation. The fractures act a conduit for Mg-rich hydrothermal fluids. The third phase of dolomitization is marked by the presence of coarse grained, curved face anhedral dolomites showing a very depleted $\delta^{18}O$ values from standard marine signatures. The more depleted $\delta^{18}O$ values suggest their formation from hydrothermal fluids. The study area lies in the Himalayan orogeny where the MBT mark the southern boundary. The fractures and various small and larger faults, resulted due to Himalayan orogeny, may provide as possible pathway for these Mg-rich hydrothermal fluids.

Acknowledgments

We would like to express our sincere appreciation to the National Centre of Excellence in Geology (NCEG), University of Peshawar for access to their petrographic lab.

References

Abed, A.M., Al-Halboosi, J.M., Al-Jibouri, A.S., Al-Hetty, S.O. (2023). 2D Seismic Stratigraphic Analysis of Harthaand Kifl Formations in Balad Area–Center of Iraq. Jordan Journal of Earth & Environmental Sciences, 14(1).

Al-Aasm, I.S., Lonnee, J., Clarke, J. (2002). Multiple fluid flow events and the formation of saddle dolomite: case studies from the Middle Devonian of the Western Canada Sedimentary Basin. Marine and Petroleum Geology, 19(3): 209-217.

Al-Aasm, I.S., Packard, J.J. (2000). Stabilization of early-formed dolomite: a tale of divergence from two Mississippian dolomites. Sedimentary geology, 131(3-4): 97-108.

Alhejoj, I., Alqudah, M., Alzughoul, K., Tarawneh, A. (2018). Post-Cretaceous Mesostructures and Their Formation Mechanisms, Jordan. Jordan Journal of Earth and Environmental Sciences, 9(2).

Al-Hejoj, I.K., Salameh, E., Abu Hamad, A. (2013). Deformed fossils and related structures in Jordan. Jordan J. Earth Environ. Sci, 5(1), 31-44.

Allan, J.R., Wiggins, W.D. (1993). Dolomite reservoirs: Geochemical techniques for evaluating origin and distribution. American Association of Petroleum Geologists.

Azmy, K., Knight, I., Lavoie, D., Chi, G. (2009). Origin of dolomites in the Boat Harbour Formation, St. George Group, in western Newfoundland, Canada: implications for porosity development. Bulletin of Canadian Petroleum Geology, 57(1): 81-104.

Azmy, K., Lavoie, D., Knight, I., Chi, G. (2008). Dolomitization of the Lower Ordovician Aguathuna Formation carbonates, Port au Port Peninsula, western Newfoundland, Canada: implications for a hydrocarbon reservoir. Canadian Journal of Earth Sciences, 45(7): 795-813.

Azmy, K., Veizer. J., Misi, A., de, Oliveira, T.F., Sanches, A.L., Dardenne, M.A. (2001). Dolomitization and isotope stratigraphy of the vazante formation, sao francisco basin, Brazil. Precambrian Research, 112 (3-4): 303–329.

Bandyopadhyay, S., Chatterjee, S., Scotese, C. (2010). The wandering Indian plate and its changing biogeography during the Late Cretaceous-Early Tertiary period. New aspects of Mesozoic biodiversity 105-126.

Bell, F.G. (2016). Fundamentals of engineering geology, Elsevier.

Calkins, J.A., T.W.O., S.K.M. A. (1975). Geology of the southern Himalaya in Hazara, Pakistan and adjacent areas.

Chatterjee, S. (1992). A kinematic model for the evolution of the Indian plate since the Late Jurassic. New concepts in global tectonics, 33-62.

Chatterjee, S., Goswami, A., Scotese, C.R. (2013). The longest voyage: Tectonic, magmatic, and paleoclimatic evolution of the Indian plate during its northward flight from Gondwana to Asia. Gondwana Research 23(1): 238-267.

Chatterjee, S., Scotese, C.R. (1999). The breakup of Gondwana and the evolution and biogeography of the Indian plate. Proceedings-Indian national science academy part A 65(3): 397-426.

Chatterjee, S., Scotese, C.R. (2007). Biogeography of the Mesozoic lepidosaurs on the wandering Indian plate, Paleontologia: Cenários de Vida, Editora Interciência. Rio de Janeiro 551-579.

Chatterjee, S., Scotese, C.R. (2010). The wandering Indian plate and its changing biogeogrphy during the Late Cretaceous–Early Tertiary period, In: Bandopadhyay, S. (Ed.), New Aspects of Mesozoic Biogeography. Springer-Verlag, Berlin Heidelberg, Germany, pp. 105–126.

Chen, D., Qing, H., Yang, C. (2004). Multistage hydrothermal dolomites in the Middle Devonian (Givetian) carbonates from the Guilin area, South China. Sedimentology 51(5): 1029-1051.

Conliffe, J., Azmy, K., Greene, M. (2012). Dolomitization of the lower Ordovician Catoche formation: Implications for hydrocarbon exploration in western Newfoundland. Marine and Petroleum Geology 30(1): 161-173.

Dietz, R.S., Holden, J.C. (1970). The breakup of Pangaea, Scientific American 223(4): 30-41.

Drivet, E., Mountjoy, E.W. (1997). Dolomitization of the Leduc Formation (Upper Devonian), southern Rimbey-Meadowbrook reef trend, Alberta. Journal of Sedimentary Research 67(3): 411-423.

Flügel, E., Flügel, E. (2004). Diagenesis, porosity, and dolomitization. Microfacies of carbonate rocks: Analysis, interpretation and application, 267-338.

Gregg, J.M., Shelton, K.L. (1990). Dolomitization and dolomite neomorphism in the back reef facies of the Bonneterre and Davis formations (Cambrian), southeastern Missouri, Journal of Sedimentary Research 60(4): 549-562.

Hou, M.C., Jiang, W.J., Xing, F.C., Xu, S.L., Liu, X.C., Xiao, C. (2016). Origin of dolomites in the Cambrian (upper 3rd-Furongian) formation, south-eastern Sichuan Basin, China. Geofluids 16(5): 856-876.

Huang, S.J., Shi, H., Mao, X.D. (2003). Diagenetic alteration of earlier Palaeozoic marine carbonate and preservation for the information of sea water. Journal of chengdu university of technology 30(1): 9-18.

Hussain, G., Fang, X., Usmani, N.A., Gardezi, S.A.H., Hussain, M., Asghar, H., Khalid, S. (2020). Structural and stratigraphic studies of Hazara-Kashmir Syntaxis, northwestern Himalaya, Pakistan, North American Academic Research 3(9): 1-14.

Hylland, M.D., Riaz., Ahmad, S. (1988). Stratigraphy and structure of the southern Gandghar range, Pakistan, Geological Bulletin University of Peshawar 1: 15-24.

Jiang, L., Cai, C.F., Wordern, R.H., Crowley, S.F., Jia, L., Zhang, K. (2016). Multiphase dolomitization of deeply buried Cambrian petroleum reservoirs, Tarim Basin, north-west China. Sedimentology 63(7): 2130–2157.

Jiang, L., Worden, R.H., Cai, C., Li, K., Xiang, L., Cai, L., He, X. (2014). Dolomitization of gas reservoirs: the upper Permian Changxing and lower Triassic feixianguan formations, northeast Sichuan Basin, China. Journal of Sedimentary Research 84(10): 792-815.

Jiang, L., Xu, Z., Shi, S., Liu, W. (2019). Multiphase dolomitization of a microbialite-dominated gas reservoir, the middle Triassic Leikoupo Formation, Sichuan Basin, China. Journal of Petroleum Science and Engineering 180: 820-834.

Khan, E., Naseem, A.A., Khan, S., Wadood, B., Rehman, F., Saleem, M., Azeem, T. (2022). Facies Analysis, Sequence Stratigraphy and Diagenetic Studies of the Jurassic Carbonates of the Kohat Basin, Northwest Pakistan: Reservoir Implications. Acta Geologica Sinica-English Edition 96(5): 1673-1692.

Khan, E.U., Naseem, A.A., Saleem, M., Rehman, F., Sajjad, S.W., Ahmad, W., Azeem, T. (2021). Petrography and geochemistry of dolomites of Samanasuk Formation, Dara Adam Khel Section, Kohat Ranges, Pakistan, Sains Malaysiana 50(11): 3205-3217.

Khan, E.U., Saleem, M., Naseem, A.A., Ahmad, W., Yaseen, M., Khan, T.U. (2020). Microfacies analysis, diagenetic overprints, geochemistry, and reservoir quality of the Jurassic Samanasuk Formation at the Kahi Section, Nizampur Basin, NW Himalayas, Pakistan. Carbonates and Evaporites 35: 1-17.

Khan, E.U., Saleem, M., Wasim Sajjad, S.M., Ahmad, Z., Javaid, Z. (2024). Reservoir heterogeneities due to diagenesis in Jurassic Samana Suk Formation Kahi section Nizampur Basin North West Himalayas Pakistan. Acta Montanistica Slovaca, 29(1).

Klootwijk, C.T., Gee, J.S., Peirce, J.W., Smith, G.M., McFadden, P.L. (1992). An early India-Asia contact: paleomagnetic constraints from Ninetyeast ridge, ODP Leg 121. Geology 20(5): 395-398.

Liang, J., Liu, S., Li, L., Dai, J., Li, X., Mou, C. (2022). Geochemical Constraints on the Hydrothermal Dolomitization of the Middle-Upper Cambrian Xixiangchi Formation in the Sichuan Basin, China. Frontiers in Earth Science 10: 927066.

Liu, M., Xiong, Y., Xiong, C., Liu, Y., Liu, L., Xiao, D., Tan, X. (2020). Evolution of diagenetic system and its controls on the reservoir quality of pre-salt dolostone: The case of the Lower Ordovician Majiagou Formation in the central Ordos Basin, China. Marine and Petroleum Geology 122: 104-674.

Machel, H.G. (2004). Concepts and models of dolomitization: a critical reappraisal, Geological Society, London, Special Publications 235(1): 7-63.

Mahboubi, A., Nowrouzi, Z., Al-Aasm, I.S., Moussavi-Harami, R., Mahmudy-Gharaei, M.H. (2016). Dolomitization of the Silurian Niur Formation, Tabas block, east central Iran: Fluid flow and dolomite evolution. Marine and Petroleum Geology 77: 791-805.

Miraj, M.A.F., Ali, A., Javaid, H., Rathore, P.W.S., Ahsan, N., Saleem, R.F., Malik, M.B. (2021). An integrated approach to evaluate the hydrocarbon potential of jurassic samana suk formation in Middle Indus basin, Pakistan. Kuwait Journal of Science 48(4).

Montanez, I.P., Read, J.F. (1992). Fluid-rock Group (Lower Ordovician), US Appalachians. Journal of Sedimentary Research 62(5): 753-778.

Moore, C.H. (2001). Diagenetic environments of porosity modification and tools for their recognition in the geologic record. Carbonate reservoirs porosity evolution and diagenesis in a sequence stratigraphic framework. Developments in Sedimentology 55: 61-88.

Naka, T., Warrich, M.Y., Hirayma, J., Hassan, S. (1996). Stratigraphy, and structure of the Precam brian to Mesozoic, especially Precambrian (?) to Lower Cambrian phosphorite bearing formations in Abbottabad, northern Pakistan. Bulletin-geological survey Japan 47: 549-576.

Nizami, A.R., Sheikh, R.A. (2010). Sedimentology of the middle Jurassic Samana Suk Formation, Makarwal section, Surghar Range, Trans Indus Ranges, Pakistan. The Geological bulletin of the Punjab University 44: 2009.

Plummer, C.C., Carlson, D., Hammersley, L. (2016). Physical geology. McGraw-Hill/Education.

Rahim, H.U., Qamar, S., Shah, M.M., Corbella, M., Martín-Martín, J.D., Janjuhah, H.T., Kontakiotis, G. (2022). Processes Associated with Multiphase Dolomitization and Other Related Diagenetic Events in the Jurassic Samana Suk Formation, Himalayan Foreland Basin, NW Pakistan. Minerals 12(10): 1320.

Rahim, H.U., Shah, M.M., Corbella, M., Navarro-Ciurana, D. (2020). Diagenetic evolution and associated dolomitization events in the middle Jurassic Samana Suk Formation, Lesser Himalayan Hill Ranges, NW Pakistan. Carbonates and Evaporites 35: 1-26.

Rahim, Y., Lia, Q., Jadoona, U.F., Lutfia, W., Khanb, J., Akhtarc, S. (2020). Microfacies analysis of late Jurassic Samana Suk formation, Hazara basin lesser Himalaya north Pakistan. Earth Sciences Malaysia (ESMY) 4(2): 102-107.

Rott, C.M., Qing, H. (2013). Early dolomitization and recrystallization in shallow marine carbonates, Mississippian Alida Beds, Williston Basin (Canada): evidence from petrography and isotope geochemistry. Journal of Sedimentary Research 83(11): 928-941.

Saboor, A., Haneef, M., Hanif, M., Swati, M.A.F. (2020). Sedimentological attributes of the Middle Jurassic peloids-dominated carbonates of eastern Tethys, lesser Himalayas, Pakistan. Carbonates and Evaporites 35: 1-17.

Sajjad, N.U.I. (2020). Microfacies Analysis and Depositional Environment of Middle Jurassic Samana Suk Formation, Chichali Nala Section, Surghar Range, Pakistan. International Journal of Economic and Environmental Geology 11(4): 00-00.

Saleem, M., Rehman, F., Naseem, A.A., Khan, E., Sajjad, S.W., Ahmad, Z. (2022). Petrographic and geochemical characteristics of dolomites in the Devonian Shogram Formation, Karakorum Ranges, North Pakistan. Current Science 123(4): 583.

Saleem, M., Sajjad, S.W., Khan, E.U., Naseem, A.A., Bangash, A.A., Rafique, A., Ahmad, W. (2022). Classification of the dolomites of Cretaceous Kawagarh formation in Hazara Basin North-west Himalayas Pakistan: evidence from field investigation, petrographic analysis and isotopic studies. Carbonates and Evaporites 37(1): 10.

Saleema, M., Rehmana, F., Khana, E.U., Sajjada, S.W., Azeema, T., Jadoona, A., Naseema, A.A. (2022). Multiphase dolomitization in Devonian Shogram Formation, Chitral, Karakorum ranges, Pakistan: Evidence from outcrop analogue, petrography, and geochemistry. Science Asia 48(3).

Searle, M., Corfield, R.I., Stephenson, B.E.N., McCarron, J.O.E. (1997). Structure of the North Indian continental margin in the Ladakh–Zanskar Himalayas: implications for the timing of obduction of the Spontang ophiolite, India–Asia collision and deformation events in the Himalaya. Geological Magazine 134(3): 297-316.

Shah, M.M., Ahmed, W., Ahsan, N., Lisa, M. (2016). Fault-controlled, bedding-parallel dolomite in the middle Jurassic Samana Suk Formation in Margalla Hill Ranges, Khanpur area (North Pakistan): petrography, geochemistry, and petrophysical characteristics. Arabian Journal of Geosciences 9: 1-18.

Shah, M.M., Rahim, H.U., Hassan, A., Mustafa, M.R., Ahmad, I. (2020). Facies control on selective dolomitization and its impact on reservoir heterogeneities in the Samana Suk Formation (middle Jurassic), Southern Hazara Basin (NW Himalaya, Pakistan): an outcrop analogue. Geosciences Journal 24: 295-314.

Shah, S.B.A., Shah, S.H.A., Ahmed, A., Munir, M.N. (2021). Source Rock Potential of Chichali and Samana Suk Formations Deposits in Panjpir Oilfield Subsurface, Punjab Platform, Pakistan: Formation Deposits in Panjpir Oilfield Subsurface. Pakistan Journal of Scientific & Industrial Research Series A: Physical Sciences 64(1): 59-64.

Shembilu, N., Azmy, K., Blamey, N. (2021). Origin of Middle-Upper Cambrian Dolomites in Eastern Laurentia: A Case Study from Belle Isle Strait, Western Newfoundland. Marine and Petroleum Geology 125: 104858.

Sibley, D.F., Gregg, J.M. (1987). Classification of dolomite rock textures, Journal of sedimentary Research 57(6): 967-975.

SM, I.S. (1977) Stratigraphy of Pakistan. Geological Survey of Pakistan Memoir, 12: 1-138.

Swart, P.K., Cantrell, D.L., Westphal, H., Handford, C.R., Kendall, C.G. (2005). Origin of dolomite in the Arab-D reservoir from the Ghawar Field, Saudi Arabia: evidence

from petrographic and geochemical constraints. Journal of Sedimentary Research 75(3): 476-491.

Tariq, M.A., Abid, Q.Z. (1993). Geological map of Pakistan (Scale 1:1,000,000). Geological Survey of Pakistan.

Tucker, M.E. (1993). Carbonate diagenesis and sequence stratigraphy, Sedimentology Review, 1: 51-72.

Tucker, M.E., Bathurst, R.G. (2009). Carbonate diagenesis. John Wiley & Sons.

Tucker, M.E., Wright, V.P. (1990). Carbonate Sedimentology. Blackwell Scientific Publications: Oxford.

Ullah, N., Saboor, A., Ahmad, W., Haneef, M., Hussain, M.S., Jalil, R., Ullah, Z. (2016). Microfacies, diagenetic fabric and depositional environment of Middle Jurassic Samana Suk Limestone, Lower Salhad, Abbottabad Pakistan. 2nd International conference on: Sustainable Utilization of Natural Resource, National Centre of Excellence in Geology, University of Peshawar, Pakistan

Wadood, B., Aziz, M., Ali, J., Khan, N., Wadood, J., Khan, A., Ullah, M. (2021). Depositional, diagenetic, and sequence stratigraphic constrains on reservoir characterization: a case study of middle Jurassic Samana Suk Formation, western Salt Range, Pakistan. Journal of Sedimentary Environments 6:131-147.

Wadood, B., Khan, S., Li, H., Liu, Y., Ahmad, S., Jiao, X. (2021). Sequence stratigraphic framework of the Jurassic Samana Suk carbonate formation, North Pakistan: Implications for reservoir potential. Arabian Journal for Science and Engineering 46(1): 525-542.

Warren, J. (2000). Dolomite: occurrence, evolution and economically important associations, Earth-Science Reviews 52(1-3): 1-81.

Weijermars, R. (1989). Global tectonics since the breakup of Pangea 180 million years ago: evolution maps and lithospheric budget. Earth-Science Reviews 26(1-3): 113-162.

Xu, W.L., Li, J.Z., Liu, X.S., Li, N.X., Zhang, C.L., Zhang, Y.Q. (2021). Accumulation conditions and exploration directions of Ordovician lower assemblage natural gas, Ordos Basin, NW China. Petroleum Exploration and Development 48 (3): 641–654.

Yeats, R.S., Hussain, A. (1987). Timing of structural events in the Himalayan foothills of northwestern Pakistan. Geological society of America bulletin 99(2): 161-176.

Zhemchugova, V.A., Evdokimov, N.V., Poort, J., Akhmanov, G.G. (2020). Lower Permian Carbonate Buildups in the Northern Timan–Pechora Basin as the Main Hydrocarbon Exploration Object. Lithology and Mineral Resources 55: 245-260.

JJEES

JJEES (2024) 15 (4): 244-249
ISSN 1995-6681

Jordan Journal of Earth and Environmental Sciences

A Modeling Approach to Study the Water Inlet Flow Effect on Slow Sand Filtration Removal of Metallic Pollutants in Unsafe Water

Yassir Barkouch[1], Abdelaziz Ait Melloul[2], Khadija Flata[3*], Sana El Fadeli[4], Abdelilah El Abbassi[5], Alain Pineau[6]

[1] Laboratory of computer mathematics and modeling of complex systems , Higher School of Technology of Essaouira, Cadi Ayyad University, Km 9, Route of Agadir, Essaouira Aljadida BP.383, Essaouira, Morocco.
[2] Higher Institute of Nursing Professions and Health Technology, ISPITS - Marrakech - Morocco.
[3] Regional Laboratory for Epidemiological Diagnosis and Environmental Hygiene, Boulevard des Hôpitaux, Gueliz-Marrakesh, Morocco.
[4] Higher Institute of Nursing Professions and Health Technology, ISPITS - Essaouira - Morocco.
[5] Laboratory of Agrifood Biotechnology and Valorization of Plant Bioressources. Department of Biology, Faculty of Science Semlalia, Cadi Ayyad University, Marrakech- Morocco.
[6] UFR de Sciences Pharmaceutiques et Biologiques, Centre de Dosage des Eléments Minéraux (CDEM), 9 rue Bias, BP 53508, 44035 Nantes, France.

Received on January 23, 2024; Accepted on September 10, 2024

Abstract

In various regions confronting water scarcity, the agricultural reuse of wastewater presents potential challenges, prompting the need for economical methods to reduce metallic pollutants, such as the implementation of slow sand filtration. This investigation sought to understand the efficacy of metallic pollutant removal using sand as an adsorbent, employing the adsorption process to develop a cost-effective strategy for treating water contaminated with heavy metals from the Tensift River. This river directly receives wastewater from the industrial unit of Zn and Pb extraction at the Draa Lasfar mine, located 13 km northwest of Marrakech City, Morocco. The results indicated that slow sand filtration efficiently purifies water, with its effectiveness significantly influenced by the water inlet flow in filtration columns. A decrease in water inlet flow prolonged the residence time of solutes in the filter bed, augmenting contact time and fostering chemical bonds between metallic trace elements and their binding sites on the sand. Logistic component analysis, ensuring coherence between the model, experimental outcomes, and interpretation, facilitated the prediction of the dynamic behavior of the adsorption mechanism in the slow sand filtration process, articulated by a single logistic model.

Keywords: *Metallic Trace Elements, Modeling, Slow Sand Filtration, Inlet Flow, Removal Efficiency, Unsafe Water Reuse.*

1. Introduction

Improving agricultural water management is critical for enhancing productivity in arid regions globally (Zhou et al., 2021; Magombeyi et al., 2018), where agriculture plays a pivotal role in sustainable development, food security, and poverty reduction. The past century, particularly the last two decades, has witnessed significant water body contamination due to diverse human activities, intensifying water management challenges amid the ongoing trends of urbanization and industrialization (Hussien et al, 2022; Hadef et al, 2021; Calmuc et al., 2020; Pham et al., 2017; Gokul et al., 2015). The escalating human population density and anthropogenic actions contribute to environmental degradation, introducing detrimental substances through resource mismanagement and improper waste disposal (Omonona and Azombe, 2024; Siddiqua et al, 2022). These substances jeopardize ecosystem stability and the renewal of natural resources such as air, water, and soil (Bani Khaled et al, 2024; Al Rabadi et al., 2023; Changyoon et al., 2023), leading to environmental mismanagement and consequent water crises like water scarcity (Chiedozie and Tosan, 2022).

Globally, water scarcity is emerging as a pivotal challenge to human health and environmental stability (Carlo et al., 2023; Al-Qawasmi and Al Sharif, 2022). The increasing demand for this vital resource has spurred innovative techniques to preserve its sustainability and ensure a secure status concerning both quantity and quality, employing novel recycling processes. Among these strategies, the reuse of non-potable water in activities with less stringent water quality standards stands out, reducing the demand for potable water and extending the service life of freshwater resources (Al-Mubaidin et al, 2022).

Various water treatment processes, tailored to pollution rates and regional disparities, facilitate the reuse of unsafe water. This study focuses on slow sand filtration, which is considered a suitable technology for purifying unsafe water, particularly in rural areas. It adeptly removes waterborne pathogens and metallic and organic components and diminishes turbidity (Maiyo et al., 2023). Originating in 1804, slow sand filtration has evolved into a widely employed technique for drinking water production (Maiyo et al., 2023; Guchi, 2015; Haig et al., 2011) and enhancing wastewater quality for reuse (Abdiyev et al., 2023; Zhang et al., 2022; Agrawal et al., 2021; Hijnen et al., 2004) or environmentally safe discharge (Islam et al., 2021).

The present study delves into the efficiency of slow sand

* Corresponding author e-mail: Kh.flata@yahoo.fr

filtration in purifying unsafe water from the Tensift River, which receives wastewater directly from the Draa Lasfar mine near Marrakech, Morocco. Physicochemical analyses were meticulously conducted on water samples before and after filtration, evaluating the filter's proficiency in removing metallic trace elements (Cd, Cu, Pb, and Zn) under varying column inlet water flow conditions. Additionally, the study aspires to pioneer a new prediction method, involving a mathematical model of the slow sand filtration process, while considering the column inlet water flow parameter, to ensure a secure status in water reclamation.

2. Material and Methods

2.1 Studied Location

Draa Lasfar mine, situated approximately 13 kilometers west of Marrakech city, is a geological site characterized by the presence of pyrite minerals. Discovered in 1953, the mine's commercial exploitation commenced in 1979, marked by the processing of minerals through flotation after primary and secondary crushing and grinding. This extraction yielded substantial production, with 60 million tons of products generated in the initial two years (1979 and 1980). Notably, Draa Lasfar mine became dormant in March 1981 but saw a resurgence in 1999 due to its rich reserves of polymetallic components, including arsenic (As), cadmium (Cd), copper (Cu), iron (Fe), lead (Pb), and zinc (Zn). The mining activities, while contributing valuable resources, have raised environmental concerns, particularly regarding the direct discharge of wastewater into the nearby Tensift River without pretreatment measures. The Draa Lasfar deposit contains 10 Mt of ore grading 5.3 wt.% Zn, 2 wt.% Pb, 0.3 wt.% Cu, and their orebodies consist dominantly of pyrrhotite (70 to 95 vol.% of sulfides, but commonly up to 90 to 95 vol.% in Zn and Cu-depleted zones), with lesser sphalerite (1 to 10 vol.%), galena (0.5 to 5 vol.%) and chalcopyrite (1 to 5 vol.%), and with local concentrations of deformed pyrite (2 to 3 vol.% of total sulfides) being arsenopyrite the most common of the minor minerals (Avila et al, 2012).

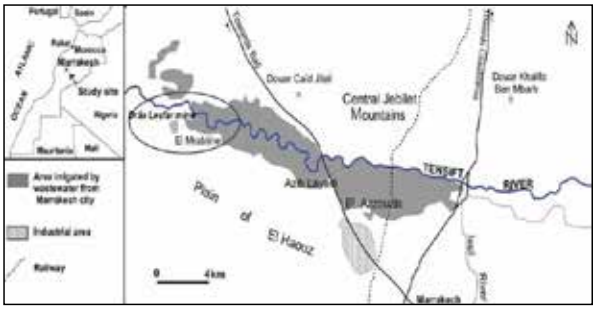

Figure 1. Geographical locations of Draa Lasfar mine and the Tensift River in the Marrakech Region.

Samples of mine wastewater and Tensift River water were collected directly, both upstream and 50 meters downstream from the point of mixing with wastewater from the Zn and Pb extraction industrial unit at Draa Lasfar mine. The collection involved using sterile plastic bottles with a capacity of 2000 milliliters, and each bottle was rinsed three times with sample water before collection. For river sample collection, a bottle with a string attached to the neck was deployed, and upon retrieval, the bottle was sealed. The collected samples were promptly transported to the laboratory in ice within an insulated container to conduct the slow sand filtration study in laboratory columns.

2.2 Slow Sand Filtration Experiment

The experimental setup for slow sand filtration involved three polypropylene plastic columns, each sharing a standard diameter (D=10cm) (Farrag et al., 2017). These columns, open at both ends, facilitated the inlet of contaminated water at the top and effluent discharge at the bottom. The study focused on assessing the efficiency of slow sand filtration in removing metallic trace elements (Cd, Cu, Pb, and Zn) from Tensift River water. This assessment was conducted by percolating untreated water through two columns filled to a uniform sand height of 10 cm. Before each experiment, a continuous overnight flow of distilled water through the columns at a rate of 20 ml/min was employed to eliminate any residual metal elements (Farrag et al., 2017).

To investigate the influence of water inlet flow rate on the dynamics of waterborne metallic pollutants, two columns with identical diameters (D=10cm) were utilized, filled to the same sand height of 10 cm. Water samples were systematically poured through these columns at three distinct flow rates: 6 ml/min, 10.1 ml/min, and 20 ml/min. Effluent from the filtration column was collected through a test tube connected to the bottom opening. Subsequently, the collected water samples were preserved in ice within a designated container and subjected to analysis within 24 hours of collection.

3. Results and Discussion

Table 1 presents the textural characteristics of the sand employed in the study. Table 2 outlines the average concentrations of lead (Pb) in Draa Lasfar mine wastewater (DW) and Tensift River water before (WB) and after (WA) the receipt of mine wastewater. Figures 2, 3, 4, and 5 depict visual representations of the concentrations of metallic trace elements (Cd, Cu, Pb, and Zn) in the reclaimed solutions (effluent).

Table 1. Particle size analysis of the sand

Sieve size (mm)	Retained weight (g)	% of retained weight	% of cumulative weight
0.3	338	16.9	16.9
0.15	1358	67.9	84.8
0.09	218	10.9	95.7
0.075	42	2.1	97.8
0.001	44	2.2	100

Table 2. Chemical and physical properties of DW, WB, and WA.

Parameters	DW	WB	WA
pH	6.79 ± 0.19	7.01 ± 0.98	7.03 ± 0.11
O_2 (mg/l)	0.21 ± 0.11	6.81 ± 0.29	6.59 ± 0.39
T (°C)	28.09 ± 0.38	27.49 ± 0.41	27.69 ± 0.48
CE (mS/cm)	4.02 ± 1,01	4.71 ± 0.78	4.39 ± 0.57
SM (mg/l)	78.28 ± 1.62	56.68 ± 2.57	57.78 ± 4.46
SO_4^{2-} (mg/l)	192.21 ± 6.36	100.72 ± 5.72	123.66 ± 8.35
Cl^- (mg/l)	2356 ± 24.51	80.73 ± 12.81	1819 ± 13.12
NH_4^+ (mg/l)	4.12 ± 1.21	5.92 ± 1.73	4.54 ± 1.22
NO_2^- (mg/l)	1.72 ± 0.41	9.14 ± 1.12	9.63 ± 1.47
Ca^+ (mg/l)	1358.68 ± 24.96	218.89 ± 27.48	468.86 ± 17.92
K^+ (mg/l)	111.1 ± 10.12	77.42 ± 20.89	104.48 ± 12.03
Na^+ (mg/l)	383.38 ± 21.78	225.34 ± 25.67	274.39 ± 19.12
PO_4^{3-} (mg/l)	6.58 ± 1.75	44.76 ± 3.48	37.57 ± 4.77
Metallic trace elements			
Cd (µg/l)	6.1 ± 0.8	3.4 ± 0.8	4.2 ± 1.2
Cu (µg/l)	89.9 ± 4.9	45.9 ± 6.5	66.9 ± 6.0
Pb (µg/l)	455,7 ± 72,5	131.9 ± 18.0	314.9 ± 42.9
Zn (µg/l)	889.1 ± 36.1	529.9 ± 31.9	797.1 ± 26.9

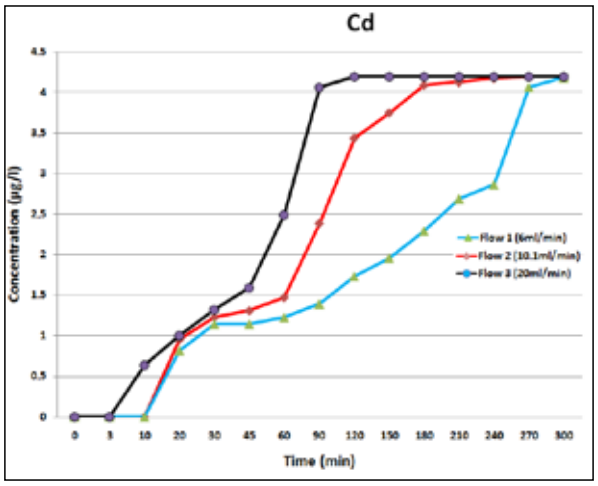

Figure 2. Cd concentration evolution in filtered water over time at three distinct inlet flow rates.

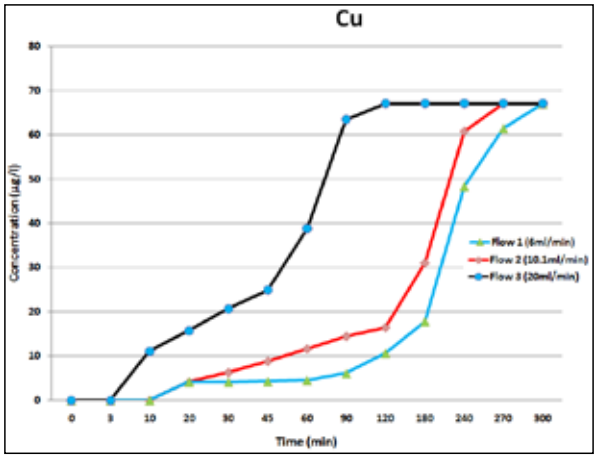

Figure 3. Cu concentration evolution in filtered water over time at three distinct inlet flow rates.

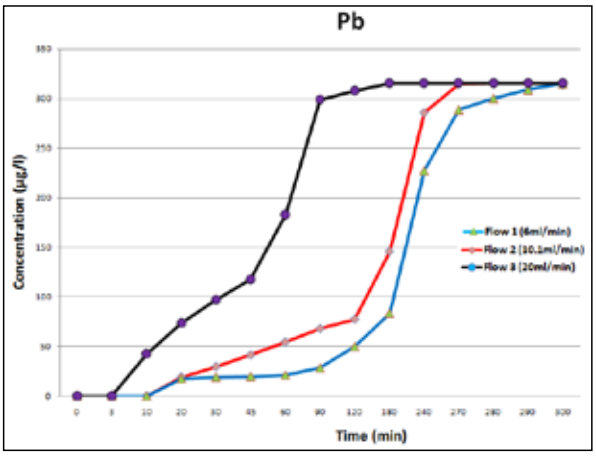

Figure 4. Pb concentration evolution in filtered water over time at three distinct inlet flow rates.

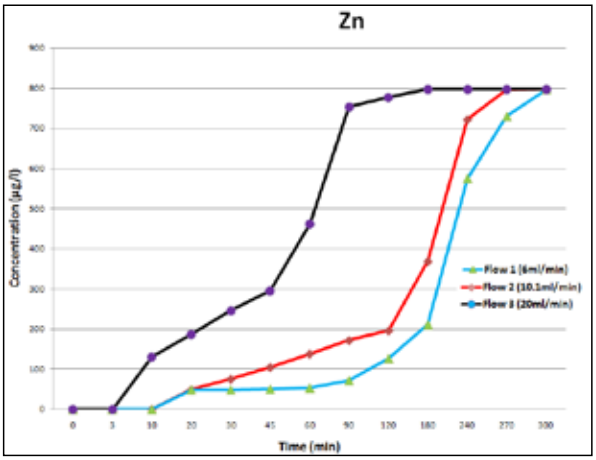

Figure 5. Zn concentration evolution in filtered water over time at three distinct inlet flow rates.

These results indicate a progressive shift in the concentrations of the investigated metallic trace elements in effluents, showing a gradual increase and stabilization toward a maximum equilibrium value (Ω), contingent on the specific

metallic trace element and its initial concentration in the inlet water (Barkouch et al., 2007). Notably, this equilibrium value remains nearly identical to the concentration of the initial water (influent).

Furthermore, the outcomes highlight that the efficiency of the filtration process, designed for water decontamination, is notably influenced by the water inlet flow rate in the filtration columns (Barkouch et al., 2018). Lower water inflow rates demonstrate a more effective removal of metallic pollutants than higher rates. This phenomenon is attributed to the prolonged residence time of metal pollutants in the sand filter due to the resistance imposed by the sand bed, facilitating the establishment of chemical bonds on exposed binding sites. The slow filtration rates result in an extended contact time between the filtered water and the sand filter, progressively enhancing the fixation of metallic pollutants until the saturation of sand binding sites, evident at the end of the filtration process (approximately 300 min).

Results also show that the removal efficiencies for specific metallic trace elements (Cd, Cu, Pb, Zn) were indeed variable, as detailed in Figures 2, 3, 4, and 5. Copper (Cu) demonstrated the highest removal efficiency, followed by cadmium (Cd), lead (Pb), and zinc (Zn). The observed removal efficiencies were dependent on the flow rate through the filtration columns. For instance, at the highest flow rate tested (20 ml/min) at 60 min, Cu removal efficiency was approximately 43.4 %, whereas Cd, Pb, and Zn removal efficiencies were around 40%, 14.3%, and 5%, respectively. As the flow rate decreased, the removal efficiencies for all metals increased, confirming the inverse relationship between flow rate and residence time in the filter bed (Casas and Bester, 2015).

The particulate nature of sand introduces distinctive behaviors, with varying residence times for solutes within different zones of the sand bed. Achieving concentration equilibrium takes considerably longer with lower water flow rates compared to higher rates with greater hydraulic conductivity. This non-equilibrium condition may arise during mass transfer processes, with weak water flow rates leading to preferential interactions between solutes and sand binding sites. As depicted in Figures 2, 3, 4, and 5, the exhaustion of sand particulate beds occurred more rapidly at higher bed water flow rates (Chowdhury et al., 2013), resulting in an earlier breakthrough point. The breakpoint time decreased with increasing water flow rate, indicating insufficient residence time for metallic pollutants to establish bonds with the sand, leading to an early breakthrough. Lower water flow rates produced extended breakthrough curves, signifying the treatment of a higher solution volume, attributed to the slower transport caused by a reduction in diffusion coefficient or mass transfer coefficient (Abdulhusain and Abd Ali, 2023).

4. Modeling of Analytical Results

Modeling is an important tool in designing, scaling up, and optimizing environmental engineering processes such as slow sand filtration (Al-Haj-Ali and Al-Matar, 2024). The process functioning dynamics of slow sand filtration columns with sand as the adsorbent can be conceptualized by analyzing experimental data obtained at the laboratory level. Several mathematical models have been designed to evaluate the efficiency and feasibility of implementing this process on a large scale (Abdiyev et al., 2023). Predicting the column adsorption process in slow sand filtration is crucial for anticipating both the breakthrough curve (concentration-like profile) and the adsorption capacity of sand for metallic trace elements under specific operating conditions (Benjelloun et al., 2021). The anticipated behavior of these columns can be projected using established models like Adams–Bohart, Thomas, and Yoon–Nelson, playing a pivotal role in designing an effective fixed-bed adsorption system with optimal conditions (Barkouch et al., 2019). Notably, these models have yet to integrate the influence of water flow rates into their mathematical expressions for water decontamination. The modeling of the slow sand filtration mechanism is based on its resemblance to compliant processes having a unique logistic model, represented by the following formula:

$$d[M](t)/dt = Q*P*[M](t)*(1 - [M](t)/\Omega)$$ (Barkouch et al., 2019)

In the equation, Q represents the water flow rate, and the constant P incorporates various parameters influencing the transfer of metallic trace elements from contaminated water into the particulate bed (Barkouch et al., 2007). Additionally, Ω signifies the maximum equilibrium value of the effluent achieved at the particulate bed's maximum adsorption capacity.

The MATLAB code employed for Cd is structured as follows:

```
T=300; dt=1; k=0.8; om=4, Q1=0.06; Q2=0.10; Q3=0.20;
t=0:dt:T;
F0=0.1;
[M,N]= size(t);
F=zeros(M,N);
F1(1)=F0;
F2(1)=F0;
for i=1:T-1
F1(i+1)= Q1*P*(1-(F1(i)/om))*F1(i)*dt + F1(i);
F2(i+1)= Q2*P*(1-(F2(i)/om))*F2(i)*dt + F2(i);
F3(i+1)= Q3*P*(1-(F3(i)/om))*F3(i)*dt + F3(i)
end
plot(t, F1,'o-black',t, F2,'R--*',t, F3,'o-b')
```

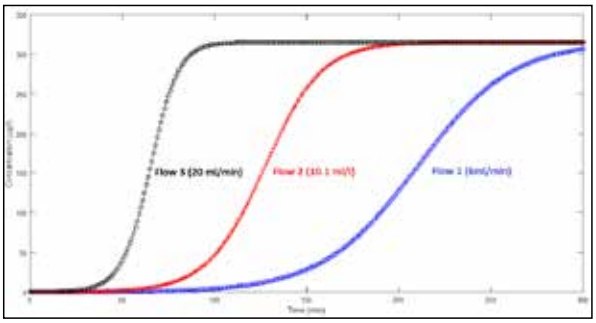

Figure 6. Breakthrough curves of metallic trace elements adsorption under different inlet water flow conditions.

5. Conclusion

This study demonstrates the effectiveness of slow sand filtration in removing metallic trace elements from the Tensift River water, which has been contaminated by wastewater discharge from the Draa Lasfar mine in the Marrakech Region, Morocco. The filtration process showed significantly better performance at lower water inlet flow rates. By decreasing the inlet flow, the residence time of solutes in the filter bed is extended, thereby enhancing contact time and facilitating the formation of chemical bonds between the metallic trace elements and the sand's binding sites. The application of a single logistic model provided a reliable framework for predicting the adsorption behavior within the slow sand filtration process.

While the results underscore the potential of slow sand filtration as an effective method for mitigating heavy metal contamination in water, several factors merit further consideration to enhance the practical application of this technique:

- Optimization of Flow Rates where the flow rate must be balanced with the water demand and filtration capacity.
- Long-term sustainability where the filter adsorption capacity should be monitored. Periodic regeneration or replacement of the sand filter might be necessary to sustain high levels of heavy metal removal over extended periods.
- Integration with other treatment methods to further improve water quality. Slow sand filtration could be integrated with other treatment technologies, such as ion exchange or advanced oxidation processes, to target a broader spectrum of contaminants.

References

Abdiyev, K., Azat, S., Kuldeyev, E., Ybyraiymkul, D., Kabdrakhmanova, S., Berndtsson, R., Khalkhabai, B., Kabdrakhmanova, A., Sultakhan, S. (2023). Review of Slow Sand Filtration for Raw Water Treatment with Potential Application in Less-Developed Countries, Water, 15(11): 2007. https://doi.org/10.3390/w15112007.

Abdulhusain, N., Abd Ali, Z. (2023). Green approach for fabrication of sand-bimetallic (Fe/Pb) nanocomposite as reactive material for remediation of contaminated groundwater using permeable reactive barrier. Alexandria Engineering Journal, 72(1): 511-530. https://doi.org/10.1016/j.aej.2023.04.028.

Agrawal, A., Sharma, N., Sharma, P. (2021). Designing an economically slow sand filter for households to improve water quality parameters. Mater Today Proceeding, 43: 1582–1586. https://doi.org/10.1016/j.matpr.2020.09.450.

Al-Haj-Ali, A.M., Al-Matar, A.K. (2024). Simulation of Breakthrough Curves of Pb Ions Adsorption by Natural Zeolitic Tuff Using Axial Dispersion and External Mass Transfer Modelsy. Jordan Journal of Earth and Environmental Sciences, 15 (1): 70-76.

Al-Mubaidin, M., Al-Hamaiedeh H., Tayel, E. (2022). Impact of the Effluent Characteristics of Industrial and Domestic Wastewater Treatment Plants on the Irrigated Soil and Plants. Jordan Journal of Earth and Environmental Sciences, 13 (3): 223-231.

Al-Qawasmi, O., Al Sharif, M. (2022). Water Audits of Academic Institutions in Water Stressed Countries; the Case of the Jordan University. Jordan Journal of Earth and Environmental Sciences, 13 (1): 54-59.

Al Rabadi, S.J., Al-Mahasneh, M., Awwad, A.M. (2023). Amelioration of nano-Kaolinite deportation for heavy Pb(II)'s, Cd(II)'s, and Cu(II)'s ions from aquatic environments. Jordan Journal of Earth and Environmental Sciences, 14 (4): 308-317.

Avila, M., Perez, G., Esshaimi, M., Mandi, L., Ouazzani, N., Brianso, J., Valiente, M. (2012). Heavy Metal Contamination and Mobility at the Mine Area of Draa Lasfar (Morocco). The Open Environmental Pollution & Toxicology Journal, 3, (Suppl 1-M2): 2-12.

Bani Khaled, E., Obeidat, M., Al-Ajlouni, A., Awawdeh, M., Abu Dalo, M. (2024). Demarcation of Groundwater Quality Using Drinking Water Quality Index (DWQI), Nitrate Pollution Index (NPI), and Irrigation Indices: A Case Study from Jerash Region. Jordan Journal of Earth and Environmental Sciences, 15 (1): 37-52.

Barkouch, Y., Ait Melloul, A., Khadiri, M.E., Pineau, A. (2019). Study of filter height effect on removal efficiency of Cd, Cu, Pb and Zn from water by slow sand filtration. Desalination and Water Treatment. 161 (2019) 337–342. doi: 10.5004/dwt.2019.24315.

Barkouch, Y., Sedki, A., Pineau, A. (2007). A new approach for understanding lead transfer in agricultural soil. Water Air Soil Pollution. 186(1-4): 3-13.

Barkouch, Y., Zahar, C., Ait Melloul, A., Flata, K., Khadiri, M.E., Pineau, A. (2018). New approach to understand the removal efficiency of some anions in well water by slow sand filtration. Annu Research Review in Biology. 23(1): 1-8. DOI: 10.9734/ARRB/2018/38905.

Benjelloun, M., Miyah, Y., Evrendilek, G., Zerrouq, F., Lairini, S. (2021). Recent Advances in Adsorption Kinetic Models: Their Application to Dye Types. Arabian Journal of Chemistry, 14(4): 103031. https://doi.org/10.1016/j.arabjc.2021.103031.

Calmuc, M., Calmuc, V., Arseni, M., Topa, C., Timofti, M., Georgescu, L.P., Iticescu, C., A. (2020). Comparative approach to a series of physico-chemical quality indices used in assessing water quality in the lower danube, Water (Switzerland), 12: 3239, doi: 10.3390/w12113239.

Carlo, I., Rossana, S., Giovanni, L., Donald, H. (2023). Water scarcity in agriculture: An overview of causes, impacts and approaches for reducing the risks.Heliyon, 9(8): e18507. https://doi.org/10.1016/j.heliyon.2023.e18507.

Casas, M.E., Bester, K. (2015). Can those organic micro-pollutants that are recalcitrant in activated sludge treatment be removed from wastewater by biofilm reactors (slow sand filters). Science of Total Environment, 506: 315-322.

Changyoon, J., Ansari, M., Anwer, A., Kim ,S., Nasar, A., Shoeb, M., Mashkoor, F. (2023). A review on metal-organic frameworks for the removal of hazardous environmental contaminants. Separation and Purification Technology, 305(15): 122416. https://doi.org/10.1016/j.seppur.2022.122416.

Chiedozie, O., Tosan, A. (2022). Groundwater Quality Around Active and Non-Active Dumpsites in Benin City, Jordan Journal of Earth and Environmental Sciences, 13 (4): 271-277.

Chowdhury ZZ, Zain SM, Rashid AK, Raêque RF, Khalid K. (2013). Breakthrough Curve Analysis for Column Dynamics Sorption of Mn(II) Ions from Wastewater by Using Mangostana garcinia Peel-Based Granular-Activated Carbon. Journal of Chemistry, 1:1-8. DOI 10.1155/2013/959761.

Farrag, A., Abdel Moghny, T., Atef, M., Saleem, S.S., Mahmoud, F. (2017). Abu Zenima synthetic zeolite for removing iron and manganese from Assiut governorate groundwater, Egypt. Applied Water Science, 7: 3087–3094. DOI 10.1007/s13201-016-0435-y.

Gokul, C.B., Animesh, S., Rashid, M.H., Monirul, H.S., Mirajul, I., Qingyue, W. (2015). Assessment of the irrigation feasibility of low-cost filtered municipal wastewater for red

amaranth (Amaranthus tricolor L cv. Surma). International Soil Water Conservation Research, 3: 239–252. http://dx.doi.org/10.1016/j.iswcr.2015.07.001.

Guchi, E. (2015). Review on Slow Sand Filtration in Removing Microbial Contamination and Particles from Drinking Water. American Journal of Food and Nutrition, 3:47–55.

Hadef, S., Zahi, F., Debieche, TH., Drouiche, A., Lekoui A. (2021). Assessment of the surface water suitability for irrigation purposes: Case of the Guenitra dam watershed (Skikda, NE Algeria). Jordan Journal of Earth and Environmental Sciences, 12 (4): 344-352.

Haig S.J., Collins G., Davies R.L., Dorea C.C., Quince C. (2011). Biological aspects of slow sand filtration: Past, present and future. Water Sci. Technol. Water Supply, 11:468–472. doi: 10.2166/ws.2011.076.

Hijnen, W.A.M., Schijven, J.F., Bonné, P., Visser, A., Medema, G.J. (2004). Elimination of viruses, bacteria and protozoan oocysts by slow sand filtration. Water Science and Technology, 50:147–154. doi: 10.2166/wst.2004.0044.

Hussien, H., Samuel, Z.A., Bokke, A.S., Bayu, A.B. (2022). Assessment of Surface Water Resources Based on Different Growth Scenarios, for Borkena River Sub-basin, Awash River Basin, Ethiopia. Jordan Journal of Earth and Environmental Sciences, 13 (3): 199-214.

Islam, M.M.M., Iqbal, M.S., D'Souza, N., Islam, M.A. (2021). A review on present and future microbial surface water quality worldwide. Environ. Nanotechnology Monitoring and Management, 16: 100523. https://doi.org/10.1016/j.enmm.2021.100523.

Magombeyi, M.S., Taigbenu, A.E., Barron, J. (2018) Effectiveness of agricultural water management technologies on rainfed cereals crop yield and runoff in semi-arid catchment: a meta-analysis. International Journal of Agriculture and Sustainability, 16 (4-5): 418-441. https://doi.org/10.1080/14735903.2018.1523828.

Maiyo, J., Dasika, S., Jafvert, C. (2023). Slow Sand Filters for the 21st Century: A Review. International Journal of Environmental Research and Public Health, 20(2): 1019. doi: 10.3390/ijerph20021019.

Omonona, O.V, Azombe, S.G. (2024). Preliminary Assessment of Trace Metals in Sediments of the Ebonyi River, Abakaliki Metallogenic Province, Nigeria. Jordan Journal of Earth and Environmental Sciences, 15 (1): 28-36.

Pham, L. (2017). Comparison between water quality index (WQI) and biological indices, based on planktonic diatom for water quality assessment in the Dong Nai River, Vietnam, Pollution, 3: 311–323. DOI: 10.7508/pj.2017.02.012.

Siddiqua, A., Hahladakis, J., Al-Attiya, W. (2022). An overview of the environmental pollution and health effects associated with waste landfilling and open dumping. Environmental Science and Pollution Research, 29: 58514–58536. https://doi.org/10.1007/s11356-022-21578-z.

Zhang, M., He, L., Zhang, X., Wang, S.; Zhang, B., Hsieh, L., Yang, K., Tong, M. (2022). Improved removal performance of Gram-negative and Gram-positive bacteria in sand filtration system with arginine modified biochar amendment. Water Research, 211: 118006.

Zhou, Q., Zhang, Y., Wu, F. (2021). Evaluation of the most proper management scale on water use efficiency and water productivity: A case study of the Heihe River Basin, China. Agricultural Water Management, 246: 106671. https://doi.org/10.1016/j.agwat.2020.106671.

JJEES

JJEES (2024) 15 (4): 250-256
ISSN 1995-6681

Jordan Journal of Earth and Environmental Sciences

Study of the Water Quality in the Tigris River Using Isotopic and Hydrochemical Techniques in South-Eastern Iraq

Amer A. Mohammed*, Ali Hasan Falih, Kamal AL-Paruany, Ali Al Maliki, Ali. A. Jasim

Scientific Research Commission, Ministry of Higher Education & Scientific Research, Baghdad, Iraq

Received on January 9, 2024; Accepted on October 2, 2024

Abstract

Isotopes and Hydrochemical analysis in groundwater were attempted in the study area of Maysan Governorate, located in southern Iraq to learn more about water quality conditions and geochemical evolution. The study also relied on the analysis of water samples for data on the main ions (Cations and Anions), as the water of the Tigris River was dominated by ions (Ca^{+2}, Mg^{+2}, Cl^{-} and SO_4^{2-}), and the water quality was classified according to the Piper alkaline classification of the calcium chloride type. Through the relationship between δ^2H and $\delta^{18}O$, there is a convergence for all areas except near the Amara Dam, where the results showed a slight depletion in the values of stable isotopes. The Umm al-Jari Canal (One of the canals that flows into the Tigris River) water system had a different isotopic fingerprint from the fingerprint of the water of the Tigris River. The rates of radioactive isotope Radon-222 (^{222}Rn) concentrations for samples from the study area ranged between (0.149 - 0.329) Bq/L and were within the normal permissible limits for radon concentration in water. The sodium absorption rate was between 12-11, which is within good water, and river water in the study area can be used for irrigation purposes. Measurement of four heavy elements, including Cadmium (Cd^{+2}) Zinc (Zn^{+2}) Copper (Cu^{+2}), and Lead (Pb^{+1}), were carried out for water samples in the study area, and all concentrations were within the permissible limits, except for the cadmium element, which was higher than the permissible limit, for drinking purposes and according to the Iraqi standard (IQS).

Keywords: *Kut , Maysan, Tigris River, Deuterium, Oxygen-18, Radon-222*

1. Introduction

The scarcity of freshwater is one of the greatest threats facing humanity today. It is not only limited to the scarcity of water supplies but also extends to the deterioration of water quality. The efficiency of wastewater treatment plants, discharging into rivers, is not high, resulting in a substantial of pollution to surface water (Al-kubaisi et al., 2020). Understanding the hydro-chemical properties of groundwater and how they evolve during water circulation processes is required to effectively protect and utilize valuable water resources and predict changes in surface water environments (Al-paruany et al., 2013).

Isotope hydrology has become a widely used technique for rational management of the global water crisis (Heydarizad et al., 2021). The isotopic composition of oxygen and hydrogen in natural water (precipitation, groundwater, and surface water) provides important information to study the origin of water as a function of geohydrological and meteorological factors such as the source of water vapor and climate change, processes involved in groundwater (water residence and travel times in aquifer systems, interrelationships between surface and groundwater, sources of pollution and salinization of groundwater, and the exchange of water movement between lakes and adjacent groundwater aquifers (Hamdan. et al., 2016).

In nature, two stable isotopes of hydrogen (^1H, protium and ^2H, deuterium) and three stable isotopes of oxygen (^{16}O, ^{17}O, ^{18}O). The measurement of ($\delta^{18}O$, δ^2H) in different water sources is one of the possibilities for measuring different water sources, and this percentage is variable according to geographical location and time. The abundance of the isotopes ^2H and ^{18}O in ocean waters is close as follows: $^2H/^1H = (155.95 \pm 0.08) \times 10^{-6}$, $^{18}O/^{16}O = (2005.20 \pm 0.45) \times 10^{-6}$ (Gat et al., 1996). These values are close to the average isotopic composition of ocean water given by Craig. The heavy isotope content of water samples is usually expressed in delta (δ) values defined as the relative deviation from the adopted standard representing the mean isotopic composition of the global ocean:

$$[\delta\ ‰] = \left(\frac{R(sample)}{R(References)} - 1\right) * 1000 \quad (1)$$

Where R Sample and R Reference standard for the isotope ratio(R) are the atom ratio ($^2H/^1H$ and $^{18}O/^{16}O$) in the sample and the reference material (standard), respectively. The isotopic concentration or abundance ratios are generally referred to as those of a specifically chosen standard. The internationally accepted standard for reporting the hydrogen and oxygen isotopic ratios of water is Vienna Standard Mean Ocean Water, V-SMOW, positive δ values indicate that the water sample is enriched in its isotopic concentration, while negative values refer to depleted water samples. (Gat et al., 1970). ^2H and ^{18}O isotopic compositions of meteoric waters (precipitation, atmospheric water vapor) are strongly correlated. If δ^2H is plotted versus $\delta^{18}O$, the data cluster along a straight line will be as follows:

$$\delta^2H = 8\delta^{18}O + 10 \quad (2)$$

Radon-222 (^{222}Rn) is a naturally occurring radioactive

* Corresponding author e-mail: abedamer5@gmail.com

gas, originating from the decay of Radium-226, a decay product of Uranium-238(^{238}U) found in rocks and soils. The most prevalent radioactive isotope of radon in the environment is Rn-222 (^{222}Rn), which has a relatively short half-life of 3.8 days. While there are two other naturally occurring isotopes, Rn-220 (Thoron) and Rn-219 (Actinon), their short half-lives (5.66 and 3.92 minutes respectively) make them negligible in comparison. Consequently, the concentration of Radon-222 (^{222}Rn) in groundwater can be significantly higher than its rate in surface water (Al-Harahsheh et al., 2020).

Isotopic techniques are utilized in various research studies to evaluate water quality and identify points of interaction between groundwater and surface water. Kamal (2015) Isotopic study of water resources in a semi-arid region, Western Iraq. Environmental Earth Sciences. Hussien (2021) used stable isotopes and Hydrochemical analysis of water samples to study the interaction between the water resources of the Euphrates River and groundwater in a limited area in the western plateau of Iraq. Al-paruany (2013) studied Hydrochemical and isotopic resources water between Hadith Dam and Al-Baghdadi Dam.

This research aims to assess the water quality of the Tigris River specifically examining the extent of environmental pollution's impact on the Tigris River's water, to protect water resources, and predict environmental changes in surface water using isotopic technologies, supported by hydro chemical analyses and heavy metal measurements. This is intended to support hydrological studies and formulate sound water policies.

2. The Study Area Location and Description

The study area is located in the cities of Kut and Amara in southern Iraq and the center of Maysan Governorate, about 320 kilometers to the southeast of the capital, Baghdad. It is on the banks of the Tigris River and about 50 kilometers from the Iranian-Iraqi border and a few kilometers from the marshes area, within the following coordinates (45^{0}47'10.7" – 47^{0}35'52.3") E (31^{0}51'2.2"– 32^{0}64'35.4") N. The climate of the region is subject to the climate conditions of arid and semi-arid regions, which are characterized by cold winters with little rain and hot, dry summers. The Tigris River forms the backbone of irrigation operations in the Amarah Governorate by penetrating it from its far north. Up to its southern borders, a number of canals that originate from Iranian territory flow into the Tigris River, including the Jabab Canal, which is located in the east of Kut and belongs to the Sheikh Saad District, extending from the Iranian border in the east to the Tigris River in the west. Other canals are the Umm al-Jari Canal (Figure 1) (Jummah et al., 2020).

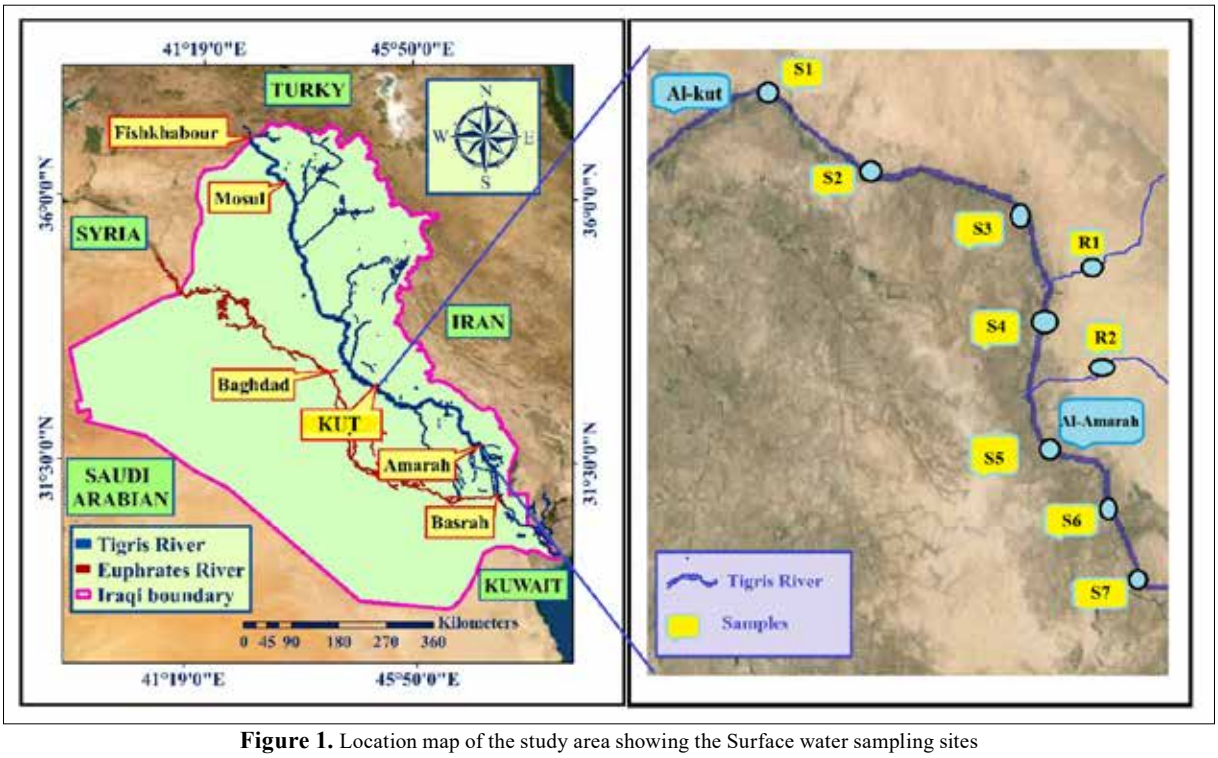

Figure 1. Location map of the study area showing the Surface water sampling sites

3. Materials and Methods

Eighteen water samples were collected from different locations along the Tigris River, during the months of March (Wet seasons) (9 samples) and August (Dry season) (9 samples) in 2022, including that of the Al-Kut Dam (S1), After the Al-Kut Dam (S2), Sheikh Saad area (S3), Ali Al-Gharbi area (S4), Ali Al-Sharqi area (S5), and the Al-Amara Dam (S6) after Al-Amara Dam (S7) (Table 1). Additionally, two samples were taken from the canals that flow into the Tigris River, namely the Jabba Canal (R1) and the Umm Al-Geri Canal (R2). Water temperature, electrical conductivity, hydrogen number, and total dissolved solids were measured directly in the field and the coordinates of each sampling site were recorded using a Global Positioning System (GPS). The chemical analyses and analysed for isotopic of samples were carried in the laboratory of water research Centre/ Ministry Science and Technology using Liquid-Water Isotope Analyser (LWIA) was used for determining ^{18}O,

^{2}H, and Use the Durridge Company RAD7 radon detector, which is designed to measure radon gas in water with high accuracy and a wide range of concentrations (Durridge Radon ,2013). The samples for hydrochemical measurement by ion chromatography.

Table 1. Locations of the Study Area.

No.	Stations	Symbol	Latitude	Longitude
1	Al-Kut Dam	S1	32^{0}64'35.4"N	45^{0}47'10.7"E
2	After Al-Kut Dam	S2	32^{0}59'24.3"N	45^{0}69'49.5"E
3	Al- Sheikh Saad	S3	32^{0}34'12.1"N	46^{0}16'07.4"E
4	Ali Al-Gharbi	S4	32^{0}28'14.6"N	46^{0}31'07.4"E
5	Ali Al-Sharqi	S5	32^{0}07'19.0"N	46^{0}44'44.7"E
6	Al-Amara Dam	S6	31^{0}51'2.2"N	47^{0}08'29.3"E
7	after Al-Amara Dam	S7	31^{0}54'55.6"N	47^{0}35'52.3"E
8	Al- Jabba Canal	R1	32^{0}39'28.7"N	46^{0} 22'54.3"E
9	Umm Al-Geri Canal	R2	32^{0}27'54.1"N	46^{0}41'15.3"E

4. Results and Discussion

4.1 Physico-chemical Properties of Water

Surface water contains different types of salts in different proportions and concentrations depending on the source and movement of this water. The results show that (Table 2) pH levels for both wet (March) and dry (August) seasons ranged from 6.81 to 7.79, and these values did not exceed the permissible limits (6.5-8.5) for drinking and irrigation purposes, as specified by WHO (2017). The Total Dissolved Solids (TDS) rates are varied, with a range of 574.16 ppm at the front of the Kut Dam (S1), while there was a significant increase in the after Amara Dam (S7), reaching 914.77 mg/L during the dry season (August). The reason for this result is attributed to its susceptibility to the leaching process from agricultural lands, as well as the inadequate drainage of water from Iranian territories and its exposure to evaporation due to high temperatures in dry season. However, all values in both seasons remained within the allowable limits of ppm (500-1000) mg/L as per WHO (2017) standards (Djoudi et al., 2023).

Table 2. Physico-chemical properties, Temperature (T) and Humidity (R.H) of samples in the study region.

Sample	Wet season		Dry season		Month	Av.T. (°C)	R.H. (%)
	pH	TDS	pH	TDS			
S1	7.23	471.37	6.81	574.16	Feb.	21.5	35.4
S2	7.21	533.37	7.2	581.77	March	26	28.2
S3	7.35	591.57	6.88	687.8	April	35.7	27
S4	7.1	689.7	6.93	711.44	May	39.82	15
S5	7.1	748.12	7.23	761.94	June	47.18	16.6
S6	7.5	793.2	7.31	851.26	July	49.33	12.9
S7	7.71	864.47	7.32	914.77	Aug.	53.17	17.9
R1	6.78	8186.91	6.78	8196	Sep.	43.33	15.2
R2	6.83	1093.85	6.83	1011	Oct.	37.86	22.5
WHO (2017)	6.5 -8.5	500-1000	6.5 -8.5	500-1000	Nov.	29.50	25.7

4.2 Cationic and Anionic Concentrations

The concentrations of cations (Calcium, Magnesium, Sodium, and Potassium) and anions (Chlorides, Sulphates, and Bicarbonates) in the water of the Tigris River in the study area were within the permissible limits internationally and locally, respectively (WHO, 2017) (Table 3). The results of chemical tests for the Canal Umm Jari (R1) water sample showed a noticeable increase, as the total values of dissolved salts reached (8168) mg/L. The reason is that it is affected by the drainage process by agricultural lands, in addition to the lack of water drainage from Iranian lands and its exposure to the evaporation process due to high temperatures. The presence of nitrate ions in water is evidence of pollution from the leakage of sewage, in addition to the second source of nitrates being nitrogen fertilizers. Nitrate values in all water samples of the Tigris River ranged from (48-65) mg/l, where we notice a relative increase of the permissible values, which are 45 mg/L (El-Naqa et al., 2021).

The reason is attributed to human activities resulting from agricultural activities, as the study area was agricultural in nature. According to the Piper Diagram, all samples in the water of the Tigris River in the study area indicate earth alkaline water with a higher percentage of alkali and prevailing sulphate and chloride, (SO_4^{2-} - Cl^- and Ca^{2+} - Mg^{2+}) (permanent hardness); (noncarbonated hardness exceeds 50 %) calcium chloride type. Figure (2) (Piper et al.,1944).

Table 3. Major Cation and Anion Concentrations Samples Water for Wet and Dry Seasons.

Sample	Ca^{+2} mg/L		Mg^{+2} mg/L		Na^{+} mg/L		K^{+} mg/L		Cl^{-1} mg/L		So_4^{-2} mg/L		Co_3^{-2} mg/L		Hco_3^{-1} mg/L		No_3^{-1} mg/L	
Season	*Wet*	*Dry*	*Wet*	*Dry*	*Wet*	*Dry*	*Wet*	*Dry*	*Wet*	*Dry*	*Wet*	*Dry*	*Wet*	*Dry*	*Wet*	*Dry*	*Wet*	*Dry*
S1	56	70	30	40	60	73	1.3	1.9	112	120	160	207	4.96	8.54	22.11	23.7	25	30
S2	62	71	38	38	68	76	1.5	1.9	128	132	178	200	5.7	8.7	24.17	24.1	28	30
S3	65	75	43	31	78	79	1.9	2.3	140	148	190	257	6.5	10.5	29.17	32.0	38	53
S4	77	79	51	33	92	97	2.1	2.3	164	174	218	233	7.1	13.14	36.50	40.0	42	40
S5	80	85	58	36	102	112	2.1	2.7	175	180	240	250	9.24	13.24	36.78	43.0	45	40
S6	85	91	62	43	112	118	1.8	2.8	195	218	243	273	9.46	15.46	42.94	48.0	42	42
S7	93	98	70	48	119	127	2.3	2.9	215	230	257	277	11	17.7	49.17	52.0	48	65
R1	743	768	520	540	1003	1023	25	27	2018	2034	3015	3043	144	154	400	429	318	325
R2	116	125	60	67	134	154	2.5	3.4	287	301	366	387	16.2	18	45.11	50.4	67	72
WHO	75-200		50-150		200		12		250-400		250-400				300-500		45	

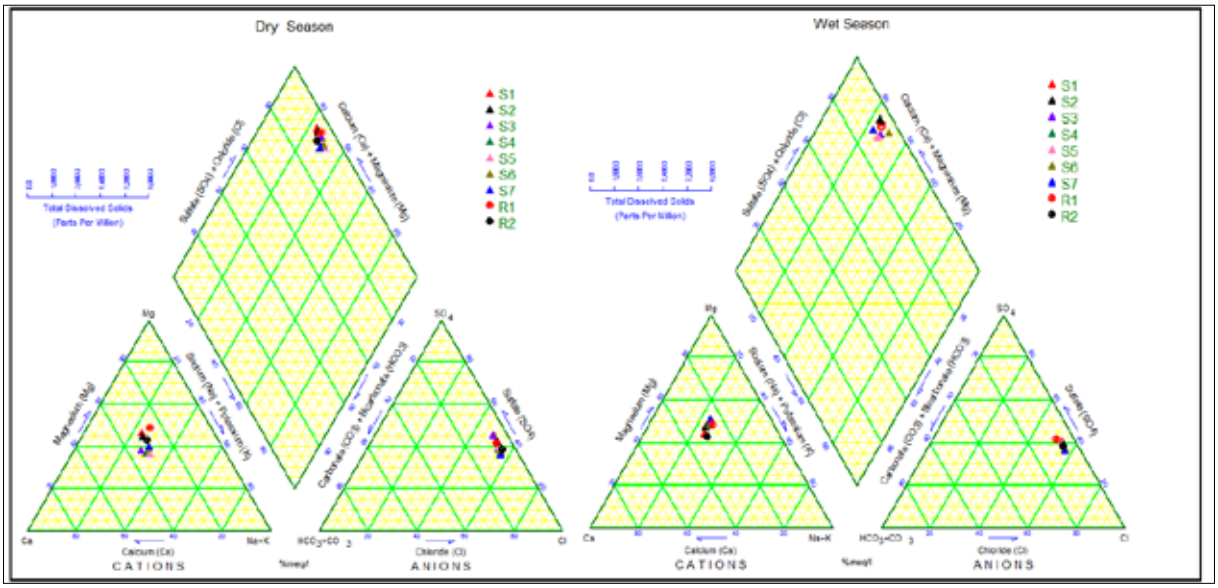

Figure 2. Type of water according Piper diagram

4.3 Heavy Element Concentrations

Pollution with heavy metals primarily resulting from human activities poses a serious health problem due to their cumulative nature, even at low concentrations. Additionally, they are non-degradable and have a severe impact on living organisms. Measurements were conducted for four trace elements Cadmium (Cd), Zinc (Zn), Copper (Cu), and Lead (Pb) in water samples from the study area or both wet and dry seasons. The average values of concentrations of Zinc (Zn) range between (0.75 mg/L - 0.94 mg/L), falling within the Iraqi standard specifications for drinking water in 2009, which set a maximum limit of 3 mg/L. Average values of concentrations of Lead (Pb) and Nickel (Ni) range between (0.008 - 0.005), within the permissible limits of (0.02, 0.01) mg/L respectively.

On the other hand, the average concentrations of cadmium (Cd) range between 0.06 mg/L and 0.078 mg/L, which are elevated at all sites compared to the Iraqi standard specifications, setting a maximum limit of 0.003 mg/L. The increase in cadmium levels in water samples can be attributed to the reduced level of the Tigris River, coupled with waste from factories and sewage water flowing into it. Industrial facilities frequently discharge cadmium-laden waste into water bodies, resulting in its accumulation. Additionally, cadmium from fertilizers and pesticides used in agriculture can enter water sources through runoff from farmland.

4.4 The Sodium Absorption Rate (SAR)

The Sodium Adsorption Ratio (SAR) is a measure used in hydrology and soil science to evaluate the suitability of water for irrigation purposes. It indicates the relative concentration of sodium ions to other (such as calcium and magnesium) in the water

$$SAR = \frac{Na}{\sqrt{\frac{Ca+Mg}{2}}} \quad (3)$$

where SARfor Na^{+}, Ca^{2+} and Mg^{2+} concentrations of ions in mill equivalents per liter (meq/L) units is examined.

Reassessing the hydrochemical characteristics of irrigation water is paramount in evaluating soil leaching issues. The detrimental impacts of elevated Sodium Adsorption Ratio (SAR) levels include salt accumulation on soil surfaces, impeding water penetration to plant roots. Certain agricultural crops exhibit high sensitivity to SAR values, rendering the use of water with high sodium concentrations in irrigation impractical. Hence, SAR values for irrigation purposes are categorized accordingly; SAR < 10 is deemed excellent for irrigation, while SAR ranging from 10 to 18 is classified as good (APHA, 2012).

The results of (SAR) were counted for Al-Kut Dam (S1), After the Al-Kut Dam (S2), Sheikh Saad area (S3), Ali Al-Gharbi area(S4), Ali Al-Sharqi area(S5), Al-Amara Dam (S6), after Al-Amara Dam (S7) and the Umm Al-Geri Canal (R2) ranged from (1.6-2.7) for both dry and wet seasons. However, the results of (SAR) Jabba Canal (R1) were (6.7-6.9). All SAR values within the study area fell within the excellent range for irrigation water quality. However, the SAR value of the (R1) sample showed a slight elevation, which can be attributed to its higher sodium content.

4.5 Isotopic Deuterium (δ^2H) and Oxygen-18 ($\delta^{18}O$)

Table 4 shows the results of isotopic analyses for the stations studied on the Tigris River and some of the systems that flow into it. The δ^2H isotope measurements for the Tigris River water in the study area during the wet season (March) were (-37.36 to -40.7) ‰, and for $\delta^{18}O$, they were (-7.87 to -6.59) ‰. These values were consistent across all areas, except in the vicinity of the Amara Dam (S6) that has more elevated concentrations. The variation in stable isotope values suggests the influence of evaporation and low discharge. Notably, there was a distinct contrast in the stable isotope results for the Tigris River between the dry and wet seasons, with values ranging from (-39.95 to -33.09) ‰ for δ^2H and (-5.55 to -7.78) ‰ for $\delta^{18}O$ during the dry season. This difference reflects the impact of higher summer temperatures and water evaporation, leading to reduced water levels in the Tigris River due to decreased discharge. The water from the Umm Jiri Canal (R1) exhibited different isotopic signatures compared to the Tigris River, with values of (-17.9 to -3.98) ‰ for δ^2H and $\delta^{18}O$, respectively. On the other hand, the isotopic concentrations of δ^2H and $\delta^{18}O$ in the water samples were measured at (R2) (35.63, -6.49) ‰, respectively. Notably, the isotopic composition of (R2) closely resembles that of the Tigris River, indicating a significant similarity between the water samples from the Tigris River and those from (R2), in contrast to the values observed in the water sample (R1).

Table 4. Isotopes data (δ2H, δ18O, d-excess) of samples in the study region.

Sample	Wet season			Dry season		
	δ^2H‰	$\delta^{18}O$‰	d-excess	δ^2H‰	$\delta^{18}O$‰	d-excess
S1	-40.7	-7.2	18.5	-39.95	-7.2	17.65
S2	-40.5	-7.78	18.4	-39.89	-7.78	17.55
S3	-40.7	-7.75	18.1	-39.88	-7.75	16.52
S4	-40.35	-7.53	17.4	-37.05	-7.53	16.34
S5	-39.35	-7.43	17	-36.38	-6.67	15.41
S6	-37.88	-6.92	16.7	-33.09	-5.55	12.93
S7	-37.36	-6.59	15.4	-33.67	-5.65	11.54
R1	-17.9	-3.98	13.9	-16.9	-3.78	12.9
R2	-35.63	-6.49	16.3	-31.63	-5.49	15.3
*VSOMW2	0	0		0	0	
*SLAP2	-427.5	-55.5		-427.5	-427.5	
*GISP	-189.8	-24.85		-189.8	-189.8	

VSOMW2, SLAP2, GISP: Standard Solution

Figure 3 depicts the distribution of water samples from the Tigris River in the study area and compares it with the Global Meteoric Water Line (GMWL), which serves as a reference line for identifying water sources and understanding the physical processes influencing isotopic compositions in meteoric waters. Additionally, the Local Meteoric Water Line (LMWL) is represented (Al-Paruany et al., 2020), consisting of isotopic values derived from a mixture of local water samples, particularly from rainfall (rain and snow) (Kattan,1997). This line acts as a reference to determine water sources based on regional factors such as variations in rainfall, temperature changes, evaporation, and fractionation processes. These factors collectively influence the relationship between deuterium and oxygen-18 isotopes, causing deviations from the global rainfall line at the local level. The equations used to establish these two lines as follows:

$\delta 2H = 7.66\ \delta^{18}O + 14.19$ (4) LMWL (Al-Naseri et al.,2022)

$\delta 2H = 8\ \delta^{18}O + 10$ (5) GMWL (Craig, 1961)

It is observed from Figure 3 that all water samples are within the boundaries of both the local and global rainfall lines. This indicates that the source of water feeding into the Tigris River is closely tied to rainfall and snowfall. The variations in the distribution of water samples can be attributed to differences in the extent of evaporation.

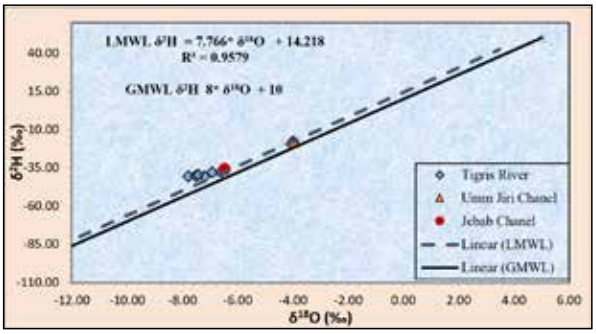

Figure 3. Stable isotopes (δ ^{8}O and δ^2H) with GMWL and LMWL

The deuterium excess (d-excess) serves as an indicator revealing the impact of evaporation on the chemical and physical characteristics of water. It is calculated using the following equation:

$d = \delta^2H - 8\delta^{18}O$ (6) (Craig, 1961)

Figure 4 illustrates the correlation between excess deuterium and the total dissolved salts (TDS) content in water samples within the study area. As the evaporation process intensifies, there is an increase in TDS values, resulting in a reduction in deuterium excess values. This decrease in deuterium excess is particularly notable in the Tigris River water samples near the Amara Dam area compared to other regions. This phenomenon is attributed to the heightened exposure of water to substantial evaporation, leading to an elevation in dissolved salts concentration (TDS) (Falih et al., 2023).

Distinct differences are evident between the wet and dry seasons, with noticeable divergence in results. This discrepancy underscores the concurrence of elevated electrical conductivity (EC) and TDS levels, indicative of the effects of evaporation during the summer season characterized by high temperatures (53°C) in August and minimal rainfall during the wet season.

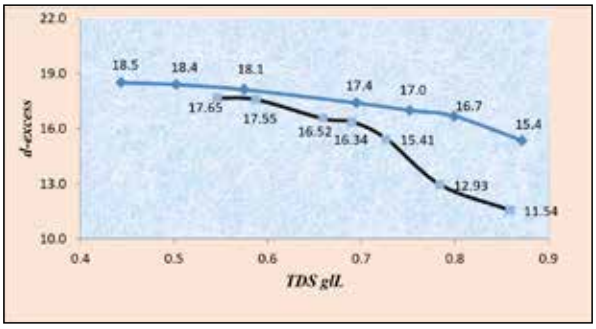

Figure 4. Relationship of deuterium excess and (TDS) for water samples in the study area

4.6 Radon -222(^{222}R)

The radioactive isotope of Radon (^{222}Rn) is one of the important environmental isotopes. It is used as an important tracer in hydrological studies due to its physical properties (it is in the form of a gas) and its short half-life (3.8 d) (Al-Paruany et al., 2021), Radon gas, once released from rocks and soil, can migrate to groundwater, surface water, and the air. The radon isotope is also considered a good indicator for identifying the interaction between groundwater and surface water. It can decide whether radon levels are below 0.4 Bq/L in surface water supplies, while they can reach around 20 Bq/L in groundwater, depending on the geological characteristics of the region and the quality of the groundwater (Mohammed et al.,2023). Concentration average of the Radon (^{222}Rn) of samples from the study area were measured and ranged between (0.149 - 0.329) Bq/L and were within the normal permissible limits for Radon concentration in water, according to the US Environmental Protection Agency (EPA), which is 11 Bq/L. (Figure 4). There is a low variation in Radon concentration between all the stations in the study area. This indicates that all locations are similar in the type of soil, sediments, and same conditions in the climate elements in these regions.

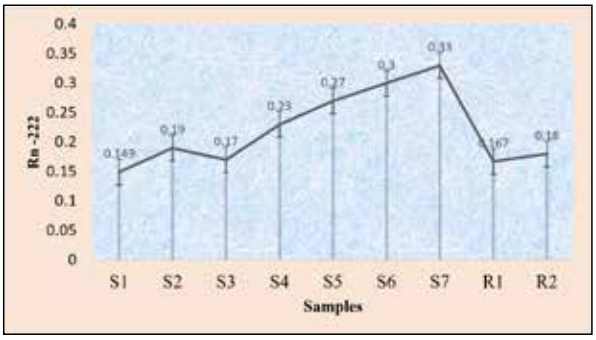

Figure 5. Radon-222 (^{222}Rn) concentrations for samples water in the study area.

5. Conclusion

The results for the stable isotopes of deuterium (^{2}H) and oxygen-18 (^{18}O) were similar for all study areas except near the Amara Dam, where the results showed depletion in the values of the stable isotopes, and the rates of stable isotope results for the waters of the Tigris River for the dry season were lower than they are in the wet season. This reflects the effect of high temperatures in the summer, the influence of the water by the evaporation process, and low river water levels of the Tigris due to lack of drainage. The water of the Umm Jiri regulator had a different isotopic fingerprint from the water of the Tigris River, while the isotopic fingerprint of the water of the Tigris River was, according to Nazim Al-Jabab, close to the waters of the Tigris River. This indicates the presence of mixing and its influence with the waters of the Tigris River. The results of the Radon-222 (^{222}Rn) isotope concentrations were within the normal limits allowed for the concentration of Radon in water, according to the US Environmental Protection Agency (EPA), which is 11 Bq/L. This indicates the low variation in Radon concentration between all the stations in the study area. This also indicates that all locations are similar in the type of soil, sediments and same conditions in the climate elements in these regions. The type (Ca^{+2} - Mg^{+2} - Cl^- - SO_4^{-2}) and the water quality is calcium chloride, which reflects the geology of the rocks of the area through which the water flows. All SAR values in study area fell within the excellent range for irrigation water quality.

Acknowledgments

The authors express their gratitude to the Iraqi Ministry of Science and Technology for providing the required analytical facilities necessary to conduct dis study. We also extend our thanks to Dr. Kamal Barzan Nada for helping us evaluate the research

References

Al-Harahsheh, S.,and Al-Dalabeeh (2020) . Measurement of Radon Levels in the Groundwater of Al-Rusaifah City in Zarqa Governorate Using Liquid Scintillation Counter .Jordan Journal of Earth and Environmental Sciences 11 (2): 98-102. DOI:10.13140/RG.2.2.20660.48000

Al-Kubaisi, M.H.(2020). Hydrochemical Facies Description to Assess the Water Quality of Habbaniya Lake, Iraq. The Iraqi Geological Journal, 53(2F), 94-107. https://doi.org/10.46717/igj.53.2F.7Ms-2020-12-30 .

Al-Naseri, S.K., Falih, A.H. and Kumar, U.S.(2022). Moisture sources and spatio-temporal variation of isotopic signatures in Iraqi precipitation. Environ Earth Sci 81, 435 https://doi.org/10.1007/s12665-022-10559-7

Al-Paruany, K. B. (2013). Hydrochemical and isotopic study of water resources between Haditha dam and site of Al-Baghdadi Dam. University of Baghdad, College of Science, 171 pages.

Al-Paruany, K. B., Ali, R. A., Ajeena, Q., Al-Kubaisi, Y., Ali, H. F.,Adwia, and Amer, A. (2020).Application of stable isotopes to evaluate the interaction between surface water and groundwater in north east of Diyala, Iraq. The Iraqi Geological Journal, 108-121.

Al-Paruany, K.B., Abdul-Hameed, A. A., Al-Hadiathy, E. H., Ali, A. A. and Amer, A. (2021).Assessment of radon gas concentration in tap water supply of Haditha Town / west Al-Anbar Governorate / Iraq. IOP Conference Series: Earth and Environmental Science, 1080(1), 012002. https://doi.org/10.1088/1755-1315/1080/1/012002 .

APHA, American Public Health Association, American Water Works Association (AWWA), and Water Environmental Federation (WEF). (2012). Standard methods for the examination of water and wastewater. 9993 pages.

Craig, H. (1961). Isotopic variations in meteoric waters. Science, 133(3465), 1702-1703. https://doi.org/10.1126/science.133.3465.1702

Djoudi, S., Pistre, S., and Houha, B. (2023). Evaluation of groundwater quality and its suitability for drinking and agricultural use in F'kirina Plain, Northern Algeria. Jordan Journal of Earth and Environmental Sciences, 14(3), 203-209.

Durridge Co. (2013). RAD7 Radon Detector User Manual. Retrieved from www.durridge.com/documentation/RAD7%20Manual.pdf

El-Naqa, A., and Al Raei, A. (2021). Assessment of Drinking Water Quality Index (WQI) in the Greater Amman Area. Jordan. Jordan Journal of Earth and Environmental Sciences, 12(4), 306-314.

Falih, A.H., Al Maliki, A., Al-lami, A.K., Jasm, A., Mohammed, A., Mahmood, A., Alameer, A., Salah, Z., Al-Ansari, N., Yaseen, Z.M. (2023) Comparative study on salinity removal methods: an evaluation-based stable isotopes signatures in ground and sea water. Applied Water Science 13(6):1–8an.

Gat, J. R. (1996). Oxygen and hydrogen isotopes in the hydrologic cycle. Annual Review of Earth and Planetary Sciences, 24, 225-262. https://doi.org/10.1146/annurev.earth.24.1.225.

Gat, J. R., and Carmi, I. (1970).Evolution of the isotopic composition of atmospheric waters in the Mediterranean Sea area. Journal of Geophysical Research Atmospheres, 75(15), 3039-3048. https://doi.org/10.1029/JC075i015p03039.

Hamdan, I., Wiegand, B., Toll, M., and Sauter, M. (2016). Spring response to precipitation events using δ18O and δ2H in the Tanour catchment, NW Jordan. Isotopes in Environmental and Health Studies, 52(6), 682–693. https://doi.org/10.1080/10256016.2016.1159205 .

Heydarizad, M., Minaei, F., Mayvan, J. E., Mofidi, A., and Minaei, M. (2021).Spatial distribution of stable isotopes (18O and 2H) in precipitation and groundwater in Iran. Isotopes in Environmental and Health Studies, 57(4), 400-419. https://doi.org/10.1080/10256016.2021.1924167 .

Hussien, S. J., and Abdulhussein, F. M. (2021)"Hydrochemical and isotopic study of water resources in khan Al-Baghdadi area, Al-Anbar Province/West of Iraq," Iraqi Journal of Science, pp. 204-217, DOI: https://doi.org/10.24996/ijs.2021.62.1.19 .

Jummah, M. S., and Al-Shammaa, A. M. (2020). Hydrochemical assessment of groundwater of Euphrates aquifer in Anah, Western Iraq for irrigation purposes, The Iraqi Geological Journal, 121-133. DOI:10.1088/1755-1315/1222/1/012045 .

Kamal, K. A., Al-Kubaisi, Q. Y., and Al-Paruany, K. B. (2015). Isotopic study of water resources in a semi-arid region, western Iraq. Environmental Earth Sciences, 74(2), 1671-1686. https://doi.org/10.1007/s12665-015-4172-6 .

Kattan, Z. (1997). Chemical and environmental isotope study of precipitation in Syria. Journal of Arid Environments, 35(4), 601-615. https://doi.org/10.1006/jare.1996.0228

Mohammed, A. A., Kamal, B. N., Ali, H. F., and Ali, A. J. (2023).Determination of radon radiation concentration in groundwater for some wells of Baghdad City. IOP Conference Series: Earth and Environmental Science, 1222(1), 012036.

Piper, A. M. (1944). A graphic procedure in the geochemical interpretation of water analyses. Eos Transactions American Geophysical Union, 25(6), 914-928. https://doi.org/10.1029/TR025i006p00914

JJEES

JJEES (2024) 15 (4): 257-264
ISSN 1995-6681

Jordan Journal of Earth and Environmental Sciences

Combined Geophysical and Soil Test Analysis Methods for Soil Precision Mapping in The Delta State University, Centre for Entrepreneurial Studies (CES) Farm, Abraka, Nigeria

Merrious Oviri Ofomola*[1], Ezekiel Onoriode Abriku[1], Bright Saturday Utieyin[2], Precious Okeoghene Otheremu[3], Ochuko Anomohanran[1]

[1]Department of Physics Delta State University Abraka, Delta State Nigeria
[2]Department of Science Laboratory Technology, Delta State Polytechnic, Otefe-Oghara, Delta State Nigeria
[3]Department of Physics, Delta State University of Science and Technology Ozoro, Delta State Nigeria

Received on August 1, 2024; Accepted on October 2, 2024

Abstract

Geophysical methods and soil test analysis have been used to study soil properties in the farm of the Centre for Entrepreneurial Studies (CES), Delta State University, Abraka, Nigeria. Vertical electrical sounding (VES), borehole geophysics, electrical resistivity tomography (ERT), and geochemical methods were used for the study. Seven VES stations were occupied along five traverses used for ERT measurements. Samples of soil close to the VES stations were taken for soil testing and to study their grain size to corroborate the results of VES and ERT. The low resistivity of the topsoil obtained from the VES agrees with the ERT and borehole log results and this ranges from fine-grained silt topsoil to sandy clay. This is a product of the partial decomposition of plants and animals forming organic matter. It ranges from 168 – 790 Ω.m with a mean value of 494 Ωm and an average depth of 2.3 m. This depth covers the upper root region of some important crops and depicts a high amount of moisture and mineral nutrients, and a fair degree of stoniness to aid adequate rooting of the crops. Also, the observed topsoil is high in porosity and water retention which are major suitable factors for the yield of tuber and stem plants. The soil test results are pH: 6.13-7.16, organic matter: 6.48-8.66 %, Nitrogen: 65.72-78.21 %, Phosphorus: 53.32-67.43 %, Copper: 14.16-22.61 mg/kg, Nickel: 1.16-3.11 mg/kg, Lead: 4.00-8.84 mg/kg, Arsenic: 0.08-0.1 mg/kg Iron: 96.33-151.63 mg/kg. These recorded concentrations are below the WHO standard for crop production.

Keywords: *Precision Agriculture, Crop Yield, Soil Test, Contamination Factor, Organic Matter*

1. Introduction

Agricultural production is declining due to soil degradation, poor soil biology, lower yield, stunted plant growth, and water erosion. Soil quality is important for agriculture, forestry, and environmental protection, but traditional methods of assessing soil can be costly and time-consuming. Properties of soil which include organic and mineral content, soil solution, and salinity are essential for precise agriculture. Soil organic matter composition is the summation of plants' and animals' remains. It provides a totality of nutrients and moisture to the soil which, in turn, reduces contraction and aids water infiltration into the soil. The soil volume is mostly consisting of stones, sand, silt, and clay. The decomposition rate is slow for soil and rich in clay, shale, and silt. This decomposition releases fewer nutrients as compared to sandy soil which will cause an improved breakdown and deployment of biological materials into the ground (Romero-Ruiz et al., 2018). Therefore, soil, rich in clay, shale, and silt, will cause a reduction in the electrical resistance of the surface soil. Soil, heavy with metal contamination, is a major concern for farming, as it can negatively affect crop growth and human health. Heavy metal contamination of the soil is a major factor, contributing to soil pollution (Anomohanran 2015; Iserhien-Emekeme et al., 2021; Ofomola et al., 2021; Rashid et al., 2023). Heavy metals, such as Fe, Zn, Ca, and Mg, are vital for human health, whereas As, Cd, Pb, and methylated classes of mercury can be dangerous even at low doses. Heavy metals have harmful effects on soil microbial communities. They can alter soil production and hinder essential plant activities (Briffa et al., 2020; Saikat et al., 2022; Mashal et al., 2017; Lu et al., 2014). Metals, absorbed by plants from soil, pose a significant health danger to the food chain. Traditional soil analysis methods involve chemical digestion, and they are time-consuming and expensive. These techniques are promising for on-site analysis of heavy metal levels in soil, which can help farmers make informed decisions regarding soil management practices. One advantage of Graphite Furnace Atomic Absorption Spectroscopy (GFAAS) over other soil analysis methods is its sensitivity and ability to detect trace amounts of elements in soil samples (Nowka et al., 1999; Ofomola, 2015; Aweto et al., 2017; Altunay et al., 2021; Liu et al., 2023). GFAAS can detect heavy metals like lead, cadmium, arsenic, and mercury in soil at concentrations as low as parts per billion (ppb), making it a highly sensitive analytical tool for environmental monitoring and research purposes. Additionally, GFAAS is a simple, fast, and precise method that requires minimal sample preparation, making it

* Corresponding author e-mail: ofomola@delsu.edu.ng

a cost-effective and efficient technique for analyzing large numbers of soil samples. GFAAS offers higher sensitivity and precision than other methods for trace element analysis in soil, allowing the detection of heavy metals at concentrations as low as parts per billion. The moisture level in the soil is vital for crop growth as it significantly impacts key physiological functions of plants, including water absorption, nutrient distribution, photosynthesis, temperature control, cell enlargement, growth, and resilience to stress. Soil moisture refers to the level of wetness in the top layer of soil relative to its ability to hold water, which is influenced by factors like precipitation, evaporation, temperature, and the properties of the soil itself. The soil moisture index (SMI), a scale without units, quantifies the moisture content of the soil and is crucial for various environmental aspects, such as agriculture and water resource management. Modern remote sensing methods have improved and refined assessments, making them more efficient for tracking indicators like soil moisture index (SMI), land surface temperature (LST), and the Normalized Difference Vegetation Index (NDVI) (Carlson et al., 1994; Ali et al., 2022). These techniques offer quick and ongoing evaluations of surface-level moisture across extensive regions. LST calculations are derived from thermal emissions, whereas NDVI measurements are based on specific segments in the realm of the electromagnetic spectrum, particularly the reflectivity on the surface within the red and near-infrared (NIR) bands. Geophysical techniques allow for fast and non-disturbing measurement of soil characteristics, like electrical conductivity, resistivity, and potential methods, making them an efficient approach for precise agriculture mapping (Ozegin and Safulu, 2022; Ganiyu et al., 2020). Electrical resistivity is vital for soil mapping and investigations, depending on the approach utilized, which can be 1D, 2D, or 3D. Aided by this technique, the near-surface zone's vertical and lateral variability can be evaluated. Electrical resistivity can be applied to agricultural areas to characterize soil factors, such as soil texture, wetness, and salinity, as well as heavy metal pollution (Turki, et al., 2019; Vásconez-Maza, et al., 2021). The outcomes of this study will establish the possibility of measuring soil salinity, soil moisture, and soil texture from geophysical methods. High salinity regions are simply distinguished with electrical resistivity, and the soil layering is marked to a depth of about 2 m, being the interval encompassing both the soil profile and the precinct where crop roots thrive (Allred et al., 2008).

Therefore, this study aimed at applying both geophysical and geochemical principles for soil mapping and characterization in the context of sustainable precise farming practices in the Centre for Entrepreneurship Study (CES) farm, Delta State University, Abraka, Delta State, Nigeria.

2.1 Materials and Methods

2.1.1 Site Description and Geology

Abraka is situated in the Western Niger Delta within latitudes 50° 48" N and longitude 60° 06" E (Figure 1), and underlying the area is the Benin Formation, extending over the River Niger with a stretch covering the west of Lagos and extending to the Calabar Flank. It has a lowland terrain typical of a coastal plain, sloping towards the River Ethiope. The climate and relative humidity range from 23 to 37°C and 50 to 70%, respectively. Also, the annual dry and wet periods are from about November to February, and March to October, respectively. Between 2000-2005, the Delta State University weather station measured the mean rainfall in the area to be 3317.8 mm. Abraka has rainforest vegetation that has been converted to farmlands and ancillary forests. However, the riverbanks are flanked by lush, dense, and swamp primary forest. Three lithostratigraphic formations make up the Geology of the area: The Akata Formation, Agbada Formation, and Benin Formation. They constitute the geological landscape, along with the Akata being the oldest and Benin the youngest. The Benin Formation is obscured by the newer Holocene sediments found in the Sombreiro-Warri Deltaic plain, as well as the Mangrove swamp and freshwater swamp wetlands located in the south of Abraka. (Ofomola et al., 2018). Thestudy area is the CES farm at Site III of the Delta State University,Abraka (Figure 2), situated in the northeastern part of Isiokolo. It has existed for about 7 years with various crops such as pineapple, cassava, banana, yam, and watermelon, cultivated on the farm.

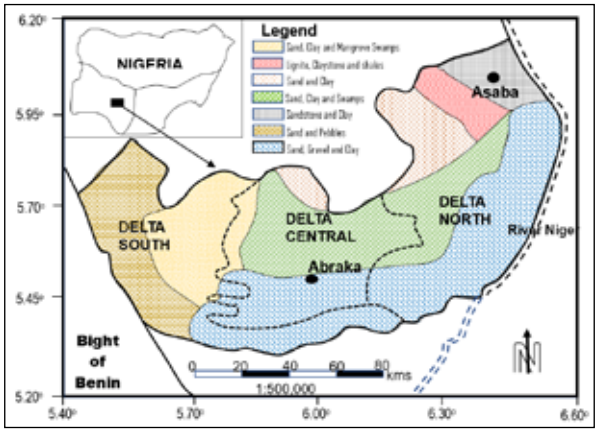

Figure 1. Geological map of Delta State showing the study area

Figure 2. Location map of DELSU showing the study area

2.2 Elctrical Resistivity Method

An electrical resistivity survey, which employed vertical electrical sounding (VES) and two-dimensional (2D) resistivity mapping was performed at the location, utilizing the ABEM Tetrameter (SAS 1000) to map the subsurface lithology and characterisation of the topsoil. The base map for the electrical survey is presented in Figure 3. A total of seven VES and five - 2D-ERT profiles were occupied using Schlumberger and modified Wenner arrays, respectively.

The Win-Resist program, Version 1.0 (Vander-Velpen, 2004) was used to produce a resistivity model of one-dimension (1D) for each sounding location. The graphs display the estimated resistivity, thicknesses, and depths of

the geoelectric strata at every VES station (Aizebeokhai, 2010).

An extended profile dimension of 100 m with the least possible electrode spacing and increment of 1 m was chosen for each 2D traverse line while using the modified Wenner electrode array setup for 5 data levels. The values of the apparent resistivity from the ERT were processed, using RES2DINV inversion software, version 3.59 (Loke 2010) to produce the inverse model resistivity, which aided in the understanding of the subsurface distribution of resistivity (Ofomola et al., 2016; Al-Amoush et al., 2017; Chinyem 2024). The program subdivides the area under the surface into a series of rectangular zones that reflect the observed data layout. The traditional Least-square approach was utilized to process the 2D data in a bid to reduce to barest. It minimizes the squared discrepancies of the variance between the actual and modeled apparent resistivity readings.

Figure 3. Base map consisting of lines and designated sampling points at the CES farm

2.3 Geochemical Method

Soil samples were collected at seven different sample points, close to the VES stations, for critical examination and analysis at the Advanced Research Laboratory of Delta State University, Abraka. This will validate the resistivity values obtained in the area (Ofomola et al., 2021). To obtain the soil in its pristine condition free from environmental contamination, samples were taken from a depth of 0.5 meters without any disruption and were promptly stored in airtight sampling bags. The soil samples were analyzed for heavy metals and rare earth elements (REE) such as copper (Cu), cobalt (Co), lead (Pb), zinc (Zn), nickel (Ni), molybdenum (Mo), cadmium (Cd), arsenic (As), using the Graphite Furnace Atomic Absorption Spectrophotometer (GFAAS). Li et al. (2017) identified this as one of the top techniques for quantifying heavy metals and REE in soils. The heavy metals are reported in ppm, whereas the concentration is given in %. One ppm is equal to one mg/kg when converting from ppm to mg/kg. Additionally, 1 g/kg = 0.001 ppm since 1 g/L or 1 g/kg equals 1 ppb, which is identical to 1 ppb.

Determination of contamination level was conducted using the contamination factor (Cf) and the pollution load index (PLI), (Tomlinson et al., 1980), where the Cf was derived using Eq. (1).

$$Cf = \frac{Cn}{Bn} \quad (1)$$

Cn is the metal concentration level, and Bn represents the baseline or average crustal elements value. A Cf (contamination factor) of up to 1 depicts low contamination, a Cf extending from more than 1 to 3 indicates moderate contamination, and a Cf above 3 means high contamination levels. Earlier studies utilized the pollution load index (PLI), alternatively recognized as Tomlinson's pollution index, and the Nemerow integrated pollution load index (NIPI) to evaluate the comprehensive pollution condition of soil specimens. (Nemerow, 1991; Tomlinson et al., 1980). The PLI was calculated using Eq. (2)

$$PLI = \sqrt[n]{cf1 \times cf2 \ldots . cfn} \quad (2)$$

where the pollution load index, PLI is determined by the number of samples, n, and contamination factor of metal n, . The PLI index runs through a scale ranging from 0 to 6, where 0 indicates no pollution, 1 signifies pollution from none to medium, 2 denotes moderate pollution, 3 is an indication of moderate to strong pollution, 4 signifies strong pollution, 5 represents pollution status from strong to very strong, and 6 signifies very strong pollution, as highlighted in studies by Finch et al. (2018), and Rashed (2010).

2.4 Soil Moisture Estimation using Landsat Image

The analysis of the Soil Moisture Index (SMI) was carried out using Landsat 8 imagery at a resolution of 30 meters, which had minimal cloud interference and was sourced from the United State Geological Survey (USGS) Earth Explorer website. The SMI analysis and mapping were executed using the raster calculator tool in ArcGIS 10.2.2, a geographic information system software. SMI maps, created using Landsat 8 images, display values ranging from 0 to 1, which indicate the comparative volume of soil moisture present in the area. On these maps, a value of 0 indicates the least amount of soil moisture, whereas a value of 1 signifies the maximum soil moisture observed on a specific day.

The computation of the SMI entailed incorporating the Normalized Difference Vegetation Index (NDVI) with the Land Surface Temperature (LST), a method used by Ijaz et al. (2020) and Tajudin et al. (2021). The SMI was determined using the formula in Eq. (3)

$$SMI = (LST_{max} - LST)/(LST_{max} - LST_{min}) \quad (3)$$

where, for a specific NDVI, $LST_{max,}$ and LST_{min} represent the highest and lowest surface temperatures, respectively, and LST refers to the surface temperature of a pixel for that NDVI, as measured through remote sensing. NDVI values, which can vary from -1 to 1, are calculated using Eq. (4)

$$NDVI = (NIR - Red)/(NIR + Red) \quad (4)$$

where NIR and Red represents the Near-infrared band and Red band, respectively.

3.1 Results and Discussion

3.1.1 Geoelectrical Resistivity Methods for Soil Profile Delineation

The results of resistivity sounding revealed inferred lithology, layer thicknesses, and depths as shown in Table 1. A geoelectric section, utilizing the borehole log information alongside vertical electrical sounding data, was constructed as shown in Figure 4. The geoelectric sections and the borehole log, upon comparison, show similar content but vary in the structure and depth associated with various soil types.

Table 1. Geoelectric parameters and related lithology

VES	LAYERS	RESISTIVITY (ohm.m)	THICKNESS (m)	DEPTH (m)	INFERRED LITHOLOGY
1	1 2 3 4 5	168.3 1942.9 2702.8 3040.1 3321.2	1.0 7.9 31.4 8.0	1.0 8.9 40.3 48.3	Lateritic Topsoil Fine sand Fine to medium-grain sand Medium to coarse sand Coarse sand
2	1 2 3 4 5	224.6 4207.9 3939.2 2965.7 3317.1	0.8 3.6 10.0 11.0	0.8 4.4 14.4 25.4	Lateritic Topsoil Sand Fine sand Fine to medium-grain sand Coarse sand
3	1 2 3	624 2674 3526	1.7 13.2	1.7 14.9	Lateritic Topsoil Fine to medium-grain sand Coarse sand
4	1 2 3 4	528 4557 2500 3695	1.5 3.6 13.5	1.5 5.1 18.6	Topsoil Fine sand Fine to medium-grain sand Coarse sand
5	1 2 3 4	790 2551 1795 2248	1.2 3.5 14.5	1.2 4.7 19.2	Lateritic Topsoil Fine sand Fine to medium-grain sand Coarse sand
6	1 2 3	597 2908 1120	0.7 3.7	0.7 4.4	Lateritic Topsoil Fine sand Coarse sand
7	1 2 3 4	523 397 2276 1628	3.1 5.2 24.2	3.1 8.3 32.5	Lateritic Topsoil Fine sand Fine to medium-grain sand Coarse sand

The outcomes of vertical electrical sounding (VES) tests, provided in Table 1, show the inferred lithology and associated resistivity and depth of different strata.

The first VES location (VES 1) has five layers, with resistivity ranging from 168.3 Ωm for the lateritic topsoil layer to 3321.2 Ωm for the coarse sand layer. The layer thicknesses range from 1.0 to 31.4 m. The inferred lithology includes topsoil, fine sand, fine to medium grain sand, medium to coarse sand and coarse sand. VES 2 also has five layers, with resistivity ranging from 224.6 Ωm for the lateritic topsoil layer to 4207.9 Ωm for the sand layer. The layers' thicknesses range from 0.8 m to 11.0 m. The inferred lithology includes lateritic topsoil, sand, fine sand, fine to medium-grain sand, and coarse sand. VES 3 has three layers, with resistivity ranging from 624 Ωm for the lateritic topsoil layer to 3526 Ωm for the coarse sand layer. The thickness of the layer ranges from 1.7 m to 13.2 m. The inferred lithology includes topsoil, fine to medium-grain sand and coarse sand.

The fourth VES location (VES 4) has four layers, with resistivity ranging from 528 Ωm for the lateritic topsoil layer to 4557 Ωm for the fine sand layer. The thickness of the layers ranges from 1.5 m to 13.5 m. The inferred lithology includes topsoil, fine sand, fine to medium-grain sand, and coarse sand. The fifth VES location (VES 5) has four layers, with resistivity ranging from 790 Ωm for the lateritic topsoil layer to 2551 Ωm for the fine sand layer. The thickness of the layer ranges from 1.2 m to 14.5 m. The inferred lithology includes lateritic topsoil, fine sand, fine to medium-grain sand, and coarse sand. VES 6 has three layers, with resistivity ranging from 597 Ωm for the topsoil layer to 2908 Ωm for the fine sand layer. The thickness of the layers ranges from 0.7 m to 3.7 m. The inferred lithology includes topsoil, fine sand and coarse sand. VES 7 has four layers, with resistivity ranging from 397 Ωm for the fine sand layer to 2276 Ωm for the fine to medium grain sand layer. The thickness of the layers ranges from 3.1 m to 24.2 m for the fine to medium-grain sand. The inferred lithology includes lateritic topsoil, fine sand, fine to medium-grain sand, and coarse sand.

Generally, the VES revealed three to five geoelectric layers across the study area. The near-surface first layer exhibits a resistivity range from 178-790 Ωm and a thickness of 0.7-3.1 m, and this mainly represents the lateritic topsoil. The second layer's resistivity and thickness vary from 397-4557 Ωm and 3.5-7.9 m, respectively, and are dominated by lateritic fine sand. The third to fifth layers constitute the saturated zone which is the basic source of moisture for the crops and has resistivity ranging 1120-3695 Ωm and thickness ranges 10.0- 31.4 m, and they represent the fine sand from medium to coarse grain sand.

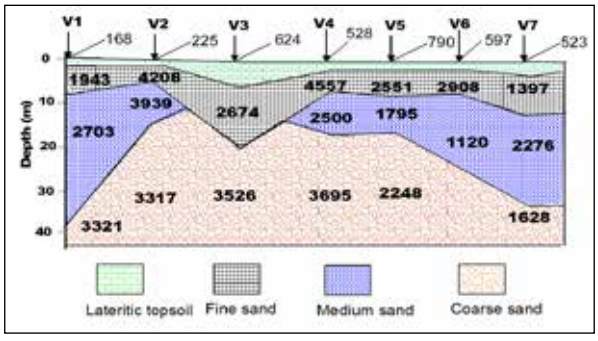

Figure 4. Geoelectric profile through VES 1 to VES 7.

3.1.2 Soil Profile Evaluation

To obtain the soil profile in the study area, borehole drilling data as well as the downhole geophysical logs were used as presented in Figure 5. The first layer consists of brownish, unconsolidated, lateritic topsoil of about 3 m thick. The dark brown coloration is due to the humus and organic matter content. This makes the soil to a depth of 3 m suitable for crop production. A reddish lateritic sand layer to a depth of 6.5 m underlain the first layer. From this lower portion, the values of resistivity and spontaneous potential logs are approximately 500 Ω. m and -0.4 mV, respectively, due to the degree of moisture. The third layer thickness is around 2.7 m, to a depth of 9.1 m, and is composed of reddish brown, fine clayey sand. Also, the composition of the fourth layer is brownish fine to medium sand, while the fifth layer is about 4.1 m thick, extending from a depth of 12.2 m - 16.3 m and is composed of brownish to yellowish fine to medium to coarse sand. The sixth layer has a depth range between 19.6 and 48.8 m and is composed of whitish, medium to coarse sand. The resistivity log shows an increase of 400 Ωm, while the SP log value shows a more stable value, indicating complete saturation.

This soil profile determination corresponds with the inferred lithology from the geoelectric section, obtained from the vertical electrical sounding which ranges from lateritic topsoil to saturated coarse sand. The resistivity of the topsoil ranges from 168 – 790 Ωm with an average value of 494 Ωm and an average depth of 2.3 m. This depth covers the uppermost root area of some significant crops such as maize, okra, cucumber, cassava, tomatoes, etc. The topsoil resistivity values depict a high amount of moisture and mineral nutrients, and they have a fair degree of stoniness to aid adequate rooting of the crops.

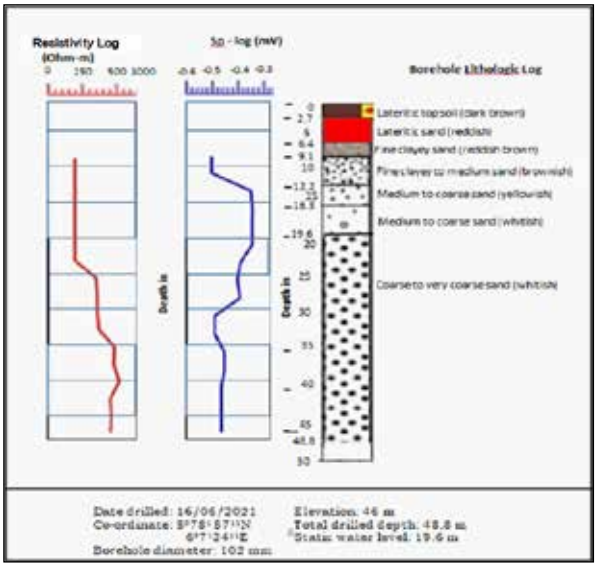

Figure 5. Cross section of the lithologic log from the borehole plotted against a downhole geophysical log in the area.

The 2D resistivity inversion models, including elevations for the traverses conducted on the CES farm, are presented in Figure 6. Six layers were identified, and they agree with the vertical electrical sounding and the borehole log. The 2D images have an approximate investigation depth of 3 m. The values, presented on the vertical edges of the sections, correspond to the elevations of each traverse line. The variation in resistivity values is a function of mineral and moisture contents and degree of compaction of the soil. The topsoil comprises lateritic clay and sandy clay with a resistivity of less than 300 Ωm and a depth of about 1.5 m. The variation in the soil compaction, moisture level, and content of organic matter is blamed for the shift in values of resistivity obtained across the traverses. Except for traverse 2, the topsoil, across the study area, is rich in moisture and mineral composition , similar to the assertion made by Ozegin and Salufu (2022). The low resistivity of fine-grained silt and clay topsoil is because of the partial decomposition of plants and animals forming organic matter. Also, the observed topsoil is high in porosity and water retention which are major suitable factors for the yield of tuber and stem plants. The second layer resistivity values greater than 600 Ωm are an indication of organic matter deficiency in the soil (Ozegin and Salufu, 2022). The soil stoniness has increased in this level, thereby reducing the effective rooting of crops and reducing the water retention capacity since the soil is now semi or non-permeable. The soil at this level also contains little or no organic matter due to the low presence of microorganisms, arising from the low water retention capacity (Verdoodt and Ranst, 2003). This is a major limitation to the crop yield capacity of the soil.

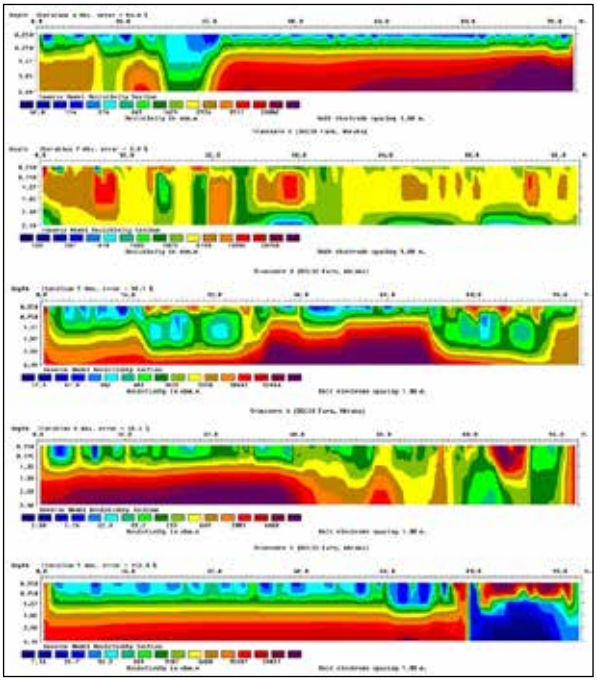

Figure 6. Results of inverted ERT profiles

3.2 Soil Analysis Results

Table 2 outlines the concentrations of major trace and rare earth elements in the soil samples collected from the study area. The pH ranges from 6.13 to 7.16 across the designated sample points in the study location. This falls within the acceptable range of 6.0 – 7.5 and indicates good soil for crop production. Organic matter content ranges from 6.48 – 8.66 % with stations 1, 2, 4, and 7 having a relatively high organic matter content. This result agrees with the VES, with topsoil of less than 600 Ωm, which is an indication that the soil exhibits moderate richness in mineral and natural organic content required for crop production (Ozegin and Salufu, 2022).

Table 2. Heavy metals detected from soil samples, compared with WHO/FAO permissible limits for heavy metals in soil.

Parameters	Crustal average (1964)	S1	S2	S3	S4	S5	S6	S7	WHO /FAO
pH	-	6.13	6.51	7.11	6.31	7.16	7.12	6.21	7.50
Organic matter (%)	-	8.37	8.21	`6.74	8.66	6.48	7.95	8.42	N/A
Total Nitrogen (%)	-	65.72	68.61	75.82	72.15	73.51	78.21	68.42	N/A
Phosphorus (mg/kg)	-	53.32	55.98	58.45	67.43	62.67	65.32	66.24	N/A
Cadmium (mg/kg)	0.1	0.06	0.08	0.02	0.10	0.11	0.04	0.07	0.8
Chromium (mg/kg)	83.0	3.10	1.47	1.31	0.42	0.56	0.19	0.59	100
Copper (mg/kg)	25.0	22.61	18.41	16.91	27.43	25.63	14.16	20.41	36
Nickel (mg/kg)	44.0	2.06	1.16	2.16	1.84	3.11	2.10	1.89	35
Lead (mg/kg)	17.0	7.46	4.86	6.11	5.11	8.84	3.67	4.00	85
Zinc (mg/kg)	71	1.09	1.17	0.98	2.16	2.94	1.81	1.94	60
Cobalt (mg/kg)	17.0	0.95	1.07	1.00	1.14	12.07	1.84	1.27	N/A
Manganese (mg/kg)	600	2.09	1.84	2.84	15.61	17.07	14.11	12.16	N/A
Iron (mg/kg)	N/A	98.41	103.41	96.33	149.11	151.63	131.63	120.74	300
Arsenic (mg/kg)	1.5	N/A	N/A	N/A	0.10	0.08	N/A	N/A	10

N/A: Means not Available.

Also, the values for total nitrogen and phosphorus range from 65.72 % - 78.21 %, and 53.32 – 67.43 mg/kg, respectively. Stations 3, 5, and 6 have lower organic matter content, with higher resistivity of the topsoil > 600 Ωm. This establishes that the area has low crop yield capacity with topsoil resistivity values, ranging from 597 – 790 Ωm. The soil nutrients spatial dissemination in the study area shows that the area around stations 1.2 4 and 7 is rich in essential soil nutrients while stations 3, 5, and 6 have low nutrients and are deficient of organic matter.

The concentration of copper (Cu) varied from 14.16 mg/kg to 22.61 mg/kg, which is under the WHO-allowed upper limit for agricultural soils of 40 mg/kg. Copper-induced toxicity is typically detected in the soil and water in industrialized areas. The concentration of nickel (Ni) ranged from 1.16 mg/kg to 3.11 mg/kg as shown in Table 2, which is also below the WHO/FAO acceptable threshold of 68 mg/kg for agricultural soils. As a micronutrient, Ni is fundamentally needed in tiny amounts for proper plant growth. However, when toxic levels are present in soil, it restricts plant development, stunts root growth, and induces chlorosis, which is characterized by the yellowing of leaves due to a lack of chlorophyll. The concentration of Lead (Pb) in the samples was between 4.00 mg/kg and 8.84 mg/kg, which falls under the acceptable threshold of 50.00 mg/kg set by WHO/FAO (2001) for agricultural soils. Arsenic (As) was not detected in the farm except in samples 4 and 5, the farm has concentrations ranging from 0.08 mg/kg to 0.1 mg/kg and are within the WHO/FAO acceptable limits of 10 mg/kg.

Also, Iron (Fe) content in the samples ranged between 96.33 mg/kg and 151.63 mg/kg. The impacts of iron (Fe), a vital micronutrient for agricultural soils, involve field yellowing and the formation of irregularly shaped regions in the subsurface. The maximum permitted content of Fe in soil, according to the WHO, is 450 mg/kg. However, the iron concentration in the CES farm is below the WHO-recommended levels. These observed concentrations render the soil at the CES farm of Delta State University free from toxicity and thereby suitable for crop production (WHO/FAO, 2001). The contamination factor and pollution index for the soil are presented in Table 3.

Table 3. Pollution index and contamination levels of the toxic elements of the soil

Toxic elements	Contamination Factor (Range)	Contamination Factor	Pollution load index (PLI)	Interpretation
Cadmium	0.2-1.1	0.69	0.60	Unpolluted
Chromium	0.0-0.04	0.01	0.01	Unpolluted
Copper	0.68-1.03	0.83	0.82	Unpolluted
Nickel	0.03-0.07	0.05	0.05	Unpolluted
Lead	0.24-0.52	0.34	0.07	Unpolluted
Zinc	0.01-0.04	0.02	0.02	Unpolluted
Cobalt	0.06-0.71	0.31	0.10	Unpolluted
Manganese	0.00-0.03	0.02	0.01	Unpolluted
Iron	N/A			Unpolluted
Arsenic	0.05-0.07			Unpolluted

The contamination factor (CF) from toxic elements of Cd, Cr, Cu, Ni, Pb, Zn, Co. Mg, and As range from 0.2 - 1.1, 0.0 - 0.04, 0.68 - 1.03, 0.03 - 0.07, 0.24 - 0.52, 0.01- 0.04, 0.06 - 0.71, 0.00-0.03 and 0.05 - 0.07, respectively. This is an indication of low to moderate contamination, low salinity, and high levels of organic material in the soil. Also, the soil

pollution load index (PLI) ranges from 0.01 - 0.82. This also indicates that the entire soil in the study area is unpolluted. The soil analysis results concur with the borehole log, VES, and electrical resistivity tomography, signifying that the soil is high in organic content.

Table 4 shows the textural analysis of the soil with silt having the dominant grain ranging from 66.2 % to 73.0 %, clay from 15.4 % to 19.4 %, and sand from 11.6 % to 16.1 %. Clay content is moderately high in the area which is an indication of the Cation Exchange Capacity (CEC) of the soil and retention of nutrients. Also, a combination of the clay and silt content increases moisture retention. These values are higher around locations 1. 2. 4 and 7 and in agreement with the soil nutrients analysis and the VES.

Table 4. Soil textural analysis results in the CES Farm

Sample	Silt (%)	Sand (%)	Clay (%)
S1	72.3	12.2	16.5
S2	66.2	14.4	19.4
S3	67.5	15.3	17.2
S4	73.0	11.6	15.4
S5	67.9	13.5	18.6
S6	70.6	12.8	16.6
S7	67.7	16.1	18.2

3.3 Soil Moisture Content Index

The soil moisture index (SMI) of the farm with an area of about 75,500 m^2, ranges from 0.184 to 0.385 as shown in Figure 7. SMI of 0.26 – 0.38 was classified as wet covering 25.7 % of the total farm area. 42.4 % of the farm has an SMI range of 0.21 to 0.26 and was classified as moist, while the remaining landmass of 31.9 % has SMI of 0.18 to 0.21, classified dry as shown in table 5. This implies that about 70% of the farm has SMI, ranging from moist to wet, making nutrients to be adequately mobilized for plant intake.

Table 5. Soil moisture content status in the study area

Soil moisture Index	Classification	Area (m^2)
0.18 – 0.21	Dry	24,100
0.21 – 0.26	Moist	32,000
0.26 – 0.38	Wet	19,400

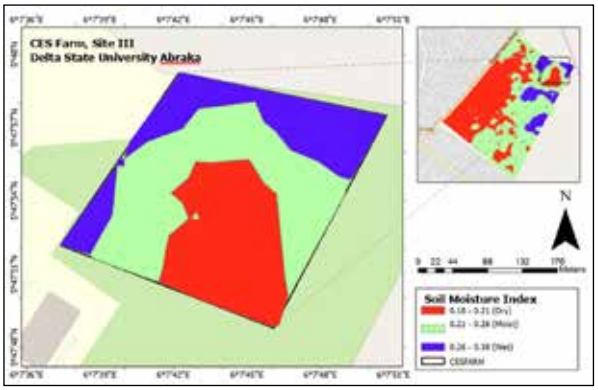

Figure 7. Soil Moisture index map of the CES farm, DELSU

3.4 Conclusion

Integrated geophysical methods and soil test analysis have been used to determine the nature of the soil in the CES farm Delta State University, Abraka, for its suitability in crop production. To maximize agricultural output while preserving soil and water resources, precise agriculture requires creating site-specific management techniques for crops based on the diversity of soil parameters. The soil of the research regions has been described, and management zones have been established, using geoelectrical resistivity imaging. The measurement of the soil fertility level of the farm was aided by a geochemical examination of earth samples and soil moisture content index from Landsat 8 imagery. The results showed that the soil is moderately rich in mineral content and organic matter required for crop production. The contamination factor and pollution index of the soil are quite low which is an indication that the soil is suitable for crop production.

Generally, determining what the soil requires to enhance crop growth is almost impossible without conducting soil analysis. Analyzing and testing soil helps understand its capacity to furnish adequate nutrients for supporting plant development and yield. Soil analysis also helps in determining the right combination of fertilizers and liming materials required for soil improvement. Therefore, with this study, using combined geophysical methods and soil test analysis in studying the evolution and pollution history of the soil have consistently demonstrated reliable results overtime.

Competing Interest Statement

In connection with this study, the authors have stated that they hold no financial or personal interests.

Data Availability Statement

All data generated by this study that supports its conclusions can be provided upon a formal request to the corresponding author.

Funding Declaration

The authors did not receive any funding from any organization for conducting this study.

Ethics Approval and Consent to Participate

Not Applicable

References

Aizebeokhai, A.P. (2010). 2D and 3D Geoelectric Resistivity Imaging: Theory and Field Design. Scientific Research and Essays 5 (23): 3592–3605.

Al-Amoush H, Abu Rajab J., Al-Tarazi E., Al-Shabeeb A.R., Al-Adamat R. Al-Fugara A. (2017). Electrical Resistivity Tomography Modeling of Vertical Lithological Contact using Different Electrode Configurations. Jordan Journal of Earth and Environmental Sciences 8(1): 27 – 34.

Al-Rashed M, Mukhopadhyay A., Al-Senafy A., Ghoneim, H. (2010). Contamination of Groundwater from Oil Field Water Disposal Pits in Kuwait. The Arabian Journal for Science and Engineering 35: 105 - 123

Ali A., Khaled H., Mostafa M., Abdulla A., Omar A., Mohammad Z., Amer M. (2022). Landsat/ MODIS Fusion for Soil Moisture Estimation over a Heterogeneous Area in Northern Jordan. Jordan Journal of Earth and Environmental Sciences 13 (4): 247-262.

Allred, B.J, Ehsani, M.R. Daniels, J.J. (2008). General considerations for Geophysical Methods Applied to Agriculture. Hand-Book of Agricultural Geophysics. 1st ed., CRC Press, Taylor and Francis Group, Boca Raton, Florida.

Altunay N., Hazer B., Tuzen M., Elik A. (2021). A New Analytical Approach for Preconcentration, Separation and Determination of Pb (II) And Cd (II) in Real Samples using a New Adsorbent: Synthesis, Characterization, and Application. Food Chemistry 359, 129923.

Anomohanran, O. (2015). Hydrogeophysical Investigation of Aquifer Properties and Lithological Strata in Abraka, Nigeria. Journal of African Earth Sciences 102: 247-253.

Aweto, K. E., Chiyem, F. I. and Ohwoghere-Asuma, O. (2017). Comparative Study of Total Dissolved Solids Evaluated from Resistivity Sounding, Water Analysis and Log Data. Scientia Africana 16(2): 38-43.

Briffa, J. Sinagra, E. and Blundell, R. (2020). Heavy Metal Pollution in the Environment and Their Toxicological Effects on Humans. Heliyon 6(9), e04691.

Carlson, T. N., Gillies, R. R., Perry, E. M. (1994). A Method to Make Use of Thermal Infrared Temperature and NDVI Measurements to Infer Surface Soil Water Content and Fractional Vegetation Cover. Remote Sensing Reviews 9(1-2): 161–173.

Chinyem, F.I. (2024). Determination of Aquifer Hydraulic Parameters and Groundwater Protective Capacity in Parts of Nsukwa Clan, Nigeria. Environmental Monitoring Assessment 196, 243.

Finch, F. Roldan, R. Walsh, L. Kelly, J., Amor, S. (2018). Analytical Methods for Chemical Analysis of Geological Materials, Government of New Foundland and Labrador, Department of Natural Resources. Department of Natural Resources, Geological Survey, Open File NFLD/3316.

Ganiyu, S.A. Olurin, O.T. Oladunjoye, M.A. Badmus, B.S. (2020). Investigation of Soil Moisture Content Over a Cultivated Farmland in Abeokuta Nigeria Using Electrical Resistivity Methods and Soil Analysis. Journal of King Saud University-Science 32 (1): 811–821.

Ijaz, M., Ahmad, H. R., Bibi, S., Ayub, M. A., Khalid, S. (2020). Soil Salinity Detection and Monitoring Using Landsat Data: A Case Study from Kot Addu, Pakistan. Arabian Journal of Geosciences 13(13): 510.

Iserhien-Emekeme, R.E., Ofomola, M.O., Ohwoghere-Asuma, O., Chinyem, F.I., Anomohanran, O. (2021). Modelling Aquifer Parameters Using Surficial Geophysical Techniques: A Case Study of Ovwian, Southern Nigeria. Modeling Earth Systems and Environment 7(4): 2297–2312.

Liu H, Cui H, Wang Y, Jiang Z, Lei L, Wei S. (2023). Accurate Determination of Trace Cadmium in Soil Samples with Graphite Furnace Atomic Absorption Spectrometry Using Metal-Organic Frameworks as Matrix Modifiers. Applied Spectroscopy 77(2):131-139.

Loke, M.H. (2010). Res2Dinv ver. 3.59 for Windows XP/ Vista/7, 2010. Rapid 2-D Resistivity & IP Inversion Using the Least-Squares Method. Geoelectrical Imaging 2D & 3D. Geotomo Software.

Lu, X. Zhang, X. Li, L.Y., Chen, H. (2014). Assessment of Metals Pollution and Health Risk in Dust from Nursery Schools in Xi'an, China. Environmental Research 128: 27–34.

Mashal K, Salahat M., Al-Qinna M, Ali Y. (2017). Assessment of Heavy Metals in Urban Areas of Al Hashmiyya City of Jordan. Jordan Journal of Earth and Environmental Sciences 8(2):61 - 67

Nemerow, N.L. (1991). Stream, Lake, Estuary and Ocean Pollution. 2nd ed., Van Nostrand Reinhold Publishing Company, New York.

Nowka, R., Marr, I.L., Ansari, T.M., Müller, H. (1999). Direct Analysis of Solid Samples by GFAAS – Determination of Trace Heavy Metals in Barytes. Fresenius' Journal of Analytical Chemistry 364: 533-540.

Ofomola, M. O, Akpolile, A.F, Anomohanran, O., Adeoye T.O, Bawallah, M.A. (2021). Detection of Trace Metal Contamination Around a Dumpsite in Iyara Area Warri Nigeria Using Geoelectrical and Geochemical Methods. Environmental and Earth Sciences Research Journal 8(3); 125-133.

Ofomola, M.O. (2015). Mapping of Aquifer Contamination Using Geoelectric Methods at a Municipal Solid Waste Disposal Site in Warri, Southern Nigeria. Journal of Applied Geology and Geophysics 3(3): 39 – 47.

Ofomola, M.O., Ako, B.D., Adelusi, A.O. (2016). Flow Direction and Velocity Determination of Dumpsite-Induced Groundwater Contamination in Part of Delta State, Nigeria. Arabian Journal of Geosciences 9, 398.

Ofomola, M.O., Iserhien-Emekeme, R.E., Okocha, F. O., Adeoye, T. O (2018). Evaluation of Subsoil Competence for Foundation Studies at Site III of the Delta State University, Nigeria. Journal of Geophysics and Engineering 15(3): 638–657.

Ozegin, K.O., Salufu S.O. (2022). Electrical Geophysical Method and GIS in Agricultural Crop Productivity in a Typical Sedimentary Environment. NRIAG Journal of Astronomy and Geophysics 11(1): 69-80.

Rashid, A., Schutte, B.J., Ulery, A., Deyholos, M.K., Sanogo, S., Lehnhoff, E.A., Beck, L. (2023). Heavy Metal Contamination in Agricultural Soil: Environmental Pollutants Affecting Crop Health. Agronomy 13(6), 1521.

Romero-Ruiz, A., Linde, N., Keller, T., Or, D. (2018). A Review of Geophysical Methods for Soil Structure Characterization. Reviews of Geophysics 56(4): 672-697.

Saikat M., Arka J. C., Abu M. T., Talha B. E., Firzan N., Ameer K., Abubakr M. I., Mayeen U. K., Hamid O., Fahad A. A., Jesus S. (2022). Impact of Heavy Metals on the Environment and Human Health: Novel Therapeutic Insights to Counter the Toxicity. Journal of King Saud University – Science 34, 101865

Tajudin, N., Ya'acob, N., Mohd Ali, D., Adnan, N. A. (2021). Soil Moisture Index Estimation from Landsat 8 Images for Prediction and Monitoring Landslide Occurrences in Ulu Kelang, Selangor, Malaysia. International Journal of Electrical and Computer Engineering 11(3): 2101-2108.

Tomlinson, D.C, Wilson, J.G, Harris, C.R, Jeffrey, D.W. (1980). Problems in The Assessment of Heavy Metals LevelsiIn Estuaries and The Formation of Pollution Index, Helgoland Marine Research 33 566–575.

Turki, N., Elaoud, A., Gabtni, H., Trabelsi, I., Khalfallah, K. K. (2019). Agricultural Soil Characterization Using 2D Electrical Resistivity Tomography (ERT) after Direct and Intermittent Digestate Application. Arabian Journal of Geosciences 12(14).

Vander-Velpen, B.P.A. (2004). WinRESIST (Version 1.0) Resistivity Depth Sounding Interpretation Software. M.Sc Research Project, ITC, Delft, the Netherland.

Vásconez-Maza, M. D., Bueso, M. C., Faz, A., Acosta, J. A., Martínez-Segura, M. A. (2021). Assessing the Behaviour of Heavy Metals in Abandoned Phosphogypsum Deposits Combining Electrical Resistivity Tomography and Multivariate Analysis. Journal of Environmental Management 278, 111517.

Verdoodt, A., Van Ranst, E. (2003). Land Evaluation for Agricultural Production in the Tropics. A Large-Scale Land Suitability Classification for Rwanda. Ghent University, Laboratory of Soil Science

WHO/FAO. (2001). Codex Alimentarius Commission. Food additives and contaminants. Joint FAO/WHO Food Standard Programme.

JJEES

JJEES (2024) 15 (4): 265-274
ISSN 1995-6681

Jordan Journal of Earth and Environmental Sciences

Evaluation of Rocks Potentials for Aggregates Production from Sandstone Complex of Afikpo Basin, Southeastern Nigeria

Stephen N. Ukpai[1]*, Chidiebere C. Ani[1], Ezekiel O. Igwe[1], Victor O. Omonona[2], Anthony Chukwu[1]

[1] Ebonyi State University, Abakaliki, Nigeria
[2] Alex Ekwueme Federal University, Ndufu Alike Ikwo, Nigeria

Received on October 14, 2023; Accepted on October 12, 2024

Abstract

Construction industries are faced with the challenges of transporting chippings from far distances due to the perceived unavailability of neighboring rock mass for aggregate processing. The consequence is not limited to road traffic, and accidents, even as rocks of competent aggregates could be nearby, nonetheless, unnoticed. This research explored and verified aggregate chips from simpler methods than customary direct (strength) analyses, using samples outside usual igneous and metamorphic products; particularly where sedimentary rocks were massively emplaced. The applicability was in Afikpo Basin, Nigeria, where consolidated sandstones were deposited in ridges and cuestas, mainly at Amasiri and Akpoha type localities, respectively, yet the region is developing, demanding certified aggregates for buildings/ roads constructions. Bulk samples of the sandstones from different parts of the basin were subjected to petrographic and grain size analyses. While quartz formed the modal mineralogy at 74–81% and feldspar less than 25%. The grains are poorly sorted and angular in convex/ concave contacts. These characteristics typified hard sandstone grouped, like greywacke. Thus, fragments of the rock mass can withstand stress relative to compression/ compaction associated with loads during and after building constructions. It is safe, therefore, to assert that the sandstones are useful as good chippings/ aggregates in infrastructural developments.

Keywords: *Aggregates, Construction, Sandstones, Stability, Afikpo Basin, Nigeria*

1. Introduction

Building collapse is often attributed to the nature of the construction materials used (Bamigboye et al., 2019). These materials involve rock aggregates (Shah et al., 2022) that usually make up over 90% of asphalt pavements and 80% of concrete used in buildings (Hussain, et al., 2022). In concretes, even though [Portland] cement is used as a binder (Ghrair et al, 2023), the strength depends on the grades of aggregates. The grades depend on the quality of the relevant mineralogical composition of parent rocks. It means that rocks may be everywhere around the earth, but the specified quality for engineering uses may not be available where needed at the neighborhood of construction sites. While lots of rocks are yet to be identified within the subsurface where hidden as bedrock around the needful sites, some have outcropped and adjoined the places were perceived as unsuitable because of inadequate verification, possibly by sticking to a particular method. Consequently, advanced but simple integrated analyses of rocks to justify their suitability have become requisite authentication techniques prior to their use in engineering constructions. The suitability of aggregate must reflect its ability to withstand limitations, such as abrasion, crushing, impacting, and disintegration when stored and processed under asphalt pavement being compacted with rollers and exposed to loading (Rehman et al., 2020). The ability depends on petrographic factors, such as mineral composition, the strength of the individual minerals, cohesion between grains, material size, and textural anisotropy (Maricic, 2014). Verification of these parameters is important in the selection of reliable rock materials for the construction of stable buildings, using the case of Afikpo Basin where massive outcrops of different rock formations exist as a group of consolidated sediments. Yet, there has been incessant failure of infrastructures in the basin, especially roads constructed with aggregates perceived to have been imported from other regions.

It was observed that the areas studied in the Afikpo Basin have been characterized by road pavement collapse after a short period of construction. The challenge created concerns between two opinions: the uncertainty over the qualities of rock materials used for the construction and questionable skills of contractor engineers who design without compliance to specifications. The uncertainty enmeshed in the first opinion has even caused negative aesthetic impacts, resulting in low demands of crushed stone [or chippings] produced within the region against the high potential supply that would have been available from active mechanized quarry industries deployed to the area. This uncertainty created a gap between supply and demand and a decline to a very low demand that has continued to affect the economy, hence, must be resolved with innovative investigations. Thus, investigation into the quality stance of the rock fabrics was the scope of the present research. The research commenced with combined petrographic and grain size analyses of sandstones adjudged as the

* Corresponding author e-mail: ukpaisteve@gmail.com

most consolidated formation of the Ezeaku Group. These mechanical tests portrayed the major chemical contents relatively. It is a novelty fact that has not been identified hitherto in petrographic studies as a relevant geologic tool in the exploration of bulk/ industrial materials for engineering constructions. On this note, the research presents part of the roles needed in sourcing raw materials for indigenous buildings and construction industries in Nigeria, following Durotoye (2003) who earlier emphasized that geologists have very important roles to play for national development. The present study demonstrated the needed role, by introducing a simplified and low-cost approach to verifying aggregate quality. It shows its affordability to mechanized and artisan entrepreneurs, encouraging massive infrastructural development by the availability of the certified quantity of aggregate quality. This can create job opportunities for sustainable development and consolidation of the national economy.

According to Orife (2003), the production of construction materials constitutes a substantial part of the national economy that has not been properly harnessed. Therefore, the general aim of the present research was to establish baseline data that can be set into the quality assurance checklist of the construction industries in the selection of reliable primary [nonmetallic minerals] materials for construction of competent infrastructures, in terms of road pavements and buildings' foundations.

2. Geology of the Area

Some previous literature recently updated by Ukpai (2020) buttressed facts that an undeveloped rift arm was formed from the break-up of the Gondwana super continent in the Jurassic era. Following the end of the rift stage, this particular arm traversed West Africa and crossed Nigeria as a trough. The trough was reaffirmed in Nigeria as Benue Trough by Hoque and Nwajide (2002) with a length and width of about 800 km and 150 km, respectively in the Northeast direction from the present Niger Delta to Lake Chad (Obaje, 2009). There was a sea level rise that affected the South Atlantic Ocean in Albian time and created a hydrologic slope towards the Benue Trough (Ukpai, 2021), resulting in a series of transgressions and regressions. A succession of these alternating hydro-geological processes culminated in sedimentary deposits. The first set was at the commencement of the transgressive episodes that produced marine sediments. Nwajide (2013) buttressed that these marine sediments, named Asu River Group, belong to the Albian age of the Lower Cretaceous Era. The second transgression of the marine sediments took place in the Cenomanian Age but was characterized by a current lower than in the former episode, hence, could not advance further than the Odukpani area; otherwise, the Odukpani Formation [mainly limestone] that formed lower limit of Upper Cretaceous era around Calabar flank. However, the absence of the Cenomanian sediments across a wider spectrum of the Benue Trough created an unconformity between the lower and upper Cretaceous eras. Subsequently, the Mamfe Formation was deposited in the Turonian Age through the Bakassi peninsula and spread via a high current to the extreme south of the trough around Afikpo Area where the sediment was originally identified near the Ezeaku River as Ezeaku shale. The thickness of sediments in the Turonian Age increased during the recession of the current [regressive episode] with continental swabs which produced sandstones, in addition to the shales constituted Ezeaku Group. Other sediments of the Upper Cretaceous era within the Benue Trough spanned from those of Coniacian age, dominated by the Awgu Formation to the Nsukka Formation of the uppermost Maastrichtian Age.

The tectonic process affected the entire Benue Trough in the Santonian time, particularly deformed sediments from the Albian to Coniacian ages; consequent upon which a regional uplift was formed. The most prominent of the deformation features was an Anticlinorium formed around the Abakaliki region at the southern part of the trough. The anticlinorium separated Afikpo and Anambra Basins, even as sediments of post-Santonian ages were later deposited across the two depocenters, with increased thickness towards Anambra Basin. This is because, the Nkporo Group, being the basal thick sediments of Anambra Basin is less thick at the southern flank of Afikpo Basin around the Edda Area, followed by negligible thickness of Mamu Formation near the confluence of Cross River and Ebonyi River around Ehugbo area, southeast flank of Afikpo Basin. However, the presence of Ajali and Nsukka Formations belonging to the uppermost Maastritchtian age is scarce in Afikpo Basin. According to Nwajide (2013), the Afikpo Basin is dominated by the Ezeaku Group, comprising shales and sandstones, as well as a minor spread of siltstones.

3. Materials and Methods

The sampled rocks were located by means of Global Positioning System (GPS) of e-Trex model following Okogbue and Ukpai (2013) who used same application and identified sampled locations. In this study, identification of the samples was systematic as it covered the rock type descriptions and associated structures, delineation, and demarcations of litho contacts, as well as measuring the attitudes of bedding planes. In the study, it is believed that rock quality for aggregates as construction material depends on the mineralogy and textural features, so some sandstone samples were collected for petrographic analysis. The petrographic analysis was carried out on samples, collected from Reynolds Construction Company (RCC) abandoned mines (NC05), Ndukwe-Amuro Setraco quarry site (NC07a), Ezeke Amuro NC10a, local quarry sites (NC12), Ezeke local quarry site (NC15), Amasiri, precious foundation school (NC14). These sandstone samples were cut into thin sections at the Department of Earth sciences (Geology), Kogi State University, Anyigba, Nigeria. The thin sections were viewed under petrographic microscope (Meiji monocular series) and photomicrography, using a compact digital camera [fixed with zoom lens] at the department of Geology, Ebonyi State University, Abakaliki, Nigeria. The petrographic analysis was intended to investigate mineral compositions of the sandstones samples and ascertain if the modal mineralogy is of such quality that can be used as aggregates. Accuracy was ensured as the analyzer and polarizer lenses of the microscope

were properly adjusted to determine change in properties of the minerals under both plane (PPL) and cross polarized lights (XPL). Interpretation of the mineralogical details was facilitated through photomicrographs following Mohamed and Abdulkader (2010). However, fossil assemblages were not analyzed because they are not within the scope of the study.

The level of textural cohesion was verified via sieve analysis, performed on selected few samples, mainly where the friable sandstones were easily accessed to determine the typical grain size distribution. About three samples, each weighing 50g, were randomly collected and labeled according to the location codes. Each sample was sieved through sieves stacked in a row of sieve openings. Slot sizes of the openings decreased downwards from the topmost largest to the least screen opening which hangs on a receiver pan at the base. The stack of sieves was placed on a mechanical shaker connected to power source, switched on and shook for 10 minutes. At switching the shaker off, the material retained on each sieve was weighed, and the results were recorded on a specially designed sieve report sheet. Sieve loss was noted and recalculated to correct the weights, and the corrected weights converted to weight percent and cumulative weight percent. The cumulative percent (%) was plotted against phi (Φ) to graphically obtain cumulative frequency curves for analyses of relevant parameters as follows:

$$\text{Mean } (\bar{X}) = \frac{\Phi 16 + \Phi 50 + \Phi 84}{3} \quad (1)$$

$$\text{Standard deviation (Sd)} = \frac{\Phi 84 + \theta 16}{4} + \frac{\Phi 95 + \theta 5}{6.6} \quad (2)$$

$$\text{Kurtosis} = \frac{\Phi 95 - \Phi 5}{2.44\,(\Phi 75 - \Phi 25)} \quad (3)$$

4. Results and Interpretation

4.1 Litho-facies analysis

Alternating sandstones were observably overlying black shales (Figs.1 [A and C]). The shale facies change to argillaceous (silty) materials towards contact with the sandstones. While the silty nature decreased away from flanks of the [Afikpo] synclinorium, the shale turned blocky outwards from the center where the sandstones dominated with sharp contacts around Amasiri area (Figures 1A and 1B) and irregular contacts at Akpoha area (Figure1C). Most of the contacts are characterized by seepages which exposed the shales to weathering due to moisture saturation. Visual inspection of the rock units showed that the sandstones are calcareous, particularly seen from inherent debris of shelly materials that easily break into powdered form when the specimen at fresh road-cut is pressed with fingers. This biological fabric may have been affected by diagenetic and depositional conditions. For this reason, bedding plane dispositions were verified to probe into paleo-geological processes associated with the rock origins and depositional environment.

Figure 1. Photographs showing the rocks units of the area (**A**) Sandstones quarried to the groundmass shale base contact (**B**) Massive sandstones ridge showing the typical alignment before the quarry process (**C**) Blocky nature of the sandstone hill flanks (**D**) Dolerite intrusion localized at few places

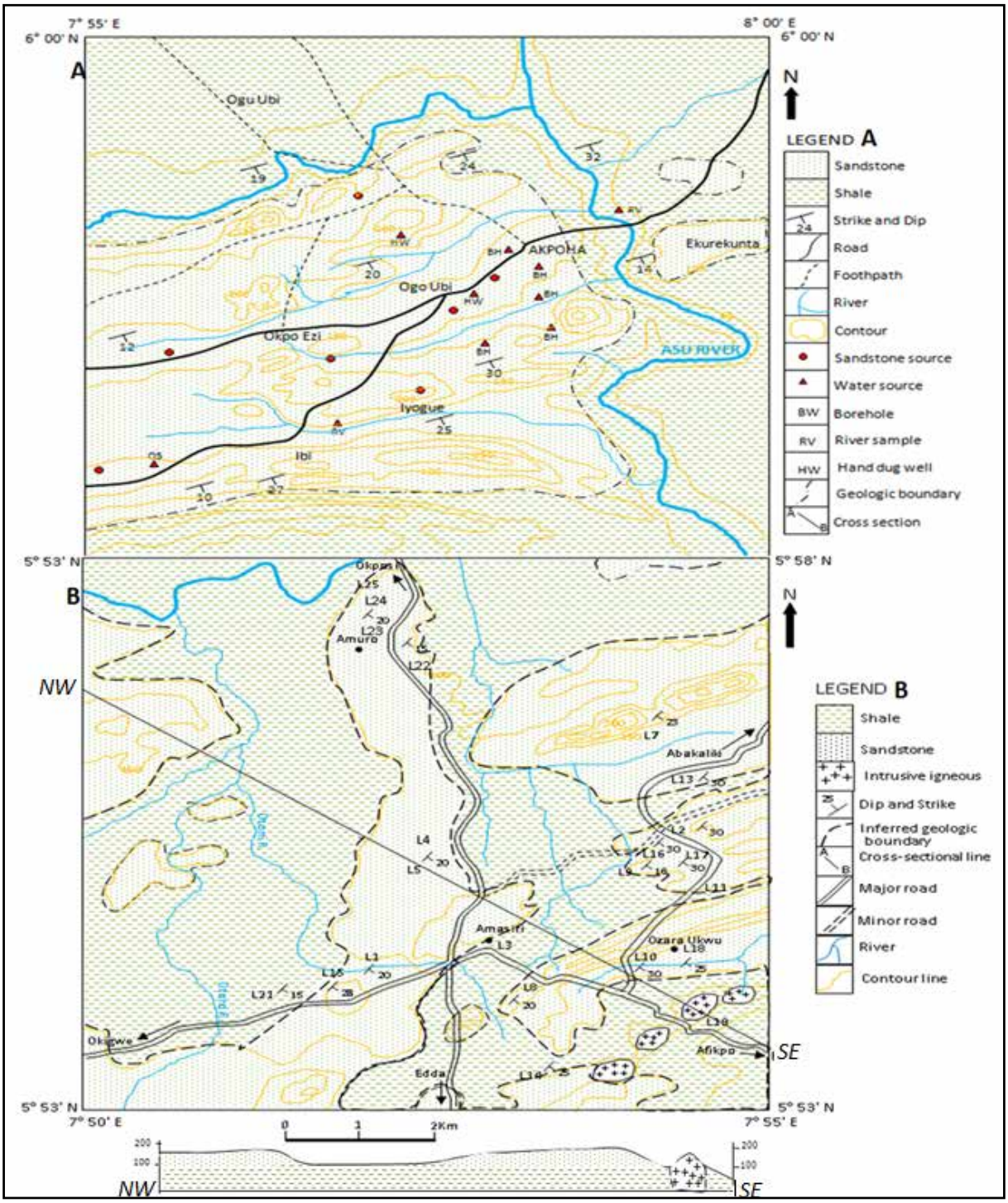

Figure 2. Geological Maps (**A**) Akpoha area (**B**) Amasiri area; and showing the typical alignment of the Ezeaku shale overlain by Amasiri-Akpoha sandstones in a section that crossed part of Amasiri area.

Attitudes of the sandstones at the natural beddings (Figure 1C) showed amount between 17^0 and 40^0; dipping southeast (Figure 2) as confirmed in planar cross beds (Tables 1A and 1B) and trough-cross bedding (Tables 2A and 2B). Both cross beds showed unimodal patterns indicating past fluvial environment that was dominated by regressive-transgressive cycles, influenced NE-SW paleo currents (Figures 3A and 3C). Based on this information, the present study affirms two major provenances. The first was controlled by the transgressive episode from the South Atlantic Ocean at the southwest from Afikpo Basin, and the second was by regression from eastern highlands at the northeast from the Basin (Figure 3B). The transgressive and regressive cycles streamlined depositions of the respective shales of marine source and sandstones of continental origin.

Table 1A. Trends of the planar cross beds of the study area.

S/No	Trend of cross-beds
1	$N55^0 – N235^0$
2	$N52^0 – N232^0$
3	$N45^0 – N225^0$
4	$N55^0 – N235^0$
5	$N60^0 – N240^0$
6	$N55^0 – N235^0$
7	$N65^0 – N245^0$
8	$N52^0 – N232^0$
9	$N48^0 – N228^0$
10	$N80^0 – N260^0$
11	$N70^0 – N250^0$
12	$N70^0 – N250^0$
13	$N65^0 – N245^0$
14	$N55^0 – N235^0$
15	$N50^0 – N230^0$
16	$N45^0 – N225^0$
17	$N50^0 – N230^0$
18	$N45^0 – N225^0$
19	$N35^0 – N115^0$
20	$N40^0 – N220^0$

Table 1B. Planar cross beds analysis using front Azimuth and its back equivalence and class interval of 30^0

S/No	Class interval	Equivalent	Frequency
1	0 – 30	181 – 210	
2	31 – 60	211 – 240	15
3	61 – 90	241 – 270	5
4	91 – 120	271 – 300	
5	121 – 150	301 – 330	
6	151 – 180	331 – 360	
			Ef = 20

Table 2A. Trends of trough cross beds

S/No	Trend of cross-beds
1	$N75^0 – N255^0$
2	$N85^0 – N265^0$
3	$N94^0 – N274^0$
4	$N96^0 – N276^0$
5	$N105^0 – N285^0$
6	$N82^0 – N262^0$
7	$N90^0 – N270^0$
8	$N108^0 – N288^0$
9	$N65^0 – N245^0$
10	$N90^0 – N270^0$
11	$N110^0 – N290^0$
12	$N100^0 – N280^0$
13	$N85^0 – N280^0$
14	$N90^0 – N270^0$
15	$N75^0 – N255^0$
16	$N70^0 – N250^0$
17	$N98^0 – N278^0$
18	$N90^0 – N270^0$
19	$N95^0 – N275^0$
20	$N82^0 – N262^0$

Table 2B. Trough cross beds analysis using front Azimuth and its back equivalence and class interval of 30^0

S/No	Class interval	Equivalent	Frequency
1	0 – 30	181 – 210	
2	31 – 60	211 – 240	
3	61 – 90	241 – 270	12
4	91 – 120	271 – 300	8
5	121 – 150	301 – 330	
6	151 – 180	331 – 360	
			Ef = 20

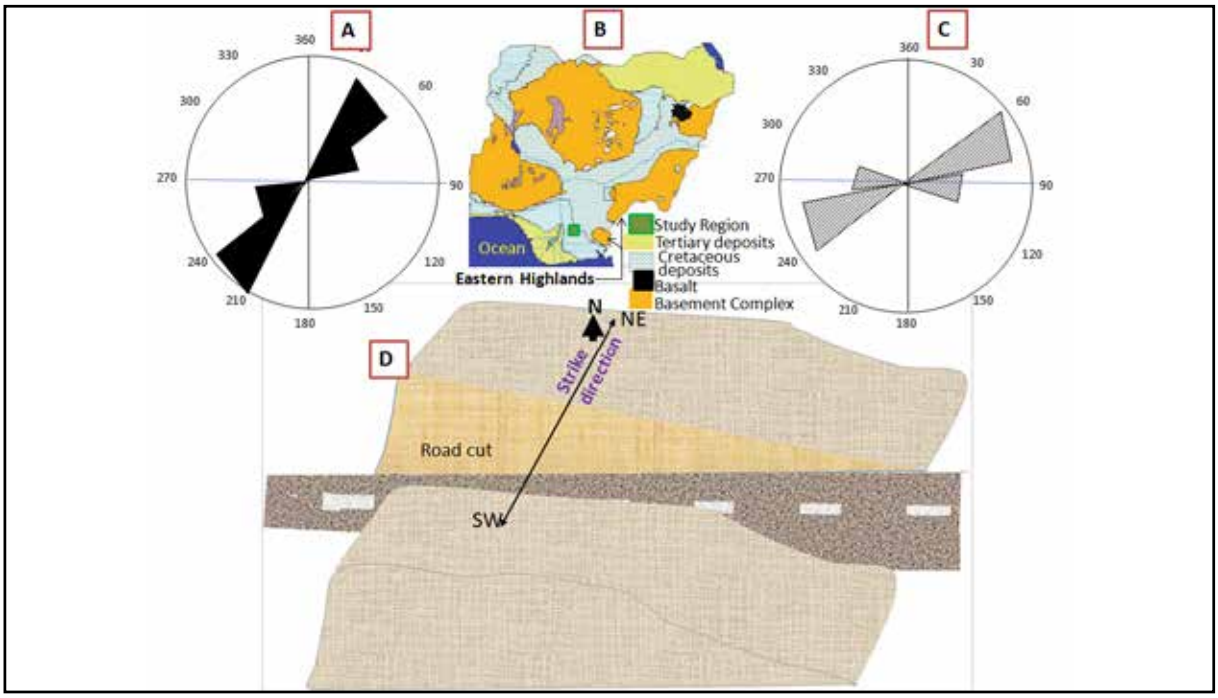

Figure 3. (**A**) Rosette diagram of the planar cross bed Azimuths (**B**) Map of Nigeria showing the generalized geology from Obaje, (2009), and (**C**) Rosette diagram of trough-cross beds (**D**) Schematic representation of the asymmetric form of the Amasiri sandstone ridge showing eastward gentler flank and westward face of steep flank

Locally, thickness of the shales was measured to a mean elevation of about 70 m above sea level at plain/ lowlands. For the sandstone cuestas, the mean thickness is about 100 m (0.1 km) where it usually occurs in ridges, mainly at the type locality around Amasiri area (Figures 1B and 2B), and up to 200 m (0.2 km), mostly at Akpoha area (Figure 2A) where it occurred in isolated hills (Figure 1C). Lengths and widths of the sandstones ridge are greater than 10 km and 0.2 km, respectively at Amasiri area, and at an average of 5 km and 0.25 km for the respective length and width of the cuestas at Akpoha area, hence, amounted to local volume of the resources from a range of 0.2 to 0.25 km³, equivalent to ton register from 70, 600,000 to 88, 300, 000 tons at Amasiri and Akpoha areas, respectively. While bioturbation is prominent on the sandstones around the hills, it is very scanty on the ridges, indicating that the Akpoha sandstones, north of Amasiri sandstone ridge (Figure 2) may have been formed under more anoxic, low energy conditions after high storms under which the ridges were formed had subsided. The ridges are asymmetrical in agreement with Nwajide (2013) who also noted west-facing steeper flank as represented in Figure 3D. The steeper side was possibly created by hitting paleo ripples from the sea, while gentler flank that faces the east showed evidence of the regressive influenced stacking of the sandstones from the eastern highlands. It is noteworthy that the first set of sandstones, deposited at the onset of the regression, that is, the Amasiri sandstones vary slightly in texture from those deposited at the later stage, like the Akpoha sandstones. Table 3 shows a higher percentage of quartz contents ranging from 75 to 81% [across samples NC 12, NC 13, NC 15, NC 16, NC 17 and NC 23] of Akpoha sandstones, than those in NC 05, NC 11, and NC 14 which range from 73 to 75% of Amasiri sandstones. However, based on the smaller number of samples analyzed from the later sandstone units, the quartz content cannot be discriminated as less than the Akpoha sandstones.

Moreover, cementation by quartz at a level greater than 75% is safe to certify the hardness of both sandstone formations. This level of hardness can be attributed to the reason why the sandstones could not be excavated mechanically during road cutting and quarry operations, but rather by blasting via detonation process. On this note, later research can focus on the investigation of the sandstone hardness via P-waves seismic survey to further decipher the rippability, following Kearey et al (2002) who had earlier reported a standard P-wave velocity 2000 ms^{-1} in sandstones rippable by mechanical excavations. It was further explained in the review that sandstones with a velocity greater than the specification require detonation with explosives. Confirmation of the hardness based on seismic velocity will not only certify the engineering application of the sandstones but also determine subsurface depth interfaces with the shales; a relevant condition for foundations/in-situ constructions.

4.2 Petrographic Analysis

Results presented in Figures 4A and 4B and a summary interpretation in Table 3 pointed out that quartz and feldspar comprise the modal mineralogy of the studied sandstones. According to Montgomery (2011), quartz-rich sand is used very largely in engineering construction. The engineering significance of the sandstones was verified based on framework composition, and in particular, the mineral types and shapes via petrographic analysis. This analysis is the best option to investigate the percentage (%) of the mineral contents. The major rock minerals like quartz, feldspars, and calcites have various ranges of resistance to weathering. But then, while quartz is the most resistant, calcite is the least. Thus, the level of aggregation [in percent] of quartz minerals in soils and rocks determines the degree of hardness as a baseline criterion selected for aggregates, chippings, and related building materials.

Discerning that the high quartz content, with the significant presence of feldspars and rock fragments in cleavage association, suspected as rhombohedral (Figures 4A and 4B), as well as the irregular grain shapes, observed under XPL view (Figure 5A), showing intact concave/ convex contacts (Figure 5B), the sandstones can be safely used as aggregates for construction materials. The relevance as aggregates was further verified through the analysis of textural character.y

Table 3. Summary interpretation of the framework composition

Sample code	Quartz %	Feldspar %	RF %	Total %	Interpreted from:
NC 05	73	13	15	100	Fig.4a
NC 11	74	16	10	100	Fig.4a
NC 14	75	15	10	100	Fig.4a
NC 23	78	13	9	100	Fig.4b
NC15	81	12	7	100	Fig.4b
NC13	79	13	8	100	Fig.4b
NC16	81	11	8	100	Fig.4b
NC17	75	14	11	100	Fig.4b
NC12	81	12	7	100	Fig.4b

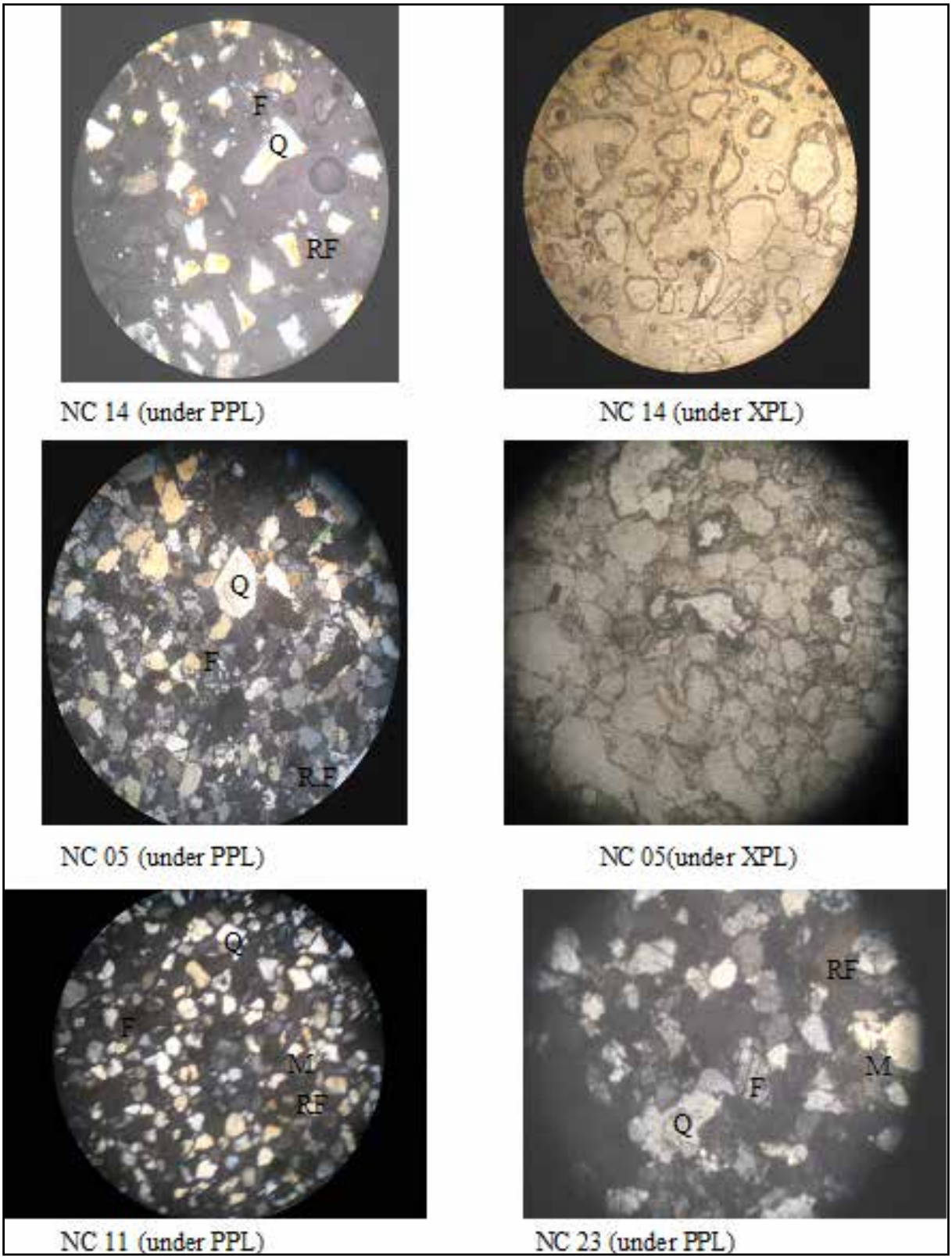

Figure 4A. Photomicrograph of Amasiri Sandstones, comprising mainly of convex to line contact, angular to sub angular grains of quartz [viewed under Meiji monocular microscope with magnification x 200].

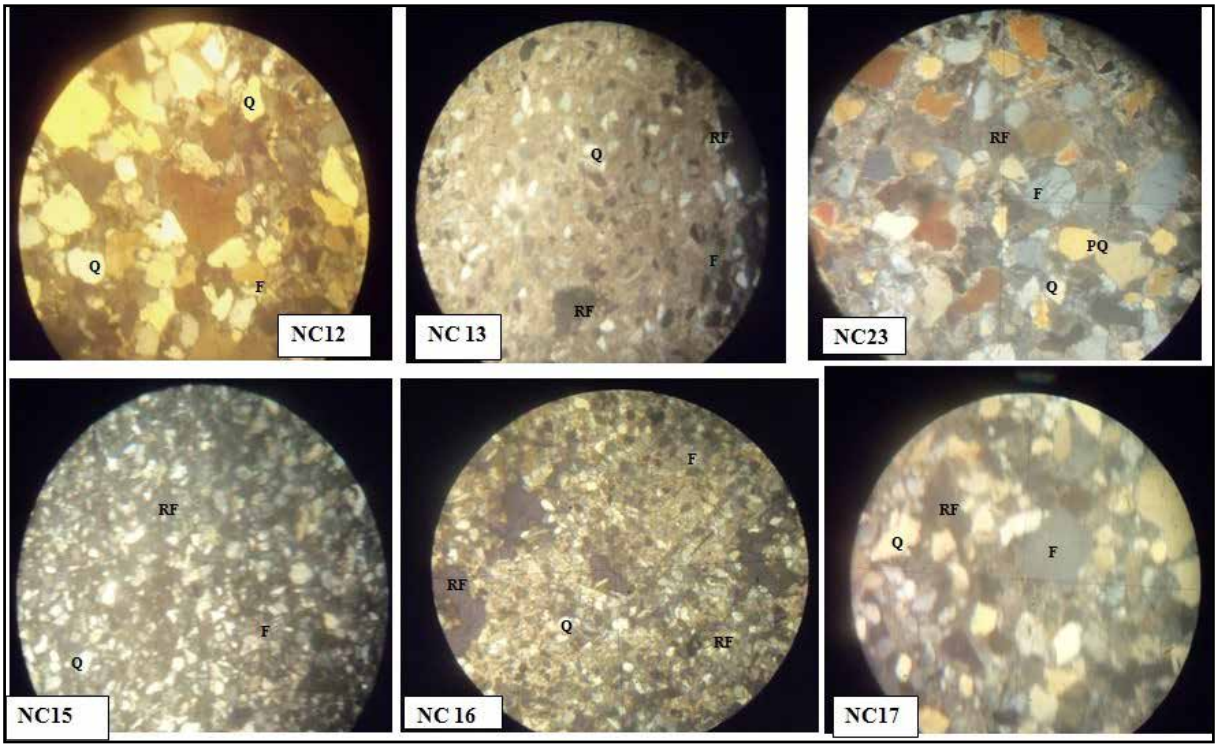

Figure 4B. Photomicrograph of Akpoha Sandstones, comprising mainly of concave-convex, angular to sub rounded grains of crystalline quartz [viewed under Meiji monocular microscope [magnification x 100].

RF= Rock Fragments suspected to constitute mainly of calcites and pyrites

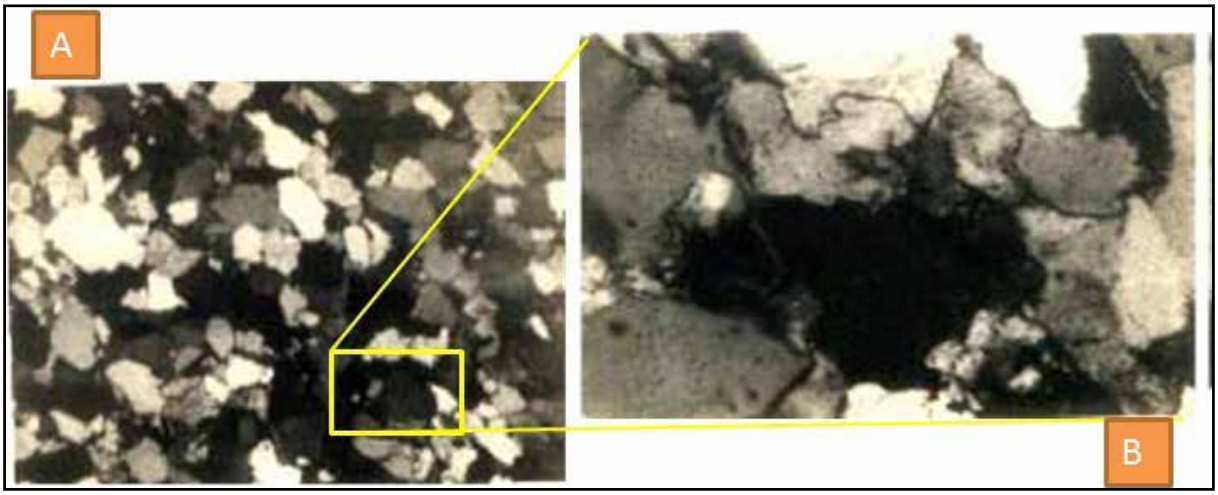

Figure 5. Photograph of the typical Sandstone sample [XPL]; (**A**) showing sub-angular to sub rounded grain shape [Magnification x 200], (**B**) a part visual enhancement showing [Magnification x 400].

4.3 Textural Analysis

The cumulative % and ϕ plotted to produce cumulative frequency curves (Figure 6-8) and the curve values extracted for analysis of the grain size parameters (Equations 1-3) produced the results in Table 5. As seen, the mean grain sizes ranged from 1.0 to 2.1 mm; the degree of sorting from 1.25 to 1.4 mm and peaked (Kurtosis) between 0.9 mm and 1.6 mm (Table 5). Interpretatively, the range of the standard deviation depicted poorly sorted rocks, indicating a mixture of different sizes of grains. Yet, the mean values pointed at the dominance of medium grains with shapes spanning from mesokurtic to leptokurtic curvatures.

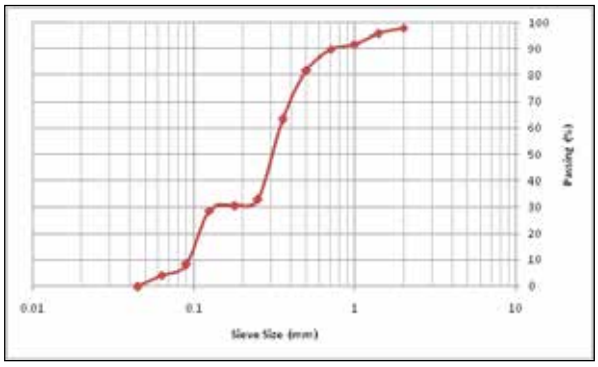

Figure 6. Grain size distribution curve for NC10a

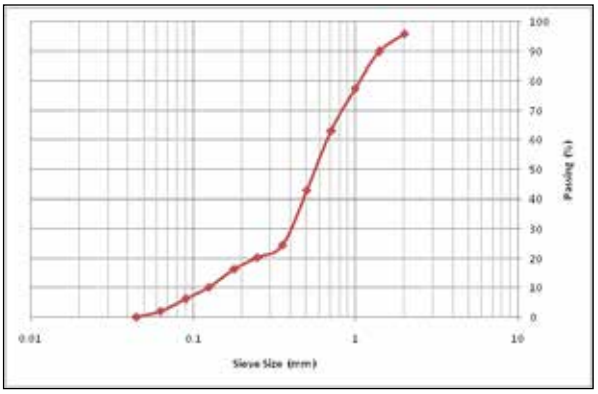

Figure 7. Grain size distribution curve for NC14

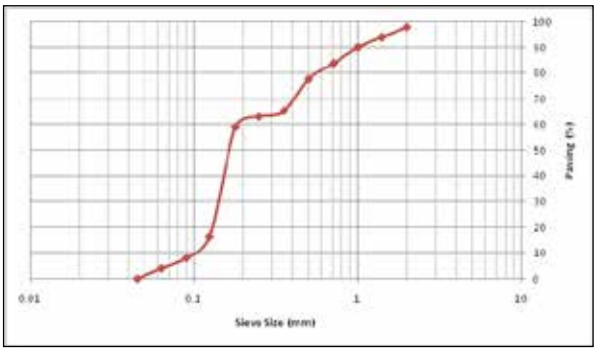

Figure 8. Grain size distribution curve for NC18

Table 4. Summary result of Textural analysis

Sample code	Mean (x)	Standard deviation (sorting)	Kurtosis
NC10a	2.0	1.25	0.953
NC14	1.0	1.4	1.640
NC18	2.1	1.35	1.077

5. Discussion

The percentage of silica-rich quartz in the sandstones certifies a high siliceous nature. According to Earle (2019), strong covalent and ionic bonding characteristics of silica tetrahedron generated hardness in quartz. The hard nature reflects compressive strength which varies in sandstones from 20 MPa to 170 MPa, depending on conditions due to digenesis and depositional environment, as well as the effect of weathering which depreciates the strength towards the lower limit. Having reviewed earlier that the studied sandstone belongs to the Ezeaku Group, the strength is therefore within the specified range; following Ukpai (2020) who studies the stability of the entire [Ezeaku] Group in the adjoining region and claimed that the bedrocks were slightly weathered, upon which the compressive strength was somewhat greater than 20 MPa. Grouping the sandstones at such a strength level of about 20 MPa reflects toughness:

Even as the sandstones sandwich shell hash debris in some places (Okoro et al., 2016), the macroscopic view was minimal during field inspection. It was observed in the present study that the calcareous portion behaves as diatomaceous earthen though it appeared insignificant, perhaps due to the minor alteration effect of the localized fossilized shells. This may subject the silica-rich quartz to possible alkali-silica reactivity. This reaction can be triggered if aggregates, processed from the rock mass, are exposed to agents of chemical activities, and moisture in particular. According to Yasir et al. (2018), damage due to the alkali (NaOH) reaction decreases the compressive strength. It means that the sandstone quality is certified for the production of aggregates used as construction materials should be supplemented by mixing concretes with adequate Portland cement [measured to compressive strength greater than 20MPa]. Furthermore, the aggregate product used in [walkway, runway, and driveway] pavements should be tarred at the surface to seal off moisture, as well as other chemical agents that may be aided by climatic conditions. These precautions will prevent sorts of degradations that can jeopardize the characteristic hardness found in the sandstones. The level of hardness and intact nature is relatively proved by the difficulty to breaking with sledge sledgehammer, coupled with the fact that the rock mass can only be extracted in-situ by blasting or detonation process. There is no doubt that the sandstones can withstand pressure when subjected to industrial crushing process to obtain desired aggregate sizes.

The reserve relevance is highly based on the proximity of the sandstone resources for marketing. Large areal extent of the outcrops, which can be suitable for budget friendly open blast mining via explosive devices, grade with respect to the local resource volume, as well as optimum quality in terms of efficient crushing strength which can raise social (enthusiastic) acceptability against the earlier negative perception. The reason for the acceptability is mainly because the aggregates cannot split into pieces when compressed into concretes, packed at pavement sub-base after rigorous exposures to loads of roller compaction which is a necessary process in road construction. This fact was supported by the modal mineralogy of the sandstones though usually controlled by quartz as also demonstrated in this study; yet quartz rich-rocks are vulnerable to thermal expansivity, but the considerable percentage of feldspar observed in the photomicrographs (Figs. 4a and b) is significant to balance the expansive characteristic because feldspar minerals are more resistant to the thermal effects. Based on this assertion, aggregates produced from the sandstone deposits can be resistant to chemical and thermal degradations.

Low water absorption of produced aggregates was suspected to enhance the mechanical property as the sandstones are devoid of coarse grain sizes that could have increased apparent porosity. Furthermore, as microstructures of coarse aggregates affect the strength of concretes (Petrounias et al., 2018), little or complete absence of the microstructures has been suspected because the studied sandstones are dominated by statistical [mean] values indicating medium grains (Table 4). Thus, finding the mineralogy has confirmed fabrics of aggregates produced from Amasiri sandstones as efficient construction materials in concretes and sub-base of road pavements. This study has, therefore, demonstrated that risk analysis of any rock potential for stable aggregates. Materials should begin with the identification of individual mineral components of aggregates used in the construction of the concerned infrastructure: an innovating efficacy just found in petrographic analysis when used for the verification of aggregate strength.

6. Conclusions

The engineering importance of consolidated sandstones was evaluated, to resolve probable perceptions that the quality is low for aggregate production. The study was applied in the Afikpo Basin where the sandstone deposit is massive in consolidated form by ridges along NE-SW trend and overlay shales, both constitute the Ezeaku Group of the Turonian age. Although, the sandstones are mainly distinguished in two litho-facies, the Akpoha and Amasiri Formations, the textures are similar with dominant medium grain sizes but slight variations in micro-facies. While concave-convex, angular to sub-rounded grains of crystalline quartz characterized the Akpoha sandstones, the micro-facies changed to convex-line contact, angular to sub-angular quartz grains in the Amasiri Formation. These textural and mineralogical characters resulted in hardness, such that the sandstones are relatively not rippable but still chippable via blasting/ detonation, hence, they can be mined by open pit method as aggregates of certified high quality, particularly for use in concretes and sub-base of roads pavements. The mineralogy also showed that the aggregate is not susceptible to thermal expansion.

Acknowledgment

The authors are grateful to the Laboratory attendants and Technologists of the Geology Laboratories of Kogi State University, Anyingba, Kogi State; and Ebonyi State University, Abakaliki, Ebonyi State where the sandstone samples were cut into thin sections and viewed under the microscope, respectively. We, the authors appreciate the erudite editors and reviewers of JJEES for the time devoted to the contributions that have enhanced the quality of the manuscript.

References

Bamigboye, G.O., Michaels, T., Ede, A., Ngene, B.U., Nwankwo, C and Davies-Iyinoluwa, E.E.(2019). The role of construction materials in building collapse in Nigeria: A review. Journal of Physics Conference Series. 1378(4): 042022

Durotoye, B (2003). Sourcing of raw materials for the building and construction Industries in Nigeria. In A.A Elueze (Ed): Contribution of Geosciences and Mining to National development. Nigerian Mining and Geosciences Society (NMGS), pp.83 – 88.

Earle, S. (2019). Physical Geology – 2nd Edition. Victoria, B.C.: BCcampus. ISBN978-1- 77420- 028-5. Retrieved from https://opentextbc.ca/physicalgeology2ed/.

Ghrair, A. M., Said, A.J., Al-Kroom, H., Al Daoud, N., Hanayneh, B., Mhanna, A and Gharaibeh, A (2023). Utilization of Jordanian Bentonite Clay in Mortar and Concrete Mixtures. Jordan Journal of Earth and Environmental Sciences, 14(1): 19-29.

Hoque, M. and Nwajide, C.S. (2002). Tectono sedimentological evolution of an elongated intracrationic basin (aulacogen. The case of the Benue Trough Nigeria). Journal of Minning and Geology, 21, 119 –126.

Hussain, J., Zhang, J., Fitria, F., Shoaib, J., Hussain, H., Asghar, A. and Hussain, S. (2022). Aggregate Suitability Assessment of Wargal Limestone for Pavement Construction in Pakistan. Open Journal of Civil Engineering, 12, 56-74. https://doi.org/10.4236/ojce.2022.121005

Kearey, P., Brooks, M., Hill, I (2002). An introduction to geophysical exploration, 3rd ed., Blackwell Science, Oxford, London, pp.262.

Maricic, A (2014). Influence of the properties of Benkovac natural stone on its durability. Doctoral work. Zagreb publications, Faculty of Mining Geology and Petroleum Engineering, University of Zagreb, pp.166.

Mohamed, K. K and Abdulkader, M. A (2010). Lithostratigraphy and Microfacies Analysis of the Ajlun Group (Cenomanian to Turonian) in Wadi Sirhan Basin, SE Jordan. Jordan Journal of Environmental Earth Science, 3(1):1-16. https://jjees.hu.edu.jo/files/v3n1/Lithostratigraphy%20and%20Microfacies

Nwajide C.S (2013). Geology of Nigeria's sedimentary basins. CSS Press, Lagose, pp. 565.

Obaje, N.G. (2009). The Benue Trough. In: Geology and Mineral Resources of Nigeria. Lecture Notes in Earth Sciences, vol. 120. Springer, Berlin, Heidelberg. https://doi.org/10.1007/978-3-540-92695-6-5.

Okogbue, C.O and Ukpai, S. N (2013). Geochemical evaluation of groundwater quality in Abakaliki area, Southeast, Nigeria. Jordan Journal of Earth and Environmental Sciences 5(1), 1-8. ISSN 1995-6681

Okoro AU, Onuigbo EN, Akpunonu EA, Obiadi II (2012) Lithofacies and pebbles morphogenesis: key to paleoenvironmental interpretation of Nkporo Formation, Afikpo sub-Basin, Nigeria. Journal of Environment and Earth Science, 2: 26–38

Okoro, A (2016) Sedimentary and petrofacies analyses of the Amasiri Sandstone, southern Benue Trough, Nigeria: implications for depositional environment and tectonic provenance. Journal of African Earth Science, 123: 258–271.

Okoro, A.U., Igwe, E.O. and Umo, I.A (2020). Sedimentary facies, paleoenvironments and reservoir potential of the Afikpo Sandstone on Macgregor Hill area in the Afikpo Sub-basin, southeastern Nigeria. SN Applied Science, 2, 1862. https://doi.org/10.1007/s42452- 020-03601-5

Orife, M.J (2003). Construction materials and sustainable national development. In A.A Elueze (Ed): Contribution of Geosciences and Mining to National development. Nigerian Mining and Geosciences Society (NMGS), pp.89–91

Petrounias, P., Giannakopoulou, P.P., Rogkala, A., Stamatis, P.M., Lampropoulou, P., Tsikouras, B. and Hatzipanagiotou, K. (2018). The effect of petrographic characteristics and physico-mechanical properties of aggregates on the quality of concrete. Minerals, 8: 577. doi: 10.3390/min8120577

Rehman, G., Zhang, G., Rahman, M.U., Rahman, N.U., Usman, T. and Imraz, M. (2020). The Engineering Assessments and Potential Aggregate Analysis of Mesozoic Carbonates of Kohat Hills Range, KP, Pakistan. Acta Geodaetica et Geophysica, 55, 477-493. https://doi.org/10.1007/s40328-020-00301-9.

Shah, S., Bin, D. O., Hussain, J., Hussain, K., Asghar, A., Hussain, H. and Rahman, A. (2022) Physio-Mechanical Properties and Petrographic Analysis of NikanaiGhar Limestone KPK, Pakistan. Open Journal of Civil Engineering, 12: 169-188.

Ukpai, S. N. (2020). Stability analyses of dams using multidisciplinary geosciences approach for water reservoir safety: case of Mpu Damsite Southeastern Nigeria. Bulletin of Engineering Geology and the Environment 80(3), 2149–2170. https://doi. org/10.1007/s10064-020-01977-7

Ukpai, S. N., Ojobor, R. G., Okogbue, C. O., Nnabo, P. N., Oha, A. I., Ekwe, A. C. & Nweke, M. O. (2021). Socio-economic influence of hydrogeology in regions adjoining coal bearing formation: water policy in Anambra Basin.Water Policy 23(3) 654–683.

Yasir, S.F., Awang, H and Ayub, M.I.H (2018). The relationship of sandstone's strength with mineral content and petrographic characteristics in Sungai Tekai, Jerantut, Pahang AIP Conference Proceedings. https://doi.org/10.1063/1.5062636

JJEES

JJEES (2024) 15 (4): 275-286
ISSN 1995-6681

Jordan Journal of Earth and Environmental Sciences

Using fuzzy Logic Method and Analytic Hierarchy Process to Mineral Potential Mapping in Janja Exploration Area (South of Nehbandan, Iran)

Nima Rahimi[1], Fariba Kargaranbafghi[2*], Mojtaba Rahimi Shahid[3], Shima Afkhami[4]

[1]Department of Geology, Faculty of Sciences, University of Tehran, Tehran, Iran
[2]Assistant professor in Tectonic Geology, Faculty of Science, Yazd University, Yazd, Iran
[3]Department of Geology, Faculty of Sciences, Ferdowsi University of Mashhad, Mashhad, Iran
[4]Department of Geology, Faculty of Sciences, Shahid Beheshti University, Tehran, Iran

Received on November 30, 2022; Accepted on November 6, 2024

Abstract

This paper describes the application of the knowledge-based fuzzy logic and analytic hierarchy process (AHP) method,integrate various exploratory geo-datasets. This application helps prepare a mineral potential map (MPM) for copper and gold exploration and determine the optimal drilling locations in the Janja exploration area. Accordingly, different exploration layers were derived from geological, geochemical, and geophysical data, including lithology, structural, alteration, copper and gold geochemical anomaly, and magnetometric geophysical layers. After obtaining normalized weights, different fuzzy operators tried combining the weighted evidential layers into potential maps. The exploration layers were prepared and weighted and then combined by fuzzy logic methods and the Analytic Hierarchy Process, finally providing the mineral potential map of the study area. According to the MPM, the high potential zones in terms of mineralization and exploration potential are the area's north and center, corresponding to diorite and granodioritic intrusions. To evaluate the performance and applicability of the approach, the productivity of the 12 drilled boreholes (Cu and Au concentration) are compared to produced MPMs. The verification results showed that AHP and fuzzy logic methods had 62.5% and 54.17% overlap with MPMs, respectively, indicating that the AHP method performed better than fuzzy logic. The prediction based on the AHP method is more accurate and can provide directions for future prospecting. Eventually, optimal drilling locations for future exploration activities were presented.

Keywords: *Analytic Hierarchy process, Exploration, Fuzzy logic, Iran, Janja, Potential Mapping.*

1. Introduction

One of the most useful tools in mineral exploration is exploratory studies using Geographic Information System (GIS). The use of this science enables the preparation and integration of different information layers in the framework of various models. It also helps organize information related to the exploration of mineral reserves (Bonham-Carter, 1994). In fact, GIS creates a suitable space to access mineral information and data analysis and determine potential exploration areas by creating a suitable database. Simultaneous access to all geological and mineral information of the region in preliminary, detailed, and semi-detailed explorations helps determine the best areas for exploration through an analysis of these data and avoids the waste of time and budget (Bonham-Carter, 1994). Thus, various methods of modeling and integration information layers are used to obtain suitable results when determining potential exploration areas, particularly, appropriate locations for detailed exploration investigations (Malczewski, 1999). Nowadays, geoscience and exploration researchers typically use Geographical Information Systems (GIS) to prepare mineral potential maps (MPM). MPM is a Multi-Criteria Decision Making (MCDM) task that prioritizes mineralized areas from high to low potential through methodologies that deal with data fusion problems. Some of these studies include An et al. (1991), Mukhopadhyay et al. (1996), Carranza and Hale (2001), Carranza (2002), Porwal et al. (2003), Ranjbar and Honarmand (2004), Porwal (2006), Karimi et al. (2008), Carranza (2010), Madani (2011), Pazand et al. (2012), and Abedi et al. (2013). These researchers have used GIS to integrate exploration data and prepare mineral potential maps. The integration of GIS and the analytic hierarchy process (AHP) are a powerful tools to solve the potential mapping problem (Carranza, 2008; Pazand et al., 2011). AHP and fuzzy logic is a decision analysis method that considers both qualitative and quantitative information and combines them by decomposing ill-structured problems into systematic hierarchies to rank alternatives based on a number of criteria (Chen et al., 2008; Srdjevic and Medeiros, 2008; Minatour et al., 2012). In addition to finding the potential of minerals, these two methods can also be used to find underground water and the potential of areas prone to landslides and soil erosion (Al-Sababhah and Al maqablah, 2023; Karimi-Sangchini et al. 2020; Mahfoud et al. 2024). In general, the main steps to prepare a mineral potential map include determining

* Corresponding author e-mail: fkargaran@yazd.ac.ir

mineralization detection factors, preparing information and factor maps, integrating the maps, and evaluating the results (Carter, 1994; Karimi et al., 2008). The high potential of the Au-Cu mineralization and the lack of studies in generating mineral potential maps in this region motivated us to construct geospatial datasets for detailed exploration. This research has weighed the information layers and mineralization evidence while applying the combined method of fuzzy logic and analytic hierarchy process (AHP) to the mineral potential mapping of the Janja exploration area (South of Nehbandan-Sistan and Baluchistan) and determine the optimal drilling locations.

2. Geographical Location

The Janja exploration area with an area of 138 km^2 is located 70 kilometers south of Nehbandan and 210 kilometers north of Zahedan at the geographical coordinates of 60 ◦23″ longitude and 31 ◦7″ latitude. This area includes parts of the geological maps of 1:250000 Zabul (Alavi Naeni et al., 1988) and 1:100000 Khunik (Eftekharnejad et al., 1990) and is located in the structural zone of eastern Iran (Sefidabe Basin) and under the Zabul-Zahedan-Saravan zone, according to the structural zoning map of Iran (Nabavi, 1976; Aghanbati, 2004). The Nehbandan-Zahedan route can be used to access this exploration area (Figure 1).

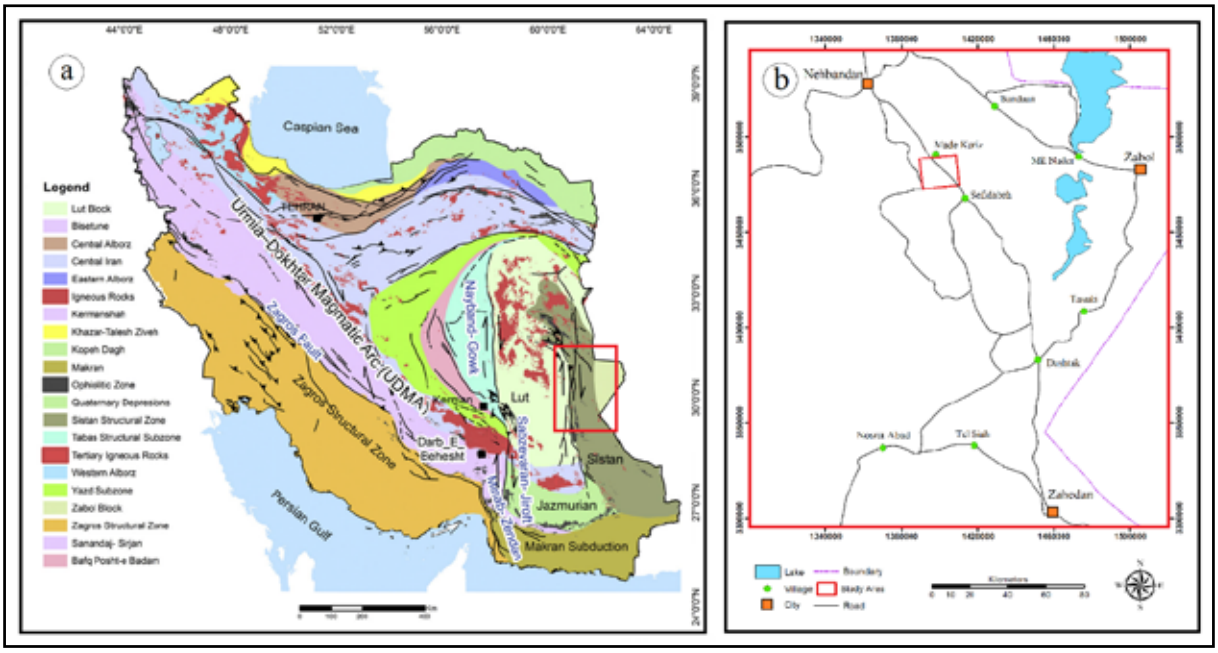

Figure 1. a) Geographical location of study area in the geological map of Iran, and **b**) Access routes to study area

3. Geological Setting

In general, the rock units of the Janja exploration area include sedimentary rocks of Upper Cretaceous to Paleocene age (turbidites and Sefidabe formation) and semi-deep igneous rocks (Figure 2). The sedimentary rocks of this area include sandstone, calcareous sandstone, shale, siltstone and pyroclastic and turbidite sediments. Semi-deep igneous rocks in this area include diorite to quartz diorite and granodiorite, intruding into the volcanic units and flysch structures (Bazzi et al., 2013). Intrusion of these intrusive bodies into the sedimentary and volcanic units of the flysch facies has led to contact metamorphism and alteration and subsequently the mineralization of copper, gold, and other valuable elements (Rahimi et al., 2022). Hypogene mineralization has occurred mainly in the form of pyrite and a slight amount of chalcopyrite, galena, and sphalerite, while supergene mineralization can also be recognized by iron oxides. Propylitic alteration is the most widespread type of alteration in the area, and Skarn zone is also locally evident in the region. It seems that the alteration and mineralization in this area is related to the intrusion of igneous intrusive bodies, and the creation of contact metamorphism and hydrothermal processes is associated with the porphyry dykes, observed in the region. Based on the mineralized samples taken from this area, the maximum grades are 60.67 ppb, 180.4 ppm, 12285 ppm, 99260 ppm, and 109300 ppm for gold, silver, copper, lead, and zinc, respectively. Based on geological studies and field observations, the mineralization in this area includes hydrothermal polymetallic veins, observed together with silica veins (Elyaspoor, 2010). The main minerals identified in these veins include galena, sphalerite, chalcopyrite, and chalcocite (Bazzi et al., 2009). The length of these mineral veins varies from 100 to 110 meters and often have a vertical dip. The thickness of the veins varies from 10 centimeters to 2 meters, and their trend can be traced up to a maximum of 200 meters. According to the studies carried out in Janja area, polymetallic mineralization of gold, silver, copper, lead, and zinc veins has obviously occurred in this area (Rahimi et al., 2020).

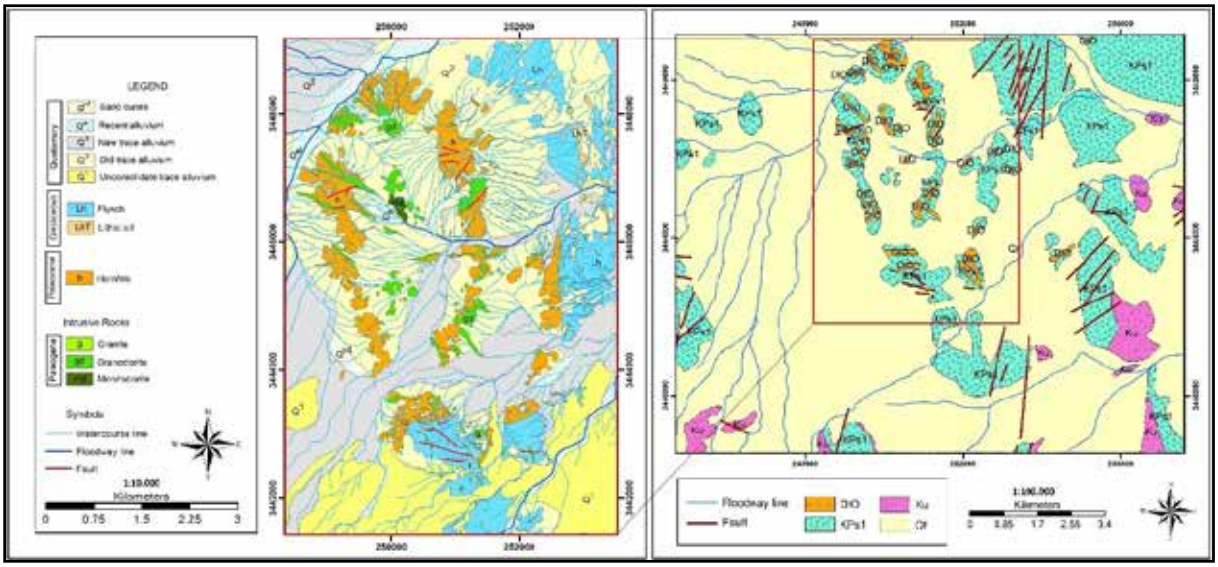

Figure 2. Geological map of Janja exploration area (Rahimi et al., 2020)

4. Materials and Methods

The current research has used library, field, and laboratory studies to collect basic information. Geological maps, satellite images, digital elevation maps, and related sources were used to extract active faults and accurately identify lithological units. Remote sensing studies, conducted on ASTER sensing images, were used to reveal argillic, propylitic, and phyllic changes, while Landsat 7 images were utilized to highlight iron oxide changes and prepare the alteration map of Janja area. The magnetometry geophysical method was employed to investigate changes in the intensity of the total magnetic field and the potential of the exploration area concerning the presence of mineral deposits. The results of geochemical sampling of 153 stream sediment samples were utilized to prepare geochemical anomaly map of copper and gold in the area, after which data preparation and analysis were conducted by ArcGIS 10.8 software. Different exploration layers were initially prepared by this software, followed by combining these layers with two methods of fuzzy logic and analysis hierarchic process. Finally, the mineral potential map of the area was prepared to determine the optimal drilling locations. Figure 3 summarizes the research methodology.

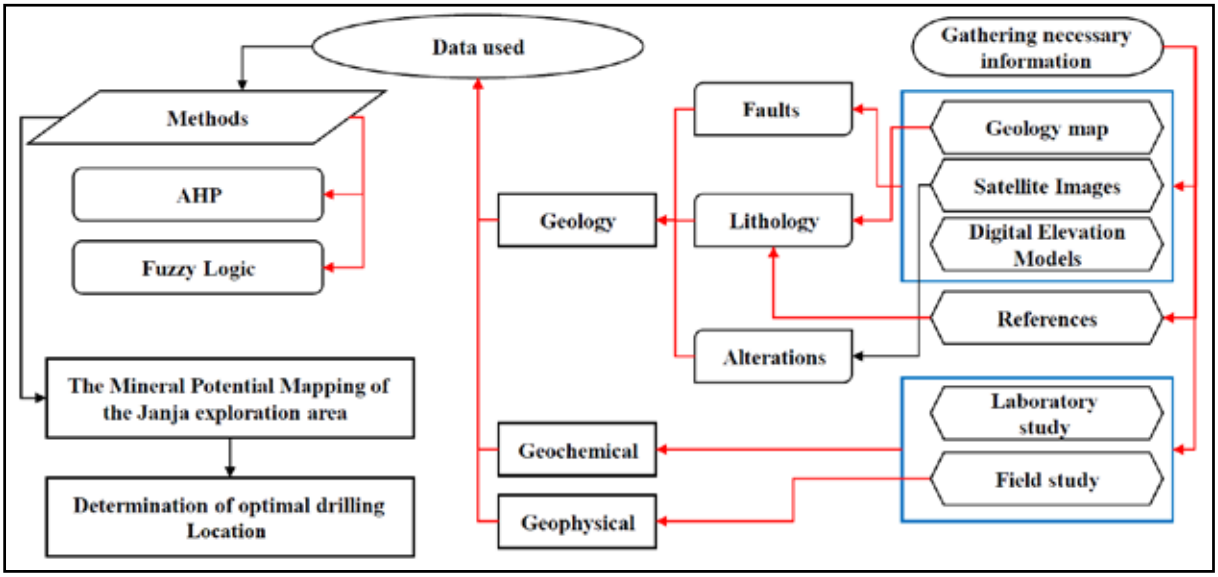

Figure 3. Research Methodology

5. Preparation of Evidential Layers Characteristics and Classification of Evidential Layers

Exploration layers effective in mineralization were determined at this step according to the geological and exploration features of the study area and using expert knowledge. These exploration layers are separated and extracted from geological maps, satellite, geochemical, geophysical data, and field studies. The prepared information layers included lithology, structural, alteration, copper-gold geochemical anomalies, and magnetometric geophysical anomalies. Each exploration layer was divided into several classes based on priority. The mineral potential map was prepared by a combination of the information layers according to the effects and values of the layers. The impact of information layers is not the same in the final model, because it is necessary to prepare weighed maps of

each information layer through a series of processes such as preparation of a buffer, reclassification, and rasterization of the maps. Then, the effective factors in weighing different exploration layers were described.

5.1 Lithological Layer

Based on the geological studies and field observations, conducted in Janja exploration area, four lithological units were found to have outcrop in this area, including semi-deep intrusive units (DIO), Cretaceous flysch unit (Ku), volcanic and pyroclastic rocks (KPS), and Quaternary unit (Qt) (Figure 4). According to field observations, the Cretaceous flysch unit acted as the host rock in the area and was cut by a semi-deep intrusive diorite body. Different rock units were finally weighed based on their importance in mineralization. The highest weight was considered for intrusive and flysch units due to the presence of mineralization in the adjacent areas of these two lithological units in Janja exploration area. Other lithological units of the region did not contribute significantly to mineralization and were assigned the lowest weight. Figure 11 presents the scoring method for these lithological units.

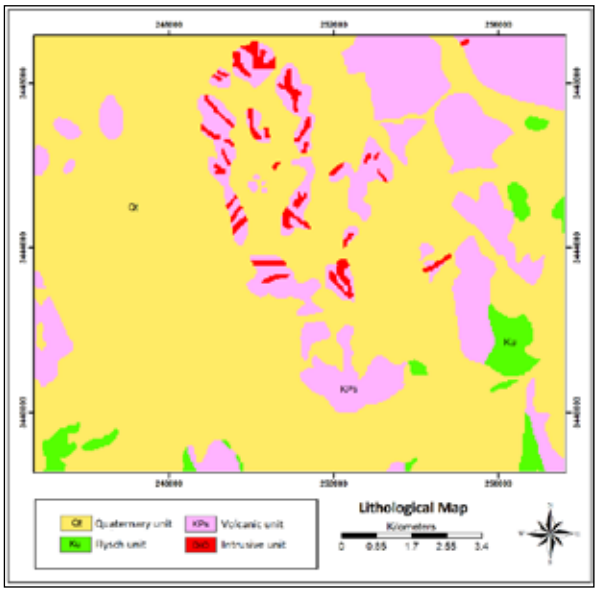

Figure 4. Lithological layer in the study area

5.2 Alteration Layer

Remote sensing studies were used on ASTER sensor images to reveal argillic, propylitic, and phyllic alterations, while Landsat 7 images were utilized to reveal iron oxide alterations and prepare the alteration map of Janja exploration area. The band ratio method was to reveal regional alterations. ASTER sensing band ratio of 7/5 was used to reveal argillic changes (kaolinite), and the ration of 3/1 from the Landsat image 7 was utilized to detect iron oxide alterations (hematite, limonite, and goethite). Besides, ASTER sensing band ratios of (9+7)/8 and 7/6 were considered to reveal propylitic (chlorite and epidote) and phyllic alterations, respectively. Finally, all these alterations were merged, forming the map of alterations in the region (Figure 5), after which these alterations were weighed according to their relationship with mineralization. Figure 11 provides the method of scoring this exploration layer.

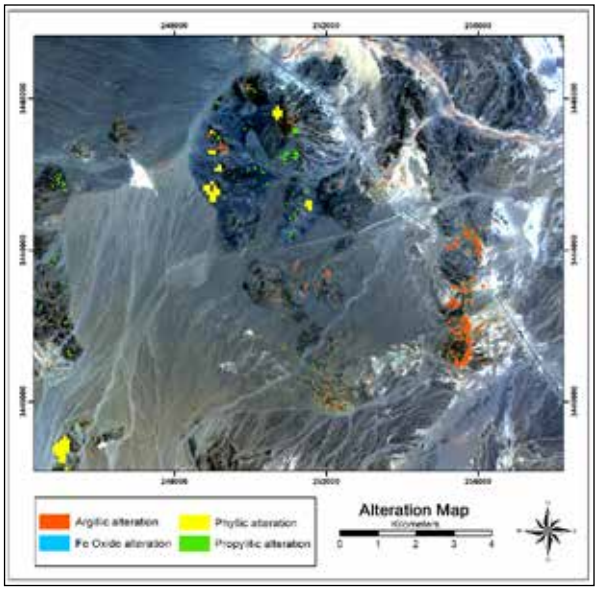

Figure 5. Alteration layer in the study area

5.3 Magnetometric Geophysical Anomaly Layer

The magnetometric geophysical method was used to investigate changes in the intensity of the total magnetic field and examine the potential of this exploration area in terms of mineral deposits. Therefore, 110 profiles with east-west and 2 profiles with north-south direction underwent magnetometry, and a total of 18115 points were measured for the intensity of the total magnetic field. A map of the total magnetic field intensity of the study area was, then, prepared after the data collection and modification (Figure 6). Then the intensity of the magnetic field was divided into 5 classes and weighed. Figure 11 presents the scoring and classification of the total magnetic field geophysical map.

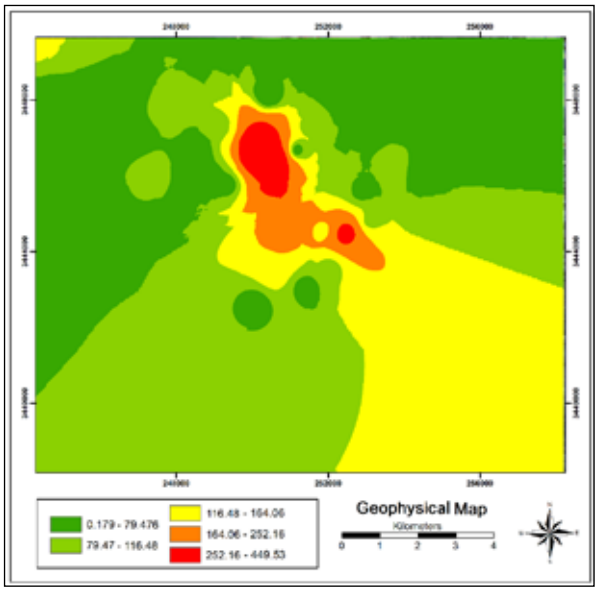

Figure 6. Geophysical layer in the study area

5.4 Geochemical Anomaly Layer

The results of geochemical sampling of 153 stream sediment samples in the region were used to prepare the geochemical map of copper and gold anomaly. Figures 7 and 8 show the location of the collection of stream geochemical samples. The construction of this exploration layer aims to figure out the behavioral patterns of copper and gold

elements in the sampling environment and to separate anomaly values related to mineralization. The isoplethic map of copper and gold elements was initially prepared (Figures 7 and 8). Then, the background, threshold limit, and anomaly values of the selected elements were calculated, using the threshold limit estimation method based on the mean values of X and the standard deviation of S. The formula (X+nS) was used to separate the anomaly from the background limit values. Accordingly, X+S was considered the threshold, and values higher than that represented different degrees of anomaly. Hence, the copper and gold geochemical anomaly maps were divided into 5 classes, assigning the highest and lowest weights to the highest-and lowest-grade elements, respectively. Figure 11 shows the scoring and classification of the copper and gold geochemical anomaly maps.

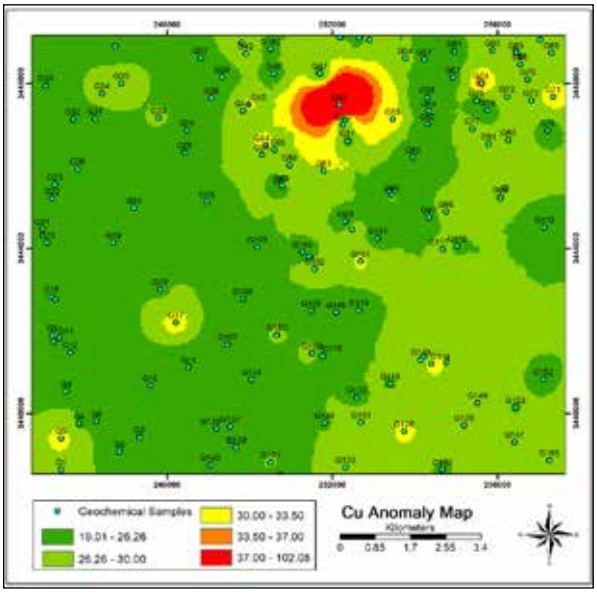

Figure 7. Geochemical layer of Cu in the study area

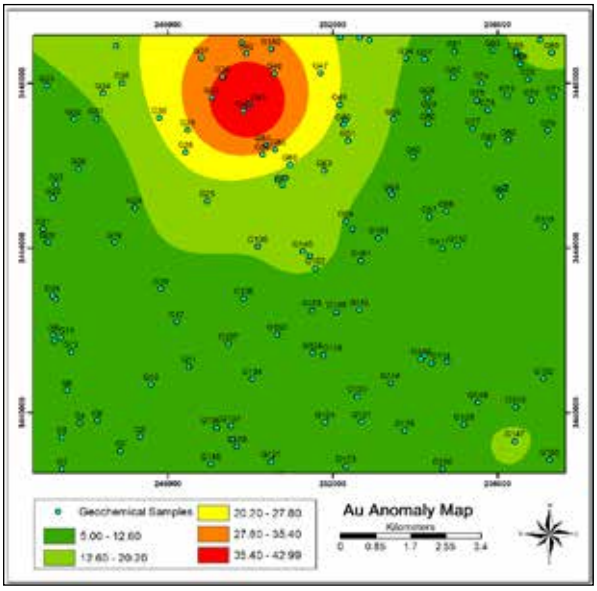

Figure 8. Geochemical layer of Au in the study area

5.5 Structural Layer

The 1:100000 geological map of Khunik and the 1:10,000 mineralogical geological map of Janja exploration area were used to prepare the map of the faults in the studied area. The faults in the study area were initially digitized, after which the 500-meters area around the main faults were divided into 6 classes at 100-meter intervals (Figure 9). Given the investigation of geochemical, geophysical, and geological anomalies, it seems that the faults in the area have occurred after mineralization, which means that this exploration layer should be given the lowest score. Next, an information layer related to faults was created by scoring each class (Figure 11).

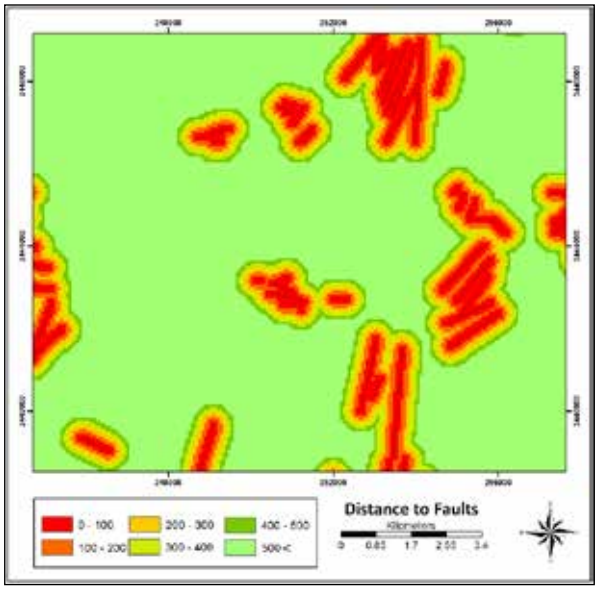

Figure 9. Structural layer in the study area

6. Results and Discussion

6.1 Analytic Hierarchy Process (AHP)

The AHP is one of the multi-criteria decision-making methods based on the relative evaluation of weights (Jiajin, 1997; Saaty, 2001). Similar to the decision theory and inconsistency analysis, this method performs measurement on quantifiable and non-objective criteria (Vargas, 1990). From the viewpoint of the founder of fuzzy logic (Saaty, 1980), this method has several advantages, including unity, complexity, cross correlation, hierarchical structure, measurement, consistency, integration, balance, collective judgment, and repetition. This method is based on pairwise comparisons of factors and allows decision makers to examine different factors while making it possible to consider different quantitative and qualitative criteria in the problem (Ngai, 2003). AHP has been proposed based on human brain analysis for complex and fuzzy problems (Chen, 2001) and includes three main steps of generating hierarchy, determining priorities, and logical compatibility (Macharis et al., 2004; Ghodsipour, 2009). This method has had recently extensive applications for the analysis of complex problems in mining, civil engineering, and geological sciences (Rahimi Shahid and Rahimi, 2016 & 2017; Rahimi Shahid et al., 2019). The AHP steps (Carranza, 2009) are presented in the following to prepare an exploration potential map and determine the areas prone to mineralization in Janja exploration area.

6.1.1. Development of AHP

The hierarchical structure is a graphical representation of a complex problem with at least three levels, at the top of which is the overall goal, and at the next levels, there

are criteria, sub-criteria, and options (Dagdeviren, 2008; Vahidnia et al., 2009). Figure 10 shows the hierarchical structure of the exploration layers of the Janja exploration area, presenting a four-level hierarchy of goal, criterion, sub-criteria, and options. Converting the topic under investigation into a hierarchical structure is the most important part of hierarchical analysis because the process of hierarchical analysis involves breaking down difficult and complex problems into partial elements that are hierarchically related and connecting the main goal of the problem to the lowest level of the hierarchy. Hence, the problem is changed into a simpler form consistent with the human nature and mind (Cimren et al., 2007).

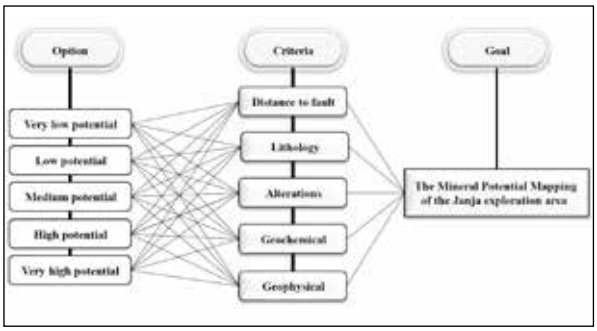

Figure 10. Hierarchical structure for mineral potential mapping in Janja exploration area.

6.1.2. Weights of Evidential Layers

After breaking down the problem into hierarchies, the elements of different levels are compared pairwise and valued based on the importance of the two criteria (Carranza, 2008). In other words, the weighing criterion for information units is based on the highest contribution of factors within the layer (Lopez and Zink, 1991). Table 1 provides the values of preferences for pairwise comparison of factors according to the importance of two criteria in the study area (Saaty, 1980).

Table 1. Preference values for pairwise comparisons (Saaty, 1980)

Verbal	Numerical
Same Importance	1
ModerateImportance	3
Strong Importance	5
Very Strong Importance	7
Absolut Importance	9
Intermediate Values	2; 4; 6 and 8

6.1.3. Preparation of Pairwise Comparison Matrix

The pairwise comparison method was used in this step to create a 5×5 matrix, after which different criteria were compared one by one, and the corresponding values were assigned based on the Saaty screening (Table 2).

Table 2. Pairwise comparison matrix for AHP

Criteria	Geochemical	Alterations	Geophysical	Lithology	Distance to fault	Weight
Geochemical	1	3	6	7	8	0.510
Alterations	0.33	1	4	5	7	0.272
Geophysical	0.16	0.25	1	4	5	0.126
Lithology	0.14	0.2	0.25	1	3	0.059
Distance to fault	0.12	0.14	0.2	0.33	1	0.033
Sum	1.75	4.59	11.45	17.33	24	1

The geometric mean of each row of the matrix was divided by the sum of the geometric mean of the columns to calculate the weight of each criterion. The resulting value for consistency ratio (CR) in the matrix was 0.09, indicating an acceptable level of weighing results. CR is a consistency index from a pairwise comparison matrix, which is randomly generated and has a value depending on the number of elements and their values. A CR value of <0.1 indicates an acceptable level of consistency in the pairwise comparisons; otherwise, the values of the ratio represent inconsistent judgments (Dey and Ramcharen, 2000).

According to investigations, the two factors of (copper-gold) geochemical anomaly and alteration were the most important influencing criteria in increasing the mineral potential of the region with weights of 0.510 and 0.272, respectively. Figure 11 shows the classification of the layers and weighing different categories due to the large number of calculations and paired matrices. Figure 11 shows the inconsistency ratio for the matrix rank of five effective factors, confirming their consistency. Finally, after the processing was performed, the exploration potential map was prepared using the AHP method (Figure 12).

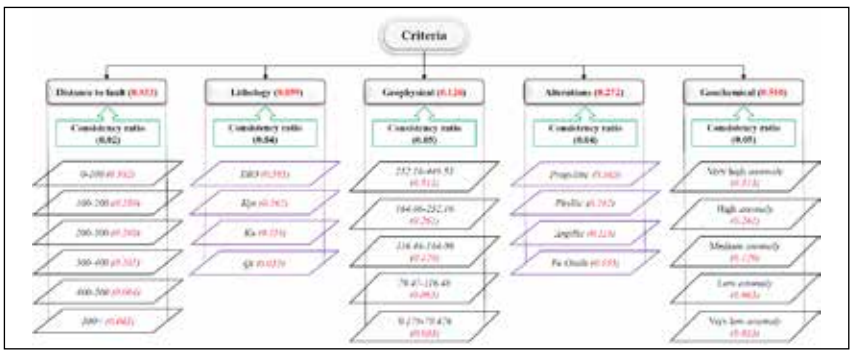

Figure 11. Calculated weights for the criteria and their classes in the AHP model

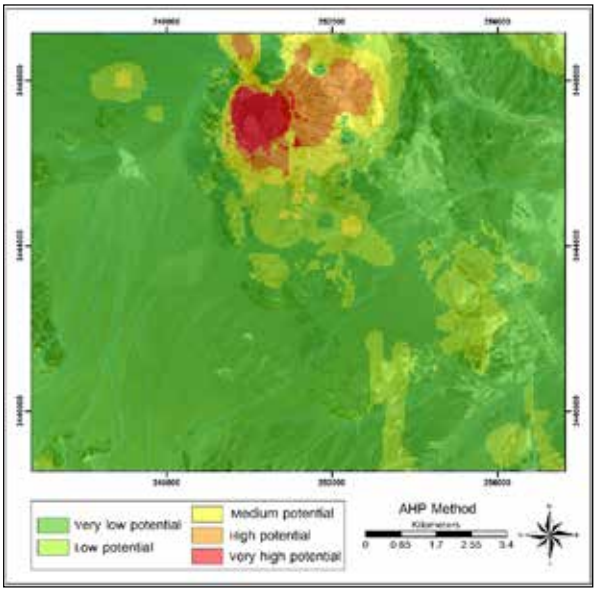

Figure 12. Mineral potential map of the study area generated from AHP method

6.2 Fuzzy Logic Method

Fuzzy logic, which is knowledge-based, is another method for the mineral potential map preparation (Whateley and Evans, 2006). Acceptable results can be achieved with the help of this method, particularly when mineralization and mineral indices are limited, expert opinions, and assignments of logical coefficients and weights to information layers (Harris et al., 2001). The fuzzy logic method was first introduced by Zadeh (1965) and is defined based on fuzzy sets with no certain limits. The fuzzy set theory uses a range of values between zero and one to express the degree or value of the members of a set (Novriadi et al., 2006; Tangestani, 2009; De Gruijter et al., 2011) with zero representing a lack of full membership and one indicating full membership (An et al., 1991). The classes of each map can have a membership value between zero and one. Fuzzy logic has been recently used in the exploration of areas with high mineralization potential, and particularly in determining areas suitable for exploratory drilling. Some research conducted in this field includes the studies by An et al. (1991), Eddy et al. (1995), Carranza et al. (1999), KourePazan Dezfouli (2008), Yousefi et al. (2012 & 2014), Shahi and Kamkar Rouhani (2013), Alaei Moghadam et al. (2014), Ghadiri-sufi and Yousefi (2016), Tabaei et al. (2017), Khajehmiri et al. (2018), and Barak et al. (2018). Table 3 shows five useful operators of And, Or, Product, Sum, and Gamma fuzzy operators used in this method to combine the exploratory data (An et al., 1991; Carter, 1994). In the provided relations, μi indicates the ith membership function, and n represents the number of membership functions supposed to be combined.

Table 3. Types of operators used in the fuzzy logic method (Bonham-Carter, 1984; An et al., 1991; Carter, 1994)

Operators	Operator relationship
Fuzzy AND	$\mu_{Combination} = MIN(\mu_A, \mu_B, \mu_C, \dots)$
Fuzzy OR	$\mu_{Combination} = MAX(\mu_A, \mu_B, \mu_C, \dots)$
Fuzzy Product	$\mu_{Combination} = \prod_{i=1}^{n} \mu_i$
Fuzzy Sum	$\mu_{Combination} = 1 - \prod_{i=1}^{n} (1 - \mu_i)$
Fuzzy Gamma	$\mu_{Combination} = (\text{Fuzzy Algebraic Sum})^{\gamma} * (\text{Fuzzy Algebraic Product})^{1-\gamma}$

This study used the three operators of Sum, Or, and Gamma to combine the exploration layers (Figure 13). The fuzzy membership function MSLarge was initially used to fuzzify all information layers. According to this function, the fuzzy membership values are calculated based on the mean and standard deviation of the initial data, where higher initial values have higher fuzzy scores. The values of all the information layers were placed in the range of 0 to 1 using the MSLarge method in the layer fuzzification step, after which all the exploration layers were fuzzified and the values of all the layers were homogenized. Then, the fuzzified layer of gold and copper geochemical anomalies was combined using the Or operator to prepare the fuzzified geochemical anomaly map of the region. In the next step, the fuzzified alteration, structural, and lithological layers were combined using the Sum fuzzy operator to obtain the map of alteration, lithology, and structure of the region. Finally, using the Gamma fuzzy operator (G=0.9), the mentioned exploration layers and the fuzzy geophysical anomaly layer were combined to provide the exploration potential model of the study area (Figure 14). According to the exploration potential map obtained by the fuzzy logic method, the highest potential was in the central and northern parts of the region, resulting from the significant overlap of geochemical and geophysical anomalies corresponding to the diorite unit outcrop in the region. Hence, this area seems to be the most optimal to conduct exploratory excavations.

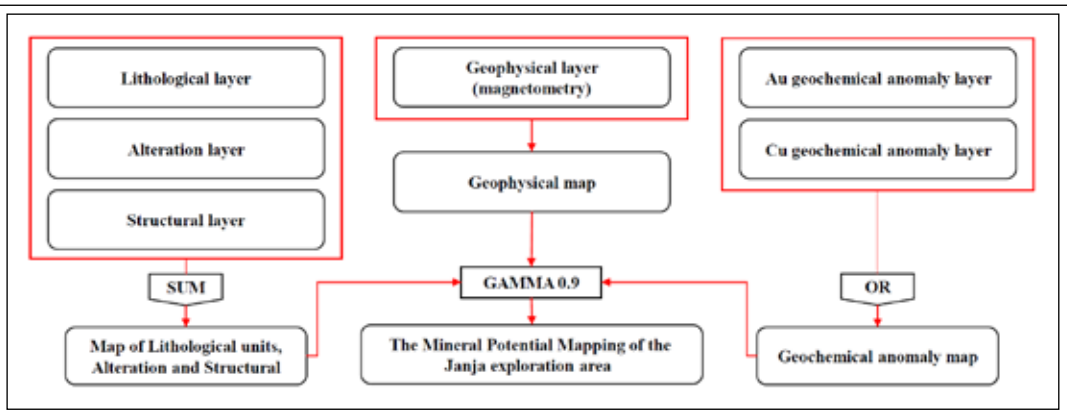

Figure 13. Flow chart of the fuzzy logic method

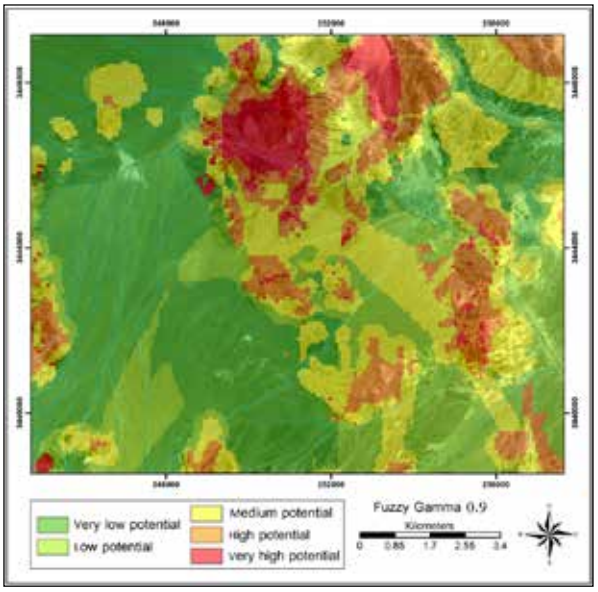

Figure 14. Mineral potential map of the study area generated from Fuzzy logic method

6.3 Evaluation of Mineral Potential Models

There are various methods for evaluating mineral potential zoning maps, one of which with extensive applications is comparing the results of these maps with the data of exploratory boreholes. Shirmard et al. (2014) used exploratory boreholes to evaluate and validate the mineral potential map of the Neysian porphyry copper deposit. In a similar study, Alaei Moghadam et al. (2014) used the results of drilling boreholes to confirm the validity of zoning. According to their results, the manual classification method with 5-class, compared to 3-class separation, had the highest compatibility with exploratory wells. The present study has also used the manual classification method with 5-class separation as the best method for zoning. The data from 12 exploratory drilling boreholes were used to evaluate the mineral potential models provided. Figure 15 shows the location of these boreholes in the mineral potential maps prepared. The profiles of copper and gold grade changes were drawn for each borehole with respect to the depth to evaluate the drilling results (Figures 16 and 17). Each borehole was placed in a certain class in terms of the amount of gold and copper considering the copper and gold grade changes, their maximum and minimum values, and the grade of copper and gold in each borehole.

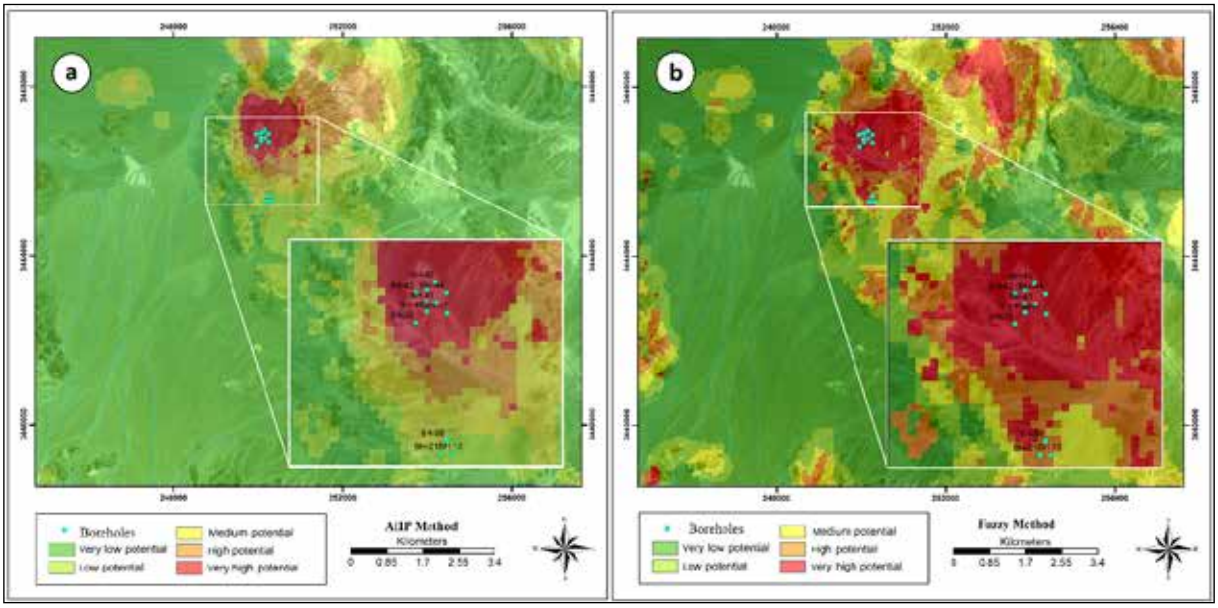

Figure 15. The location of the boreholes in mineral potential maps prepared by a) fuzzy logic and b) AHP method

The pixel values of the exploratory boreholes were matched with the drilling results to evaluate the prepared maps (Table 4). First, the prepared mineral potential maps were separated into 5 classes using manual classification methods. The values of the pixels related to the boreholes in the mineral potential maps were then extracted, determining the class of each borehole based on the values of each pixel in one of the defined classes. Then, the class, determined for each borehole, was compared with the status of that borehole according to Table 4, which defines the very high, high, average, low, and very low mineral potentials with values of 5 to 1, respectively. If the class of boreholes overlaps with their existing status, zero is recorded in the final evaluation table. On the other hand, if the status of the actual class of the borehole differs from its status on the map, one of the values -1, -2, -3, and -4 is recorded in the final evaluation table. The overlap of each prepared map with exploratory boreholes was calculated using Eq. (1)

$$a = 1 - \frac{e}{E} \quad (1)$$

In which, a, e, and E represent the overlap of boreholes with prepared maps, the number of negative points, and the total number of non-overlap. Eq. (2) was used to calculate the total number of the boreholes non-overlap. Table 4 shows the evaluation of maps prepared by the AHP and fuzzy logic methods. According to the results, AHP and fuzzy logic methods had 62.5% and 54.17% overlap, respectively, indicating that AHP had better performance than fuzzy logic. A study by Yousefifar et al. (2013) also showed that AHP was the most suitable among the index overlay methods, AHP, and fuzzy logic methods for combining exploration layers in Dalli (copper and gold) porphyry deposits. In the study, conducted by Hossein Ali et al. (2008), 88% of overlap was

found by the comparison of the mineral potential map prepared by AHP and the results of exploratory boreholes:

(number of boreholes with real average condition × 1) +
(number of boreholes with non-average real condition × 2) = total number of conditions (2)

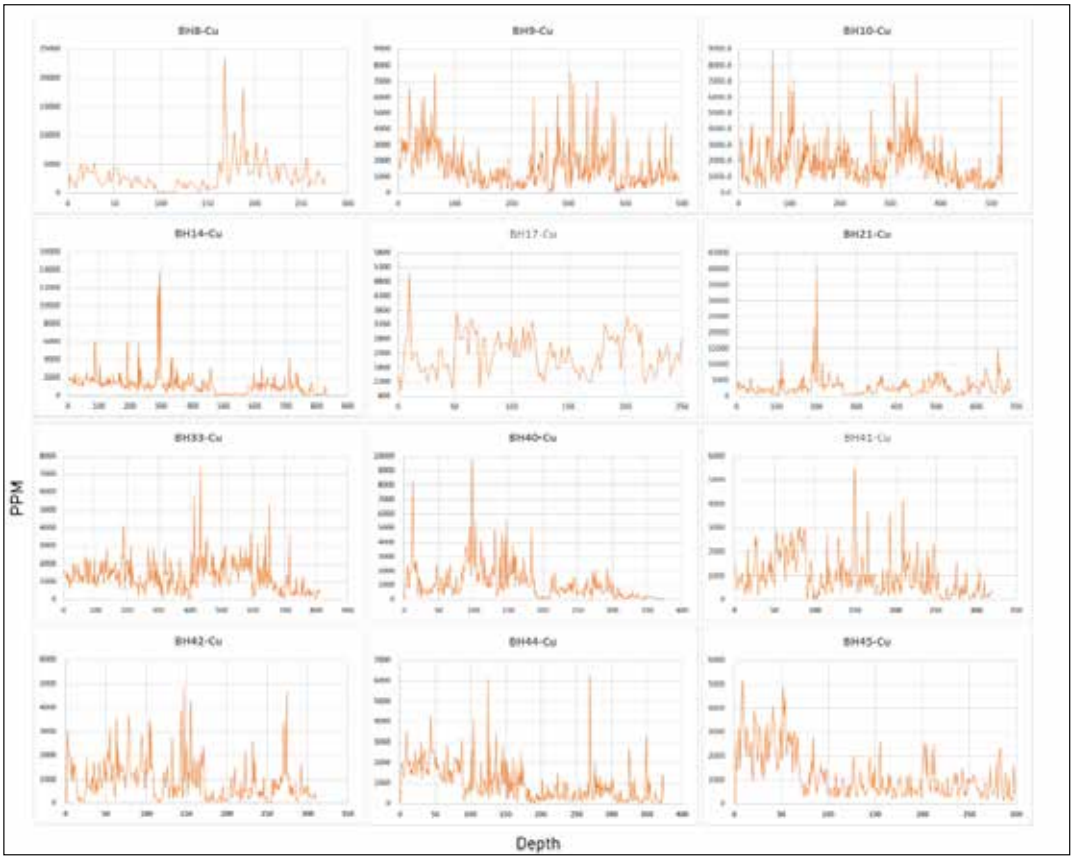

Figure 16. Cu concentration (ppm) versus depth (m) in exploratory boreholes in the study area

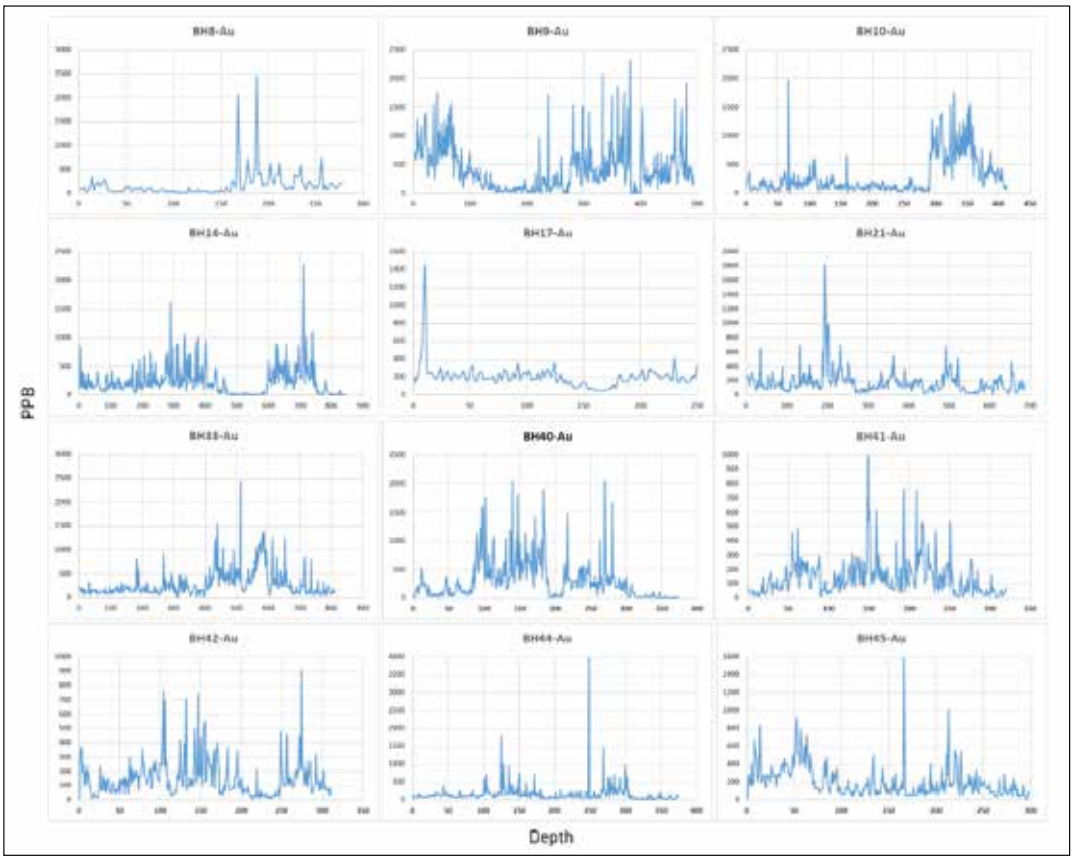

Figure 17. Au concentration (ppb) versus depth (m) in exploratory boreholes in the study area

Table 4. Overlap of exploratory boreholes with mineral potential maps

The original status of the borehole		AHP		Fuzzy Logic	
Borehole	Status	Status	Assessment	Status	Assessment
BH-08	2	2	0	4	-2
BH-09	2	5	-3	5	-3
BH-10	2	2	0	4	-2
BH-14	5	5	0	5	0
BH-17	5	5	0	5	0
BH-21	4	2	-2	4	0
BH-33	5	5	0	5	0
BH-40	5	5	0	5	0
BH-41	4	5	-1	5	-1
BH-42	4	5	-1	5	-1
BH-44	4	5	-1	5	-1
BH-45	4	5	-1	5	-1
Match rate (%)		62.5		54.17	

6.4 Providing Optimal Drilling Locations

Figure 18 shows the best location to continue exploration drilling according to the investigations conducted and the exploration potential maps prepared. Hence, it is recommended to carry out new drilling operations only in the optimal areas located on this map. As shown in this Figure, the northern portion of the study area is the best location for future excavations. This area covers around 6 km^2 and corresponds to the geological unit of diorite and granodiorite porphyry.

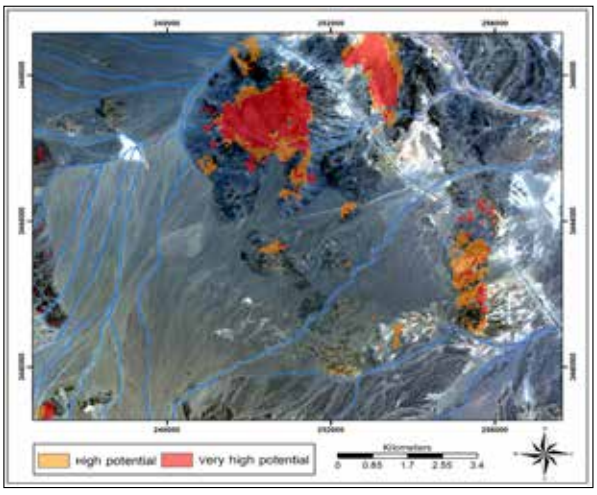

Figure 18. The location of high potential areas for future exploratory investigations

6. Conclusion

The current study used two methods of fuzzy logic and analytic hierarchy process to prepare a mineral potential map and determine optimal drilling locations in Janja exploration area situated in the structural zone of eastern Iran. The final exploration map resulting from the combination of lithology, structural, alteration, Cu and Au geochemical anomalies, and magnetometric geophysical anomaly, obtained by these two methods, confirmed the high exploration potential in the central and northern parts of the region. Accordingly, a significant overlap of the anomalies of the mentioned maps was indicated in this area, and the presence of minerals was confirmed. The mineral potential maps, prepared by the results of exploratory boreholes, were then compared and validated in terms of the accuracy of the results. According to the comparison between the results of drilling boreholes and the exploration potential map, prepared by these two methods, the AHP method led to a higher level of accuracy than the fuzzy logic method. This difference is because AHP measures the importance of each exploration layer based on expert opinion and their priority according to exploration principles compared to other layers, reducing the possibility of error and confirming the validity of the method through the inconsistency rate calculation. Following all the studies and processing conducted, a region with an area of 6 $km^{2,}$ corresponding to the geological unit of diorite and granodiorite, can be considered for future exploratory investigations, particularly in Janja exploration area. Accordingly, it will be possible to avoid the waste of money and time in areas without any mineralization potential if future exploration activities focus on such areas.

Acknowledgment

The authors would like to express their sincere gratitude to the management of Iran Minerals Production and Supply Company (IMPASCO) for providing the required data and all supports. Two anonymous reviewers are genuinely appreciated for their constructive, valuable and insightful comments on this research that highly improved the quality of the work.

References

Abedi, M., Torabi, SA., Norouzi, GH. (2013). Application of fuzzy AHP method to integrate geophysical data in a prospect scale, a case study: Seridune copper deposit. Bollettino di Geofisica Teoricaed Applicata 54: 145–164.

Aghanbati, A. (2004). Geology of Iran. Geological Survey of Iran p. 605.

Alaei Moghadam, S., Karimi, M., Mesgari, M.S., Saheb Zamani, N. (2014). Modeling process of mineral potential mapping using Fuzzy inference systems (Case study: Chah Firoozeh Copper Deposit). Scientific Quarterly Journal, Geosciences 93: 53-66.

Alavi Naeini, M., Eftekhar Nejad, J., Aghanbati, A. (1988). Zabol 1:250.000 Geological Map. Geological Survey of Iran.

Al-Sababhah, A., Al maqablah, M. (2023). Integrated Evaluation of Soil Erosion-prone Areas Based on the GIS Technique and the Analytic Hierarchy Process on Hillside Slopes, Northwest of Jordan, Jordan Journal of Earth and Environmental Sciences 14 (2): 158-174.

An, P., Moon, W.M., Rencz, A. (1991). Application of fuzzy set theory for integration of geological, geophysical and remote sensing data. Canadian Journal of Exploration Geophysics 27: 1-11.

Barak, S., Bahroudi, A., Jozanikohan, G. (2018). Exploration of Kahang porphyry copper deposit using advanced integration of geological, remote sensing, geochemical and magnetics data. Journal of Mining & Environment 9: 19-39.

Bazzi, A., Boomeri, M., Elyaspoor, N. (2009). Stream sediment geochemical exploration in Janja Mountain, Sefidababeh, East of Iran. 17th Iranian Crystallography and Mineralogy Conference, Bu Ali Sina University, Hamedan, Iran.

Bazzi, A., Boomeri, M., Elyaspoor, N. (2013). Petrography and geochemistry of intrusive rocks in Janja Mountain, east of Iran. 21st Iranian Crystallography and Mineralogy Conference, Sistan and Baluchestan University, Iran.

Bonham-Carter, G. (1994). Geographic Information Systems for

Geoscientists: Modelling with GIS. Pergamon Press, Oxford p. 398.

Carranza, E. (2010). Improved wildcat modelling of mineral prospectivity. Resource Geology 60: 129–149.

Carranza, E., Hale, M. (2002). Wildcat mapping of gold potential, Baguio district, Philippines. Transactions of the Institution of Mining and Metallurgy (Section B-Applied Earth Science), 111: 100–105.

Carranza, E.J.M. (2009). Controls on mineral deposit occurrence inferred from analysis of their spatial pattern and spatial association with geological features. Ore Geology Review 35: 383-400.

Carranza, E.J.M., Hale, M. (2001). Geologically constrained fuzzy mapping of gold mineralization potential, Baguio District, Philippines. Journal of Natural Resources Research 10: 125–136.

Carranza, E.J.M., Hale, M., Mangaoang, J.C. (1999). Application of mineral exploration models and GIS to generate mineral potential maps as input for optimum land-use planning in the Philippines. Natural Resources Research 8: 165–173.

Carrenza, E.J.M. (2008). Geochemical anomaly and mineral prospectivity mapping in GIS. Handbook of Exploration and Environmental Geochemistry 11, p. 368.

Chen, MF., Tzeng, GH., Ding, CG. (2008). Combining fuzzy AHP with MDS in identifying the preference similarity of alternatives. Appl Soft Comput 8,110–117.

Chen, Y. (2001). Implemetingan Hierarchy Process by Fuzzy integral. International Journal of Fuzzy Systems 3: 493–502.

Cimren, E., Catay, B., Budak, E. (2007). Development of a machine tool selection system using AHP. The International Journal of Advanced Manufacturing Technology 35: 363–376.

Dagdeviren, M. (2008). Decision making in equipment selection: an integrated approach with AHP and PROMETHEE. Journal of Intelligent Manufacturing 19: 397–406.

De Gruijter, J.J., Walvoort, D.J.J., Bragato, G. (2011). Application of fuzzy logic to Boolean models for digital soil assessment. Journal of Geoderma 166: 15–33.

Dey, P.K., Ramcharan, E.K. (2000). Analytic hierarchy process helps select site for limestone quarry expansion in Barbados. Journal of Environmental Management 88: 1384–1395.

Eddy, B.G., Bonham-Carter, G.F., Jefferson, C.W. (1995). Mineral resource assessment of the Parry Islands, high Arctic, Canada: a GIS based fuzzy logic model, in Proc. Can. Conf. on GIS, CD ROM Session C3, Can. Ins. Geomatics, Ottawa, Canada, Paper 4.

Eftekhar Nejad, J., Alavi Naeini, M., Aghanabati, A. (1990). Khunik 1:100.000 Geological map. Geological Survey of Iran.

Elyaspoor, N. (2010). Metallic mineralization and economic geology study in Sefidabeh area (Janja Mountain), east of Iran. Ms.c. thesis, Sistan and Baluchestan University, Iran.

Ghadiri Sufi, E., Yousefi, M. (2016). Combination of data and knowledge driven fuzzy approaches in mineral potential modeling for generating target areas. Scientific Quarterly Journal, Geosciences 25: 11-18.

Ghodsipour, H. (2009). Discussions in Multi-criteria Decision Making, Analytical Hierarchy Process. 7th Edition, Amirkabir University of Technology Publications, p. 220.

Harris, J., Wilkinson, L., Heather, k., Fumerton, S., Bernier, M., Ayer, J., Dahn, R. (2001). Application of GIS Processing Techniques for Producing Mineral Prospectivity Maps – A Case study: Mesothermal Au in the Swayze Greenstone Belt, Ontario, Canada. Natural Resources Research 10: 91-124.

Hossein Ali, F., Al Sheikh, A., Rajabi, M.A. (2010) Investigation of weighting spatial information methods in GIS (case study: preparation of mineral potential map). Scientific-Research Journal of Remote Sensing and GIS of Iran 1: 73-88.

Jiajin, Y., Lee, H. (1997). An AHP decision model for facility location selection. Facilities 15: 241–254.

Kargaranbafghi, F., Kheirandish Ravari, M., Rahimi Shahid, M. (2020). Seismic hazard analysis of Zarand city using AHP-GIS. Italian Journal of Engineering Geology and Environment 1: 5-16.

Karimi, M., Menhaj, M., Mesgari, M. (2008). Mineral potential mapping of copper minerals using fuzzy logic in GIS invironment, Beijing, China ISPRS, 170-181.

Karimi-Sangchini, E., Emami, S. N., Shariat-Jafari, M., Rezazadeh, F., Raeisi, H. (2020). Landslide Hazard Zonation Using Multivariate Statistical Models in the Doab Samsami Watershed, Chaharmahal Va Bakhtiari Province, Iran. Jordan Journal of Earth and Environmental Sciences 11 (3): 174-182.

Khajehmiri, Z., Shayestehfar, M.R., Moeinzadeh, H. (2018). Identification of probable porphyritic Au-Cu mineralization zones in the South Seachangi using AHP and FAHP methods. Scientific Quarterly Journal, Geosciences 27: 217-230.

Kourehpazan Dezfouli, A. (2008). Principles of Fuzzy Set Theory and its Application in Water Engineering Problem Modeling. Second Edition. Amirkabir University of Technology Publications, p. 261.

Lopez, H.J., Zink J.A. (1991). GIS-assisted modelling of soil-induced mass movement hazards: a case study of the upper Coello river basin, Tolima, Colombia. Interdenominational Theological Center 4: 202–220.

Macharis, C., Springael, J., Brucker, K.D., Verbeke, A. (2004). PROMETHEE and AHP: the design of operational synergies in multicriteria analysis. Strengthening PROMETHEE with ideas of AHP. European Journal of Operational Research 153: 307–317.

Madani, A. (2011). Knowledg e-driven GIS modeling technique for gold exploration, Bulghah gold mine area, Saudi Arabia. The Egyptian Journal of Remote Sensing and Space Sciences 14: 91–97.

Mahfoud, Z., Maref , N., Bemmoussat, A. (2024). Delineation of Potential Groundwater Area in Semi-arid and Arid Region: A Case Study of Wadi Mekerra North West Algeria Using Remote Sensing, GIS and Analytic Hierarchy Process. Jordan Journal of Earth and Environmental Sciences 15 (3): 162-173.

Malczewski, J. (1999). GIS and Multicriteria Decision Analysis. John Wiley & Sons INC.

Minatour, Y., Khazaei, J., Ataei, M. (2012). Earth dam site selection using the analytic hierarchy process (AHP): a case study in the west of Iran. Arabian J Geosci. doi:10.1007/s12517-012-0602-x.

Moon, C.J., Whateley, M.K.G., Evans, A.M. (2006). Introduction to Mineral Exploration (2nd Edition). Blackwell Publishing, Oxford, p. 481.

Mukhopadhyay, B., Hazra, N., Sengupta, S.R., Kumar Das, S. (1996). Mineral potential map by a knowledge driven GIS modeling: an example from Singhbhum Copper Belt, Jharkhad. Geological Survey of India.

Nabavi, M.H. (1976). Introduction of Geology of Iran. Geological Survey of Iran, p. 109.

Ngai, E.W.T. (2003). Selection of web sites for online advertising using the AHP. Information and Management 40: 233–242.

Novriadi, H.P.M., Darijanto, T. (2006). Applying Fuzzy Logic Method in mineral potential mapping for epithermal gold mineralization in the Island of Flores, East Nusa Tenggara using geographical information systems (GIS). Proceeding of 9th International Symposium on Mineral Exploration, 62-68.

Pazand, K., Hezarkhani, A., Ataei, M. (2012). Using TOPSIS approaches for predictiporphyry Cu potential mapping: a case study in Ahar-Arasbaran area (NW, Iran). Geology science 49: 62–71.

Pazand, K., Hezarkhani. A., Ataei, M., Ghanbari, Y. (2011)

Combining AHP with GIS for predictive Cu porphyry potential mapping: a case study in Ahar Area (NW, Iran). Natural Res Res 20 (4):251–262.

Porwal, A., Carranza, E., Hale, M. (2003). Knowledge-driven and Data-driven Fuzzy Models for Predictive Mineral Potential Mapping. Natural Resources Research 12: 1–25.

Porwal, A., Carranza, E.J.M., Hale, M. (2006). A hybrid fuzzy weights-of-evidence model for mineral potential mapping. Jourrnal of Natural Resources Research 15: 1-14.

Rahimi Shahid, M., Kargaran, F., Rahimi, N. (2019). Seismicity and Seismic Hazard Analysis of Shahid Dam Site. Journal of Geographic Space 64: 121-140.

Rahimi Shahid, M., Rahimi, N. (2016). Landslide Hazard zoning central part of the Semirom city. Journal of Environmental Geology 33: 12-24.

Rahimi Shahid, M., Rahimi, N. (2017). Earthquake hazard zoning using Analytical Hierarchy Process (AHP) and GIS techniques (Case study: central part of the Semirom city). Journal of New Findings in Applied Geology 22: 109-118.

Rahimi, N., Niroomand, S., Lotfi, M., and Rahimi Shahid, M. (2022). Geology, mineralization, alteration and fluid inclusion studies of the Janja porphyry Cu-Mo deposit, Sistan Suture Zone, SE Iran. Scientific Quarterly Journal of Geosciences, 32(3), 13-30.

Rahimi, N., Niroomand, Sh., Adib Fard, Sh., Rastani, Sh., Masoumi, I., Rahimi Shahid, M. (2020). Using statistical and fuzzy logic methods to mineral potential mapping in the Janja exploration area (South of Nehbandan, Iran). 8Th Iranian mining engineering conference, February, p. 10.

Ranjbar, H., Honarmand, M. (2004). Integration and analysis of airborne geophysical and ETM+ data for exploration of porphyry type deposits in the Central Iranian Volcanic Belt using fuzzy classification. International Journal of Remote Sensing 25: 4729–4741.

Saaty, T. (1980). The Analytic Hierarchy Process, Planning, Priority Setting, Resource Allocation. McGraw-Hill, New York, USA, p. 281.

Saaty, T. (2001). Decision Making for Leaders: The Analytic Hierarchy Process for Decisions in a Complex World. RWS Publications, Pittsburg.

Shahi, H., Kamkar Rouhani, A. (2013). Exploration of Hydrothermal Gold Reserves Using Different Types of Fuzzy Operators by GIS in Torbat-e-Heydariyeh area. Journal of Applied Geology 9: 43-51.

Shirmard, H., Bahrudi, A., Adeli, A. (2014). Fuzzy Analysis Hierarchy Process method in spatial information system to determine optimum drilling points in Nisian porphyry copper deposit. Scientific-Research Quarterly of Geographical Information (Sephehr) 24: 91-100.

Srdjevic, B., Medeiros, YDP. (2008). Fuzzy AHP assessment of water management plans. Water Resour Manage 22,877–894.

Tabaei, M., Mansouri Esfahani, M., Rasekh, P., Esna-ashari, A. (2017). Mineral prospectivity mapping in GIS using fuzzy logic integration in Khondab area, western Markazi province, Iran. Journal of Tethys 5: 367-379.

Tangestani, M. (2009). A comparative study of Dempster–Shafer and fuzzy models for landslide susceptibility mapping using a GIS: An experience from Zagros Mountains, SW Iran. Journal of Asian Earth Sciences 35: 66–73.

Vahidnia, M.A., Alesheikh, A.A., Alimohammadi, A. (2009). Hospital Site Selection Using Fuzzy AHP and Its Derivatives. Journal of Environmental Management 90: 3048- 3056.

Vargas, L.G. (1990). An overview of the analytic hierarchy process and its applications. European Journal of Operational Research 48: 2-8.

Yousefi, M., Kamkar-Rouhani, A., Carranza, E.J.M. (2012). Geochemical mineralization probability index (GMPI): a new approach to generate enhanced stream sediment geochemical evidential map for increasing probability of success in mineral potential mapping. Journal of Geochemical Exploration 115: 24–35.

Yousefi, M., Kamkar-Rouhani, A., Carranza, E.J.M. (2014). Application of staged factor analysis and logistic function to create a fuzzy stream sediment geochemical evidence layer for mineral prospectivity mapping. Geochemistry: Exploration, Environmental, Analysis 14: 45-58.

Yousefifar, S., Khakzad, A., Asadi Haruni, H., Jafari, M., Vathoughi Abedini, M. (2013). Using the combined methods of overlap index, fuzzy and analysis hierarchical process to determine the potential areas of copper and gold in the northern part of the Dali porphyry deposit. Earth Sciences Quarterly 21: 49-58.

Zadeh, L.A. (1965). Fuzzy sets. IEEE Information and Control 8: 338–353.

JJEES

JJEES (2024) 15 (4): 287-297
ISSN 1995-6681

Jordan Journal of Earth and Environmental Sciences

Removal of Color from Textile Dyeing Effluents Using Coagulation-Flocculation Process Coupled with Adsorption on Nanoparticles Process

Md Abu Sayed and Md Golam Mostafa*

Water Research Lab, Institute of Environmental Science, University of Rajshahi, Rajshahi 6205, Bangladesh

Received on August 28, 2023; Accepted on November 6, 2024

Abstract

Textile dyeing industries discharge large volumes of effluents that threaten sustainable water resources and environmental management. This study aimed to explore the feasibility of treating discharge textile dye effluents by combining coagulation and adsorption processes to achieve the required discharge wastewater standards. The X-RD analysis results confirmed that the synthesized iron-oxide particles were found to be within the nano-size range (10-20 µm). The chemical coagulation process showed about 75% color removal efficiency, and the cumulative color removal efficiency achieved was 99.5% in combined coagulation, followed by the adsorption process with iron-oxide nanoparticle adsorbents (IONPs). The SEM images showed the rough and porous surface of virgin IONPs, having a slightly hazy and smooth surface for the adsorbed IONPs. The EDX analysis confirmed the presence of various metal ions on the IONPs surface. The study illustrated that the combination of coagulation-flocculation (C-F) and adsorption onto IONPs was more efficient for decolorizing textile dyeing effluents than the single coagulation process. The study observed that the coagulant $FeSO_4$ and the adsorbent IONPs have the potential to treat textile dyeing effluents and achieve the required standards for discharging the effluent into the environment.

Keywords: *Dyeing Effluents, Coagulation-Flocculation, Adsorption, Color Removal, Nanoparticles, Water*

1. Introduction

Bangladesh, a developing country, has been industrialized over the last two decades in various sectors. Thousands of textiles in Bangladesh use a huge amount of water, chemicals, and dyes in the finishing and dyeing processes. Particularly, synthetic dyes are extensively used in various branches of the textile industry (Islam and Mostafa, 2018b; Slama et al., 2021), the leather industry (Chowdhury et al., 2015; Monira et al., 2023), the food industry (Zahedi et al., 2020), and so on, producing a huge volume of dyeing effluents. In textiles, 93% of the raw water, used for production, comes out as strongly colored wastewater due to dyes containing high chemical oxygen demand (COD), biological oxygen demand (BOD), a large number of suspended solids, total dissolved solids (TDS), extreme pH, concentrated organic compounds, and heavy metals (Hossen and Mostafa, 2023; Wijannarong et al., 2013). Crops, grown on polluted soils, may cause trace metals to be absorbed and, subsequently, accumulated along the food chain posing potential threats to animal and human health (Dahnoun and Djadouni, 2020). More than 70,000 tons of approximately 10,000 dyes and pigments are produced annually worldwide, of which approximately 20-30% are discharged as effluents from the curing and finishing processes of textiles (Patil and Shrivastava, 2015). About 20–30% of the 10,000 dyes and pigments, used in the textile industry, are reactive dyes, which include azo, anthraquinone, phthalocyanine, formazine, oxazine, etc. (Islam and Mostafa, 2022; Papić et al., 2004). The overwhelming majority of synthetic dyes exhibit a considerable structural diversity, and most of them are azo derivatives. Azo dyes represent about 60% of all reactive dyes utilized by the textile industry. Due to the presence of carcinogenic compounds such as naphthalene, benzamine, and other aromatic compounds, the dye effluent becomes toxic even at its lower concentrations (Gil et al., 2011). The exhaustion properties of azo dyes are poor, and they obstruct light penetration, interrupt photosynthetic movement, and prevent the growth of biota (Tareque et al., 2023; Islam and Mostafa, 2018a). The color of the effluents is aesthetically unpleasant to aquatic bodies. It hinders the oxygenation ability of water, disturbs the whole aquatic ecosystem and food chain, and poses a thoughtful risk to human health. The problem is even more acute in developing countries like Bangladesh, where rapid population growth and industrialization have increased the complexity of wastewater (Rahim and Mostafa, 2021; Saha el al., 2021; Ntuli et al., 2011; Qasim and Mane, 2013).

Hence, there is an urgent requirement for the development of innovative, but low-cost techniques, by which dye molecules can be removed. Many techniques, including coagulation-flocculation, electro-coagulation, adsorption, ion exchange, advanced oxidation processes (O_3/H_2O_2, H_2O_2/UV, and photo-catalysis), flotation, membrane techniques (ultra-filtration, nanofiltration, and reverse osmosis), ozonation, radiolysis, and biological degradation, have been successfully used to remove the color from wastewater (Sayed and Mostafa, 2021, 2023; Deng and Zhao, 2015; Fan et al., 2008; Mostafa and Hoinkis, 2012). However, due to

* Corresponding author e-mail: mgmostafa@ru.ac.bd

some drawbacks of the aforementioned single process, as wastewater contains a complex mixture of variable contents, conventional techniques could not be implemented at scale in the industry. The C-F technique, coupled with adsorption, offers high efficiency of dye removal, less produced sludge, coagulant savings, and economic feasibility (Papić et al., 2004). Various adsorbents, such as montmorillonite, bentonite clay, nanoparticles, petroleum wastes, tannin-rich materials, sawdust, fly ash, sugar industry wastes, chitosan, peat moss, scrap tires, etc. (Kandisa et al., 2016) and agricultural unused materials include banana peel (Annadurai et al., 2002), rice husk (Malik, 2003), date pit (Banat et al., 2003), almond shell (Ardejani et al., 2008), etc. are being studied for removing of color, COD, and BOD at changed operational settings (Rafatullah et al., 2010). Among the various adsorbents, nanoparticles have drawn great attention due to their outstanding physicochemical properties, including small size, larger surface area, and magnetic properties. Adsorption by nanoparticles is a promising and attractive alternative for the treatment of azo-containing dyes and is inexpensive and readily available. The cost-effectiveness, higher environmental stability, higher adsorption capability, and nontoxic nature of IONPs make them suitable for wastewater treatment (Crane and Scott, 2012). Another exclusive property that favors using IONPs in the field of adsorption is magnetism, which makes the separation process easier. Therefore, IONPs can be easily separated with the help of a magnetic field after the adsorption. Several chemical methods can be used to synthesize IONPs, such as micro-emulsions (Salvador et al., 2021), hydrothermal synthesis (Ge et al., 2009), thermal decomposition (Unni et al., 2017), co-precipitation (Al-Alawy et al., 2018), sol-gel method (Kayani et al., 2014), and the colloidal chemistry method (Krans et al., 2020). Among these, chemical co-precipitation is probably the simplest and most promising method for the production of nanomaterials, as the procedure is relatively simple and a large amount of controlled particle size of IONPs can be synthesized (Al-Alawy et al., 2018). The study synthesized IONPs by co-precipitation of ferric and ferrous ions in an alkaline solution at 80 °C, and, then, it was used for the removal of color, COD, and BOD from textile dyeing effluent. The study aimed to investigate the feasibility of a coagulation process coupled with nanoparticle adsorbents to achieve a higher color removal efficiency in treating textile dye effluents.

2. Materials and Methods

2.1 Sample collection and analysis for characterization

The textile dyeing effluent was collected in a five-liter pre-washed plastic container from Sirajganj District in Bangladesh. Before sampling, the containers were washed with diluted acid and double distilled water, and just before sampling, they were rinsed with the effluents to be sampled. pH, dissolved oxygen (DO), and electrical conductivity (EC) were measured on the spot by a portable multimeter. A few mL of concentrated HNO_3 and HCl were added to the effluent to prevent the growth of microbial bacteria, and the containers were sealed to prevent air oxidation. The effluents were analyzed before and after treatment using different analytical techniques, including titration, gravimetric, and spectrophotometric methods. Some of the physicochemical parameters were determined as per standard methods (APHA, 2012).

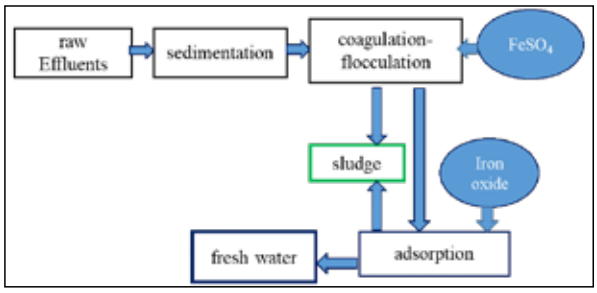

Figure 1. Flow chart of the experiment

2.2 Coagulation-flocculation experiments

Figure 1 shows a simplified experimental setup that describes different stages of C-F and adsorption processes. The collected effluents were kept overnight for sedimentation. It was then placed in the jar test apparatus for C-F experiments, and the supernatant, obtained after C-F, was subjected to the adsorption process to get fresh water. The C-F process was conducted to obtain optimal process parameters, such as, coagulant doses (100 mg/L to 1200 mg/L), pH (3 to 12), temperature (25 to 50 °C), contact time (15 to 180 min.), and mixing speed (30 to 180 rpm). Each beaker was filled with the desired volume of effluent and added the desired amount of coagulant dose. The solution was stirred rapidly for 1.5 min. to ensure complete dispersion of the coagulants, followed by slow mixing to aid in the formation of flocs. The pH of the sample was adjusted in the range of 3-12 with 0.01 M HCl and/or 0.01 M NaOH solution before being subjected to the jar test. At the end of the sedimentation period, the supernatant was collected from the top of the beaker and the absorbance was measured using UV-visible spectrophotometer (SHIMADZU UV-mini1240) of the treated effluents at its λ_{max}. All experiments were conducted thrice and mean values were taken. The color removal percentage was calculated using the following equation (Hoong and Ismail, 2018):

$$\text{Color removal (\%)} = \frac{A_0 - A_f}{A_0} \times 100 \quad (1)$$

where A_0 and A_f are the initial and final absorbance of the untreated and treated effluents, respectively.

2.3 Batch adsorption experiments

After C-F experiments, batch adsorption studies were carried out at different doses (0.5 to 3.0 g/L) of synthesized IONPs adsorbent, keeping other parameters constant. Then, the adsorption of color was studied at pH values of 2.0 to 12.0 at different contact times (10, 15, 20, 30, 45, 60, 90, 120, and 180 min.) at 30 °C to get the optimum values. The experimental procedure is as follows: 100 mL of effluent was taken in 250 mL beakers loaded with a definite dose of IONPs after adjusting the pH of the effluent with 0.01 M HCl and/or 0.01 M NaOH solutions. The solution was stirred vigorously in an electric shaker at 180 rpm for a predefined time, and the beaker was, then, placed on the magnet. The effluents became colorless due to the magnetic separation of dye-loaded adsorbents. The mixture was decanted to measure its concentration with a UV-visible spectrophotometer by

measuring the absorbance at a wavelength corresponding to the maximum absorbance of the sample. All batch adsorption studies were conducted three times, and mean values were taken. The color removal efficiency of the adsorption process was calculated using the same equation used in the coagulation process stated above.

2.4 Adsorption kinetics

The pseudo-first-order equation and pseudo-second-order equation are used to illustrate the adsorption kinetics of the adsorbent surfaces. The pseudo-first-order equation can be expressed in the following form (Ho and McKay, 1998; Mostafa et al., 2011):

$$log(q_e - q_t) = log(q_e) - \frac{k_1}{2.303}t \quad (2)$$

where q_e and q_t are the amounts of adsorbate adsorbed (mg g^{-1}) at equilibrium and at time t (min.) respectively, and k_1 is the pseudo-first-order rate constant (L min^{-1}).

The pseudo-second-order equation can be stated as the following (Ho and McKay, 1999):

$$\frac{t}{q_t} = \frac{1}{k_2 q_e^2} + \frac{1}{q_e}(t) \quad (3)$$

where k_2 is the rate constant of pseudo-second-order adsorption (g $mg^{-1}min^{-1}$).

3. Results and Discussion

3.1 Characterization of the effluents

Table 1 shows the physicochemical characteristics of the effluent. The collected effluents were highly colored and aesthetically unpleasant, and the values of all the parameters exceeded the DoE-BD standard, indicating that the wastewater was extremely polluted. Due to its color and higher levels of pollutants, the wastewater cannot be disposed of in any treatment plants before a pre-treatment stage. The untreated wastewater discharge has potential threats to surface water quality, aquatic life, and the entire environment. Therefore, it is imperative to improve the treatment method to reduce the impact of the effluents on the environment. Hence, the study looked for ways to improve the treatment of dyeing effluents through coagulation with $FeSO_4$, coupled with adsorption on nanoparticles.

Table 1. Physicochemical characteristics of the effluents

Parameters		Color	pH	EC, µS/cm	TDS, mg/L	TSS, mg/L	DO, mg/L	COD mg/L	BOD mg/L
Results	Ef1	pink red	11.3	6240	4337	475	1.4	3732	1156
	Ef2	greenish black	11.2	6082	4025	400	1.6	3480	1065
DoE standard		-	6-9	1200	2100	150	-	200	50

3.2 Optimization of Coagulant

3.2.1 Effect of coagulant dose

In the C-F process, the dose is one of the most important factors to consider. Essentially, a small dose or overdosing would result in poor flocculation. The effects of coagulant doses (100-1200 mg/L) on the removal of color were shown in Figure 2, which illustrates that for small dosages (especially below 500 mg/L), color removal was rather low, while for 700 mg/L dosages, the removal efficiency of color was around 73%. The color removal efficiency of $FeSO_4$ coagulant increased gradually with dose due to the higher positive charge and polymeric effects of $FeSO_4$ (Joo et al., 2007). Furthermore, the high concentrations (>700 mg/L) of the coagulant may confer positive charges on the particle surface (a positive zeta potential), thus re-dispersing the particles, resulting in a decrease in color removal (Patel and Vashi, 2015). A similar result was observed in the ferrous sulfate coagulant, which showed more than 90% color removal efficiency at a coagulant dosage of 1600 mg/L (Jindal et al., 2016).

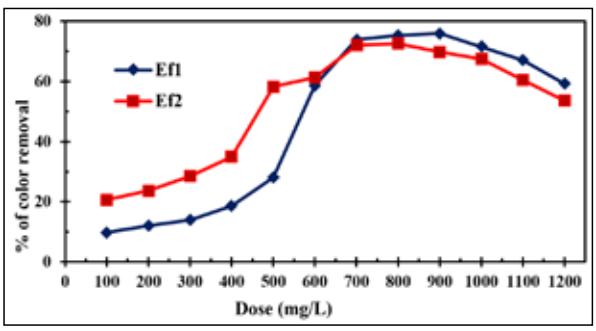

Figure 2. Effect of coagulant dose on color removal efficiency [pH 11.30, T 30 °C, contact time 30 min., and mixing speed 30 min.]

3.2.2 Effects of pH

One of the most important variables in the coagulation process using inorganic salts is the pH. This is because the inorganic coagulant is converted into different ionic species as the pH value changes, thus influencing the coagulation (Rodrigues et al., 2013). Figure 3 shows a decrease in percentage removal with an increase in pH for Ef1, but the percentage removal is increasing for Ef2 at pH ranges from 3 to 5. This is because, in the acidic region, Fe salt hydrolyzes to form monomeric Fe hydrolyzed species. Hence, soluble Fe^{2+} and $Fe(OH)^+$ cations play an important role in destabilizing the negatively charged dye particles via charge neutralization, and thus color removal takes place at lower pH but too little because of the lack of formation of neutral $Fe(OH)_2$ precipitates (Wong et al., 2007). The formation of Fe^{2+}, $Fe(OH)^+$, and neutral $Fe(OH)_2$ hydrolysis species with large surface areas capable of adsorbing soluble dye is maximized at an alkaline pH, and color removal occurs via charge neutralization and sweep flocculation (Perng and Bui, 2014; Suman et al., 2018). The maximum color removal efficiency of $FeSO_4$ was about 75% at the optimum pH of 11.0. A study showed that each coagulant was effective in decolorization within a specific pH range, which depended strongly on the nature of the wastewater, and the color removals were 91.4% for cotton at pH 9.4 and 93.8% for acrylic effluents at pH 8.3, respectively, using $FeSO_4$ coagulant (Rodrigues et al., 2013). At another pH, the complexes of hydrolysis products caused a decrease in the removal efficiency (Perng and Bui, 2014).

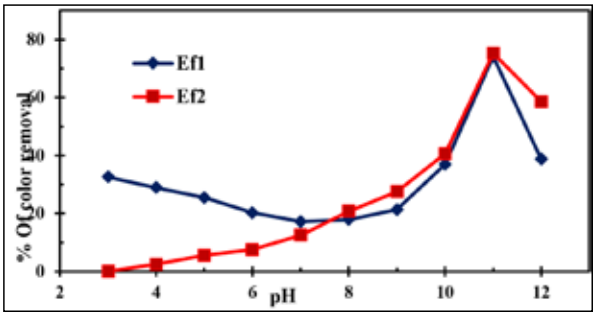

Figure 3. Effects of pH on color removal efficiency for Ef1 and Ef2 samples [coagulant dose 700 mg/L, temp 30 °C, contact time 30 min., and mixing speed 30]

3.2.3 Effects of temperature

Temperature affects the solubility of the metal hydroxide precipitate and the rate of formation of the metal hydrolysis products. Low temperature affects coagulation processes by altering coagulant solubility, increasing water viscosity, and retarding the kinetics of hydrolysis reactions. As shown in Figure 4, the effect of temperature on color removal is marked, increasing from 58% at 25°C up to 73% at 35°C for Ef1 and 68% to 76% for Ef2, and the % removal was not increased further up to 50°C, rather slightly decreasing for both effluents. This is because coagulation with hydrolyzing metals is less efficient at lower temperatures and has a pronounced detrimental effect on flocculation kinetics (Duan and Gregory, 2003). It has been reported that a decrease in temperature, (0-24°C), impairs the flocs› strength and virtually the flocs› formation efficiency, which results in a decrease in aggregation rate and bad settling (Fitzpatrick et al., 2004). The increased performance with temperature may be a consequence of the improved kinetics as occurs in most chemical reactions (Rodrigues et al., 2013). As the temperature increases from 30 to 35°C, the viscosity of the water decreases, and brown movement becomes fierce gradually as a result of the hydrolysis of the Fe(II) ion and increased competition for bonding by the macromolecules, and this accelerates the coagulation processes (Misau and Yusuf, 2016). The reasons behind decreased performance above 35°C were floc breakage increases, and floc reformation decreases at higher temperatures. Warmer temperatures generally produce bigger flocs that break more easily and reform less well, suggesting a weaker floc settlement. At high temperatures (above 35 °C), breakage in terms of floc size reduction is greater (Brabty, 2006).

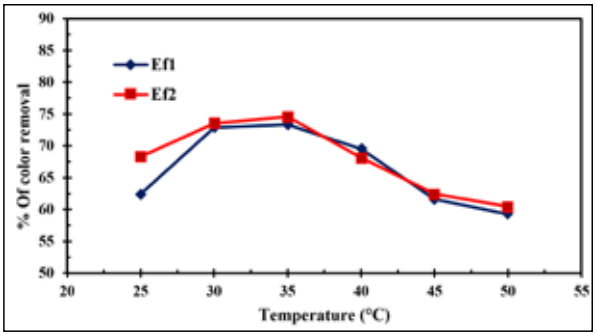

Figure 4. Effect of temperature on color removal efficiency for effluent Ef1 and Ef2 [coagulant dose 700 mg/L, pH 11.00, mixing speed 30 and settling time 30 min]

3.2.4 Effect of contact time

Contact time plays a vital role in flocs formation and growth in the flocculation process. The effect of contact time on the coagulation of dyeing effluents was studied using a time range of 15 min. to 180 min. and keeping other parameters constant. The trends that had been illustrated in Figure 5 showed that a longer or shorter contact time would result in poor performance of $FeSO_4$ for binding and bridging in the case of both effluents. In a short period, the collisions between the flocculants and colloids are not efficient to precipitate suspended solids. The color removal efficiency significantly dropped from 73% to about 56% with increasing reaction time from 30 min. to 180 min. for Ef1 and 73% to 53% for Ef2, respectively. This is because longer mixing times lead to an increase in floc breakage and limit the size of the flocs formed. The small-size flocs are not dense enough to settle down and thus, indirectly cause the sample to be turbid again (Hassan et al., 2009). This phenomenon is observed in Figure 5, which shows a lower percentage of reductions at longer contact times (i.e., 180 minutes). Similar results were reported as the restabilization phenomenon by Klimiuk et al. (1999).

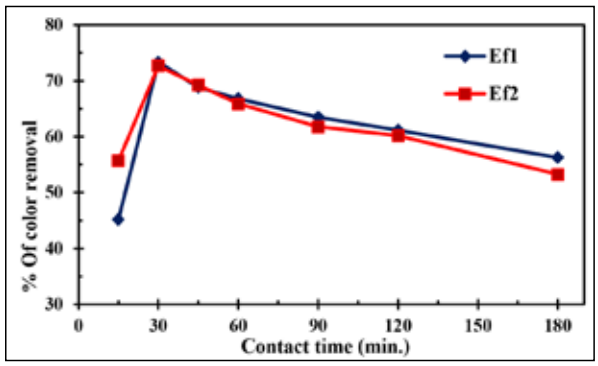

Figure 5. Effects of contact time on color removal efficiency for effluent Ef1 and Ef2 [coagulant dose 700 mg/L, pH 11.00, temp. 30 °C, mixing speed 30 and settling time 30 min.]

3.2.5 Effects of mixing speed

Mixing speed is one of the important factors in achieving higher color removal efficiency of the coagulants during the coagulation process. In this study, the effects of agitation speeds between 15 and 180 rpm were investigated. The results showed that the color removal efficiency of $FeSO_4$ increased with increasing mixing speeds between 15 and 45 rpm. These results might be caused by the fast flocs formation and high sludge precipitation rates of the inorganic coagulant. The color removal efficiency gradually decreased as the agitation speed increased. This trend showed that floc formation and breakage were intensely affected by the mixing rate (Xu et al., 2010). The highest color removal might be caused by increasing shear stress and breakage of flocs with increasing agitation speed. Figure 6 shows that the color removal efficiency was about 75% and 76% for Ef1 and Ef2, respectively, at an optimum mixing speed of 45 rpm. Similar results were observed in an experiment, which showed that about 74% of color removal was obtained by $FeSO_4$ for the cotton dyeing effluent (Xu et al., 2010).

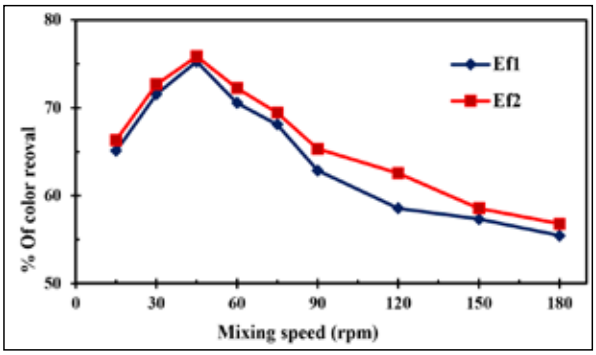

Figure 6. Effects of mixing speed on color removal efficiency for Ef1 and Ef2 [dose 700 mg/L, pH 11.00, temp. 30°C, and contact time 30 min.]

3.3 Adsorption followed by coagulation

Adsorption can be an effective and versatile method for wastewater treatment, particularly when combined with chemical treatment methods. For better effluent treatment, optimal adsorption conditions must be determined. Several studies have illustrated that optimizing the parameters greatly influences the adsorption efficiencies of color and COD (Nayl et al., 2017; Nure et al., 2017; Wasti and Awan, 2016).

3.3.1 Effects of adsorbent dose

Figure 7 shows the effect of varying the adsorbent dose on the adsorption of color from effluents. The percentage of color removal increased with increasing doses from 1.0 to 3.0 g/L up to a maximum, after which increasing the dose of IONPs did not improve color removal. This is because the active sites could be effectively utilized when the dose was low. But at higher adsorbent dosages, it is more likely that a significant portion of the available active sites remains uncovered, leading to lower specific uptake (Patel and Vashi, 2010). The number of active sites for the sorption also increases by increasing the adsorbent dose, thus increasing the amount of adsorption. When the surface active sites are covered completely, the extent of adsorption reaches equilibrium (Zobayer et al., 2013). So, it is clear that equilibrium was attained after a dose of 1.5 g/L. The maximum removal efficiencies found were 94% and 95% for Ef1 and Ef2, respectively, at doses of 1.5 g/L for both effluents.

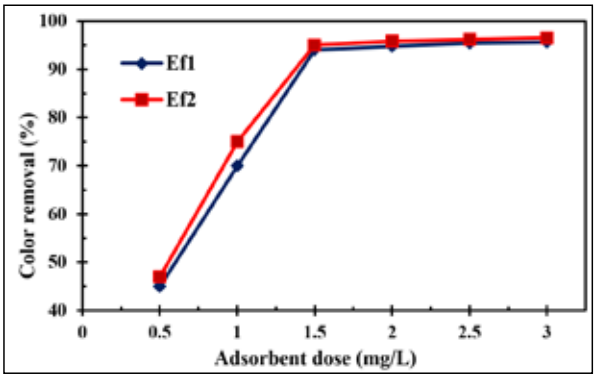

Figure 7. Effects of adsorbent dose on color removal efficiency (pH 7.0, contact time 30 min., temp. 30°C, and mixing speed 180 rpm)

3.3.2 Effects of pH

pH is an important parameter that affects the adsorption of dye molecules. The effect of the initial pH of the textile effluents on dye adsorption onto IONPs was assessed at different pH values, ranging from 2 to 12, with an optimum dose. Figure 8 shows that the maximum color removal was obtained around the neutral pH. Nevertheless, at optimum pH 6.0, more than 95 % and 96% of the color for Ef1 and Ef2, respectively, was removed by IONPs. The results showed that the adsorption was favorable in both acidic and basic environments. The electrostatic interactions between the nanoparticle surface and the functionalized dye molecule play a crucial role in the adsorption of dyes by IONPs. These interactions are greatly influenced by the pH of the sample, as it directly affects the surface charge of the nanoparticles. As the pH of zero-point charge (pHpzc) of IONPs is around 7.5 (Nassar and Ringsred, 2012), the adsorption of ionized dye on iron oxide surfaces could be due to electrostatic attraction. The surface charge is positive at pH values lower than pHzpc, neutral at pHzpc and negative at pH values higher than it. Therefore, in a relatively basic solution, pH >pHpzc, there is a high electrostatic attraction between the negatively-charged iron oxide and the positively-charged dye molecules. In contrast, as the pH of the solution falls, the proportion of positively charged sites rises while the proportion of negatively charged sites falls. This led to increased negatively charged dye adsorption but a decrease in positively-charged dye adsorption (Nassar et al., 2015). Simply to say, lower pH favors anionic dye adsorption and higher pH cationic dye adsorption and vice-versa (Salleh et al., 2011). In this study, the adsorptive dye removal was not significantly affected by solution pH, which suggests that the dye present in the textile wastewater sample might be multifunctional, and accordingly, it could be adsorbed in either basic or acidic environments (Nassar et al., 2015).

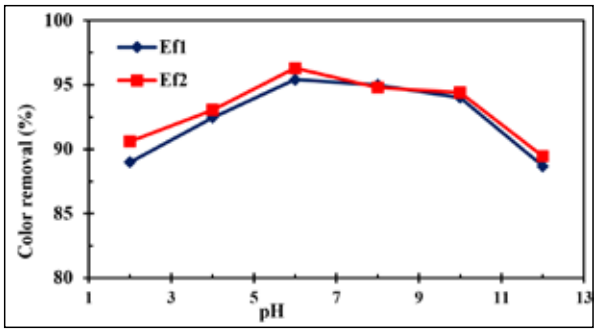

Figure 8. Effects of pH on the color removal efficiency of adsorbent (dose 1.5 g/L, contact time 30 min, temp. 30°C, and mixing speed 180 rpm)

3.3.3 Effects of contact time

Figure 9 shows the adsorption of color by IONPs as a function of contact time from 05 to 180 minutes at an adsorbent dose of 1.5 g/L at 30 °C for both effluents at pH 6.0. As seen, the adsorption was very rapid at the initial stages and then approached equilibrium just after 45 minutes i.e., the adsorption capacity increases with the increase in contact time until equilibrium is reached (Al-trawneh, 2015). This may be due to the larger surface area of IONPs at the very beginning of color adsorption. As the adsorption sites are depleted, the rate at which the dye molecules are

transported from the exterior to the interior sites of the adsorbent particles controls the dye uptake rate (Patel and Vashi, 2010). At equilibrium, about 96% and 98% of color were removed from Ef1 and Ef2, respectively (Figure 9). The relation between the removal of dyes and contact time was studied by (Hashemian et al., 2013), where adsorption increased with an increase in contact time. It was found that more than 75% of the dye removal occurred in the first 45 min., and thereafter the rate of adsorption was found to be slow. The rapid adsorption was due to the availability of the surface porosity of the adsorbent, which led to fast adsorption of dyes, the later slow rate of adsorption is due to the slow pore diffusion of the solute ion into the bulk of the adsorbent. El-Sayed et al. (2014) studied that the removal rapidly increased in the first 10 min. but then slowly increased to reach equilibrium because of the strong attraction forces between methylene blue dye and the adsorbent.

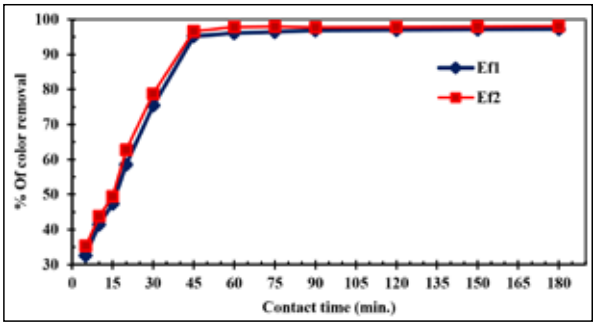

Figure 9. Effects of contact time on color removal efficiency for Ef1 and Ef2 (dose 1.5 g/L, temp. 30°C, and mixing speed 180 rpm)

3.4 Adsorption kinetics

The experimental data were fitted to the pseudo-first-order and pseudo-second-order equations as shown in Figure 10 and Figure 11. The higher R^2 values of the experimental data (greater than 0.99) and good agreement of the calculated q_e values with that of the experimental qe values at 30 °C (Table 2), recommended that the adsorption procedure followed a pseudo-second order kinetic reaction mechanism (Jafar et al., 2015).

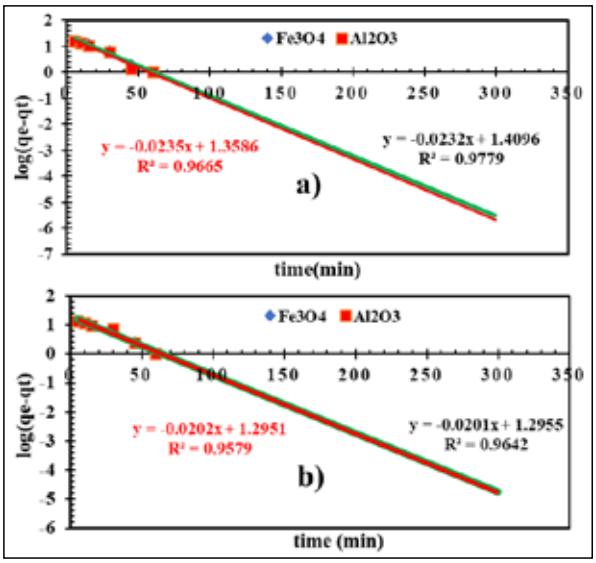

Figure 10. Pseudo -1st order kinetic plots of adsorption for textile dyeing effluents a) Ef1, and b) Ef2 onto IONPs

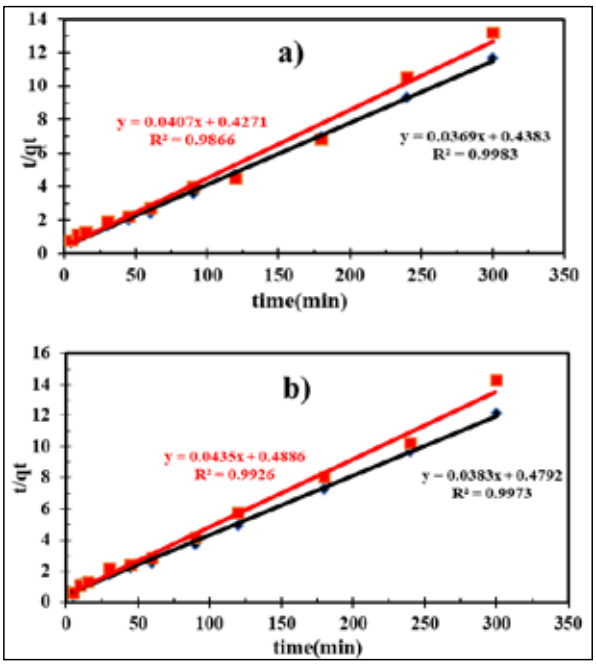

Figure 11. Pseudo -2nd order kinetic plots of adsorption for textile dyeing effluents a) Ef1, and b) Ef2 onto IONPs

Table 2. Kinetic parameters calculated by pseudo-first-order and pseudo-second-order equations for dyes adsorbed on IONPs

Parameters	Pseudo-first-order kinetics		Pseudo-second-order kinetics	
	Ef1	Ef2	Ef1	Ef2
Rate constant	0.0534	0.0462	3.1210^{-3}	3.0610^{-3}
q_e cal. (mg/g)	25.68	19.74	27.70	26.11
q_e exp. (mg/g)	24.86	23.85	25.68	19.74
R^2	0.9779	0.9642	0.9983	0.9973

3.5 Comparative studies

It has been reported by different researchers that the percentages of color removal were in the range of 6 to 74.5, using various inorganic coagulants such as $MgCl_2$, $FeSO_4$, lime, PAC, and ferric sulfate as shown in Table 3, even though the dosage was high. Alum removed about 74% color but the dosage was too high. In the present study, $FeSO_4$ coagulant proved effective as it removes 75.3%, and 76.0% color from real textile effluents Ef1 and Ef2, respectively. It indicates that different coagulant was suitable for the treatment of various types of the textile dyeing effluents.

Table 4 compares the maximum dye adsorption capacity of IONPs and other adsorbents published in the literature. In comparison, it is clear that the maximum adsorption capacity of IONPs is superior to most of other adsorbents. Although the adsorption capacity of Palladium nanoparticles AC and alumina nanoparticles is also high, the use of synthetic IONPs is much more economical than other adsorbents due to their large surface area, economic feasibility, and small diffusion resistance (Afkhami et al., 2010). Moreover, the adsorbed dye can be easily desorbed to free the adsorbent, which could be further used to treat wastewater. This suggests that the adsorption property of IONPs gives the material great potential for applications in color and COD removal from wastewater.

Table 3. Comparison of ferrous sulfate with different coagulants in color removal from textile effluents

Coagulant	Dyes / Effluents	Dose (mg/L)	% of color removal	Reference
$MgCl_2$	Effluents	2000	62	(Mohamed et al., 2014)
$FeSO_4$	textile wastewater	200	6	(Patabandige et al., 2020)
Lime	Textile effluent	700	53.9	(Zorpas et al., 2012)
PAC	Textile wastewater	30	44.5	(Bazrafshan et al., 2015)
$Fe_2(SO_4)_3$	Textile wastewater	70000	57.9	(Patel and Vashi, 2010)
Alum	Dyeing wastewater	5000	74	(Kumar et al., 2008)
Alum	Textile wastewater	70000	74.5	(Patel and Vashi, 2010)
$FeSO_4$	Dyeing effluent (Ef1)	700	75.3	This study
$FeSO_4$	Dyeing Effluent (Ef2)	700	76.0	This study

Table 4. Comparison of iron oxide nanoparticle and other adsorbents for dye removal from the dyeing effluents

Adsorbent	Dyes	Maximum adsorption capacity, (mg/g)	References
Palladium nanoparticles AC	Congo red	126.58	(Ahmadi et al., 2015)
TiO_2/GMAC	Reactive Black 5	56	(Belayachi et al., 2015)
Bentonite clay	Reactive Black 5	29.38	(Amin et al., 2015)
Kaolin	Procion brilliant red	3.51	(Rahman et al., 2013)
Sepiolite	Reactive Yellow 138:1	3.23	(Rahman et al., 2015)
Alumina nanoparticle	Color black G	263.16	(Bhargavi et al., 2015)
Sawdust Carbon	Methylene blue	12.49 - 51.4	(Salleh et al., 2011)
Ficus Carica Bast AC	Methylene blue	30-45	(Pathania et al., 2017)
Magnetite nanoparticle	Mixture of dyes (Ef1)	208.3	This study
Magnetite nanoparticle	Mixture of dyes (Ef2)	39.2	This study

3.6 Economic feasibility study

The study selected the best coagulant and adsorbent in terms of color and COD removal efficiency and compared with other treatment methods in terms of cost-effectiveness, as shown in Table 5. The economic feasibility study mainly focused on the total costs of chemical reagents. The main chemicals used in the treatment processes were $FeSO_4$ for the C-F process and synthesized Fe_3O_4 nanoparticles for adsorption. The quantity of coagulant and adsorbent required for 1 m^3 was calculated from the quantity of coagulant and adsorbent required for 1 L of effluent. The operating cost was calculated based on the recent market price in December, 2023. In comparison with other research, the present study achieved the highest percentage of color removal with the lowest cost.

Table 5. Comparison of the treatment cost with others

Sample	Coagulant + adsorbent	Amount (Kg/m^3)	% of color/COD removal	Cost ($/$m^3$)	Reference
Effluent	$Fe_2(SO_4)_3$ + Activated carbon	70 + 9	71.4	86.5	(Patel and Vashi, 2010)
Textile effluents	$Al_2(SO_4)_3$	0.6	93.12	0.75	(Couto Junior et al., 2013)
Effluent	$Al_2(SO_4)_3$ + Activated carbon	1 + 1	48.20	1.960	(Mukherjee, 2014)
Ef1	$FeSO_4$ + IONPs	0.6 + 2.5	99.0	0.45	This study
Ef2	$FeSO_4$ + IONPs	0.6 + 2.5	99.5	0.45	This study

4. Conclusion

The study used FeSO4 as a coagulant and synthesized IONPs as adsorbents to determine the effectiveness of these materials for removing color from dyeing effluents. The IONPs were synthesized by a simple co-precipitation method controlled by the pH and temperature of the reaction media. The X-RD analysis results confirmed that the synthesized iron-oxide particles were found to be within the nano-size range (10–20 µm). The optimal conditions for coagulation-flocculation (C-F) treatment were found at pH 11.0, coagulant dose 700 mg/L, reaction time 30 min, mixing speed 45 rpm, and temperature 30 °C, at which the color removal efficiency was about 75 %. The study showed that a combination of coagulation and adsorption on IONPs for the discoloration of textile effluents was more efficient than the coagulation-flocculation process alone. In the combination process, more than 99.5% color removal was achieved for both effluents. The SEM images showed the rough and porous surface of virgin IONPs having a slightly hazy and smooth surface for the adsorbed IONPs. The EDS analysis confirmed the presence of various metal ions on the IONPs surface. Finally, it can be concluded that the combination of chemical

coagulation and adsorption processes has the potential to remove color from textile wastewater.

Conflict of Interest:

The authors ensured that there was no direct or indirect involvement of human, animal, or any biological elements that have been tested that may arise any conflict of interest in this research. Moreover, the authors declare that they have no conflicts of interest in the subject matter or materials discussed in the manuscript.

Acknowledgements

One of the authors would like to thank the University Grants Commission, Bangladesh, for granting the UGC fellowship.

References

Afkhami, A., Saber-Tehrani, M., and Bagheri, H. (2010). Modified maghemite nanoparticles as an efficient adsorbent for removing some cationic dyes from aqueous solution. Desalination, 263(1-3): 240–248. https://doi.org/10.1016/j.desal.2010.06.065

Ahmadi, K., Ghaedi, M., and Ansari, A. (2015). Comparison of Nickel Doped Zinc Sulfide and/or Palladium Nanoparticle Loaded on Activated Carbon as Efficient Adsorbents for Kinetic and Equilibrium Study of Removal of Congo Red Dye. Spectrochimica Acta - Part A: Molecular and Biomolecular Spectroscopy, 136 (Part C) : 1441 - 1449, doi:10.1016/j.saa.2014.10.034.

Al-Alawy, A.F., Al-Abodi, E.E., and Kadhim, R.M. (2018). Synthesis and Characterization of Magnetic Iron Oxide Nanoparticles by Co-Precipitation Method at Different Conditions. Journal of Engineering, 24(10): 60-72. https://doi.org/10.31026/j.eng.2018.10.05

Al-trawneh, S. A. (2015). Studies on Adsorptive Removal of Some Heavy Metal Ions by Calix [4] Resorcine, Jordan Journal of Earth and Environmental Sciences Volume, 7(1): 1-9.

Amin, M.T., Alazba, A.A., and Shafiq, M. (2015). Adsorptive Removal of Reactive Black 5 from Wastewater Using Bentonite Clay: Isotherms, Kinetics and Thermodynamics. Sustainability, 7(11): 15302-15318, doi:10.3390/su71115302.

Annadurai, G., Juang, R.S., and Lee, D.J. (2002). Use of cellulose-based wastes for adsorption of dyes from aqueous solutions. Journal of Hazardous Materials, 92(3): 263-274. https://doi.org/10.1016/S0304-3894(02)00017-1

APHA. (2012). Standard methods for examination of water and waste water. 20th Ed., American Public Health Association. http://books.google.com/books?id=buTn1rmfSI4C&pgis=1

Ardejani, F.D., Badii, K., Limaee, N.Y., Shafaei, S.Z., and Mirhabibi, A.R. (2008). Adsorption of Direct Red 80 dye from aqueous solution onto almond shells: Effect of pH, initial concentration and shell type. Journal of Hazardous Materials, 151(2-3): 730-737. https://doi.org/10.1016/j.jhazmat.2007.06.048

Banat, F., Al-Asheh, S., and Al-Makhadmeh, L. (2003). Evaluation of the use of raw and activated date pits as potential adsorbents for dye containing waters. Process Biochemistry, 39(2): 193-202. https://doi.org/10.1016/S0032-9592(03)00065-7

Belayachi, H., Bestani, B., Benderdouche, N., and Belhakem, M. (2015). The Use of TiO2 Immobilized into Grape Marc-Based Activated Carbon for RB-5 Azo Dye Photocatalytic Degradation. Arabian Journal of Chemistry, 12(8): 1-10. doi:10.1016/j.arabjc.2015.06.040.

Bhargavi, R.J., Maheshwari. U., and Gupta, S. (2015). Synthesis and Use of Alumina Nanoparticles as an Adsorbent for the Removal of Zn(II) and CBG Dye from Wastewater. International Journal of Industrial Chemistry, 6(1): 31-41, doi:10.1007/s40090-014-0029-1.

Brabty, J. (2006). Coagulation and flocculation in water and waste water treatment, 2nd Ed., IWA publishing.

Bazrafshan, E., Alipour, M.R., and Mahvi, A.H. (2015). Textile Wastewater Treatment by Application of Combined Chemical Coagulation, Electrocoagulation, and Adsorption Processes. Desalination and Water, 57(20): 1-13, doi: 10.1080/19443994.2015.1027960

Chowdhury, M., Mostafa, M.G., Biswas, T.K., Mandal, A., and Saha, A.K. (2015). Characterization of the Effluents from Leather Processing Industries. Environmental Processes, 2(1): 173-187. https://doi.org/10.1007/s40710-015-0065-7

Couto Junior, O.M., Barros, M.A.S.D., and Pereira, N.C. (2013). Study on coagulation and flocculation for treating effluents of textile industry. Acta Scientiarum -Technology, 35(1): 83-88. https://doi.org/10.4025/actascitechnol.v35i1.11685

Crane, R.A., and Scott, T.B. (2012). Nanoscale zero-valent iron: Future prospects for an emerging water treatment technology. Journal of Hazardous Materials, 211-212: 112-125. https://doi.org/10.1016/j.jhazmat.2011.11.073

Deng, Y., and Zhao, R. (2015). Advanced Oxidation Processes (AOPs) in Wastewater Treatment. Current Pollution Reports, 1: 167-176. doi.org/10.1007/s40726-015-0015-z

Dahnoun, K., and Djadouni, F. (2020). Effects of Heavy-Metal Pollution on Soil Microbial Community, Plants, and Human Health, Jordan Journal of Earth and Environmental Sciences, 11(3): 234-240.

Duan, J., and Gregory, J. (2003). Coagulation by hydrolysing metal salts. Advances in Colloid and Interface Science, 100-102: 475-502. https://doi.org/10.1016/S0001-8686(02)00067-2

El-Sayed, G.O., Yehia, M.M., and Asaad, A.A. (2014). Assessment of activated carbon prepared from corncob by chemical activation with phosphoric acid. Water Resources and Industry, 7-8: 66-75. https://doi.org/10.1016/j.wri.2014.10.001

Fan, L., Zhou, Y., Yang, W., Chen, G., and Yang, F. (2008). Electrochemical degradation of aqueous solution of Amaranth azo dye on ACF under potentiostatic model. Dyes and Pigments, 76(2): 440-446. https://doi.org/10.1016/j.dyepig.2006.09.013

Fitzpatrick, C.S.B., Fradin, E., and Gregory, J. (2004). Temperature effects on flocculation, using different coagulants. Water Science and Technology, 50(12): 171-175. https://doi.org/10.2166/wst.2004.0710

Gao, B.Y., Yue, Q.Y., Wang, Y., and Zhou, W.Z. (2007). Color removal from dye-containing wastewater by magnesium chloride. Journal of Environmental Management, 82(2): 167-172. https://doi.org/10.1016/j.jenvman.2005.12.019

Ge, S., Shi, X., Sun, K., Li, C., Uher, C., Baker, J.R., Banaszak Holl, M.M., and Orr, B.G. (2009). Facile hydrothermal synthesis of iron oxide nanoparticles with tunable magnetic properties. Journal of Physical Chem C. 113(31): 13593-13599. doi.org/10.1021/jp902953t

Gil, A., Assis, F.C.C., Albeniz, S., and Korili, S.A. (2011). Removal of dyes from wastewaters by adsorption on pillared clays. Chemical Engineering Journal, 168(3): 1032-1040. https://doi.org/10.1016/j.cej.2011.01.078

Harrelkas, F., Azizi, A., Yaacoubi, A., Benhammou, A., and Pons, M.N. (2009). Treatment of textile dye effluents using coagulation-flocculation coupled with membrane processes or adsorption on powdered activated carbon. Desalination, 235(1-3): 330-339. https://doi.org/10.1016/j.desal.2008.02.012

Hashemian, S., Salari, K., Salehifar, H., and Yazdi, Z.A. (2013). Removal of azo dyes (violet B and violet 5R) from aqueous solution using new activated carbon developed from orange peel. Journal of Chemistry, 2013(8): 1-10. https://doi.org/10.1155/2013/283274

Hassan, M.A.A., Li, T.P., and Noor, Z.Z. (2009). Coagulation and Flocculation Treatment of Wastewater in Textile Industry

Using Chitosan. Journal of Chemical and Natural Resources Engineering, 4(1): 43-53. http://www.fkkksa.utm.my/jcnre/images/Vol4/dr.

Hoong, H.N.J., and Ismail, N. (2018). Removal of Dye in Wastewater by Adsorption-Coagulation Combined System with Hibiscus sabdariffa as the Coagulant. MATEC Web of Conferences, 152(01008): 1-14. https://doi.org/10.1051/matecconf/201815201008

Ho, Y.S., and McKay, G. (1998). A Comparison of Chemisorption Kinetic Models Applied to Pollutant Removal on Various Sorbents. Process Safety and Environmental Protection, 76(4): 332-40, doi:10.1205/095758298529696.

Ho, Y.S., and McKay, G. (1999). Pseudo-Second Order Model for Sorption Processes. Process Biochemistry, 34: 451-65.

Ho, Y.S., and McKay, G. (2000). The Kinetics of Sorption of Divalent Metal Ions onto Sphagnum Moss Peat. Water Research, 34(3): 735-742, doi:10.1016/S0043-1354(99)00232-8

Hossen, M.A. and Mostafa, M.G. (2023). Assessment of heavy metal pollution in surface water of Bangladesh. Environmental Challenges, 13:100783. doi.org/10.1016/j.envc.2023.100783

Islam, M.R., and Mostafa, M.G. (2022). Adsorption kinetics, isotherms and thermodynamic studies of methyl blue in textile dye effluent on natural clay adsorbent. Sustainable Water Resources Management, 8:52 (Springer). https://doi.org/10.1007/s40899-022-00640-1

Islam, M.R., and Mostafa, M.G. (2018a). Removal of a Reactive Dye from Synthetic Wastewater Using PAC and Fecl3 Coagulants. J. Life Earth Sci., 13: 39-44.

Islam, M.R., and Mostafa, M.G. (2018b). Textile Dyeing Effluents and Environment Concerns - A Review. Journal of Environmental Science and Natural Resources, 11(1-2): 131-144. https://doi.org/10.3329/jesnr.v11i1-2.43380

Jafar, B.M., Hamadneh, I., Khalili, F.I., and Al-dujaili, A.H. (2015). Kinetic Study on Adsorption of Fatty HydroxamicAcids by Natural Clays. Jordan Journal of Earth and Environmental Sciences, 7(1): 11-17.

Jindal, A., Sharma, P.S.K., Jyothi, P.M. (2016). Colour and COD Removal in Textile Effluents using Coagulation Flocculation. International Journal of Innovative Research in Science, Eng. and Tech., 5(6): 10233-10239. https://doi.org/10.15680/IJIRSET.2015.0506139

Joo, D.J., Shin, W.S., Choi, J.H., Choi, S.J., Kim, M.C., Han, M.H., Ha, T.W., Kim, Y.H. (2007). Decolorization of reactive dyes using inorganic coagulants and synthetic polymer. Dyes and Pigments, 73: 59-64. https://doi.org/10.1016/j.dyepig.2005.10.011

Junior, O.M.C., Barros, M.A.S.D., Pereira, N.C. (2013). "Study on Coagulation and Flocculation for Treating Effluents of Textile Industry." Acta Scientiarum -Technology, 35(1): 83-88, doi:10.4025/actascitechnol.v35i1.11685.

Kandisa, R.V., KV, N.S., Shaik, K.B., and Gopinath, R. (2016). Dye Removal by Adsorption: A Review. Journal of Bioremediation & Biodegradation, 7(6): 1-4. https://doi.org/10.4172/2155-6199.1000371

Karadag, D., Tok, S., Akgul, E., Ulucan, K., Evden, H., and Kaya, M.A. (2006). Combining adsorption and coagulation for the treatment of azo and anthraquinone dyes from aqueous solution. Industrial and Engineering Chemistry Research, 45(11): 3969-3973. https://doi.org/10.1021/ie060164+

Kayani, Z.N., Arshad, S., Riaz, S., and Naseem, S. (2014). Synthesis of Iron Oxide Nanoparticles by Sol-Gel Technique and Their Characterization. IEEE Transactions on Magnetics, 50(8): https://doi.org/10.1109/TMAG.2014.2313763

Khatun, M.H., and Mostafa, M.G. (2022). Optimization of Dyeing Process of Natural Dye Extracted from Polyalthia longifolia Leaves on Silk and Cotton Fabrics. Journal of Natural Fibers, Taylor & Francis. https://doi.org/10.1080/15440478.2022.2081281

Klimiuk, E., Filipkowska, U., and Korzeniowska, A. (1999). Effects of pH and Coagulant Dosage on Effectiveness of Coagulation of Reactive Dyes from Model Wastewater by Polyaluminium Chloride (PAC). Polish Journal of Environmental Studies, 8(2): 73–79.

Krans, N.A., Van Uunen, D.L., Versluis, C., Dugulan, A. ., Chai, J., Hofmann, J.P., Hensen, E.J.M., Zečević, J., and De Jong, K.P. (2020). Stability of Colloidal Iron Oxide Nanoparticles on Titania and Silica Support. Chemistry of Materials, 32(12): 5226-5235. https://doi.org/10.1021/acs.chemmater.0c01352

Kumar, P., Prasad, B., Mishra, I.M., and Chand, S. (2008). Decolorization and COD Reduction of Dyeing Wastewater from a Cotton Textile Mill Using Thermolysis and Coagulation. Journal of Hazardous Mat., 153(1-2): 635-45, doi:10.1016/j.jhazmat.2007.09.007.

Lee, J.W., Choi, S.P., Thiruvenkatachari, R., Shim, W.G., and Moon, H. (2006). Evaluation of the performance of adsorption and coagulation processes for the maximum removal of reactive dyes. Dyes and Pigments, 69(3): 196-203. doi.org/10.1016/j.dyepig.2005.03.008

Malik, P.K., and Saha, S.K. (2003). Oxidation of direct dyes with hydrogen peroxide using ferrous ion as catalyst. Separation and Purification Technology, 31(3): 241-250. https://doi.org/10.1016/S1383-5866(02)00200-9

Misau, I.M., and Yusuf, A.A. (2016). Characterization of Water Melon Seed Used as Water Treatment Coagulant. Journal of Adv. Studies in Agri., Biologi. and Env. Sci., 3(2): 22-29.

Mohamed, R.M.S.R., Nanyan, N.M., Rahman, N.A., Kutty, N.M.A., Kassim, A.H.M. (2014). Colour Removal of Reactive Dye from Textile Industrial Wastewater Using Different Types of Coagulants. Asian Journal of Applied Sciences, 2(5): 650-57, https://www.ajouronline.com/index.php/AJAS/article/view/1734.

Monira, U. and Mostafa, M.G. (2023). Leather industrial effluent and environmental concerns: a review. Sustainable Water Res. Management, 9: 181, doi.org/10.1007/s40899-023-00969-1

Mostafa, M. G. and Hoinkis, J. (2012). Nanoparticles Adsorbent for Arsenic Removal from Drinking Water: A Review. International Journal of Environmental Science, Management and Engineering Research, 1(1): 20-31(India). http://www.ijesmer.com

Mostafa, M.G., Chen, Y.H., Jean, J.S., Liu, C.C. and Lee, Y.C. (2011). Kinetics and mechanism of arsenate removal by nanosized iron oxide-coated perlite. Journal of Hazardous Materials, 187: 89-95. https://doi.org/10.1016/j.jhazmat.2010.12.117

Mukherjee, S. (2014). Studies on removal of organic and inorganic load from waste water using coagulation-flocculation and advanced techniques. PhD thesis, Maulana Abul Kalam Azad University of Technology, West Bengal, India. Retrieved from https:// library.wbut.ac.in/cgi-bin/koha/opacretrieve-file.pl

Nassar, N.N., Marei, N.N., Vitale, G., and Arar, L.A. (2015). Adsorptive removal of dyes from synthetic and real textile wastewater using magnetic iron oxide nanoparticles: Thermodynamic and mechanistic insights. Canadian Journal of Chemical Engineering, 93(11): 1965-1974. https://doi.org/10.1002/cjce.22315

Nassar, N.N., and Ringsred, A. (2012). Rapid adsorption of methylene blue from aqueous solutions by goethite nanoadsorbents. Environmental Engineering Science, 29(8): 790-797. https://doi.org/10.1089/ees.2011.0263

Nayl, A.E.A., Elkhashab, R.A., El Malah, T., Yakout, S.M., El-Khateeb, M.A., Ali, M.M.S., and Ali, H.M. (2017). Adsorption studies on the removal of COD and BOD from treated sewage using activated carbon prepared from date palm waste. Environmental Science and Pollution Research, 24(28): 22284-22293. https://doi.org/10.1007/S11356-017-9878-4

Nourmoradi, H., Zabihollahi, S., Pourzamani, H.R. (2015). Removal of a common textile dye, navy blue (NB), from aqueous solutions by combined process of coagulation–flocculation followed by adsorption. Desalination and Water Treatment, 57(11): 5200-5211. https://doi.org/10.1080/19443994.2014.1003102

Ntuli, F., Kuipa, P.K., Muzenda, E. (2011). Designing of sampling programmes for industrial effluent monitoring. Environmental Science and Pollution Research, 18(3): 479-484. https://doi.org/10.1007/s11356-010-0395-y

Nure, J.F., Shibeshi, N.T., Asfaw, S.L., Audenaer, W., and Hulle, S.W.V. (2017). COD and colour removal from molasses spent wash using activated carbon produced from bagasse fly ash of matahara sugar factory, Oromiya region, Ethiopia. Water SA, 43(3): 470-479. https://doi.org/10.4314/wsa.v43i3.12

Papić, S., Koprivanac, N., Lončarić Božić, A., and Meteš, A. (2004). Removal of some reactive dyes from synthetic wastewater by combined Al(III) coagulation/carbon adsorption process. Dyes and Pigments, 62(3): 291–298. https://doi.org/10.1016/S0143-7208(03)00148-7

Patabandige, D.S.B.T., Wadumethrige, S.H., and Wanniarachchi, S. (2020). Decolorization and Cod Removal from Synthetic and Real Textile Dye Bath Wastewater Containing Reactive Black 5. Desalination and Water Treatment, 197: 392-401, doi:10.5004/dwt.2020.25954.

Patel, H., and Vashi, R.T. (2010). Treatment of Textile Wastewater by Adsorption and Coagulation. E-Journal of Chemistry, 7(4): 1468-1476.

Patel, H., and Vashi, R.T. (2015). Use of Naturally Prepared Coagulants for the Treatment of Wastewater from Dyeing Mills. In Characterization and Treatment of Textile Wastewater. Butterworth Heinemann, Elsevier, 225 Wyman Street, Waltham, MA 02451, USA. https://doi.org/10.1016/b978-0-12-802326-6.00006-x

Pathania, D., Sharma, S., and Singh, P. (2017). Removal of methylene blue by adsorption onto activated carbon developed from Ficus carica bast. Arabian Journal of Chemistry, 10(1): S1445-S1451. https://doi.org/10.1016/j.arabjc.2013.04.021

Patil, M.R., and Shrivastava, V.S. (2015). Adsorption removal of carcinogenic acid violet19 dye from aqueous solution by polyaniline-Fe2O3 magnetic nano-composite. Journal of Materials and Environmental Science, 6(1): 11-21.

Perng, Y.S., and Bui, H.-M. (2014). Decolorization of reactive dyeing wastewater by ferrous ammonium sulfate hexahydrate. J. of Vetnamese Env., 5(1): 27-31. doi.org/10.13141/JVE

Qasim, W., and Mane, A.V. (2013). Characterization and treatment of selected food industrial effluents by coagulation and adsorption techniques. Water Resources and Industry, 4: 1-12. https://doi.org/10.1016/j.wri.2013.09.005

Rahim, M.A., and Mostafa, M.G. (2021). Impact of Sugar Mills Effluent on Environment around Mills Area, AIMS Environmental Science, 8(1): 86-99. doi: 10.3934/environsci.2021006

Rahman, A., Kishimoto, N., Urabe, T. (2015). Adsorption Characteristics of Clay Adsorbents - Sepiolite, Kaolin and Synthetic Talc-for Removal of Reactive Yellow 138:1. Water and Environment Journal, 29(3): 375-82, doi:10.1111/wej.12131.

Rahman, A., Urabe, T., Kishimoto, N. (2013). Color Removal of Reactive Procion Dyes by Clay Adsorbents. Procedia Env. Sci., 17: 270-78, doi:10.1016/j.proenv.2013.02.038.

Rafatullah, M., Sulaiman, O., Hashim, R., and Ahmad, A. (2010). Adsorption of methylene blue on low-cost adsorbents: A review. Journal of Hazardous Materials, 177(1-3): 70-80. https://doi.org/10.1016/j.jhazmat.2009.12.047

Rodrigues, C.S.D., Madeira, L.M., and Boaventura, R.A.R. (2013). Treatment of textile dye wastewaters using ferrous sulphate in a chemical coagulation/flocculation process. Environmental Technology, 34(6): 719-729. https://doi.org/10.1080/09593330.2012.715679

Saha, M.K., Ara, R., Kadir, S.D., and Mostafa, M.G. (2021). Environmental Vulnerability of people to Brick Kiln Hazards. SPC Journal of Env. Sci., 3(1): 23-31. doi: 10.14419/jes.v3i1.31609

Salleh, M.A.M., Mahmoud, D.K., Karim, W.A.W.A., and Idris, A. (2011). Cationic and Anionic Dye Adsorption by Agricultural Solid Wastes: A Comprehensive Review. Desalination, 280(1-3), 1-13, doi:10.1016/j.desal.2011.07.019

Salvador, M., Gutiérrez, G., Noriega, S., Moyano, A., Blanco-López, M.C., and Matos, M. (2021). Microemulsion synthesis of superparamagnetic nanoparticles for bioapplications. Int. Journal of Molecular Sciences, 22(1): 1-17. https://doi.org/10.3390/ijms22010427

Sayed, M.A. and Mostafa, M.G. (2023). Characterization of Textile Dyeing Effluent and Removal Efficiency Assessment of Al2(SO4)3 Coagulant. Asian Journal of Applied Science and Technology (AJAST), 7(3): 195-212. DOI: https://doi.org/10.38177/ajast.2023.7314

Sayed, M.A., and Mostafa, M.G. (2021). Efficiency Assessment of FeSO4 Coagulant on Yarn Dyeing Industrial Effluent. BAUET JOURNAL, 3(1), 50-58. https://journal.bauet.ac.bd/wp-content/uploads/2021/12/Art-6-.pdf.

Shakil, M.S.Z., and Mostafa, M.G. (2021). Water Quality Assessment of Paper Mills Effluent Discharge Areas. Al-Nahrain Journal of Science, 24 (3): 63-72.

Slama, H.B., Bouket, A.C., Pourhassan, Z., Alenezi, F.N., Silini, A., Cherif-Silini, H., Oszako, T., Luptakova, L., Golińska, P., and Belbahri, L. (2021). Diversity of Synthetic Dyes from Textile Industries, Discharge Impacts and Treatment Methods. Applied Sciences (Switzerland), 11(14): 1-21. https://doi.org/10.3390/app11146255

Suman, A., Ahmad, T., and Ahmad, K. (2018). Dairy wastewater treatment using water treatment sludge as coagulant: a novel treatment approach. Environment, Development and Sustainability, 20(4): 1615-1625. https://doi.org/10.1007/s10668-017-9956-2

Tareque, M.H., Islam, M.A., and Mostafa, M.G. (2023). Photocatalytic decomposition of textile dyeing effluents using TiO2, ZnO, and Fe2O3 catalysts. Nep J Environ Sci, 10(2): 49-58. https://doi.org/10.3126/njes.v10i2.46704

Unni, M., Uhl, A.M., Savliwala, S., Savitzky, B.H., Dhavalikar, R., Garraud, N., Arnold, D.P., Kourkoutis, L.F., Andrew, J.S., and Rinaldi, C. (2017). Thermal Decomposition Synthesis of Iron Oxide Nanoparticles with Diminished Magnetic Dead Layer by Controlled Addition of Oxygen. ACS Nano, 11(2): 2284-2303. https://doi.org/10.1021/acsnano.7b00609

Wasti, A., and Awan, M.A. (2016). Adsorption of textile dye onto modified immobilized activated alumina. Journal of the Association of Arab Universities for Basic and Applied Sciences, 20: 26-31. https://doi.org/10.1016/j.jaubas.2014.10.001

Wijannarong, S., Aroonsrimorakot, S., Thavipoke, P., Kumsopa, A., and Sangjan, S. (2013). Removal of Reactive Dyes from Textile Dyeing Industrial Effluent by Ozonation Process. APCBEE Procedia, 5: 279-282. https://doi.org/10.1016/j.apcbee.2013.05.048

Wojnárovits, L., and Takács, E. (2008). Irradiation treatment of azo dye containing wastewater: An overview. Radiation Physics and Chemistry, 77(3): 225-244. https://doi.org/10.1016/j.radphyschem.2007.05.003

Wong, P.W., Teng, T.T., and Norulaini, N.A.R.N. (2007). Efficiency of the coagulation-flocculation method for the treatment of dye mixtures containing disperse and reactive dye. Water Quality Research Journal of Canada, 42(1): 54-62. https://doi.org/10.2166/wqrj.2007.008

Xu, W., Gao, B., Yue, Q., Wang, Y. (2010). Effect of shear force

and solution pH on flocs breakage and re-growth formed by nano-Al13 polymer. Water Research, 44(6): 1893-1899. https://doi.org/10.1016/j.watres.2009.11.029

Zahedi, M., Shakerian, A., Rahimi, E., and Sharafati C.R. (2020). Determination of Synthetic Dyes in Various Food Samples of Iran's Market and their Risk Assessment of Daily Intake. Egyptian J. of Veterinary Sci., 51(1): 23-33. https://doi.org/10.21608/ejvs.2019.16590.1095

Zobayer, B.M.M., Mahmudul, H.M., Kaniz, F., Islam, M.M.S., Rahman, K.M., and Akhtarul, I.M. (2013). Treatment of Textile Effluent of Fokir Knitwear in Bangladesh Using Coagulation-Flocculation and Adsorption Methods. International Research Journal of Environmental Sciences, 2(6): 49-53.

Zorpas, A.A., Voukallib, I., Loizia, P. (2012). Chemical Treatment of Polluted Waste Using Different Coagulants. Desalination and Water Treatment, 45(1-3): 291-96, doi:10.1080/19443994.2012.692043

JJEES

JJEES (2024) 15 (4): 298-306
ISSN 1995-6681

Jordan Journal of Earth and Environmental Sciences

Assessment of Water Consumption in Water Scarce Regions by Using Statistical Analysis: A Case Study of El-Maten Region, Lebanon

Fatima Abou Abbass [1, 3*], Nada Nehme[1], Bachar Koubaissy[2], Zeinab Ibrahim[3], Rabih Khalife[4], Rita Zahran[1], Jihane Karameh[5], Khaled Tarawneh[6]

[1]Faculty of Agricultural Engineering and Veterinary Medicine, Lebanese University, Dekwaneh, Lebanon.
[2]Faculty of Science, Lebanese University, Branch 5, Nabatieh, Lebanon.
[3]Doctoral school of science and technology, Hadath, Lebanon.
[4]Faculty of Engineering, Lebanese University, Branch 2, Roumieh, Lebanon.
[5]Department of Statistics, CNAM-ISSAE, Beirut, Lebanon.
[6]Mining and Mineral Engineering Department, Faculty of Engineering, Al Hussein Bin Talal University, Jordan.

Received on October 3, 2024; Accepted on November 6, 2024

Abstract

Water resources in the Middle East, a scarce water region, are of paramount importance for sustaining both biotic and abiotic systems. However, these resources face significant stress due to climate change and increasing demand driven by human development. Lebanon, located in a sub-humid climatic zone along the Eastern Mediterranean, presents a unique case for water scarcity. This study assesses domestic and sectorial water consumption in the El-Maten Region of Lebanon. It aims at identifying the key factors, impacting water supply. A total of 441 surveys were collected from household consumers in the region, and the data were processed using IBM SPSS (v. 25) for statistical analysis. The findings indicate that the average daily water consumption per capita is 150 liters. Water availability issues were reported by 34% of the surveyed population, while 56% expressed concerns about water quality. In order to meet their needs, 48% of consumers resorted to secondary water sources, such as vendors, springs, rainwater harvesting, or wells. The study concludes that over one-third of the consumers experience water shortages throughout the year, while more than their half face problems with the water quality they receive. These findings underline the inefficiencies in the current water distribution systems, and suggest the need for improvements in both infrastructure and governance. In this respect, the study calls for immediate policy interventions focused on improving water quality standards to ensure sustainable water supply throughout the year. It is also important to address climate change impacts through strengthening water conservation practices and enhance public awareness toward sustainable water resource management in Lebanon.

Keywords: *Climate Change, Water Supply, Scarcity, Sustainability, Lebanon.*

1. Introduction

Water is a crucial resource to all aspects of life as it supports the biological functions of living beings and makes habitat for numerous species, in addition to its role in sustaining ecosystems. Climate change significantly impacts water resources, particularly due to population growth and increases water consumption for irrigation and agriculture, causing stress on the planet and its ecosystems (Cloy and Smith, 2015), (Haddeland et al., 2014). There are shifts reported in the hydrological cycle and changes in evapotranspiration, humidity, precipitations, runoff and other factors that are creating different water distribution and regimes (Hagemann et al., 2013). Water scarcity is a global geo-environmental issue, worsened by population growth and climate change, particularly in the Mediterranean region, including Lebanon, where imbalanced supply/demand exists (Abou Abbass et al., 2023).

Lebanon, a small country with a population of around 4.8 million, is a biodiversity hotspot due to its unique natural characteristics and 220 km coastal length (Skaf et al., 2019; Myers et al., 2000). Lebanon's diverse physiography, characterized by three major geomorphological features: Mount-Lebanon, Bekaa Plain, and Anti-Lebanon, creates a climatic barrier that captures wet air masses, resulting in high precipitation rates including rainfall and snow (Shaban, 2019).

The quantity of water obtained from the public water sector is typically regarded as the water supply; however, alternate sources of supply are used when this quantity is not enough to meet consumer demands (Shaban, 2019). The vast majority of water comes from groundwater boreholes, bottled water, water commerce, harvested water, and pipes that the public water sector obtains (Shaban, 2016).

Lebanon faces environmental issues like desertification, land degradation, and water scarcity due to climate change, affecting precipitation, dry periods, and warmer meteorological conditions (Lelieveld et al., 2012; Haddad et al., 2014). Therefore, the agriculture sector is highly

* Corresponding author e-mail: fatima.abouabbass@ul.edu.lb

influenced by water scarcity, and thus, only around 50% of cultivated lands in Lebanon are irrigated. They suffer from drought spells and decrease in crop yields (Haddad et al., 2014). In addition, the extreme temperature, irregular weather patterns, and water-related consequences also affect the crops (Lesk et al., 2016).

Furthermore, Lebanon occupies 14 major rivers, more than 30 major streams, two thousand springs (> 10 l/sec), along with other water surface and groundwater resources, thus, the quantity and quality of the water resources in Lebanon are endangered. Water replenishment is changed because of deforestation, soil erosion, drainage methods, irrigation practices, and other activities. This will lead to more water scarcity and deteriorates water quality (Nehme et al., 2019; Nehme et al., (2021) (a) and (b)). Moreover, pollution is widespread across Lebanon, where pristine water sources are scarce. Rivers suffer from contamination and many aquifers exhibit elevated pollution levels (Nehme and Haydar, 2018; Nehme et al., 2019; Nehme et al., 2020; Haydar et al., 2022).

The amount and quality of water are impacted by careless water use. However, there are differences in water consumption around the world. One example of this is the water footprint variance (Hoekstra and Chapagain, 2007), which shows that patterns of water use vary greatly between geographical areas and are influenced by a variety of factors.

Water used for domestic purposes includes both outdoor and indoor applications. On the other side, outdoor water usage includes mainly car washes and watering gardens, while indoor water uses include drinking, bathing, and laundry (Grimble, 1999). The amount of water daily required by each individual to meet their household's needs is known as domestic water per capita consumption (World Health Organization, WHO, 2011).

This study aims to quantitatively assess water consumption in Lebanon's El-Maten Region, updating estimates, understanding socioeconomic characteristics, and proposing technical solutions to address the water crisis due to climate change and population growth, focusing on primary and secondary resources.

2. Materials and Methods

2.1. Study area

With about 2,032,600 inhabitants, Mount Lebanon is the most densely populated region in Lebanon and accounts for 42% of the nation's total population. The districts of Baabda, El-Maten, Aley, Chouf, Keserwan, and Jbeil make up the region. Geographically, El-Maten region lies between 300 and 2,100 meters above sea level in the Lebanon. It has a population of 511,000 people and accounts for 10.6% of Lebanon's population and has the second highest number of households in Mount Lebanon, most of which are apartments. The average household size in El-Maten is 3.5 persons, slightly lower than the national average of 3.8 (Central Administration of Statistics - District Statistics Based on the Labour Force and Household Living Conditions Survey 2018-2019).

Figure 1. Map showing the study area of El-Maten Region.

2.2. Methodology

In order to calculate the consumption patterns and regimes among the population of El-Maten, an inventory and field research were done, along with a survey targeting valuable information about water consumption.

The household water consumption survey comprised three sections, while the field survey included a general section on socio-demographic information, followed by detailed sections on water consumption across various sectors in the Maten Region. Data collection was conducted using both traditional hard-copy surveys and an electronic version via the "Google Forms" platform (Figure 2).

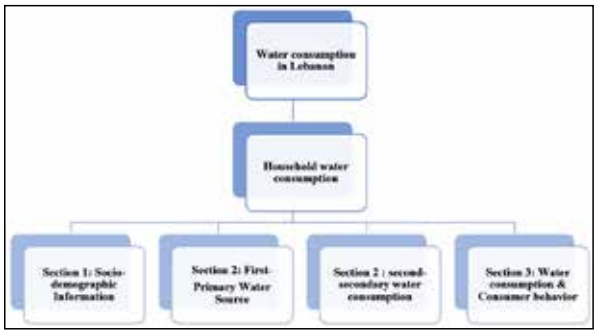

Figure 2. The organization structure of the Google form.

A pilot test was carried out to evaluate the effectiveness of the survey procedures before the full questionnaire was administered to gather data from households and sectors (Okimiji et al., 2021). The goal was to ensure a representative sample by including a diverse range of individuals from various demographic groups. Participation in the survey was anonymous and voluntary. A total of 441 responses were collected and focused on household water consumption, distributed throughout the study area.

2.3. Statistical Data Analysis

Descriptive statistics, such as frequency, percentage, mean, and standard deviation were used to summarize the data. In order to investigate the relationships and connections between independent variables (demographic and socioeconomic) and dependent variable Y (monthly water usage of households), non-parametric statistical methods (such as the Chi-square test of independence) were performed (Motho et al., 2022).

A Microsoft Office Excel file was adopted, and data was then treated using SPSS (v 25). In the study, the key characteristics of the data are described using descriptive statistics. It gives brief explanation of the measures and the sample. It serves as the foundation for almost all quantitative data analyses, along with basic graphic analysis. Pearson Chi-Square tests were used with a significance level of 0.05 in all the Pearson Chi-Square tables for relationship between categorical variables study.

2.4. Demographic Values

The general survey covers 441 samples, taken from the villages of Dekwaneh, Mansouriye, Fanar, Douar, Ain Saadeh, Jdeideh, Sin El Fil, Broumana, Bsalim, Zalka, Bourj Hammoud, Biaqout, Sabtiyeh and Sad El Baouchrieh. Other villages were put under the category of others in Table 1.

Table 1. Distribution of survey numbers over the villages.

El- Maten Region	Number of surveyed people in each village of El-Maten Region
Dekwaneh	168
Mansouriye	47
Fanar	20
Douar	16
Ain Saadeh	14
Jdeideh	13
Sin el Fil	11
Broumana	10
Bsalim	10
Zalka	10
Bourj Hammoud	10
Biaqout	8
Sabtiyeh	8
El Baouchrieh	7
Other Villages	89
Total	**441**

3. Results and discussion

3.1. Water Consumption for Household in El-Maten

The social and demographic composition of a community is described by socio-demographic parameters, which are essential for understanding and predicting patterns within population. Socioeconomic factors, such as occupation, education, and income are linked to demographic elements like population size, growth, density and distribution. In this study, the influence of various socio-demographic characteristics on water consumption was analyzed. 66% of the survey participants were females, and 34% were males, indicating that women, who are less busy, interested, or available, were more likely to participate. Participants came from diverse age groups, and their distribution is shown in Figure 3. This finding aligns with previous research that has demonstrated a significant correlation between gender and household water demand (Fielding, et al., 2012; Jordán-Cuebas et al., 2018; Joshi, 2020; Makki, et al., 2003; Van Koppen, 2001).

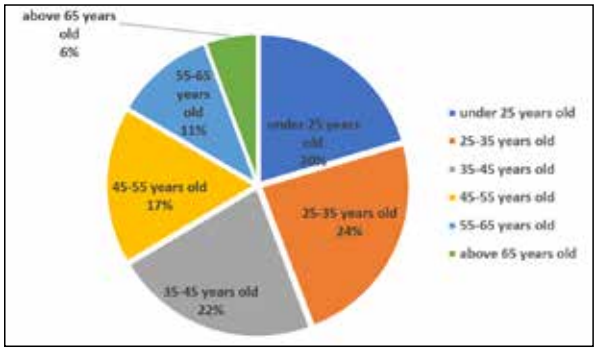

Figure 3. Distribution of the general survey participant's age groups in El- Maten Region.

The results in Figure 4 show the educational level of surveyed participants. The majority of participants (46%) holds postgraduate degrees, while only 1% of participants are uneducated. This is consistent with the idea that more educated individuals are generally more comfortable using applications and platforms like Google Forms for surveys.

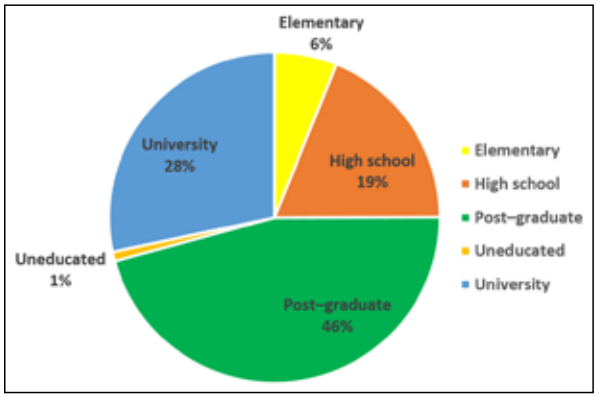

Figure 4. Percentage of surveyed educated participants in El- Maten Region.

Participants were spread between private and public sector, with students and other different occupations, which is shown in Figure 5.

The data suggest a clear trend of household downsizing in the El-Maten Region, with a significant rise in single- and two-person households and a general decline in larger family units. As shown in Figure 6, one-person households represent a remarkable 28% of the total, reflecting a shift towards more individualized living arrangements. Two-person households are the most common, making up 40% of the total survey in contrast. Four-person households account for only 5%. Similarly, three-person households comprise 16% of the total, while five-person households show a slight decrease, making up just 2%. This trend aligns with findings by Schleich and Hillenbrand's (2009) study in Germany, which reported that smaller household sizes tend to have a higher per capita water demand.

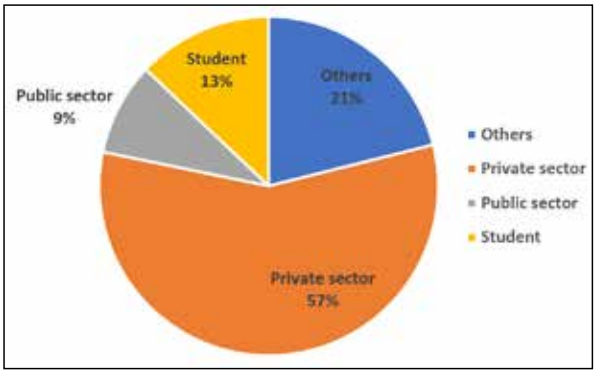

Figure 5. Distribution of the participants' occupation in El- Maten Region.

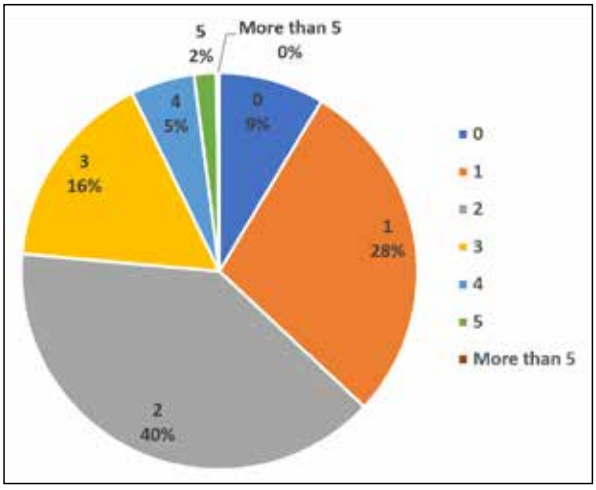

Figure 6. The number of people per household in El-Maten Region.

The majority of participants (68%) has household earnings of more than 500 $ per month, as shown in Figure 7. In the El-Maten Region, 2% of participants earn less than 100 $ per month, and 9% of participants report earning between 100 $ and 300 $ per month.

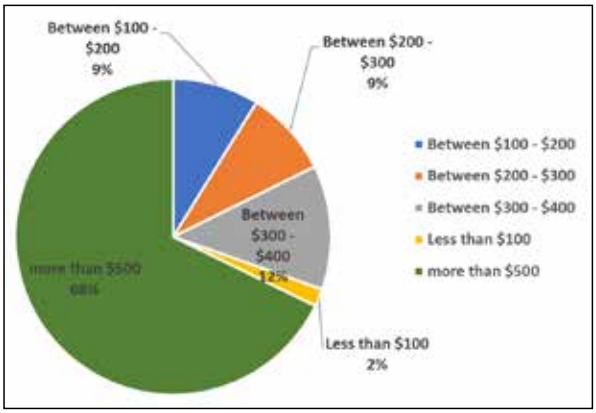

Figure 7. Distribution of the income per household in El-Maten Region.

3.2. Water Use: Primary and Secondary Resources

According to the surveyed units, 71% of the cases, the government's public water supply served as the main source of water. However, other primary sources included private wells, springs, and water harvesting, which accounted for the remaining percentage (Figure 8).

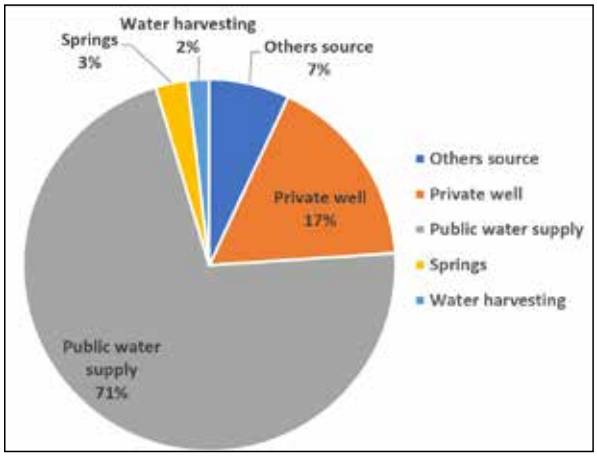

Figure 8. Distribution of primary water sources in El- Maten Region.

A full year of water availability issues was reported by 34% of participants, while 45% experienced issues during summer, and 14% during autumn as shown in Figure 9. Water availability in summer is often dependent on the volume of precipitated water during the winter and spring months. Lebanon's water resources are abundant, but seasonal climate, infrastructure issues, and regional disparities lead to varying water availability throughout the year.

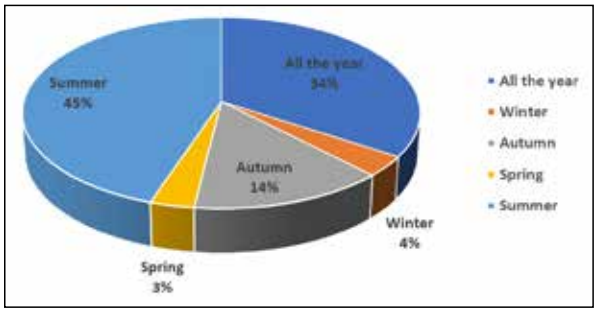

Figure 9. Seasonal availability issue of the primary water resource in El- Maten Region.

Approximately 56% of participants reported issues with the water quality from their primary source, facing various problems such as muddy water, unpleasant odor, and changes in taste, color, diseases, and other concerns.

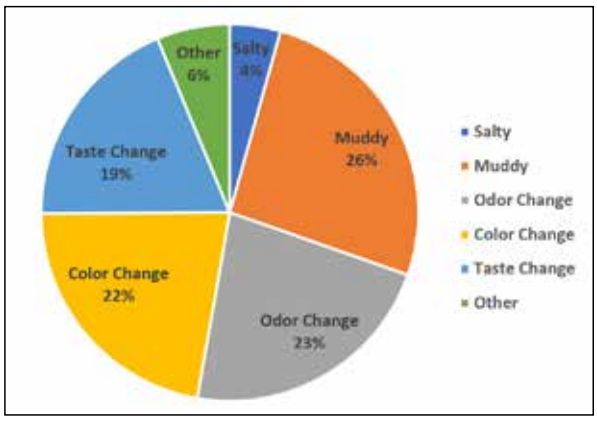

Figure 10. Percentages of water quality problems encountered in El-Maten Region.

As shown in Figure 11, only about half of the participants relies solely on their primary water source, while approximately 48% of surveyed households depend on a secondary water source to meet their water needs. These secondary sources include vendors, springs, rainwater harvesting, or wells, underscoring the necessity of diversified water supply strategies in water-stressed regions.

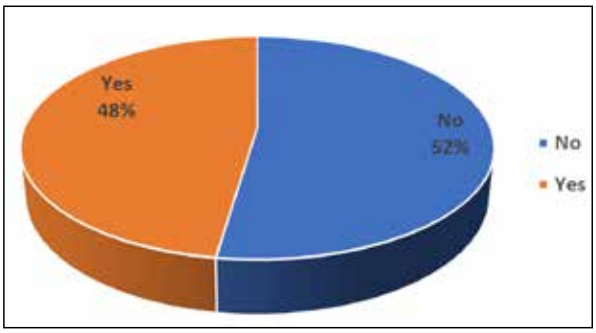

Figure 11. Presence of a secondary water source in El- Maten Region.

Agricultural use can be considered as lower for secondary water sources due to the higher cost associated with application uses. In contrast, the reliance on secondary sources for drinking water was higher, which can be attributed to low satisfaction levels with the quality and safety of drinking water from primary sources (as shown in Figures 12 and 13). This highlights the critical issue of access to safe drinking water, driving many households to seek alternative sources.

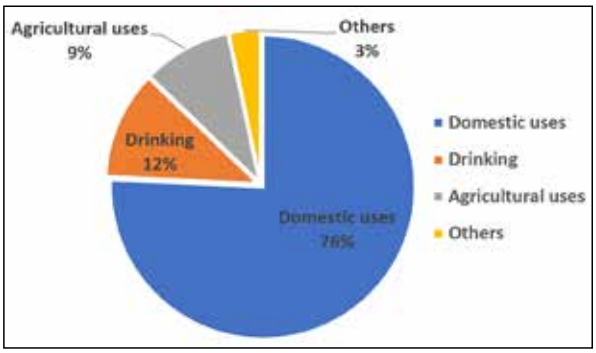

Figure 12. Purposes of use of the primary water resource in El-Maten Region

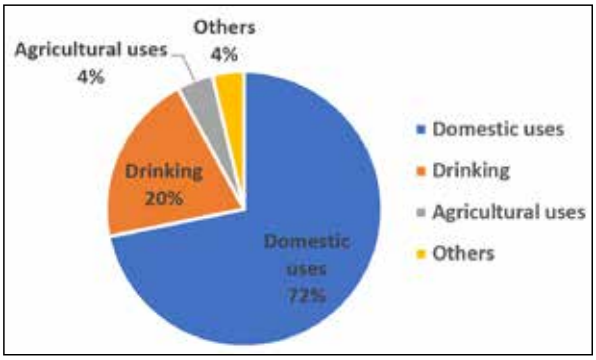

Figure 13. Purposes of use of the secondary water resource in El-Maten Region.

Income plays a significant role in influencing water consumption, as customers tend to adjust their water use based on price levels. Households with higher income consume more water than those with lower income. The consumption increasing as income rises and decreasing when the primary breadwinner loses employment (Willis et al., 2013; Agthe and Billings, 2002). However, due to inconsistent public water service provision, 48% of households also rely on water trucks as an additional source. 16% of consumers purchased more than 20 barrels (1 barrel equal to 200 liter) of water per month, with one barrel equaling 200 liters (Figure 14). The cost of water varied, with prices ranging from less than 1 USD per barrel to over 3 USD per barrel, as illustrated in Figure 15.

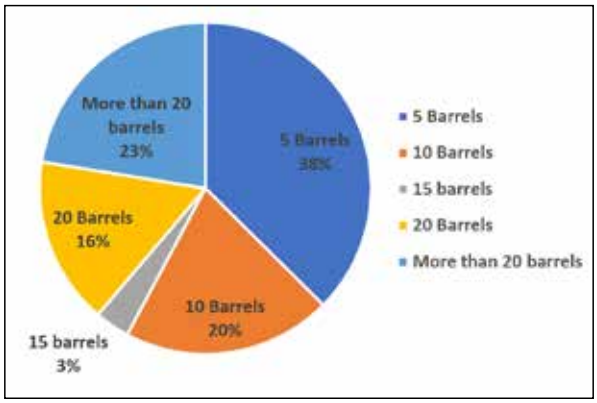

Figure 14. Purchased water percentages in El- Maten Region.

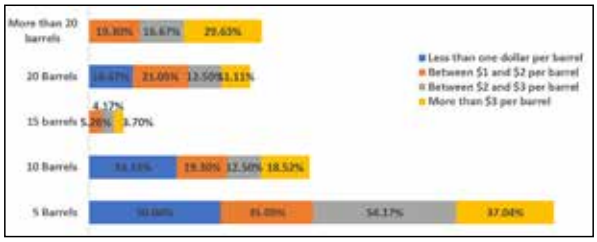

Figure 15. Variation of the amount of money paid on extra water resources with bought quantity in El- Maten Region.

The proportion of individuals with higher education degrees is greater among those with medium to high levels of water knowledge, as shown in Figure 16.

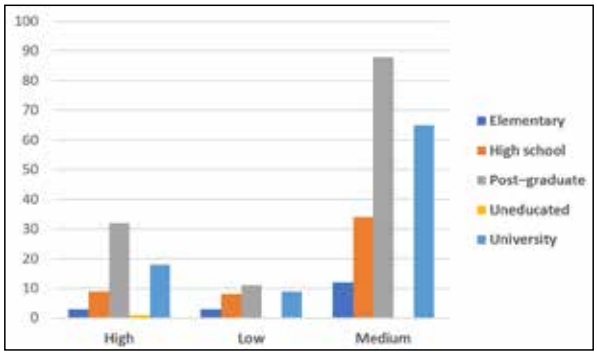

Figure 16. Assessment of the knowledge about water resources with respect to the educational level in El- Maten Region.

While most participants are well-educated and reported as having moderate to high awareness of water-related issues, only 10% indicated in the Figure 17. That is due to the installation of water-saving devices such as low-flow showerheads, sensors, or flow restrictors in their homes. This suggests that water conservation is not effectively promoted through current knowledge or innovative approaches targeted at building professionals, homeowners, or practitioners, indicating a need for better guidance and

incentives in adopting water-saving technologies. Reduced water consumption could impact employment in agriculture and industry but may also create new opportunities in water management and conservation, depending on economic adaptation.

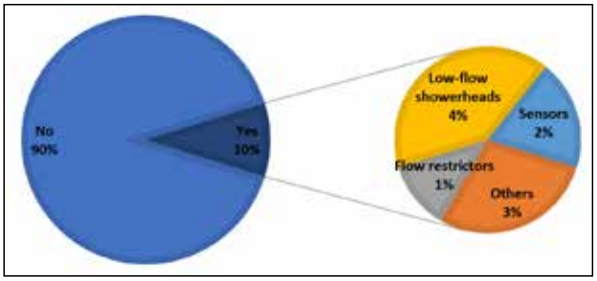

Figure 17. Installation of water-saving devices at home in El-Maten Region.

Approximately two-thirds of participants expressed dissatisfaction with their access to safe drinking water, leading 93% to prefer bottled water as the primary source. Additionally, about two-thirds of the participants indicated a willingness to pay more for sustainable water solutions.

Sustainability is increasingly becoming a priority for consumers in their purchasing decisions. The results indicated that 65% of surveyed consumers were willing to pay more, even beyond their current water bill to improve water supply and support sustainable water solutions. This demonstrates a growing recognition of the importance of sustainability in water management.

The survey on drinking water needs varies across age groups due to differences in body composition, activity levels, and overall health. The quantity of drinking water consumed, as shown in Figure 18, predominantly ranges between 1 and 2 liters/day/capita across all age groups.

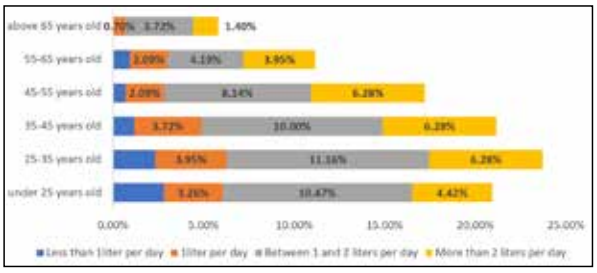

Figure 18. Drinking water consumption by age group in El-Maten Region.

3.3. Data Analysis

To estimate the monthly water consumption per capita (in liters) in the El-Maten Region, Figure 19 outlines the steps used for calculation. The total water consumption per capita is the sum of water from primary and secondary sources. The quantity from primary sources was calculated by using these formul

- $Quantity\ from\ primary\ source\ = (Availability\ from\ Primary\ Water\ Source/month) \times (\ water\ tank\ used\ in\ home) \times (Water\ Tank\ Capacity/barrel)$
- $Quantity\ from\ primary\ source\ per\ capita\ /barrel = \frac{Quantity\ from\ primary\ source}{number\ of\ household}$
- $Quantity\ from\ primary\ source\ per\ capita\ by\ litre\ = (Quantity\ from\ primary\ source\ per\ personby\ barrel) \times 200\ litre$

The quantity from secondary sources was determined by using these formulas:

- $Quantity\ from\ secondary\ source = Regularity\ of\ Water\ Purchases\ from\ Vendors \times Quantity\ of\ Water\ Purchased\ per\ Occasion$

The findings of this study reveal that the average monthly water consumption per capita is 4,501 liters in the El-Maten Region, which equates to an average daily consumption of 150.048 liters per capita. Water consumption levels in El-Maten show that 48% of the population consumes less than 75 liters per day, while 23% fall under the normal consumption level, and 29% are categorized as having higher-than-average consumption (Figure 19).

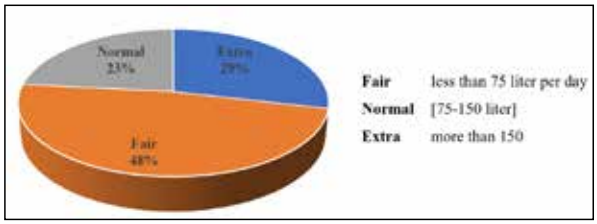

Figure 19. Level of water consumption per day per capita in El-Maten Region.

Figure 20 shows the average of monthly water consumption per capita if consumers use water for watering gardens and washing their cars equal (and other uses) to 5953 liters per capita, two times more than consumers that did not use water for gardens and cars 3541 liters per capita. Consumers that wash their cars but they do not have a garden consume 672 liters per capita less than consumers that they do not watering gardens or washing cars.

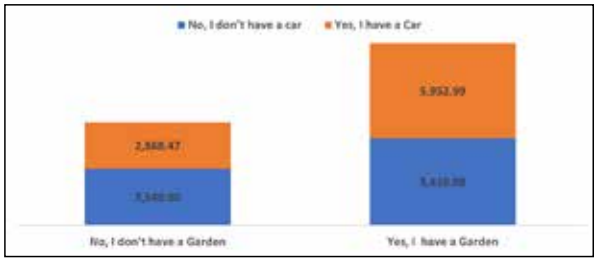

Figure 20. Average of monthly water consumption (liter per capita) with washing cars and watering gardens in El-Maten Region.

3.4. Water Consumption Per Capita among Socio- Economic Characteristics

The findings of this study reveal that respondents with university education have the highest average water consumption, at 4,885 liters per capita. In comparison, respondents with high school education consume an average of 3,347 liters per capita, while those without formal education have the lowest consumption, averaging 2,616 liters per capita (Figure 21). These findings align with previous studies, such as Clarke and Brown (2006) in Melbourne, Villar-Navascués and Alfredo (2018) in municipalities along the Spanish Mediterranean coast, and Fan et al., (2013) in the Yangling District, China. These researchers investigated the influence of socio-demographic and economic factors on domestic water consumption. These investigations also demonstrate that higher education levels are associated with increased household water usage. However, it is crucial to remember that income and education are frequently linked, making it challenging to discern how income and education affect water use.

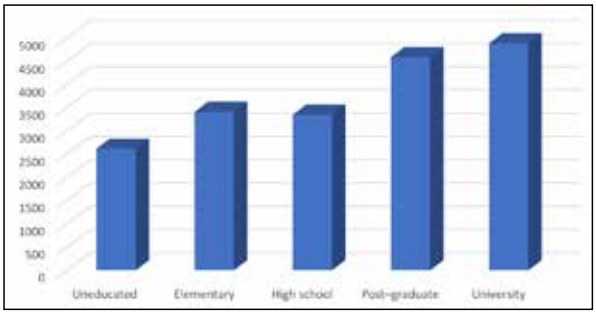

Figure 21. Histogram showing the average monthly water consumption (liter per capita) among the education levels in El-Maten Region.

Income is one of the most important elements that affects how much water households use (Mesert, 2008). Water use and income level are directly correlated, with higher incomes often resulting in higher water consumption (Schwartz and Johnson, 1992). Figure 22 illustrates that the average monthly water consumption per capita was 5,801 liters, with variations ranging from 2,04 to 5,802 liters depending on household income level. Households with an income, exceeding 1,000 $ per month, consumed at least three times more water than those earning less than $200 per month.

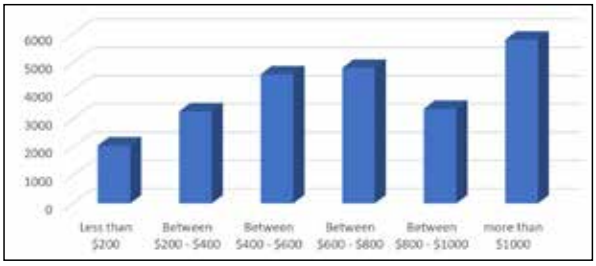

Figure 22. Histogram showing the average of monthly water cost per capita (USD) among the income levels in El-Maten Region.

The relationship between age groups and the consideration of using reusable bottled water showed an asymptotic significance of 0.843, which is greater than 0.05 (Table 2). This indicates that there is no significant relationship between age group and the use of reusable bottled water.

Table 2. Chi-Square test of age group and the use of reusable water bottles.

	Value	df	Asymptotic Significance (2-sided)
Pearson Chi-Square	5.666[a]	10	0.843
Likelihood Ratio	5.630	10	0.845
N of Valid Cases	441		
a. 2 cells (11.1%) have expected count less than 5. The minimum expected count is 2.38.			

The relationship between education level and the consideration of using reusable water bottles showed an asymptotic significance of 0.229, which is greater than 0.05, indicating no significant relationship (Table 3). However, when comparing the asymptotic significance of age (0.843) and education (0.229) in relation to the use of reusable bottled water, education will be lower. Although both are greater than 0.05, the lower significance level for education suggests that education may have a stronger influence on the consideration of using reusable bottled water than age does.

Table 3. Chi-Square test of education and the use of reusable water bottles.

	Value	df	Asymptotic Significance (2-sided)
Pearson Chi-Square	10.546[a]	8	0.229
Likelihood Ratio	11.609	8	0.170
N of Valid Cases	441		
4 cells (26.7%) have expected count less than 5. The minimum expected count is .38.			

The relationship between education and the disposal of bottled water revealed a significant dependence (Table 4), with an asymptotic significance of 0.003, which is less than 0.05. This indicates that education has a meaningful impact on bottled water disposal practices. The result suggests that higher levels of education are associated with greater environmental awareness, leading to more responsible disposal of bottled water.

Table 4. Chi-Square test of education and the disposal of water bottles.

	Value	df	Asymptotic Significance (2-sided)
Pearson Chi-Square	29.407[a]	12	0.003
Likelihood Ratio	28.799	12	0.004
N of Valid Cases	441		
9 cells (45.0%) have expected count less than 5. The minimum expected count is .10.			

4. Conclusion and Recommendations

Water consumption in Mount Lebanon, specifically in El-Maten Region, was assessed through a survey of 441 participants. The results showed that 34% of respondents experienced issues with year-round water availability from their primary source, rising to 45% during the summer months. Additionally, 56% of participants reported problems with the quality of water from their primary source. Nearly half of 48% of respondents had access to a secondary water source. It can be concluded that drinking water usage from primary sources was lower due to a lack of trust in the quality of drinking water

It can be argued that the secondary water resources serve as alternative or supplementary water sources, helping to balance demand and supply when primary sources such as water from rivers, lakes, or groundwater are insufficient or unavailable. These secondary resources are significant in regions experiencing water scarcity or where primary sources are under stress. It was found that the purposes of water use between primary and secondary sources were largely similar. 76% of primary resources a re for domestic uses while 72% of go for the secondary resources.

Addressing water issues in the region requires multifaceted solutions. Education and raising awareness about climate change, water scarcity, and responsible water use are crucial. Water resources will also be significantly protected by improved water management practices, such as stronger legal frameworks and enforcement of rules, and by the sustainable supply of high-quality water. This can be followed by maintaining infrastructure, especially freshwater systems that is essential for reducing water loss

through leaks and ensuring good water quality. Investments in water-efficient technologies at the national, municipal, and household levels, along with pricing mechanisms such as tariffs or consumption-based pricing, could reduce water waste. Developing solutions for water treatment and reuse, such as wastewater treatment for non-potable uses or rainwater harvesting, would also help safeguard water resources.

The study suggests that household water consumption could be further reduced with the installation of water-saving appliances, highlighting the potential for water conservation in El-Maten region. Currently, there is a lack of detailed research on domestic water use in the region. These findings provide insights into water use patterns and offer baseline information to help develop water efficiency programs. A deep understanding of household water use would enable local water companies to better plan and manage water resources for current and future water demand. This information could also improve forecasting of water demand in the region.

Recommendations:

- The opportunities are to improve the water availability and quality, where water infrastructure is underdeveloped or poorly maintained.
- The improvement of Education and Environmental Awareness campaigns in promoting sustainable water practices.
- Maintaining water infrastructure is crucial to preventing leaks and guaranteeing the quality of fresh water. Investments in water-efficient technologies and consumption-based tariffs also significantly impact water conservation.
- The effective water management policies, including legal frameworks and stricter regulation enforcement, are necessary to protect water resources.

Declarations

Conflicts of interests: The authors declare that they do not have any conflict of interest involving the process of reviewing and publishing or any other related implementation for our manuscript.

References

Abou Abbass , F., Nehme, N., Koubaissy, B., Ibrahim, Z., Diab, W., and Tarawneh, K. (2023). Assessment of Chemical and Microbiological Drinking Water of Beirut and Mount Lebanon. Journal of Environment and Earth Science, 13, 1–12.

Agthe, D.E., and Billings,R.B.,(2002). Water price influence on apartment complex water use. Journal of water resources planning and management, volume 128, Issue5.

Central Administration of Statistics—District statistics based on the Labour Force and Household Living Conditions Survey 2018-2019. (n.d.). Retrieved September 1, 2023, from http://cas.gov.lb/index.php/demographic-and-social-en/population-en/79-english/222-district-statistics-based-on-the-labour-force-and-household-living-conditions-survey-2018-2019#mount-lebanon.

Clarke, J.M., and Brown, R.R. (2006). Understanding he factors that influence domestic water consumption within Melbourne. Australasian Journal of Water Resources, 10 (3), 261-268.

Cloy, J. M., and Smith, K. A. (2015). Greenhouse Gas Emissions. In Reference Module in Earth Systems and Environmental Sciences. Elsevier.

Fan, Y., Li, H., and Miguez Macho, G., Global Patterns of Groundwater Table Depth. Science, volume 339, Issue 6122, pp. 940-943.

Fielding, K. S., Russell, S., Spinks, A., and Mankad, A. (2012). Determinants of household water conservation: The role of demographic, infrastructure, behavior, and psychosocial variables. Water Resources Research, 48(10).

Grimble, R. (1999). Economic instruments for improving water use efficiency: theory and practice. Agricultural Water Management, 40, 77–82.

Haddad, E. A., Farajalla, N., Camargo, M., Lopes, R. L., and Vieira, F. V. (2014). Climate change in Lebanon: Higher-order regional impacts from agriculture. REGION, 1(1), 9–24.

Haddeland, I., Heinke, J., Biemans, H., Eisner, S., Flörke, M., Hanasaki, N., Konzmann, M., Ludwig, F., Masaki, Y., Schewe, J., Stacke, T., Tessler, Z. D., Wada, Y., and Wisser, D. (2014). Global water resources affected by human interventions and climate change. Proceedings of the National Academy of Sciences, 111(9), 3251–3256.

Hagemann, S., Chen, C., Clark, D. B., Folwell, S., Gosling, S. N., Haddeland, I., Hanasaki, N., Heinke, J., Ludwig, F., Voss, F., and Wiltshire, A. J. (2013). Climate change impact on available water resources obtained using multiple global climate and hydrology models. Earth System Dynamics, 4(1), 129–144.

Haydar C. M., Tarawneh K., Nehme N., Amaireh M., Yaacoub A., and Diab W. (2022). Heavy Metals Content in Water and Sediments in the Upper Litani River Basin, Lebanon. Journal of Geoscience and Environment Protection, 10, pp:139-158.

Hoekstra, A., and Chapagain, A., (2007). Water Foot prints of Nations: Water Use by People as a Function of Their Consumption Pattern. Water Resources Management, Volume 21 (1), pp. 35-48.

Jordán-Cuebas, F., Krogmann, U., Andrews, C. J., Senick, J. A., Hewitt, E. L., Wener, R. E., and Plotnik, D. (2018). Understanding apartment end-use water consumption in two green residential multistory buildings. Journal of Water Resources Planning and Management, 144(4), 04018009.

Joshi, D. (2020). Misunderstanding gender in water: Addressing or reproducing exclusion. In Gender, water and development (pp. 135–153). Routledge.

Lelieveld, J., Hadjinicolaou, P., Kostopoulou, E., Chenoweth, J., El Maayar, M., Giannakopoulos, C., Hannides, C., Lange, M. A., Tanarhte, M., Tyrlis, E., and Xoplaki, E. (2012). Climate change and impacts in the Eastern Mediterranean and the Middle East. Climatic Change, 114(3), 667–687.

Lesk, C., Rowhani, P., & Ramankutty, N. (2016). Influence of extreme weather disasters on global crop production. Nature, 529(7584), Article 7584.

Makki, M. H., Abd-El-Khalick, F., and BouJaoude, S. (2003). Lebanese secondary school students' environmental knowledge and attitudes. Environmental Education Research, 9(1), 21–33.

Motho, M., Kolawole, O.D., Motsholapheko, M.R., and Mogomotsi, P.K. (2022). Influence of household demographic and socio-economic factors on water demand in Ngamiland District, Botswana. water science, 36 (1), 48-59.

Myers, N., Mittermeier, R. A., Mittermeier, C. G., da Fonseca, G. A. B., and Kent, J. (2000). Biodiversity hotspots for conservation priorities. Nature, 403(6772), Article 6772.

Nehme N, Haydar C M (2018) "The physical and chemical and microbial characteristics of Litani river water", The Litani River Lebanon: an assessment and current challenges water science and technology library, springer, p5.

Nehme, N., Haidar, C., Diab, W., Tarawneh, K., and Villiéras, F. (2019). Assessment of Heavy Metal Pollution in the Sediments of the Lower Litani River Basin, Lebanon. 10, 104–112.

Nehme N., Haydar C. M., Dib A., Ajouz N., Tarawneh K. (2020) Quality Assessment of Groundwater in the Lower Litani Basin (LLRB), Geosciences Research Journal. Vol. 5, No. 1, pp:1-14.

Nehme N., Haydar C. M., Rammal M., Abou Abbass F., Rammal H., Al Ajouz N. (2021) Study of the water assessment in the Alhujair Valley in Lebanon. J.Mater.Environ.Sci., Vol. 12, Issue 11: 1392-1404 (a)

Nehme N., Haydar C. M., Al-Jarf Z., Abou Abbass F., Moussa N., Youness G., and Tarawneh K. (2021) Assessment of the physicochemical and microbiological water quality of Al-Zahrani River Basin, Lebanon. Jordan Journal of Earth and Environmental Sciences, 12(3), 206-213.(b)

Okimiji O., Adedeji O., Oguntoke O., Shittu O., Aborisade M., Ezennia O. (2021) Analysis of socio-economic and housing characteristics In some selected slum area in Lagos State Metropolis, Nigeria using Geographical Information System. Jordan Journal of Earth and Environmental Sciences, 12(2), 134-144.

Skaf, L., Buonocore, E., Dumontet, S., Capone, R., and Franzese, P. P. (2019). Food security and sustainable agriculture in Lebanon: An environmental accounting framework. Journal of Cleaner Production, 209, 1025–1032.

Schleich, J., and Hillenbrand, T., (2009). Determinants of residential water demand in Germany. Ecological Economics, 68(6), 1756–1769.

Schwartz, J.B. and Johnson, R.W., (1992). Maximizing the economic impact of urban water supply and sanitationinvestments, water and sanitation for health project report, Washington: Office of Health, Bureau forResearch and Development, 1992, 82, 10-11.

Shaban, A., (2016) Managing and Leading a Diverse Workforce: One of the Main Challenges in Management. Procedia-Social and Behavioral Sciences, 230, 76-84.

Shaban, A. (2019). Striking challenges on water resources of Lebanon. In Hydrology-The Science of Water. IntechOpen

Van Koppen, B. (2001). Gender in integrated water management: An analysis of variation. In Natural Resources Forum (Vol. 25, 4, pp. 299–312). Oxford, UK: Blackwell Publishing Ltd.

Villar-Navascués, R.A., and Pérez-Morales, A.(2018).Factors Affecting Domestic Water Consumption on the Spanish Mediterranean Coastline. The Professional Geographer, 70 (3), 513-525.

Willis R., Stewart R.,Giurco D.,Talepour M.R., Mousavinejad A., (2013). End use water consumption in households: impact of socio-demographic factors and efficients devices. Journal of Cleaner Production, volume 60, pp. 107-115.

World Health Organization. (July, 2011). Guidelines for drinking water quality.

JJEES

JJEES (2024) 15 (4): 307-316
ISSN 1995-6681

Jordan Journal of Earth and Environmental Sciences

Geoscientific Applications of Atomic Structure Calculations for Fe Ions (Fe II–Fe V) Using FAC Code

Safeia Hamasha* and Maher Abu-Alrous

Department of Physics, The Hashemite University, P.O. Box 330127, Zarqa 13133, Jordan

Received on October 14, 2024; Accepted on December 14, 2024

Abstract

This study presents atomic structure and spectral calculations for iron ions (Fe II–Fe V) using the Fully Relativistic Configuration Interaction (RCI) approach of the Flexible Atomic Code (FAC). The method generates critical atomic data, including energy levels, transition probabilities, wavelengths, oscillator strengths, and radiative rates, all of which are essential for geoscientific applications. It successfully identifies major spectral features across various transition bands, which are particularly significant for mineral spectroscopy under high-temperature and high-pressure conditions.

FAC's relativistic approach achieves remarkable accuracy in fine-structure details and wavelength precision, especially for higher ionization states, aligning closely with data from the National Institute of Standards and Technology (NIST). This precision makes it invaluable for applications requiring detailed spectroscopic data, such as studies of Deep-Earth mineral stability and high-resolution spectroscopic analyses. The calculated spectra span the extreme ultraviolet (EUV) to ultraviolet (UV) ranges, offering valuable insights into the behavior of iron ions within the Earth's crust and mantle, where extreme conditions drive mineral formation and transformation.

These findings provide essential atomic data for modeling iron-bearing minerals and support various applications, including mineral exploration, remote sensing, and geochemical modeling. The dual-method approach employed in this study balances computational efficiency with spectral accuracy, offering flexibility for future research. Expanding this methodology to include additional transition metals could enhance atomic datasets, broadening its relevance across geophysical and other scientific applications.

Keywords: *Iron ions, atomic structure, FAC code, mineral stability, geosciences, electronic configurations.*

1. Introduction

Iron is among the most abundant and influential elements in the Earth's crust, mantle, and core, playing a pivotal role in shaping planetary structure and driving both geophysical and geochemical processes. Its diverse oxidation states, ranging from neutral Fe I to highly ionized Fe ions, make it a central subject in studies of mineral stability and redox dynamics within geosciences (Khudhur et al., 2018; Tarawneh et al., 2021). Research has shown that iron significantly contributes to the Earth's magnetic field through its core interactions and influences phase transformations and mineral stability in silicate minerals in the crust and mantle (Zeng et al., 2008; Bovolo, 2005). Additionally, iron participates in redox reactions that regulate the cycling of major elements like oxygen and sulfur under high-temperature and high-pressure conditions (Frost & McCammon, 2008; O'Neill et al., 2018).

In geochemical studies, accurate atomic data for ionized iron is indispensable. Iron ions dominate the electronic structure of numerous minerals, influencing the spectral lines observed in mineral samples, particularly under varying environmental conditions in the Earth's crust and upper mantle (Badro et al., 2013; Abusalem et al., 2019). Investigations into the behavior of Fe ions under extreme pressure and temperature conditions have revealed that their spectral data provide valuable insights for applications in remote sensing, mineral exploration, and modeling Deep-Earth geochemistry (Li et al., 2020).

To generate precise atomic data, researchers employ tools such as the Cowan code and the Flexible Atomic Code (FAC). These computational methods enable highly accurate calculations of spectral lines, energy levels, and transition probabilities (Cowan, 1981; Gu, 2008). FAC, freely available through the International Atomic Energy Agency (https://www-amdis.iaea.org/FAC/), is particularly suited for studying complex electronic configurations in Fe ions.

Previous work by Sultana Nahar and colleagues utilized fully relativistic methods to calculate oscillator strengths, lifetimes, and fine-structure transitions across multiple ionization states of iron (Nahar, 2008; Nahar & Pradhan, 2011). Their benchmark data, particularly for highly ionized states, has been instrumental in astrophysical and plasma studies. Nahar's work demonstrated high precision in line positions and transition probabilities, particularly for forbidden transitions critical to modeling low-density environments.

* Corresponding author e-mail: safeia@hu.edu.jo

Building on this foundation, the present study employs FAC's Fully Relativistic Configuration Interaction (RCI) method to assess computational efficiency and spectral accuracy in geoscientific applications. This approach is essential for accurately modeling Fe ions, particularly in high-ionization states like Fe IV and Fe V, where electronic complexity requires advanced methods to account for relativistic and electron-correlation effects (Gu, 2008).

This paper presents the results of atomic structure and spectral calculations for Fe II–Fe V ions, alongside synthetic spectra and identified strong transition lines. These prominent transitions are expected to appear in observed or experimental spectra of Fe ions. The findings are highly relevant for high-precision modeling of iron-bearing minerals, which is increasingly important for geophysical and environmental studies.

2. Theoretical Background: Fully Relativistic Configuration Interaction (RCI) Method

To construct a comprehensive atomic database for iron ions (Fe II to Fe V), the Fully Relativistic Configuration Interaction (RCI) method of the Flexible Atomic Code (FAC) is employed. This method provides detailed insights into the atomic structure and spectral properties of atoms and ions. By utilizing the Dirac equation, the FAC-RCI method incorporates relativistic effects, which are critical for accurately modeling complex multi-electron systems such as iron and its ions.

This approach enables the precise calculation of key spectral properties, including energy levels, transition wavelengths, and radiative probabilities, facilitating a robust analysis of the atomic structure of iron ions under relativistic constraints (Gu, 2008). Such precision is crucial for applications that require detailed spectroscopic data, especially in high-energy geophysical and geochemical contexts.

For a more in-depth understanding of relativistic atomic structure and configuration interaction, readers are encouraged to consult the foundational work of Grant (2007) and the comprehensive discussions on many-body relativistic treatments in atomic physics by Lindgren and Morrison (2012). These resources provide valuable context for the theoretical framework underpinning the FAC-RCI method.

3. Results and Discussion

The Flexible Atomic Code (FAC) was employed to calculate atomic structure data for Fe II, Fe III, Fe IV, and Fe V ions, with a focus on the Fully Relativistic Configuration Interaction (RCI) method. This approach accounts for electron-electron correlation effects and spin-orbit coupling, both of which are crucial for accurately modeling complex multi-electron systems like iron ions. FAC generates detailed atomic data, including transition energies, optically allowed transition rates, oscillator strengths, and radiative probabilities for each ionized state.

The calculations primarily involved transitions of M-shell electrons (n = 3) to higher energy levels (n = 4, 5, 6, 7, and 8). These transitions span the extreme ultraviolet (EUV) and ultraviolet (UV) spectral ranges, making them particularly relevant for modeling the behavior of iron ions under the high-temperature and high-pressure conditions often encountered in geophysical and geological contexts. FAC's relativistic framework is especially advantageous for capturing fine-structure splitting in highly ionized states, where relativistic effects significantly impact atomic structure calculations.

The study focused on four ionization states of iron: Mn-like Fe (Fe II), Cr-like Fe (Fe III), V-like Fe (Fe IV), and Ti-like Fe (Fe V) ions. FAC computations were used to determine electron transitions from the M-shell (n = 3) to higher shells, producing essential atomic parameters such as energy levels, transition probabilities, and oscillator strengths. Synthetic spectra for these ions were generated using Doppler line broadening profiles at a temperature T_{Dopp}=1200 ºK, sufficient to produce clear and well-defined spectral lines. Figures 1–4 illustrate these synthetic spectra, covering the spectral ranges of interest for each ion.

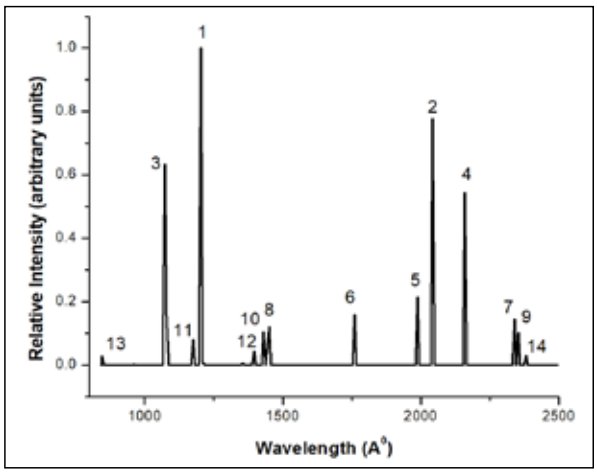

Figure 1. Synthetic spectrum of Fe II ion produced by FAC's RCI method, indicating strong transitions within the UV spectral region.

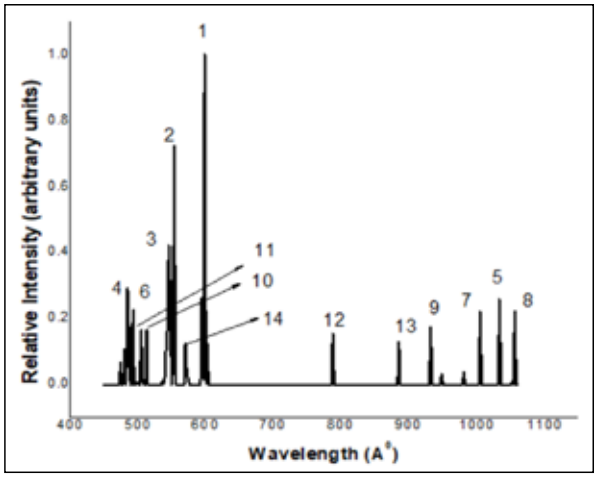

Figure 2. Synthetic spectrum of Fe III ion produced by FAC's RCI method, indicating strong transitions within the EUV to UV spectral region.

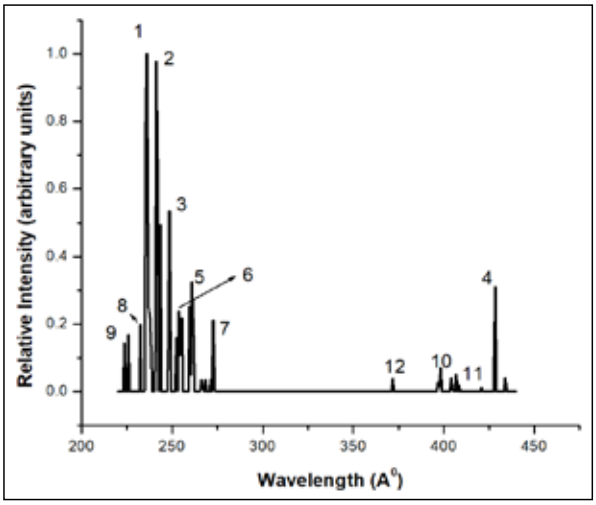

Figure 3. Synthetic spectrum of Fe IV ion produced by FAC's RCI method, indicating strong transitions within the EUV spectral region.

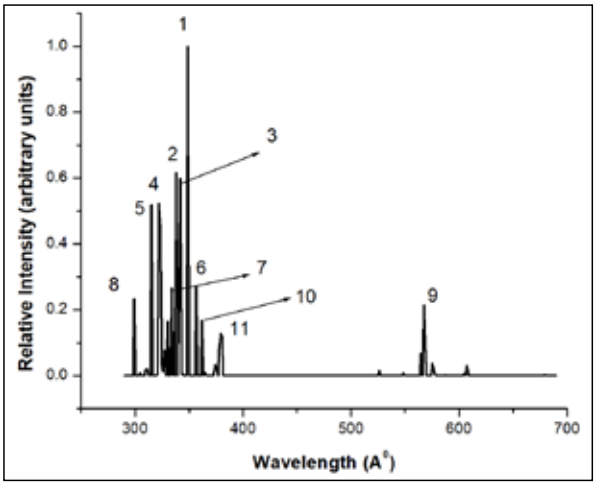

Figure 4. Synthetic spectrum of Fe V ion produced by FAC's RCI method, indicating strong transitions within the EUV spectral region.

The ground-state configurations and significant transitions for each ion are detailed in Table 1. These configurations form the basis for spectral analysis, with transitions grouped according to their intensity and spectral significance. The most important spectral lines expected to appear in experimental spectra are identified and labeled in the synthetic spectra. These prominent lines, predominantly 3-4 transitions, are summarized in Table 2. Table 2 presents the peak number (peak #), the electronic configuration of the upper state (configuration (up)), the parity P of the upper state (P (up)), the total angular momentum of the upper state (J (up)), the electronic configuration of the lower state (configuration (low)), the parity P of the lower state (P (low)), the total angular momentum of the lower state (J (low)), the transition energy in electron volts (ΔE), the weighted oscillator strength (gf_{ij}), the radiative transition probability (A_r (s^{-1})), the calculated wavelength in angstroms (λ(Å)) and the wavelength listed in NIST database in angstroms (λ_{NIST} (Å)).

Transitions from 3-5 and 3-6 groups, while present, are less intense and exhibit shorter wavelengths. Transitions from 3-6 are particularly weak and unlikely to appear in experimental spectra under standard conditions. When compared with the NIST database, all calculated lines in this study were found to be consistent with listed transitions. However, this work focuses specifically on strong transitions that are most likely to appear in real iron spectra under geophysical conditions, emphasizing their relevance for applications such as mineral spectroscopy and geochemical modeling. Detailed findings of each ion are offered in the following subsections:

3.1 Mn-like Fe (Fe II) ion strong transitions

The ground-state configuration of Fe II was identified as [Ne] $3s^2\ 3p^6\ 4s^2\ 3d^5$ or equivalently [Ar] $4s^2\ 3d^5$. To streamline the analysis, only single-electron excitations were considered, and transitions with low radiative probabilities were omitted, as these are unlikely to appear in observed Fe ion spectra. This selection resulted in a large set of significant transitions, among which the strongest lines predominantly occurred within the 3d–4f transition group. The most intense line was observed at a wavelength of λ = 1201 Å.

The full spectral range for Fe II transitions spans from 900 Å to 2500 Å, placing these transitions within the ultraviolet (UV) spectrum, a region critical for high-energy geophysical applications. While Fe II exhibits a rich array of transition lines, this study focused on the strongest bands likely to appear under normal conditions in experimental spectra. Table 2 summarizes the most prominent transitions, while Figure 1 presents the synthetic spectrum generated for Fe II using a Doppler line profile at a broadening temperature T_{Dopp}=1200ºK. This temperature highlights the notable contributions of 3d–4f and 3d–4p transitions.

Higher-order transitions, such as 3d–5p and 3d–6p, were also identified in the spectra but exhibit significantly lower intensities compared to the dominant 3d–4 transitions. These weaker lines are less likely to have a notable presence in real Fe II spectra under typical geophysical conditions.

The calculated spectra for Fe II reveal distinct intensity distributions, which are valuable for developing geophysical models. Accurate representation of UV emissions is essential for studying high-temperature mineral phases and the behavior of iron ions in Earth's crust and mantle. By identifying strong transitions and high-probability configurations, this data enables more precise modeling of iron-bearing minerals under extreme conditions, contributing to the understanding of high-temperature and high-pressure geochemical processes.

3. 2 Cr-like Fe (Fe III) ion strong transitions

for Fe III, the electronic configurations and prominent transition lines are detailed in Tables 1 and 2. Similar to Fe II, the transitions primarily involve M-shell electrons (n = 3) moving to outer shells (n = 4, 5, 6, 7, and 8). The ground-state configuration, [Ne] $3s^2\ 3p^6\ 3d^6$, forms the foundation for transition calculations. Single-electron excitations were considered, and transitions with significant probabilities were filtered, resulting in over 357 prominent transitions, summarized in Table 2. Among these, the strongest transition occurs within the 3d–4f series at a wavelength of λ = 599 Å.

The full spectral range for allowed transitions in Fe III

spans 370 Å to 1075 Å, positioning these lines within the Extreme Ultraviolet (EUV) to ultraviolet (UV) region. This range is critical for high-temperature applications in geosciences, including mineral stability modeling and phase transition studies. Figure 2 presents the synthetic spectrum generated using the FAC-RCI method, incorporating Doppler line broadening at a temperature T_{Dopp}=1200ºK. The spectrum highlights the dominance of 3d–4f transitions, specifically from [Ar] $4s^2\,3d^4$ to [Ar] $4s^2\,3d^3\,4f$. These transitions are followed in intensity by 3d–4p and then 3d–4s transitions.

The pronounced dominance of the 3d–4f transitions underscores a characteristic pattern in Fe III, where higher-energy excitations to f orbital produce intense spectral lines. This behavior is particularly valuable for applications requiring precise EUV data, such as studies of high-energy geochemical environments.

The FAC-derived spectra for Fe III provide a comprehensive dataset that captures fine-structure splitting and delivers precision in energy level spacing. These results align closely with the NIST database benchmarks, confirming the reliability of FAC for generating accurate atomic data. This level of detail is crucial for modeling the behavior of Fe III in high-energy geochemical contexts, such as those found in the Earth's upper mantle or during high-temperature mineral reactions. FAC's ability to accurately capture these transitions establishes its utility in studies of iron-bearing minerals, where such detailed spectral data are indispensable.

3.3 V-like Fe (Fe IV) ion strong transitions

The configurations and transition lines for Fe IV are depicted in Tables 1 and 2. They illustrate M-shell excitations from n = 3 to n = 4, 5, 6, 7, and 8 shells. The ground-state configuration of Fe IV ion is: [Ne] $3s^2\,3p^6\,4s^2\,3d^3$. The calculated spectral data for V-like Fe ion is done by considering single electron excitations, where the calculated data contains both strong and weak transitions; therefore we filtered the data for strong transitions, resulting in 246 significant transitions. Two particularly strong transitions groups are identified; 3d-4f and 3d-4p groups. The strongest transition is identified to be from [Ar] $3d_{3/2}^{\,2}\,3d_{5/2}^{\,2}\,4f_{5/2}$ (J_f) to [Ar] $3d_{3/2}^{\,2}\,3d_{5/2}^{\,3}$ (J_i) with λ = 348 Å. The synthetic spectrum of Fe IV ion is shown in Figure 3, presenting dominant 3d–4d transitions, and the spectral range is in the EUV range, which are of particular significance for geochemical analysis.

Among 3-5 transitions, the strongest calculated transition was in the 3d–5f series, with a wavelength of λ = 223.04 Å, but because of 3-5 transitions have low radiative transition probabilities they might not appear in real experimental Fe IV ion's spectrum. The entire spectral range of Fe IV ion for optically allowed transitions spans from 190 Å to 435 Å, placing these transitions within the Extreme Ultraviolet (EUV) region. This range is particularly relevant for applications in high-temperature geophysical environments where EUV data is critical.

The FAC-calculated data for Fe IV ion's 3d–4f and 3d–4p transitions provide high-resolution insight into fine-structure splitting and transition probabilities, line up closely with experimental and NIST database. These transitions, which produce strong emission lines within the EUV range, are highly relevant for geochemical and mineralogical studies, as they enable detailed modeling of Fe IV ion's behavior under extreme conditions, such as high pressures and temperatures in Earth's upper mantle. FAC's precise handling of these transitions in Fe IV ion underscores its value in generating accurate atomic data, which is crucial for simulating the spectroscopic properties of iron-bearing minerals. This level of detail enhances our understanding of the spectroscopic behavior of Fe IV in geological environments and supports its application in remote sensing and high-temperature mineral phase studies.

3. 4 Ti-like Fe (Fe V) ion strong transitions

For Fe V ion, the electronic configurations and strongest transitions are provided in Tables 1 and 2. Calculated spectral data presents M-shell transitions from n = 3 to outer shells (n = 4, 5, 6, 7, and 8). The ground-state configuration for Fe V ion is: [Ne] $3s^2\,3p^6\,4s^2\,3d^2$, which serves as the reference point for this ion's spectroscopic calculations. Like prior ions, only single-electron excitations were considered. The produced spectral data table contains large file of strong and weak transitions, so it was filtered to strong transition lines only. This filtering process resulted in 300 significant transitions. Transitions that contribute to the Fe V spectrum are summarized in Table 2. Among the identified transitions, the most prominent line is in the 3d–4f series, with a wavelength of λ = 236 Å. This intense transition, a characteristic of Fe V ion, represents the highest transition rate observed across the Fe V ion series, signifying strong radiative decay in this particular configuration. The spectroscopic data for Fe V ion, particularly the intense 3d–4f transitions, is crucial for understanding iron's behavior in geoscientific contexts where high ionization states are present within high-temperature mineral phases or under extreme conditions in the Earth's mantle. These findings underscore Fe V ion's relevance in studies of mineral stability and transformation, as well as in modeling the spectroscopic properties of iron-bearing minerals in geological environments.

The complete spectral range for allowed transitions in Fe V ion spans the spectral range from 223 Å to 434 Å, situating these transitions firmly within the extreme ultraviolet (EUV) region, which is pertinent to high-energy geophysical environments. The synthetic spectrum for Fe V ion is displayed in Figure 4. Doppler line profile is used to account for temperature-based broadening.

This EUV spectral profile is particularly relevant for high-temperature geoscience applications, as it provides insight into the behavior of iron ions under extreme conditions, such as those found in the Earth's upper mantle or core-mantle boundary, where temperatures exceed several thousand Kelvin. In these environments, iron undergoes high degrees of ionization, and its EUV emissions can be critical for remote sensing in high-energy astrophysical and geophysical contexts. Additionally, Fe ions prominent 3d–nf transitions contribute significantly to the opacity of iron in high-temperature and high-pressure mineral phases,

influencing the thermal conductivity and stability of iron-bearing compounds within Earth's mantle. This data can support simulations of mantle convection, mineral phase transitions, and core-mantle boundary dynamics, enhancing our understanding of Earth's internal processes and the thermal evolution of planetary interiors where iron plays a key role.

FAC-RCI method is used to produce synthetic spectra for Fe II–Fe V with strong alignment in major spectral features, which are critical for mineral spectroscopy in geosciences. This alignment in major transition lines is consistent with findings by Nahar (2008), where their results are listed in NIST database. Their work demonstrated similar patterns across Fe ionization states. Our results support the reliability of FAC- RCI methods in capturing key transitions for iron ions, providing confidence in their applicability across varied research fields. However, FAC's fully relativistic configuration interaction approach offers greater precision in resolving fine structures, especially for higher ionization states like Fe IV and Fe V. Nahar's work underscores the significance of fine structure in modeling highly ionized iron in low-density environments, such as those encountered in astrophysics. FAC's detailed fine-structure resolution is beneficial for geophysical models requiring accuracy in high-ionization states.

FAC's findings are aligned closely with NIST database and compares well with the precision achieved in Nahar's results for highly ionized Fe ions used in astrophysical spectra. This precision is valuable for applications that require exact wavelength data, such as high-resolution mineral spectroscopy.

4. Summary and Conclusions

This study demonstrated the effectiveness of FAC's Fully Relativistic Configuration Interaction (RCI) method in calculating atomic data for Fe II–Fe V ions. The results align closely with NIST data, though FAC exhibited high accuracy in fine-structure details and wavelength precision, particularly for high ionization states. These findings underscore FAC's potential for high-precision mineral spectroscopy and Deep-Earth geophysics, where accurate fine-structure and relativistic corrections are critical.

Conflict of Interest

The authors declare that they have no conflicts of interest.

References

Abusalem, M, Awwad, A., Ayad, J., Abu Rayyan, A. (2019). Green Synthesis of Hematite (A-Fe2O3) Nanoparticles Using Extract Influenced Seed Germination and Seedling Growth of Tomatos. Jordan Journal of Earth and Environmental Sciences, 10(3), 161-166.

Badro, J., Fiquet, G., François, Guyot, F., Rueff, J. P., Struzhkin, V. V., Vankó, G., Monaco, G. (2003). Iron Partitioning in Earth's Mantle: Toward a Deep Lower Mantle Discontinuity. Science: 789-791. doi:10.1126/science.1081311. https://www.science.org/doi/abs/10.1126/science.1081311

Bovolo, C. I. (2005). The physical and chemical composition of the lower mantle. Philosophical Transactions A, 363(1837):2811-35. Doi: 10.1098/rsta.2005.1675

Cowan, R.D. (1981) The Theory of Atomic Structure and Spectra. University of California Press, Berkeley.

Frost, D. J., & McCammon, C. A. (2008). The redox state of Earth's mantle. Annual Review of Earth and Planetary Sciences, 36(1):389-420. Doi: 10.1146/annurev.earth.36.031207.124322

https://doi.org/10.1146/annurev.earth.36.031207.124322

Grant, I. P. (2007). Relativistic quantum theory of atoms and molecules: Theory and computation. Springer. Doi: https://doi.org/10.1007/978-0-387-35069-1

Gu, M. F. (2008). Flexible Atomic Code. Canadian Journal of Physics, 86: 675-689.

https://doi.org/10.1139/p07-197

Khudhur, N. S., Shelan Mustafa Khudhur, S.M., Ahmad, I. N. (2018). An Assessment of Heavy Metal Soil Contamination in a Steel Factory and the Surrounding Area in Erbil City. JJEES 9(1),1-11.

Li, X., Liu, J., Hu, Q., Li, J., & Mao, Z. (2020). Iron oxides in Earth's lower mantle. Journal of Geophysical Research: Solid Earth, 125(11), e2020JB020706. doi:10.1029/2020JB020706.

Lindgren, I., & Morrison, J. (2012). Atomic many-body theory (2nd ed.). Barnes & Noble, Springer.

Nahar, S. N. (2008). Relativistic atomic data for Fe ions: Energy levels and transition probabilities for Fe XVII–Fe XXV. Physical Review A, 78(5), 052501. doi:10.1103/PhysRevA.78.052501

Nahar, S. N., & Pradhan, A. K. (2011). High-precision calculations for Fe XVII–Fe XXVI: Oscillator strengths and lifetimes. The Astrophysical Journal Supplement Series, 194(2), 43. doi:10.1088/0067-0049/194/2/43

National Institute of Standards and Technology (NIST). (n.d.). Atomic Spectra Database. Retrieved from https://www.nist.gov/pml/atomic-spectra-database.

O'Neill, H. S. C., Berry, A. J., Guilherme Mallmann, G. (2018). The oxidation state of iron in Mid-Ocean Ridge Basaltic (MORB) glasses: Implications for their petrogenesis and oxygen fugacities. Earth and Planetary Science Letters, 504:152-162. https://doi.org/10.1016/j.epsl.2018.10.002

Tarawneh, K., Eleyan, I., Alalwan, R., Sallam,S, Hammad,S. (2021) Assessment of heavy metals contamination levels in surfaces soil in Baqa'a area, Jordan. JJEES 12(4): 285-294 ISSN

Zeng, Z. Y., Hu, C. E., Chen, X. R., and Ling-Cang Cai, L. C., Jing, F. Q. (2008). Magnetism and phase transitions of iron under pressure. Journal of Physics: Condensed Matter, 20(42): 425217. Doi:10.1088/0953-8984/20/42/425217. https://dx.doi.org/10.1088/0953-8984/20/42/425217.

Table 1. Electronic configurations that were used in FAC-RCI code for transitions from n= 4 → 5, 6, 7, 8 transitions in Fe ions (Fe II–Fe V).

Ion	Shell number	Electron Configuration
Fe II	n=4	Ground State: $1s^2\ 2s^2\ 2p^6\ 3s^2\ 3p^6\ 3d^6\ 4s^1$ or $[Ar^{18}]\ 3d^6\ 4s^1$ $[Ar^{18}]\ 3d^6\ 4p^1$, $[Ar^{18}]\ 3d^6\ 4d^1$, $[Ar^{18}]\ 3d^6\ 4p^1 4f^1$
	n= 5	$[Ar^{18}]\ 3d^6\ 5s^1$, $[Ar^{18}]\ 3d^6\ 5p^1$, $[Ar^{18}]\ 3d^6\ 5d^1$, $[Ar^{18}]\ 3d^6\ 5f^1$, $[Ar^{18}]\ 3d^6\ 5g^1$
	n= 6	$[Ar^{18}]\ 3d^6\ 6s^1$, $[Ar^{18}]\ 3d^6\ 6p^1$, $[Ar^{18}]\ 3d^6\ 6d^1$, $[Ar^{18}]\ 3d^6\ 6f^1$, $[Ar^{18}]\ 3d^6\ 6g^1$, $[Ar^{18}]\ 3d^6\ 6h^1$
	n= 7	$[Ar^{18}]\ 3d^6\ 7s^1$, $[Ar^{18}]\ 3d^6\ 7p^1$, $[Ar^{18}]\ 3d^6\ 7d^1$, $[Ar^{18}]\ 3d^6\ 7f^1$, $[Ar^{18}]\ 3d^6\ 7g^1$, $[Ar^{18}]\ 3d^6\ 7h^1$
	n= 8	$[Ar^{18}]\ 3d^6\ 8s^1$, $[Ar^{18}]\ 3d^6\ 8p^1$, $[Ar^{18}]\ 3d^6\ 8d^1$, $[Ar^{18}]\ 3d^6\ 8f^1$, $[Ar^{18}]\ 3d^6\ 8g^1$, $[Ar^{18}]\ 3d^6\ 8h^1$
Fe III	n= 4	Ground State: $1s^2\ 2s^2\ 2p^6\ 3s^2\ 3p^6\ 3d^6\ 4s^2$ or $[Ar^{18}]\ 3d^6\ 4s^2$ $[Ar^{18}]\ 3d^6\ 4s^1\ 4p^1$, $[Ar^{18}]\ 3d^6\ 4s^1 4d^1$, $[Ar^{18}]\ 3d^6\ 4s^1\ 4f^1$
	n=5	$[Ar^{18}]\ 3d^6\ 4s^1\ 5p^1$, $[Ar^{18}]\ 3d^6\ 4s^1 5d^1$, $[Ar^{18}]\ 3d^6\ 4s^1\ 5f^1$, $[Ar^{18}]\ 3d^6\ 4s^1\ 5g^1$,
	n= 6	$[Ar^{18}]\ 3d^6\ 4s^1\ 6p^1$, $[Ar^{18}]\ 3d^6\ 4s^1$ 6d1, $[Ar^{18}]\ 3d^6\ 4s^1\ 6f^1$, $[Ar^{18}]\ 3d^6\ 4s^1\ 6g^1$, $[Ar^{18}]\ 3d^6\ 4s^1\ 6h^1$
	n= 7	$[Ar^{18}]\ 3d^6\ 4s^1\ 7p^1$, $[Ar^{18}]\ 3d^6\ 4s^1$ 7d1, $[Ar^{18}]\ 3d^6\ 4s^1\ 7f^1$, $[Ar^{18}]\ 3d^6\ 4s^1\ 7g^1$, $[Ar^{18}]\ 3d^6\ 4s^1\ 7h^1$
	n= 8	$[Ar^{18}]\ 3d^6\ 4s^1\ 8p^1$, $[Ar^{18}]\ 3d^6\ 4s^1$ 8d1, $[Ar^{18}]\ 3d^6\ 4s^1\ 8f^1$, $[Ar^{18}]\ 3d^6\ 4s^1\ 8g^1$, $[Ar^{18}]\ 3d^6\ 4s^1\ 8h^1$
Fe IV	n= 4	Ground State: $1s^2\ 2s^2\ 2p^6\ 3s^2\ 3p^6\ 3d^6\ 4s^2\ 4p^1$ or $[Ar^{18}]\ 3d^6\ 4s^2\ 4p^1$ $[Ar^{18}]\ 3d^6\ 4s^1\ 4p^2$, $[Ar^{18}]\ 3d^6\ 4s^2 4d^1$, $[Ar^{18}]\ 3d^6\ 4s^2\ 4f^1$, $[Ar^{18}]\ 3d^6\ 4s^1\ 4d^2$,$[Ar^{18}]\ 3d^6\ 4s^1\ 4f^2$
	n=5	$[Ar^{18}]\ 3d^6\ 4s^2\ 5p^1$, $[Ar^{18}]\ 3d^6\ 4s^2 5d^1$, $[Ar^{18}]\ 3d^6\ 4s^2\ 5f^1$, $[Ar^{18}]\ 3d^6\ 4s^2\ 5g^1$, $[Ar^{18}]\ 3d^6\ 4s^1\ 5p^2$, $[Ar^{18}]\ 3d^6\ 4s^1 5d^2$, $[Ar^{18}]\ 3d^6\ 4s^2\ 5f^1$, $[Ar^{18}]\ 3d^6\ 4s^2\ 5g^1$
	n= 6	$[Ar^{18}]\ 3d^6\ 4s^2\ 6p^1$, $[Ar^{18}]\ 3d^6\ 4s^2$ 6d1, $[Ar^{18}]\ 3d^6\ 4s^2\ 6f^1$, $[Ar^{18}]\ 3d^6\ 4s^1\ 6g^1$, $[Ar^{18}]\ 3d^6\ 4s^2\ 6h^1$, $[Ar^{18}]\ 3d^6\ 4s^1\ 6p^2$, $[Ar^{18}]\ 3d^6\ 4s^1\ 6d^2$, $[Ar^{18}]\ 3d^6\ 4s^1\ 6f^2$, $[Ar^{18}]\ 3d^6\ 4s^1\ 6g^2$, $[Ar^{18}]\ 3d^6\ 4s^1\ 6h^2$
	n= 7	$[Ar^{18}]\ 3d^6\ 4s^2\ 7p^1$, $[Ar^{18}]\ 3d^6\ 4s^2$ 7d1, $[Ar^{18}]\ 3d^6\ 4s^2\ 7f^1$, $[Ar^{18}]\ 3d^6\ 4s^2\ 7g^1$, $[Ar^{18}]\ 3d^6\ 4s^2\ 7h^1$, $[Ar^{18}]\ 3d^6\ 4s^1\ 7p^2$, $[Ar^{18}]\ 3d^6\ 4s^1\ 7d^2$, $[Ar^{18}]\ 3d^6\ 4s^1\ 7f^2$, $[Ar^{18}]\ 3d^6\ 4s^2\ 7g^1$, $[Ar^{18}]\ 3d^6\ 4s^1\ 7h^2$
	n= 8	$[Ar^{18}]\ 3d^6\ 4s^2\ 78p^1$, $[Ar^{18}]\ 3d^6\ 4s^2$ 8d1, $[Ar^{18}]\ 3d^6\ 4s^2\ 8f^1$, $[Ar^{18}]\ 3d^6\ 4s^2\ 8g^1$, $[Ar^{18}]\ 3d^6\ 4s^2\ 8h^1$, $[Ar^{18}]\ 3d^6\ 4s^1\ 8p^2$, $[Ar^{18}]\ 3d^6\ 4s^1\ 8d^2$, $[Ar^{18}]\ 3d^6\ 4s^1\ 8f^2$, $[Ar^{18}]\ 3d^6\ 4s^2\ 8g^1$, $[Ar^{18}]\ 3d^6\ 4s^1\ 8h^2$
Fe V	n= 4	Ground State: $1s^2\ 2s^2\ 2p^6\ 3s^2\ 3p^6\ 3d^6\ 4s^2\ 4p^2$ or $[Ar^{18}]\ 3d^6\ 4s^2\ 4p^2$ $[Ar^{18}]\ 3d^6\ 4s^2\ 4p^1\ 4d^1$, $[Ar^{18}]\ 3d^6\ 4s^2\ 4p^1\ 4f^1$, $[Ar^{18}]\ 3d^6\ 4s^2\ 4d^1\ 4f^1$, $[Ar^{18}]\ 3d^6\ 4s^1\ 4p^2\ 4d^1$, $[Ar^{18}]\ 3d^6\ 4s^1\ 4f^3$, $[Ar^{18}]\ 3d^6\ 4s^1\ 4p^2\ 4f^1$, $[Ar^{18}]\ 3d^6\ 4s^1\ 4p^1\ 4f^2$, $[Ar^{18}]\ 3d^6\ 4s^1\ 4p^3$, $[Ar^{18}]\ 3d^6\ 4s^1\ 4d^3$ $[Ar^{18}]\ 3d^6\ 4s^1\ 4f^4$
	n=5	$[Ar^{18}]\ 3d^6\ 4s^2\ 4p^1\ 5d^1$, $[Ar^{18}]\ 3d^6\ 4s^2\ 4p^1\ 5f^1$, $[Ar^{18}]\ 3d^6\ 4s^2\ 4d^1\ 5f^1$, $[Ar^{18}]\ 3d^6\ 4s^1\ 4p^2\ 5d^1$, $[Ar^{18}]\ 3d^6\ 4s^1\ 5f^3$, $[Ar^{18}]\ 3d^6\ 4s^1\ 4p^2\ 5f^1$, $[Ar^{18}]\ 3d^6\ 4s^1\ 4p^1\ 5f^2$, $[Ar^{18}]\ 3d^6\ 4s^1\ 5p^3$, $[Ar^{18}]\ 3d^6\ 4s^1\ 5d^3$ $[Ar^{18}]\ 3d^6\ 4s^1\ 5f^4$
	n= 6	$[Ar^{18}]\ 3d^6\ 4s^2\ 4p^1\ 6d^1$, $[Ar^{18}]\ 3d^6\ 4s^2\ 4p^1\ 6f^1$, $[Ar^{18}]\ 3d^6\ 4s^2\ 4d^1\ 6f^1$, $[Ar^{18}]\ 3d^6\ 4s^1\ 4p^2\ 6d^1$, $[Ar^{18}]\ 3d^6\ 4s^1\ 6f^3$, $[Ar^{18}]\ 3d^6\ 4s^1\ 4p^2\ 6f^1$, $[Ar^{18}]\ 3d^6\ 4s^1\ 4p^1\ 6f^2$, $[Ar^{18}]\ 3d^6\ 4s^1\ 6p^3$, $[Ar^{18}]\ 3d^6\ 4s^1\ 6d^3$ $[Ar^{18}]\ 3d^6\ 4s^1\ 6f^4$
	n= 7	$[Ar^{18}]\ 3d^6\ 4s^2\ 4p^1\ 7d^1$, $[Ar^{18}]\ 3d^6\ 4s^2\ 4p^1\ 7f^1$, $[Ar^{18}]\ 3d^6\ 4s^2\ 4d^1\ 7f^1$, $[Ar^{18}]\ 3d^6\ 4s^1\ 4p^2\ 7d^1$, $[Ar^{18}]\ 3d^6\ 4s^1\ 7f^3$, $[Ar^{18}]\ 3d^6\ 4s^1\ 4p^2\ 7f^1$, $[Ar^{18}]\ 3d^6\ 4s^1\ 4p^1\ 7f^2$, $[Ar^{18}]\ 3d^6\ 4s^1\ 7p^3$, $[Ar^{18}]\ 3d^6\ 4s^1\ 7d^3$ $[Ar^{18}]\ 3d^6\ 4s^1\ 7f^4$
	n= 8	$[Ar^{18}]\ 3d^6\ 4s^2\ 4p^1\ 8d^1$, $[Ar^{18}]\ 3d^6\ 4s^2\ 4p^1\ 8f^1$, $[Ar^{18}]\ 3d^6\ 4s^2\ 4d^1\ 8f^1$, $[Ar^{18}]\ 3d^6\ 4s^1\ 4p^2\ 8d^1$, $[Ar^{18}]\ 3d^6\ 4s^1\ 8f^3$, $[Ar^{18}]\ 3d^6\ 4s^1\ 4p^2\ 8f^1$, $[Ar^{18}]\ 3d^6\ 4s^1\ 4p^1\ 8f^2$, $[Ar^{18}]\ 3d^6\ 4s^1\ 8p^3$, $[Ar^{18}]\ 3d^6\ 4s^1\ 8d^3$ $[Ar^{18}]\ 3d^6\ 4s^1\ 8f^4$

Table 2. Strong electric dipole transitions atomic data calculated for n=3- 4 of the iron ions Fe II–Fe V

peak #	configuration (up)	P (up)	J (up)	configuration (low)	P (low)	J (low)	ΔE (eV)	gfij	Ar (s^{-1})	λ (Å)	λ_{NIST}(Å)
Fe II											
1	$3d_{3/2}^2\ 3d_{5/2}^4\ 4f_{5/2}$	1	6.5	$3d_{3/2}^3\ 3d_{5/2}^4$	0	5.5	10.314	0.527	1.74E+08	1202.06	1203.84
1	$3d_{3/2}^2\ 3d_{5/2}^4\ 4f_{5/2}$	1	5.5	$3d_{3/2}^3\ 3d_{5/2}^4$	0	5.5	10.317	0.617	2.37E+08	1201.68	1201.55
1	$3d_{3/2}^2\ 3d_{5/2}^4\ 4f_{7/2}$	1	3.5	$3d_{3/2}^2\ 3d_{5/2}^5$	0	2.5	10.324	0.533	3.08E+08	1200.89	1200.89
2	$3d_{3/2}\ 3d_{5/2}^5\ {}^4p_{1/2}$	1	3.5	$3d_{3/2}^3\ 3d_{5/2}^4$	0	3.5	5.082	0.723	1.01E+08	2439.54	--
2	$3d_{3/2}^3\ 3d_{5/2}^3\ 4p_{1/2}$	1	3.5	$3d_{5/2}^3$	0	4.5	6.070	0.733	1.47E+08	2042.55	--
3	$3d_{3/2}^2\ 3d_{5/2}^4\ 4f_{5/2}$	1	4.5	$3d_{3/2}^3\ 3d_{5/2}^4$	0	5.5	11.565	0.325	1.89E+08	1072.06	1071.58
3	$3d_{3/2}^2\ 3d_{5/2}^4\ 4f_{7/2}$	1	5.5	$3d_{3/2}^3\ 3d_{5/2}^4$	0	5.5	11.574	0.456	2.21E+08	1071.19	1071.25
3	$3d_{3/2}^2\ 3d_{5/2}^4\ 4f_{5/2}$	1	6.5	$3d_{3/2}^3\ 3d_{5/2}^4$	0	5.5	11.579	0.224	9.32E+07	1070.70	1070.12
4	$3d_{3/2}^2\ 3d_{5/2}^4\ 4p_{1/2}$	1	0.5	$3d_{5/2}^3$	0	1.5	5.741	0.257	1.84E+08	2159.72	--
4	$3d_{3/2}\ 3d_{5/2}^5\ {}^4p_{1/2}$	1	1.5	$3d_{3/2}^3\ 3d_{5/2}^4$	0	2.5	5.740	0.392	1.40E+08	2160.06	--
5	$3d_{3/2}^2\ 3d_{5/2}^4\ {}^4p_{1/2}$	1	4.5	$3d_{5/2}^3$	0	4.5	6.236	0.907	1.53E+08	1988.18	1988.66
5	$3d_{3/2}\ 3d_{5/2}^5\ {}^4p_{1/2}$	1	3.5	$3d_{3/2}^3\ 3d_{5/2}^4$	0	3.5	6.224	0.536	1.13E+08	1991.93	1991.54
6	$3d_{3/2}^2\ 3d_{5/2}^4\ 4p_{1/2}$	1	1.5	$3d_{3/2}^2\ 3d_{5/2}^5$	0	2.5	7.041	0.281	1.51E+08	1760.84	1761.37
7	$3d_{3/2}^3\ 3d_{5/2}^3\ 4p_{1/2}$	1	1.5	$3d_{3/2}^3\ 3d_{5/2}^4$	0	2.5	5.300	0.308	9.38E+07	2339.13	--
8	$3d_{3/2}^3\ 3d_{5/2}^3\ 4f_{7/2}$	1	0.5	$3d_{3/2}^3\ 3d_{5/2}^4$	0	1.5	8.535	0.136	2.15E+08	1452.62	1452.40
8	$3d_{3/2}^3\ 3d_{5/2}^3\ 4f_{7/2}$	1	0.5	$3d_{3/2}^3\ 3d_{5/2}^4$	0	0.5	8.545	0.087	1.38E+08	1450.87	1450.86
9	$4p_{1/2}$	1	0.5	$3d_{3/2}^2\ 3d_{5/2}^5$	0	0.5	5.269	0.296	1.78E+08	2352.98	--
10	$3d_{3/2}^2\ 3d_{5/2}^4\ 4f_{5/2}$	1	3.5	$3d_{3/2}^3\ 3d_{5/2}^4$	0	2.5	8.661	0.446	1.81E+08	1431.52	1431.57
10	$3d_{3/2}^2\ 3d_{5/2}^4\ 4f_{5/2}$	1	2.5	$3d_{3/2}^3\ 3d_{5/2}^4$	0	1.5	8.672	0.602	3.27E+08	1429.62	1429.96
11	$3d_{3/2}^3\ 3d_{5/2}^3\ 4f_{5/2}$	1	0.5	$3d_{3/2}^2\ 3d_{5/2}^5$	0	0.5	10.586	0.063	1.53E+08	1171.12	1171.08
11	$3d_{3/2}^3\ 3d_{5/2}^3\ 4f_{5/2}$	1	0.5	$3d_{3/2}^2\ 3d_{5/2}^5$	0	0.5	10.547	0.041	9.99E+07	1175.47	1175.83
12	$3d_{3/2}^2\ 3d_{5/2}^4\ {}^4p_{1/2}$	1	1.5	$3d_{3/2}^3\ 3d_{5/2}^4$	0	2.5	8.881	0.117	1.00E+08	1396.04	1396.62
12	$3d_{3/2}^2\ 3d_{5/2}^4\ 4p_{1/2}$	1	2.5	$3d_{3/2}^3\ 3d_{5/2}^4$	0	3.5	8.866	0.179	1.02E+08	1398.31	1397.57
13	$3d_{3/2}^3\ 3d_{5/2}^3\ 4p_{1/2}$	1	1.5	$3d_{3/2}^2\ 3d_{5/2}^5$	0	0.5	5.211	0.386	1.14E+08	2379.16	--
14	$3d_{3/2}^2\ 3d_{5/2}^4\ 4f_{5/2}$	1	6.5	$3d_{3/2}^3\ 3d_{5/2}^4$	0	5.5	14.667	0.148	9.87E+07	845.30	--

Table 2. Strong electric dipole transitions atomic data calculated for n=3- 4 of the iron ions Fe II–Fe V

peak #	configuration (up)	P (up)	J (up)	configuration (low)	P (low)	J (low)	ΔE (eV)	gfij	Ar (s^{-1})	λ (Å)	λ_{NIST}(Å)
Fe III											
1	$3d_{3/2}^2\ 3d_{5/2}^3\ 4f_{7/2}$	1	4	$3d_{3/2}^2\ 3d_{5/2}^4$	0	4	2.07E+01	0.786	1.62E+09	599.18	598.53
1	$3d_{3/2}^3\ 3d_{5/2}^2\ 4f_{7/2}$	1	0	$3d_{3/2}^3\ 3d_{5/2}^3$	0	1	2.07E+01	0.095	1.77E+09	599.18	598.53
1	$3d_{3/2}^2\ 3d_{5/2}^3\ 4f_{7/2}$	1	2	$3d_{3/2}^2\ 3d_{5/2}^4$	0	2	2.07E+01	0.312	1.16E+09	598.58	598.53
1	$3d_{5/2}^5\ 4f_{5/2}$	1	3	$3d_{3/2}\ 3d_{5/2}^5$	0	3	2.07E+01	0.395	1.05E+09	598.92	598.53
1	$3d_{5/2}^5\ 4f_{5/2}$	1	2	$3d_{3/2}^3\ 3d_{5/2}^3$	0	1	2.07E+01	0.207	7.71E+08	598.57	598.53
1	$3d_{3/2}\ 3d_{5/2}^4\ 4f_{5/2}$	1	5	$3d_{3/2}^2\ 3d_{5/2}^4$	0	4	2.07E+01	1.123	1.90E+09	598.43	598.53
1	$3d_{3/2}^2\ 3d_{5/2}^3\ 4f_{5/2}$	1	4	$3d_{3/2}\ 3d_{5/2}^5$	0	3	2.07E+01	0.898	1.86E+09	598.41	598.53
2	$3d_{3/2}^2\ 3d_{5/2}^3\ 4f_{7/2}$	1	6	$3d_{3/2}^3\ 3d_{5/2}^3$	0	6	2.24E+01	0.766	1.29E+09	553.04	--
2	$3d_{3/2}^2\ 3d_{5/2}^3\ 4f_{7/2}$	1	5	$3d_{3/2}^2\ 3d_{5/2}^3\ 4s_{1/2}$	0	5	2.24E+01	0.590	1.17E+09	553.86	--
2	$3d_{3/2}^2\ 3d_{5/2}^3\ 4f_{7/2}$	1	6	$3d_{3/2}^2\ 3d_{5/2}^3\ 4s_{1/2}$	0	5	2.24E+01	1.369	2.29E+09	553.68	--
3	$3d_{3/2}\ 3d_{5/2}^4\ 4f_{7/2}$	1	5	$3d_{3/2}^2\ 3d_{5/2}^4$	0	4	2.27E+01	0.702	1.42E+09	546.94	--
3	$3d_{3/2}^2\ 3d_{5/2}^3\ 4f_{5/2}$	1	5	$3d_{3/2}^2\ 3d_{5/2}^4$	0	4	2.27E+01	0.382	7.74E+08	546.89	--
4	$3d_{3/2}\ 3d_{5/2}^4\ 4f_{7/2}$	1	7	$3d_{3/2}^3\ 3d_{5/2}^3$	0	6	2.56E+01	0.391	7.40E+08	484.53	--
4	$3d_{3/2}^2\ 3d_{5/2}^3\ 4f_{7/2}$	1	3	$3d_{3/2}^2\ 3d_{5/2}^4$	0	2	2.56E+01	0.164	6.66E+08	484.58	--
5	$3d_{3/2}^2\ 3d_{5/2}^3\ 4p_{1/2}$	1	3	$3d_{3/2}^2\ 3d_{5/2}^4$	0	4	1.20E+01	1.064	7.38E+08	1033.49	1033.82
6	$3d_{3/2}^2\ 3d_{5/2}^3\ 4f_{5/2}$	1	4	$3d_{3/2}^2\ 3d_{5/2}^4$	0	4	2.52E+01	0.329	1.00E+09	492.59	--
6	$3d_{3/2}^2\ 3d_{5/2}^3\ 4f_{7/2}$	1	2	$3d_{3/2}\ 3d_{5/2}^5$	0	3	2.52E+01	0.152	8.33E+08	492.75	--
6	$3d_{3/2}\ 3d_{5/2}^4\ 4f_{5/2}$	1	3	$3d_{3/2}^2\ 3d_{5/2}^4$	0	4	2.52E+01	0.158	6.19E+08	492.45	--
6	$3d_{3/2}\ 3d_{5/2}^4\ 4f_{7/2}$	1	2	$3d_{3/2}\ 3d_{5/2}^5$	0	3	2.52E+01	0.207	1.14E+09	492.65	--
6	$3d_{3/2}\ 3d_{5/2}^4\ 4f_{7/2}$	1	3	$3d_{3/2}^2\ 3d_{5/2}^4$	0	4	2.52E+01	0.174	6.87E+08	492.05	--
7	$3d_{3/2}^2\ 3d_{5/2}^3\ 4p_{1/2}$	1	2	$3d_{3/2}^2\ 3d_{5/2}^4$	0	4	1.23E+01	0.806	7.60E+08	1005.13	1005.1
8	$3d_{3/2}^2\ 3d_{5/2}^3\ 4p_{1/2}$	1	4	$3d_{3/2}^2\ 3d_{5/2}^4$	0	2	1.18E+01	0.314	6.31E+08	1051.53	1052.75
9	$3d_{3/2}^2\ 3d_{5/2}^3\ 4p_{1/2}$	1	2	$3d_{3/2}\ 3d_{5/2}^5$	0	3	1.33E+01	0.410	6.30E+08	932.17	932.68
10	$3d_{3/2}^2\ 3d_{5/2}^3\ 4f_{5/2}$	1	5	$3d_{3/2}^2\ 3d_{5/2}^4$	0	4	2.41E+01	0.299	6.84E+08	514.79	--
10	$3d_{3/2}^2\ 3d_{5/2}^3\ 4f_{7/2}$	1	4	$3d_{3/2}^2\ 3d_{5/2}^4$	0	4	2.41E+01	0.478	1.34E+09	514.07	--
11	$3d_{5/2}\ 4f_{7/2}$	1	3	$3d_{3/2}^2\ 3d_{5/2}^4$	0	2	2.46E+01	0.185	6.95E+08	503.24	--
11	$3d_{5/2}\ 4f_{7/2}$	1	2	$3d_{3/2}^2\ 3d_{5/2}^4$	0	2	2.46E+01	0.141	7.43E+08	503.19	--
12	$3d_{3/2}^2\ 3d_{5/2}^3\ 4p_{1/2}$	1	3	$3d_{3/2}^2\ 3d_{5/2}^4$	0	4	1.57E+01	0.434	6.67E+08	787.54	787.66
13	$3d_{3/2}^2\ 3d_{5/2}^3\ 4p_{1/2}$	1	3	$3d_{3/2}^2\ 3d_{5/2}^4$	0	4	1.40E+01	0.672	8.17E+08	885.00	885.20
14	$3d_{3/2}^2\ 3d_{5/2}^3\ 4f_{7/2}$	1	5	$3d_{3/2}^2\ 3d_{5/2}^3\ 4s_{1/2}$	0	5	2.17E+01	0.494	9.16E+08	571.83	--
14	$3d_{3/2}^2\ 3d_{5/2}^3\ 4f_{7/2}$	1	6	$3d_{3/2}^2\ 3d_{5/2}^3\ 4s_{1/2}$	0	5	2.17E+01	0.529	8.30E+08	571.77	--
14	$3d_{3/2}^2\ 3d_{5/2}^3\ 4f_{5/2}$	1	2	$3d_{3/2}^3\ 3d_{5/2}^3$	0	1	2.17E+01	0.182	7.47E+08	570.81	--
14	$3d_{3/2}\ 3d_{5/2}^4\ 4f_{7/2}$	1	3	$3d_{3/2}^2\ 3d_{5/2}^4$	0	2	2.17E+01	0.216	6.33E+08	570.84	--
14	$3d_{3/2}\ 3d_{5/2}^4\ 4f_{5/2}$	1	4	$3d_{3/2}\ 3d_{5/2}^5$	0	3	2.17E+01	0.610	1.39E+09	570.65	--

Table 2. Strong electric dipole transitions atomic data calculated for n=3- 4 of the iron ions Fe II–Fe V

peak #	configuration (up)	P (up)	J (up)	configuration (low)	P (low)	J (low)	ΔE (eV)	gfij	Ar (s^{-1})	λ (Å)	λ_{NIST}(Å)
Fe IV											
1	$3d_{3/2}^2\ 3d_{5/2}^2\ 4f_{5/2}$	1	5.5	$3d_{3/2}^2\ 3d_{5/2}^3$	0	4.5	3.55E+01	1.164	5.30E+09	349.30	--
1	$3d_{3/2}\ 3d_{5/2}^3\ 4f_{5/2}$	1	6.5	$3d_{3/2}^2\ 3d_{5/2}^3$	0	5.5	3.56E+01	1.547	6.06E+09	348.68	--
1	$3d_{3/2}^2\ 3d_{5/2}^2\ 4f_{5/2}$	1	2.5	$3d_{3/2}\ 3d_{5/2}^4$	0	3.5	3.55E+01	0.227	2.07E+09	348.81	--
1	$3d_{3/2}\ 3d_{5/2}^3\ 4f_{5/2}$	1	3.5	$3d_{3/2}^2\ 3d_{5/2}^3$	0	4.5	3.56E+01	0.301	2.07E+09	348.46	--
1	$3d_{3/2}^2\ 3d_{5/2}^2\ 4f_{5/2}$	1	5.5	$3d_{3/2}^2\ 3d_{5/2}^3$	0	4.5	3.56E+01	0.961	4.40E+09	348.45	--
1	$3d_{3/2}^3\ 3d_{5/2}\ 4f_{5/2}$	1	6.5	$3d_{3/2}\ 3d_{5/2}^4$	0	5.5	3.56E+01	1.140	4.47E+09	348.59	--
2	$3d_{3/2}^2\ 3d_{5/2}^2\ 4f_{5/2}$	1	5.5	$3d_{3/2}^2\ 3d_{5/2}^3$	0	5.5	3.66E+01	0.489	2.37E+09	338.68	--
2	$3d_{3/2}^2\ 3d_{5/2}^2\ 4f_{7/2}$	1	6.5	$3d_{3/2}^2\ 3d_{5/2}^3$	0	5.5	3.66E+01	1.557	6.47E+09	338.65	--
2	$3d_{3/2}^2\ 3d_{5/2}^2\ 4f_{7/2}$	1	5.5	$3d_{3/2}^2\ 3d_{5/2}^3$	0	5.5	3.66E+01	0.350	1.70E+09	338.40	--
2	$3d_{3/2}^2\ 3d_{5/2}^2\ 4f_{5/2}$	1	7.5	$3d_{3/2}^2\ 3d_{5/2}^3$	0	6.5	3.67E+01	1.835	6.69E+09	338.07	--
2	$3d_{3/2}^2\ 3d_{5/2}^2\ 4f_{7/2}$	1	4.5	$3d_{3/2}^2\ 3d_{5/2}^3$	0	4.5	3.67E+01	0.373	2.18E+09	338.08	--
2	$3d_{3/2}^2\ 3d_{5/2}^2\ 4f_{7/2}$	1	5.5	$3d_{3/2}\ 3d_{5/2}^4$	0	5.5	3.66E+01	0.511	2.48E+09	338.43	--
3	$3d_{3/2}^3\ 3d_{5/2}\ 4f_{7/2}$	1	1.5	$3d_{5/2}$	0	2.5	3.62E+01	0.130	1.85E+09	342.52	--
3	$3d_{3/2}^2\ 3d_{5/2}^2\ 4f_{7/2}$	1	0.5	$3d_{3/2}^2\ 3d_{5/2}^3$	0	1.5	3.62E+01	0.070	1.99E+09	342.78	--
3	$3d_{3/2}^3\ 3d_{5/2}\ 4f_{7/2}$	1	3.5	$3d_{3/2}^2\ 3d_{5/2}^3$	0	3.5	3.61E+01	0.295	2.09E+09	342.98	--
3	$3d_{3/2}^2\ 3d_{5/2}^2\ 4f_{7/2}$	1	4.5	$3d_{3/2}^2\ 3d_{5/2}^3$	0	4.5	3.62E+01	0.341	1.94E+09	342.16	--
4	$3d_{3/2}^3\ 3d_{5/2}\ 4f_{5/2}$	1	3.5	$3d_{3/2}^2\ 3d_{5/2}^3$	0	2.5	3.84E+01	0.380	3.04E+09	322.65	--
4	$3d_{3/2}^2\ 3d_{5/2}^2\ 4f_{5/2}$	1	4.5	$3d_{3/2}^2\ 3d_{5/2}^3$	0	3.5	3.85E+01	0.517	3.31E+09	322.43	--
4	$3d_{3/2}^2\ 3d_{5/2}^2\ 4f_{7/2}$	1	5.5	$3d_{3/2}^2\ 3d_{5/2}^3$	0	4.5	3.85E+01	0.630	3.37E+09	322.20	--
4	$3d_{3/2}\ 3d_{5/2}^3\ 4f_{7/2}$	1	6.5	$3d_{3/2}^2\ 3d_{5/2}^3$	0	5.5	3.85E+01	0.772	3.55E+09	321.94	--
4	$3d_{3/2}^3\ 3d_{5/2}\ 4f_{5/2}$	1	2.5	$3d_{3/2}^2\ 3d_{5/2}^3$	0	2.5	3.85E+01	0.456	4.89E+09	321.96	--
4	$3d_{3/2}^2\ 3d_{5/2}^2\ 4f_{7/2}$	1	4.5	$3d_{3/2}^2\ 3d_{5/2}^3$	0	3.5	3.85E+01	0.390	2.51E+09	321.95	--
5	$3d_{3/2}\ 3d_{5/2}^3\ 4f_{5/2}$	1	3.5	$3d_{3/2}^2\ 3d_{5/2}^3$	0	2.5	3.93E+01	0.473	3.97E+09	315.44	--
5	$3d_{3/2}^2\ 3d_{5/2}^2\ 4f_{7/2}$	1	4.5	$3d_{3/2}^2\ 3d_{5/2}^3$	0	3.5	3.93E+01	0.460	3.08E+09	315.30	--
5	$3d_{3/2}\ 3d_{5/2}^3\ 4f_{5/2}$	1	2.5	$3d_{3/2}^2\ 3d_{5/2}^3$	0	2.5	3.93E+01	0.242	2.71E+09	315.34	--
5	$3d_{3/2}^2\ 3d_{5/2}^2\ 4f_{7/2}$	1	5.5	$3d_{3/2}^2\ 3d_{5/2}^3$	0	4.5	3.93E+01	0.499	2.79E+09	315.09	--
5	$3d_{3/2}^2\ 3d_{5/2}^2\ 4f_{5/2}$	1	3.5	$3d_{3/2}^2\ 3d_{5/2}^3$	0	3.5	3.93E+01	0.332	2.78E+09	315.12	--
5	$3d_{3/2}\ 3d_{5/2}^3\ 4f_{7/2}$	1	4.5	$3d_{3/2}^2\ 3d_{5/2}^3$	0	3.5	3.93E+01	0.394	2.64E+09	315.11	--
5	$3d_{3/2}\ 3d_{5/2}^3\ 4f_{5/2}$	1	3.5	$3d_{3/2}\ 3d_{5/2}^4$	0	2.5	3.93E+01	0.249	2.09E+09	315.33	--
5	$3d_{3/2}\ 3d_{5/2}^3\ 4f_{5/2}$	1	2.5	$3d_{3/2}\ 3d_{5/2}^4$	0	1.5	3.93E+01	0.174	1.95E+09	315.21	--
5	$3d_{5/2}^4\ 4f_{5/2}$	1	1.5	$3d_{3/2}^2\ 3d_{5/2}^3$	0	0.5	3.94E+01	0.130	2.18E+09	315.03	--
6	$3d_{3/2}^2\ 3d_{5/2}^2\ 4f_{5/2}$	1	3.5	$3d_{3/2}\ 3d_{5/2}^4$	0	2.5	3.48E+01	0.579	3.81E+09	355.95	--
6	$3d_{3/2}^3\ 3d_{5/2}\ 4f_{7/2}$	1	2.5	$3d_{3/2}^2\ 3d_{5/2}^3$	0	1.5	3.49E+01	0.234	2.05E+09	355.73	--
6	$3d_{3/2}^2\ 3d_{5/2}^2\ 4f_{7/2}$	1	0.5	$3d_{3/2}^2\ 3d_{5/2}^3$	0	0.5	3.49E+01	0.090	2.39E+09	355.52	--
6	$3d_{3/2}\ 3d_{5/2}^3\ 4f_{5/2}$	1	4.5	$3d_{3/2}^2\ 3d_{5/2}^3$	0	3.5	3.48E+01	0.638	3.35E+09	356.70	--
8	$3d_{3/2}\ 3d_{5/2}^3\ 4f_{7/2}\ 3$	1	6.5	$3d_{3/2}\ 3d_{5/2}^4$	0	5.5	4.14E+01	0.407	2.17E+09	299.35	--
9	$3d_{3/2}^3\ 3d_{5/2}\ 4p_{1/2}$	1	5.5	$3d_{3/2}^2\ 3d_{5/2}^3$	0	5.5	2.18E+01	1.100	1.90E+09	567.42	--
10	$3d_{3/2}\ 3d_{5/2}^3\ 4f_{7/2}$	1	2.5	$3d_{3/2}^2\ 3d_{5/2}^3$	0	2.5	3.42E+01	0.317	2.68E+09	362.02	--
11	$3d_{3/2}\ 3d_{5/2}^3\ 4f_{7/2}$	1	3.5	$3d_{3/2}^2\ 3d_{5/2}^3$	0	2.5	3.27E+01	0.325	1.88E+09	379.69	--
11	$3d_{3/2}\ 3d_{5/2}^3\ 4f_{7/2}$	1	3.5	$3d_{3/2}\ 3d_{5/2}^4$	0	3.5	3.26E+01	0.352	2.03E+09	379.92	--
11	$3d_{3/2}\ 3d_{5/2}^3\ 4f_{7/2}$	1	4.5	$3d_{3/2}^2\ 3d_{5/2}^3$	0	4.5	3.27E+01	0.361	1.67E+09	379.42	--
11	$3d_{3/2}\ 3d_{5/2}^3\ 4f_{7/2}$	1	4.5	$3d_{3/2}\ 3d_{5/2}^4$	0	3.5	3.27E+01	0.734	3.40E+09	379.62	--
11	$3d_{3/2}\ 3d_{5/2}^3\ 4f_{7/2}$	1	0.5	$3d_{3/2}^2\ 3d_{5/2}^3$	0	0.5	3.26E+01	0.071	1.64E+09	380.07	--

Table 2. Strong electric dipole transitions atomic data calculated for n=3- 4 of the iron ions Fe II–Fe V

peak #	configuration (up)	P (up)	J (up)	configuration (low)	P (low)	J (low)	ΔE (eV)	gfij	Ar (s^{-1})	λ (Å)	λ_{NIST}(Å)
Fe V											
1	$3d_{3/2}^2\ 3d_{5/2}\ 4f_{7/2}$	1	1	$3d_{3/2}^2\ 3d_{5/2}^2$	0	0	5.25E+01	0.164	6.55E+09	236.14	--
1	$3d_{3/2}\ 3d_{5/2}^2\ 4f_{5/2}$	1	2	$3d_{3/2}^3\ 3d_{5/2}$	0	1	5.25E+01	0.339	8.13E+09	236.02	--
1	$3d_{3/2}\ 3d_{5/2}^2\ 4f_{5/2}$	1	2	$3d_{3/2}^2\ 3d_{5/2}^2$	0	2	5.25E+01	0.219	5.23E+09	236.14	--
1	$3d_{3/2}^3\ 4f_{5/2}$	1	1	$3d_{3/2}^3\ 3d_{5/2}$	0	1	5.25E+01	0.137	5.45E+09	236.13	--
1	$3d_{3/2}\ 3d_{5/2}^2\ 4f_{5/2}$	1	2	$3d_{3/2}^3\ 3d_{5/2}$	0	1	5.25E+01	0.656	1.57E+10	236.03	--
1	$3d_{3/2}\ 3d_{5/2}^2\ 4f_{5/2}$	1	2	$3d_{5/2}^4$	0	2	5.25E+01	0.344	8.24E+09	236.00	--
1	$3d_{3/2}\ 3d_{5/2}^2\ 4f_{7/2}$	1	5	$3d_{3/2}\ 3d_{5/2}^3$	0	4	5.25E+01	1.178	1.28E+10	236.11	--
2	$3d_{3/2}^2\ 3d_{5/2}\ 4f_{7/2}$	1	4	$3d_{3/2}^3\ 3d_{5/2}$	0	3	5.14E+01	0.360	4.58E+09	241.22	--
2	$3d_{3/2}^2\ 3d_{5/2}\ 4f_{7/2}$	1	5	$3d_{3/2}^2\ 3d_{5/2}^2$	0	4	5.14E+01	0.409	4.26E+09	241.25	--
2	$3d_{3/2}\ 3d_{5/2}^2\ 4f_{5/2}$	1	5	$3d_{3/2}\ 3d_{5/2}^3$	0	4	5.14E+01	2.591	2.70E+10	241.35	--
2	$3d_{3/2}\ 3d_{5/2}^2\ 4f_{5/2}$	1	3	$3d_{3/2}^3\ 3d_{5/2}$	0	3	5.13E+01	0.283	4.62E+09	241.75	--
2	$3d_{3/2}\ 3d_{5/2}^2\ 4f_{5/2}$	1	3	$3d_{3/2}\ 3d_{5/2}^3$	0	2	5.13E+01	0.710	1.16E+10	241.87	--
2	$3d_{5/2}^3\ 4f_{5/2}$	1	2	$3d_{3/2}\ 3d_{5/2}^3$	0	2	5.13E+01	0.264	6.02E+09	241.75	--
2	$3d_{5/2}^3\ 4f_{5/2}$	1	2	$3d_{3/2}\ 3d_{5/2}^3$	0	1	5.13E+01	0.546	1.25E+10	241.79	--
2	$3d_{3/2}\ 3d_{5/2}^2\ 4f_{7/2}$	1	4	$3d_{3/2}\ 3d_{5/2}^3$	0	3	5.14E+01	0.876	1.11E+10	241.25	--
3	$3d_{3/2}\ 3d_{5/2}^2\ 4f_{7/2}$	1	0	$3d_{3/2}\ 3d_{5/2}^3$	0	1	4.99E+01	0.131	1.42E+10	248.55	--
3	$3d_{3/2}^3\ 4f_{5/2}$	1	3	$3d_{5/2}^4$	0	2	4.98E+01	0.355	5.45E+09	248.97	--
3	$3d_{5/2}^3\ 4f_{5/2}$	1	3	$3d_{3/2}^2\ 3d_{5/2}^2$	0	2	4.99E+01	0.617	9.52E+09	248.59	--
3	$3d_{3/2}\ 3d_{5/2}^2\ 4f_{5/2}$	1	1	$3d_{5/2}^4$	0	0	4.99E+01	0.148	5.32E+09	248.59	--
4	$3d_{5/2}^3\ 4p_{1/2}$	1	2	$3d_{3/2}\ 3d_{5/2}^3$	0	3	2.89E+01	1.065	7.74E+09	428.31	--
5	$3d_{3/2}\ 3d_{5/2}^2\ 4f_{7/2}$	1	5	$3d_{3/2}^2\ 3d_{5/2}^2$	0	4	4.73E+01	0.458	4.05E+09	261.84	--
5	$3d_{3/2}\ 3d_{5/2}^2\ 4f_{7/2}$	1	3	$3d_{3/2}\ 3d_{5/2}^3$	0	3	4.74E+01	0.427	5.95E+09	261.38	--
6	$3d_{3/2}^2\ 3d_{5/2}\ 4f_{7/2}$	1	2	$3d_{3/2}^3\ 3d_{5/2}$	0	1	4.88E+01	0.208	4.31E+09	254.02	--
6	$3d_{3/2}\ 3d_{5/2}^2\ 4f_{7/2}$	1	4	$3d_{3/2}\ 3d_{5/2}^3$	0	4	4.88E+01	0.690	7.90E+09	254.30	--
6	$3d_{3/2}\ 3d_{5/2}^2\ 4f_{7/2}$	1	5	$3d_{3/2}^2\ 3d_{5/2}^2$	0	5	4.88E+01	0.870	8.17E+09	254.11	--
7	$3d_{3/2}\ 3d_{5/2}^2\ 4p_{1/2}$	1	3	$3d_{3/2}\ 3d_{5/2}^3$	0	4	3.34E+01	0.631	4.35E+09	371.69	--
7	$3d_{3/2}\ 3d_{5/2}^2\ 4f_{7/2}$	1	3	$3d_{3/2}^2\ 3d_{5/2}^2$	0	2	4.54E+01	0.585	7.49E+09	272.84	--
7	$3d_{3/2}\ 3d_{5/2}^2\ 4f_{5/2}$	1	2	$3d_{3/2}^2\ 3d_{5/2}^2$	0	2	4.55E+01	0.583	1.05E+10	272.34	--
8	$3d_{3/2}^2\ 3d_{5/2}\ 4f_{7/2}$	1	5	$3d_{3/2}^2\ 3d_{5/2}^2$	0	4	5.34E+01	1.851	2.08E+10	232.38	--
8	$3d_{3/2}\ 3d_{5/2}^2\ 4f_{7/2}$	1	4	$3d_{3/2}\ 3d_{5/2}^3$	0	3	5.34E+01	1.463	2.01E+10	232.38	--
8	$3d_{3/2}\ 3d_{5/2}^2\ 4f_{5/2}$	1	3	$3d_{3/2}^2\ 3d_{5/2}^2$	0	2	5.34E+01	1.125	1.99E+10	232.28	--
9	$3d_{3/2}^2\ 3d_{5/2}\ 4f_{5/2}$	1	2	$3d_{3/2}^2\ 3d_{5/2}^2$	0	2	5.50E+01	0.228	5.98E+09	225.54	--
9	$3d_{3/2}^2\ 3d_{5/2}\ 4f_{5/2}$	1	3	$3d_{3/2}^2\ 3d_{5/2}^2$	0	2	5.50E+01	0.606	1.14E+10	225.52	--
9	$3d_{3/2}^2\ 3d_{5/2}\ 4f_{7/2}$	1	4	$3d_{3/2}^2\ 3d_{5/2}^2$	0	3	5.49E+01	0.915	1.33E+10	225.69	--
10	$3d_{3/2}^3\ 4p_{1/2}$	1	0	$3d_{3/2}^3\ 3d_{5/2}$	0	1	3.11E+01	0.164	6.92E+09	398.12	398.08
10	$3d_{3/2}^2\ 3d_{5/2}\ 4p_{1/2}$	1	1	$3d_{3/2}^2\ 3d_{5/2}^2$	0	2	3.11E+01	0.271	3.81E+09	398.12	398.38
10	$3d_{3/2}\ 3d_{5/2}^2\ 4p_{1/2}$	1	4	$3d_{3/2}\ 3d_{5/2}^3$	0	4	3.11E+01	0.877	4.09E+09	398.68	398.42
11	$3d_{3/2}\ 3d_{5/2}^2\ 4p_{1/2}$	1	5	$3d_{3/2}^2\ 3d_{5/2}^2$	0	6	3.05E+01	2.638	9.65E+09	407.15	407.41

المملكة الأردنية الهاشمية

صندوق دعم البحث العلمي

الجامعة الهاشمية

المجلة الأردنية
لعلوم الأرض والبيئة

JJEES

مجلة علمية عالمية محكمة

المجلد (١٥) العدد (٤)

http:// jjees.hu.edu.jo/

ISSN 1995-6681

المجلة الأردنية لعلوم الأرض والبيئة

مجلة علمية عالمية محكمة

المجلة الأردنية لعلوم الأرض والبيئة: مجلة علمية عالمية محكمة ومفهرسة ومصنفة، تصدر عن عمادة البحث العلمي في الجامعة الهاشمية وبدعم من صندوق البحث العلمي - وزارة التعليم العالي والبحث العلمي، الأردن.

ترسل البحوث إلكترونيا إلى البريد الإلكتروني التالي:

رئيس تحرير المجلة الأردنية لعلوم الأرض والبيئة

jjees@hu.edu.jo

لمزيد من المعلومات والأعداد السابقة يرجى زيارة موقع المجلة على شبكة الانترنت على الرابط التالي:

www.jjees.hu.edu.jo

المملكة الأردنية الهاشمية صندوق دعم البحث العلمي الجامعة الهاشمية

JJEES

المجلة الأردنية لعلوم الأرض والبيئة

المجلد (15) العدد (4)

مجلة علمية عالمية محكمة تصدر بدعم من صندوق دعم البحث العلمي

ISSN 1995-6681 jjees.hu.edu.jo كانون الأول 2024